ABSTRACT

Title of dissertation: ULTRAFAST CONTROL OF SPIN AND MOTION IN TRAPPED IONS

Jonathan Albert Mizrahi
Doctor of Philosophy
2013

Dissertation directed by: Professor Christopher Monroe
Joint Quantum Institute
University of Maryland Department of Physics and National Institute of Standards and Technology

Trapped atomic ions are a promising medium for quantum computing, due to their long coherence times and potential for scalability. Current methods of entangling ions rely on addressing individual modes of motion within the trap and applying qubit state dependent forces with external fields. This approach can limit the speed of entangling gates and make them vulnerable to decoherence due to coupling to unwanted modes or ion heating. This thesis is directed towards demonstrating novel entanglement schemes which are not limited by the trap frequency, and can be made almost arbitrarily fast. Towards this goal, I report here on the first experiments using ultrafast laser pulses to control the internal and external states of a single trapped ion. I begin with experiments in ultrafast spin control, showing how a single laser pulse can be used to completely control both spin degrees of freedom of the ion qubit in tens of picoseconds. I also show how a train of weak pulses can be

used to drive Raman transitions based on a frequency comb. I then discuss experiments using pulses to rapidly entangle the spin with the motion, and how careful spectral redistribution allows a single pulse to execute a spin-dependent momentum kick. Finally, I explain how these spin-dependent momentum kicks can be used in the future to create an ultrafast entangling gate. I go over how such a gate would work, and present experimentally realizable timing sequences which would create a maximally entangled state of two ions in a time faster than the period of motion in the trap.

ULTRAFAST CONTROL OF SPIN AND MOTION IN TRAPPED IONS

by

Jonathan Albert Mizrahi

Dissertation submitted to the Faculty of the Graduate School of the
University of Maryland, College Park in partial fulfillment
of the requirements for the degree of
Doctor of Philosophy
2013

Advisory Committee:
Professor Christopher Monroe, Chair/Advisor
Professor William Phillips
Professor J.V. Porto
Professor Howard Milchberg
Professor Luis Orozco

"There is a single light of science, and to brighten it anywhere is to brighten it everywhere." —Isaac Asimov

To Amanda

Acknowledgments

A trapped ion may work well in a vacuum, but I do not. The work presented here would not have happened without the hard work of many people. First, I have been fortunate to have an excellent advisor, Chris Monroe. I have learned a tremendous amount from Chris. He allowed me great leeway in determining how to proceed day-to-day, while still always being involved and guiding the long-term scientific path. He took something of a risk taking me on as a new graduate student with no experimental background and no clear trajectory, and for that I am extremely grateful.

During my time on this experiment, I have had the privilege of working with Wes Campbell, Crystal Senko, Qudsia Quraishi, Charlie Conover, Ilka Geisel, Kale Johnson, and Brian Neyenhuis. When I first joined the experiment, Wes was an excellent mentor, and taught me much about how to be an effective experimental physicist. For a period of time, it was just myself and Crystal working on the experiment, and her hard work was instrumental to many of the results. Towards the end of graduate school, I worked most closely with Brian and Kale. Both have been great lab partners, and have provided a fresh perspective on the experiment and its direction.

In addition to those I worked with directly, I benefited greatly from interactions with all the other members of the ion trapping lab during my time in grad school. From puzzling over bizarre data to hunting for missing pieces of equipment, everyone in the lab has contributed in some way to this work. In no particular order, they

are: Susan Clark, Dave Hayes, Kenny Lee, David Hucul, Peter Maunz, Dzmitry Matsukevich, Steve Olmschenk, Volkan Inlek, Rajibul Islam, Simcha Korenblit, Jake Smith, Aaron Lee, Phil Richerme, Kihwan Kim, Ming-Shien Chang, Emily Edwards, Jon Sterk, Andrew Manning, Le Luo, Taeyoung Choi, Shantanu Debnath, Caroline Figgatt, Ken Wright, Daniel Brennan, Geoffrey Ji, and Chenglin Cao. I would also like to particularly acknowledge David Hucul's work in designing the blade trap described in chapter 2.

This work would not be possible without the support of funding agencies. I would particularly like to thank the National Science Foundation Physics Frontier Center at JQI, which has supported me. The work presented here is also supported by grants from the U.S. Army Research Office with funding from the DARPA OLE program, IARPA and the MURI program, the NSF PIF Program, and the European Commission AQUTE program.

I likely would never have found myself in graduate school were it not for the encouragement of my parents, Joan and Maurice Mizrahi. They have been nothing but supportive throughout, and I can't thank them enough. I have also benefited from the love and support of my whole family, including my siblings and my parents-in-law. I would in particular like to thank my father-in-law, Bob Denemark, for taking the time to read my thesis and make helpful editorial suggestions.

Lastly, I could not have done any of this without the constant love and support from my wonderful wife, Amanda. She has helped me continuously throughout my six years of graduate school, enduring late night hours and weekend trips to the lab. She encouraged me to go into experimental physics and quantum information,

recognizing before I did that it was what I really wanted to be doing. For all that and more, this thesis is dedicated to her.

And, on one final note, I cannot help but acknowledge the contributions of my son, Ethan. He may have done nothing to directly further the completion of this thesis, but the smiles when I came home at the end of the day made the whole process more enjoyable.

Table of Contents

List of Tables

List of Figures

List of Abbreviations

AC	Alternating Current
AM	Amplitude Modulation
AOM	Acousto-optic Modulator
ATC	American Technical Ceramics
Ba	Barium
CCD	Charge-coupled device
CF	ConFlat
CoM	Center of Mass
CW	Continuous Wave
DC	Direct Current
DDS	Direct Digital Synthesizer
ECDL	External Cavity Diode Laser
EOM	Electro-optic Modulator
FM	Frequency Modulation
HC	Hermitian Conjugate
HO	Harmonic Oscillator
ICCD	Intensified charge-coupled device
JQI	Joint Quantum Institute
NA	Numerical Aperture
Nd:YVO_4	Neodymium-doped yttrium orthovanadate
NEG	Non-Evaporable Getter
OFHC	Oxygen Free High Conductivity
ORNL	Oak Ridge National Laboratories
PBS	Polarizing Beam Splitter
PDH	Pound Drever Hall
PID	Proportional Integral Differential
PMT	Photo-Multiplier Tube
PSD	Power Spectral Density
PZT	Piezo-Electric Transducer (or the specific type of piezo-electric transducer: Lead Zirconate Titanate: $Pb[Zr_xTi_{1-x}]O_3$)
QC	Quantum Computing
QE	Quantum Efficiency
QI	Quantum Information
RC	Resistor/Capacitor
REMPI	Resonantly Enhanced Multi-Photon Ionization
RF	Radio Frequency
RWA	Rotating Wave Approximation
SDK	Spin-Dependent Kick
SMA	Sub-Miniature Version A
TA	Tapered Amplifier
TDC	Time-to-Digital Converter
TIQI	Trapped Ion Quantum Information
UHV	Ultra-High Vacuum
Yb	Ytterbium

Chapter 1

Introduction

1.1 Quantum Information

Over the past few decades, the ability to precisely control quantum systems has opened the door to the field of *quantum information*. Quantum information broadly refers to the use of quantum phenomena as a tool to encode and process information. Quantum information has a number of exciting applications. These include *quantum simulation*, in which a well-controlled quantum system is used to emulate the behavior of another, poorly understood quantum system; *quantum cryptography*, in which a quantum system is used to ensure secure communication; and *quantum computing*, in which a quantum system is manipulated to perform an algorithm. The work described here deals with quantum information using trapped atomic ions, which is relevant to all of these applications.

The advantage of using quantum building blocks in these applications rests with the phenomenon of *entanglement*. Entanglement is a uniquely quantum phenomenon, in which separate objects can have correlations beyond those allowed classically. Entanglement provides a new resource which algorithms can draw upon

to enable dramatically faster solutions to certain classes of problems [1].

In classical information, the basic element of information is the bit, which can be in one of two states, typically denoted 0 or 1. A bit is the smallest unit which contains information, and all larger sets of information can be represented by strings of bits. Because a bit can only be in one of two states, the bit's "state space" is zero-dimensional.

In quantum information, the analogous role is played by the quantum bit or "qubit." There are similarly two basis states, denoted $|0\rangle$ and $|1\rangle$, where the symbol $|\cdot\rangle$ follows Dirac's bra-ket notation for quantum states. However, unlike in classical information, qubits can be in superpositions of $|0\rangle$ and $|1\rangle$. An arbitrary qubit can be written as:

$$|\psi\rangle = \sin\left(\frac{\theta}{2}\right)|0\rangle + e^{i\phi}\cos\left(\frac{\theta}{2}\right)|1\rangle \tag{1.1}$$

A qubit can be visualized as corresponding to a point on the surface of a sphere, known as the *Bloch sphere* [1]. This visualization is shown in figure 1.1. From this representation, it is clear that a qubit's state space is two-dimensional.

On the Bloch sphere, the angles θ and ϕ in equation 1.1 correspond to polar and azimuthal angles, respectively. The north pole therefore represents $|1\rangle$ and the south pole $|0\rangle$. Upon measurement of a qubit in the basis $\{|0\rangle, |1\rangle\}$, it will collapse into either $|1\rangle$ with probability $\cos^2\frac{\theta}{2}$, or $|0\rangle$ with probability $\sin^2\frac{\theta}{2}$. Therefore, θ indicates how close the state is to either $|0\rangle$ or $|1\rangle$. The other angle, ϕ, is known as the *phase* of the qubit. The physical understanding of ϕ is more difficult to see than that of θ. Its effect is seen in the response of the qubit to rotations on the Bloch

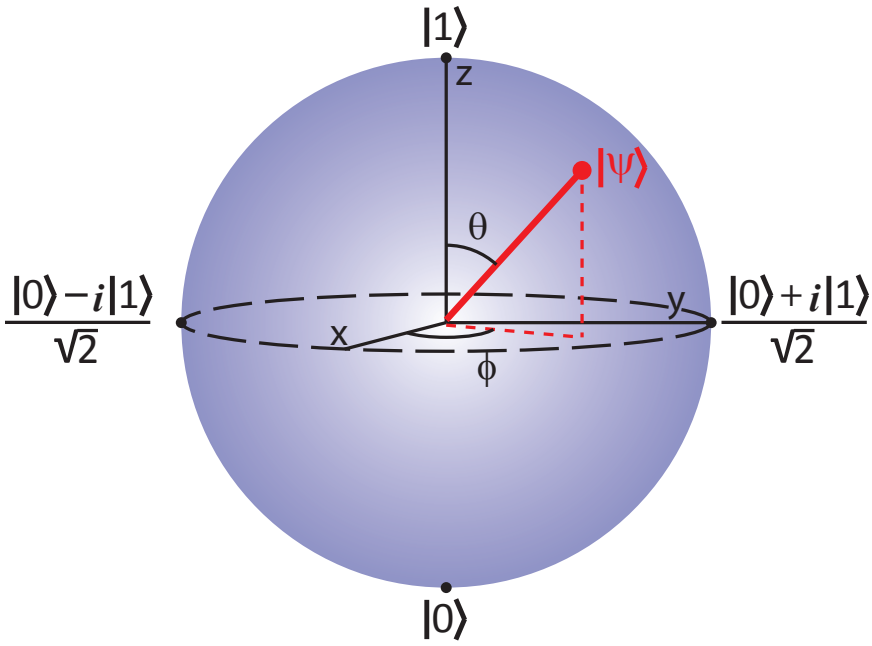

Figure 1.1: Bloch sphere representation of a qubit. The north and south poles are $|0\rangle$ and $|1\rangle$ respectively. Every other point on the sphere represents some superposition of $|0\rangle$ and $|1\rangle$, as in equation 1.1.

sphere – qubits with equal θ but different ϕ will respond differently to rotations. A qubit is a far richer object than its classical analog, which is confined to the poles of the Bloch sphere.

All of this, however, could effectively be represented using a classical analog computer, with continuous physical variables. A classical analog computer is no more capable than a classical digital computer. What makes qubits powerful is that the state of two separate qubits cannot necessarily be understood by describing the state of each qubit separately. Two qubits can be *entangled*. For example, two qubits a and b can be in a superposition of both being $|0\rangle$ or both being $|1\rangle$. Such a state is written:

$$|\psi\rangle_{a,b} = \frac{1}{\sqrt{2}} \left(|0\rangle_a |0\rangle_b + |1\rangle_a |1\rangle_b \right) \tag{1.2}$$

This state cannot be divided into separate parts for a and b, and has no classical

analog. Such states were famously highlighted by Einstein, Podolsky, and Rosen in [2] as paradoxical, now known as the EPR paradox. A measurement performed on a or b will instantaneously collapse the joint wave function of both qubits, even when a and b are widely separated. Einstein described such behavior as representing "spooky action at a distance." It was later shown by John Bell in [3] that the behavior exhibited by states such as that in equation 1.2 differs from the behavior of any conceivable classical state. A wide range of experiments have now shown that nature does in fact exhibit this "spooky" behavior [4–8]. Indeed, this spookiness underlies what makes quantum computers powerful and interesting.

1.2 Building a Quantum Computer

Building a functional quantum computer is a daunting experimental challenge. First believed impractical, the discovery of error correction methods (which allow some degree of imperfection), together with rapid progress in quantum control of diverse systems, has made quantum computing appear to be an achievable goal. The experimental requirements were clearly laid out by DiVincenzo [9]. Slightly restated, they are:

1. A well-defined set of quantum levels which can be identified as qubits.

2. Complete control over the states of individual qubits. This includes the ability to initialize a qubit (typically to $|0\rangle$) and the ability to execute Bloch sphere rotations on any qubit.

3. The ability to execute entangling operations (gates) between different qubits.

4. The ability to measure the state of any qubit.

5. Extraordinarily good isolation from the environment. More precisely, the rate at which any qubit becomes entangled with its environment (the coherence time) must be significantly slower than the time it takes to perform a quantum gate[1].

6. Lastly, scalability to systems of many qubits, while still fulfilling all of the above requirements.

Despite the difficulties inherent in meeting all of these requirements, many different physical implementations have been proposed, and it is a very active field of research [10]. Possible experimental platforms include:

- Trapped atomic ions [11–13]
- Neutral atoms in optical lattices [14, 15]
- Photons [10, 16]
- Quantum Dots [17, 18]
- Superconductors [19, 20]
- Nitrogen-Vacancy centers in diamonds [21]

This list is hardly complete, but provides an idea of the breadth of possibilities. Each implementation above has different advantages and disadvantages, and struggles

[1]Error correction allows for the total algorithm time to be longer than the coherence time, as errors between gates can be corrected.

with different aspects. The work discussed in this thesis deals entirely with quantum computing using trapped atomic ions.

1.3 Trapped Ions

Trapped ion quantum computing is arguably the most mature experimental QI platform. A qubit is identified with two long-lived energy levels of the ion, and each ion represents one qubit. Different ions can be coupled to one another via their collective motion [22], or via their emitted photons [8]. Trapped ions can be very well isolated from the environment in an ultra-high vacuum, resulting in extremely long coherence times. There are well-established means for single and multiple qubit control. High fidelity entanglement of ions is now routinely achieved [23–27], as well as implementations of schemes for analog quantum simulation [28–30] and digital quantum algorithms [31–33]. Over the last fifteen years, progress has been rapid. Figure 1.2 shows the number of ions faithfully entangled since the first successful two-ion entanglement experiments.

The main obstacle currently facing trapped ion quantum computing is scaling up the number of ions that can be coherently controlled in a single system [11]. Current state-of-the-art systems are limited to ~10 ions. However, in order to outperform a classical computer at tasks such as factoring, a trapped ion quantum computer would need to control thousands of trapped ions, both for computation and for error-correction overhead (One notable exception is quantum simulations, in which systems as small as 40 qubits cannot be simulated on a classical com-

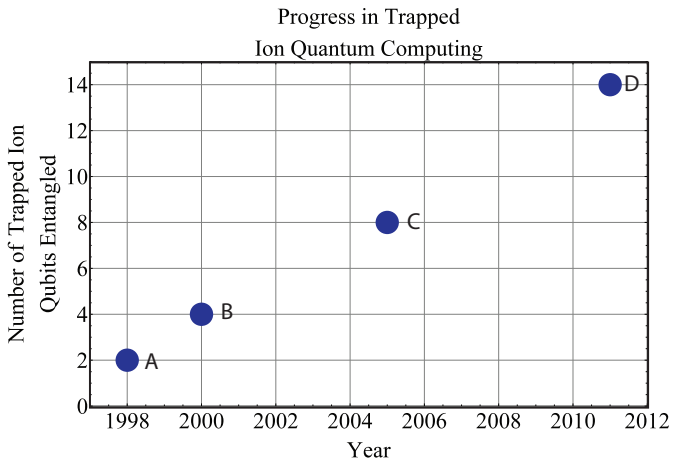

Figure 1.2: Progress in trapped ion quantum computing, compilation courtesy of Ref. [34]. A: Ref. [35]; B: Ref. [24]; C: Ref. [25]; D: Ref. [27]

puter [36]).

The technique that has become standard for entangling trapped ions is that of Mølmer and Sørensen, described in Refs. [37–39]. In that scheme, the ions are coupled via virtual excitation of phonons, using a single normal mode of motion. The remarkable feature of this scheme is that for sufficiently cold ions, it is independent of ion temperature. This is in stark contrast to the original ion entanglement proposal of Cirac and Zoller [40], which required the ions to be in their motional ground state (a far more difficult experimental requirement). The Mølmer-Sørensen gate requires the ions to be cooled to the *Lamb-Dicke regime*. The Lamb-Dicke regime is a constraint on the ion's wave packet size, which states that the extent of the ion wave packet is much smaller than the wavelength of the laser exciting the transition.

The requirement that an individual mode of motion be addressed places a limit on the maximum speed of such a gate – it must be significantly slower than the gap between normal mode frequencies of the trap. This follows from a basic

fact from Fourier transform theory, which states that to resolve a spectral feature with resolution $\Delta\omega$ requires a time of order $1/\Delta\omega$. Therefore, if a gate functions by resonantly coupling to one mode of motion and no other, it must be much slower than the inverse of the difference between neighboring mode frequencies.

The Mølmer-Sørensen gate has proven highly successful over the past decade. It has been used to create two ion entanglement with greater than 99% fidelity [23], and allowed many of the advances mentioned above. However, a number of problems arise when it is scaled to large chains of ions. In general, a chain of N ions will have $3N$ normal modes of motion. Each of these modes will typically have a different frequency. For large N, the spectrum of modes therefore becomes very dense. Based on the Fourier speed limit mentioned above, the requirement to couple to just one mode means that the gate speed will have to slow down significantly as N grows. This will make the gate more vulnerable to a variety of noise sources, discussed below. This problem can be ameliorated by increasing the normal mode frequencies, which can be done by reducing the size of the ion trap. However, that has resulted in significantly higher heating rates, which reduce the fidelity of the entanglement.

There are also technical issues related to the laser driving the gate. Because the qubit levels are coupled via a Raman transition, off-resonant coupling to the excited state can result in spontaneous emission. The laser can also change the qubit frequency via a differential light shift (also called an AC Stark shift). Depending on the size of this shift, small laser intensity differences at different ions can result in significantly reduced gate fidelities. These issues are reduced if the laser frequency is further from resonance, at the expense of requiring more laser power to achieve

the same gate speed. Trapped ion frequencies are typically in the ultraviolet (UV), and high power UV lasers are often not readily available.

These issues are being attacked from a number of different directions. There are ongoing efforts to reduce heating rates [41, 42]. To limit the number of ions in a chain at one time, ions could be shuttled around a chip between trap regions dedicated to computation versus others dedicated to storage [43, 44]. This way, computations involving many ions could be performed, with only a few ions being addressed at any one time. Alternatively, computations could be performed on many small chains of ions, which could then be remotely entangled via their emitted photons [13]. Addressing the issue of laser induced decoherence, there has been recent work on "laser-less" gates, wherein the qubit levels are directly coupled [45].

In this thesis, I discuss a different approach from those outlined above. This work is directed towards using high power UV pulses to create an entangling gate that differs greatly from the Mølmer-Sørensen gate. This new gate, proposed theoretically in [46, 47], works by applying carefully timed sequences of ultrafast spin-dependent momentum kicks. This ultrafast gate does not spectroscopically resolve sidebands, and as such does not suffer from the speed limitations discussed above. It can, in principle, operate far faster than a trap period. By going so fast it is less sensitive to a wide range of noises sources which decrease in amplitude with frequency ("$1/f$" noise). Moreover, the fast gate proposed is completely independent of ion temperature (so long as the motion remains harmonic), and so avoids the requirement of cooling to the Lamb-Dicke regime. As such, it is insensitive to ion heating, a serious issue in many ion trapping experiments. This fast gate is enabled

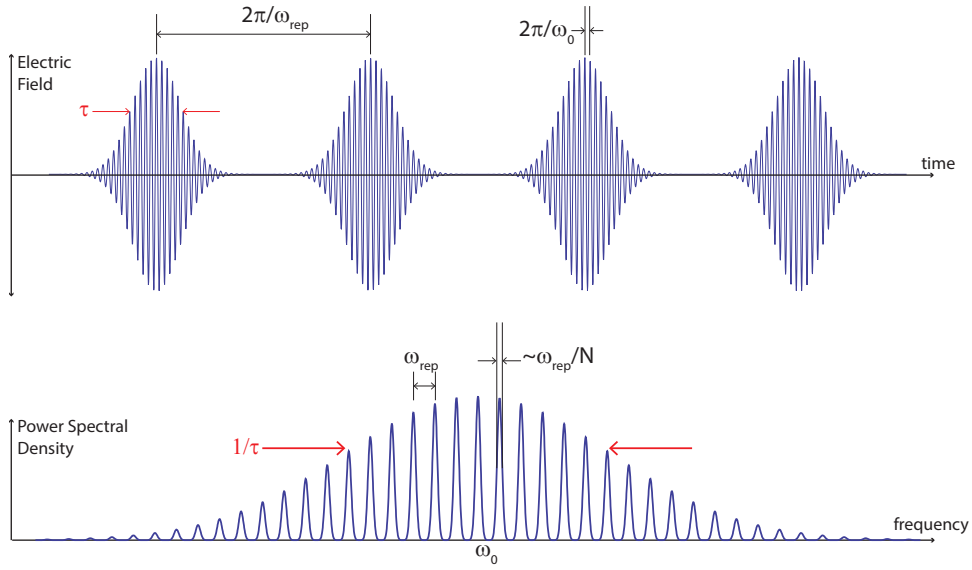

Figure 1.3: A sequence of pulses produced by a mode-locked laser produces a frequency comb. In frequency space, the repetition rate of the pulse train ω_{rep} becomes the spacing of comb lines. The bandwidth of the comb is determined by the duration of each pulse τ. The width of each comb tooth goes down as the number of pulses N increases, approximately as ω_{rep}/N. The center frequency of the comb ω_0 is determined by the carrier frequency of the pulse train.

by high power mode-locked lasers, which are a new tool for ion trapping. These lasers offer a number of advantages, as I will now discuss.

1.4 Pulsed Lasers and Frequency Combs

A *mode-locked laser* is a laser that produces a periodic sequence of ultrashort, phase-coherent pulses. The pulse duration of such a laser can be anywhere from femtoseconds to picoseconds, although all the pulses in this work are ~10 picosecond duration. The Fourier transform of such a pulse train is a *frequency comb*, which consists of many sharp lines separated by the repetition rate of the pulse train. This is shown in figure 1.3.

Over the past decade, such frequency combs have revolutionized the field of

optical frequency metrology [48–51]. This is due to the broad spectrum of lines with a precisely controllable and measurable spacing (the repetition rate) present in a frequency comb. This spectrum allows it to serve as a precise connection between distant frequencies. In the context of metrology, this feature is used as a ruler in which the spacings between comb lines serve as tick marks. In the context of coherent control, widely spaced comb lines in a frequency comb can be used to directly bridge large frequency gaps between energy levels in a controllable way. Because of this application, mode-locked lasers have a bright[2] future as a tool for qubit manipulation in a number of different quantum computer architectures. They have already been used to effectively control diverse quantum systems, including multilevel atoms [52], molecules [53] and semiconductor spin states [54, 55]. In this thesis, I discuss their use in controlling trapped ions. Much of this work has previously been reported in [56–59].

From a technical standpoint, the large bandwidth inherent in a comb eliminates some of the complexity and expense of driving Raman transitions. For hyperfine qubits in ions, the frequency splitting is typically several GHz. Bridging this gap with CW beams requires either two separate phase-locked lasers, or a high frequency electro-optic modulator (EOM) (which is typically inefficient). By contrast, a single mode-locked laser has sufficient bandwidth to directly drive the transition, without the need for a second laser or a high frequency EOM. Moreover, it is not necessary to stabilize either the carrier-envelope phase or the repetition rate of the mode-locked laser, as will be discussed later. This enables the use of commercially

[2]ha-ha-ha

available, industrial lasers.

The major advantage of using pulsed lasers, however, lies in their enormous instantaneous intensity. Typical repetition rates for the lasers used in this thesis are around 100 MHz. This means that for a 10 ps pulse, the duty cycle is $\sim 10^{-3}$. The instantaneous intensity in a single pulse is therefore three orders of magnitude larger than that of a continuous wave (CW) laser of equal average power. This has several advantages. First, large instantaneous intensity allows efficient harmonic generation. Therefore, pulsed sources of ultraviolet light typically have far higher average power than CW sources. This high average power in turn allows operating with a larger detuning, which reduces some of the sources of laser-induced decoherence mentioned above. More fundamentally, the large instantaneous intensity allows ion manipulation far faster than would be possible with a CW laser. This ultrafast manipulation opens the door to the ultrafast entangling gates mentioned above. Because of these advantages, pulsed lasers will likely prove to be a key element in the trapped ion toolbox in the years to come.

1.5 Outline

In what follows, I will present our work on controlling trapped ions using fast laser pulses. The layout is as follows:

- Chapter 2 goes over the fundamentals of ion trapping. This includes the dynamics of the RF Paul trap, normal modes of motion of two ions, and experimental construction of a Paul trap.

- Chapter 3 covers the details of using $^{171}Yb^{+}$ as a qubit. There I outline the procedure used for ionization and loading, Doppler cooling, state preparation, and state detection. The experimental background described in chapters 2-3 provide the framework for the main work presented in chapters 4-6.

- Chapter 4 explains ultrafast spin control with fast pulses. An analytic solution is developed, and experimental results presented for multiple regimes of pulse energy.

- Chapter 5 presents ultrafast spin-motion entanglement. There I explain how an impulsive spin-dependent kick is created, and show data demonstrating the predicted effects.

- Chapter 6 shows how a two ion gate would work using the techniques described here, and concludes with an outlook for the future.

Chapter 2

Ion Trapping

Ion traps have become a major tool to achieve diverse goals, including optical frequency standards for atomic clocks [60–62], precision spectroscopy [63–67], tests of fundamental physics [68–70], and (as in this work) quantum information [11]. These applications have been enabled by the ability to laser cool trapped atomic ions [71, 72]. This creates a pristine, exquisitely controlled quantum system.

The two main types of ion traps are the Penning trap [73] and the RF Paul trap [74]. All of the work described herein was done using a Paul trap. What follows is an overview of the mechanism by which a Paul trap operates, followed by the experimental details of the traps used in this work.

Ideally, an ion would be trapped via a configuration of electrodes which produce a stable potential minimum at some point in space. The ion would then sit at that point, and any perturbation from the center would result in a restorative force back towards the center. Electric field lines of such a potential are shown in figure 2.1(a). Unfortunately Earnshaw's theorem states that such a potential is impossible to realize. Earnshaw's theorem can be understood via one of Maxwell's equations,

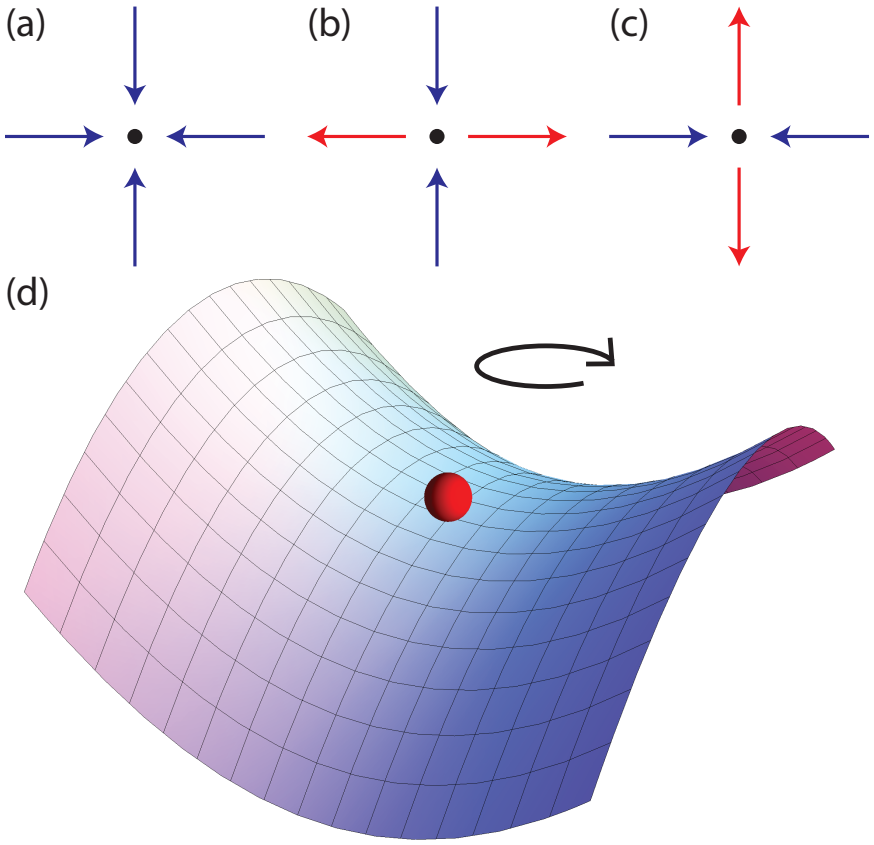

Figure 2.1: Different electric field configurations. (a) is physically impossible, but (b) and (c) are allowed. Alternating rapidly between (b) and (c) creates an effective trap[2]. (d) is a mechanical equivalent: a ball can be trapped in a saddle if the saddle is spinning.

which states that the electric field $\mathbf{E}$ in vacuum must be divergence-free [75]:

$$\nabla \cdot \mathbf{E} = 0 \tag{2.1}$$

A potential of the form described above would have a non-zero divergence, and is therefore impossible. For any static set of voltages, the equilibrium position of the ion will always be unstable along some direction.

A Paul trap circumvents this restriction by using dynamic fields instead of static fields. At any given instant in time, the equilibrium point is stable along

[2]In (a)-(c), the electric field lines perpendicular to the plane of the page should be understood to create a stable minimum, i.e. the electric field lines above and below the page are pointing into the page. Indeed, (a) would be possible if the elecric field lines perpendicular to the page were pointing out of the page, creating an unstable equilibrium.

one axis and unstable along another, as in figure 2.1(b) and (c). The trick is then to rapidly alternate between which axis is stable and which is unstable. The time averaged force felt by the ion is then a restoring force in all directions [73]. This is called a pondermotive potential. A mechanical analog to this type of effect is shown in figure 2.1(d) – a ball can be trapped in a saddle if the saddle is rotating.

A number of different geometries can be used to create the potential described above. Two were used in the work presented here. The first is a six electrode configuration known as a four rod trap, shown in figure 2.2. The four rods create the oscillating potential. Two of the rods are driven with an oscillating voltage, while the other two rods are at a fixed DC voltage (typically close to ground). The oscillation frequency is generally tens of MHz, hence these rods are designated the radiofrequency (RF) rods. When the RF voltage is positive, electric field lines point from the RF rods to the DC rods. When the voltage is negative, the field lines reverse. This creates the pondermotive potential in the plane orthogonal to the rods. Confinement along the axis of the trap is provided by two endcaps which are held at a static, positive voltage.

The second geometry is shown in figure 2.3. It consists of four blades in the place of the four rods. The blades are arranged in an X, as seen in the figure. As with the four rod trap, there are two RF blades and two DC blades. However, each DC blade consists of five separate electrodes, each of which can be at a different voltage. There are therefore a total of ten DC electrodes and two RF electrodes. Axial confinement is created by increasing the outer segment voltages relative to the inner segments. This geometry allows slightly more flexibility, as will be discussed

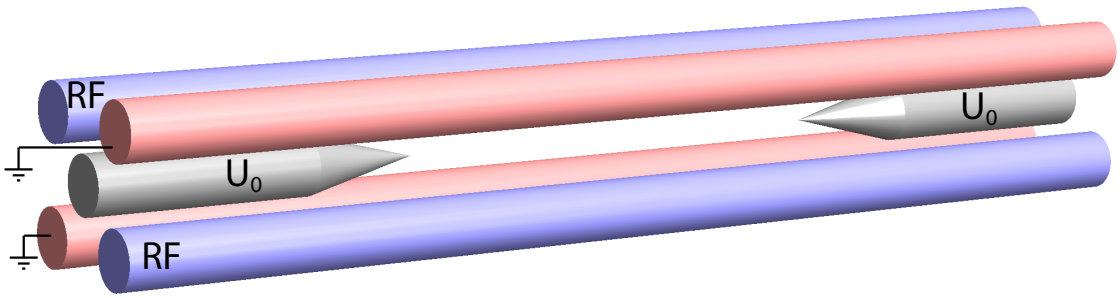

Figure 2.2: Drawing of four rod RF trap. The two light blue rods are driven with an oscillating voltage, while the two light red rods are kept at a fixed voltage (approximately 0 V, shown grounded here). The two endcap needles are kept at a fixed, positive voltage to provide axial confinement.

later. The theory description below is written with the four rod trap in mind, but applies equally well to the blade trap.

2.1 RF Trap Theory

With the broad outline described above, I will now briefly go over the theoretical analysis of the dynamics of an RF Paul trap. I will not attempt to completely cover this topic, but merely to outline its salient features. The interested reader can consult many excellent and thorough analyses [73, 74, 76, 77].

Let the axis of symmetry of the trap define the z-axis, the plane joining the centers of the RF rods define the x-z plane, and that joining the DC rods define the y-z plane. Let the origin refer to the center point of the trap. I will refer to the z-axis as the axial direction, and the x and y axes as the transverse (also called radial) directions. Let the voltage applied to the RF rods be given by $V(t) = V_0 \cos(\Omega t)$, where V_0 is the RF amplitude and Ω is the RF frequency. Let the voltages applied to the two endcaps be equal, and given by U_0. If the four rods were

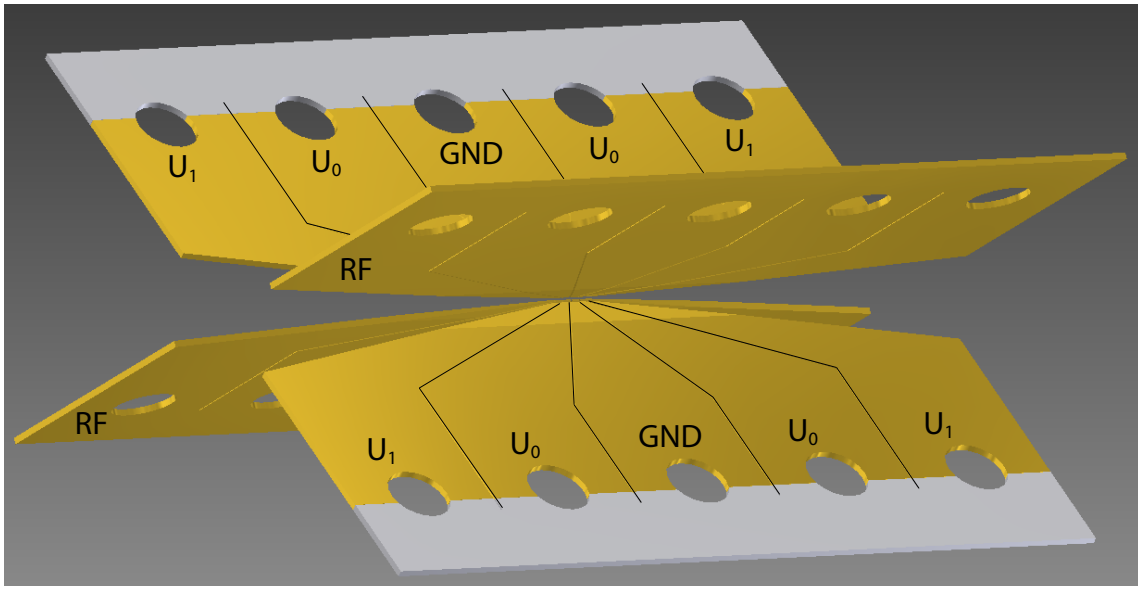

Figure 2.3: Drawing of blade trap used here. The mechanism is the same as the four rod trap, except that the DC blades are segmented into 5 segments. Axial confinement is then generated by the outer segments, which are held at U_0 and U_1. Micromotion compensation and principal axis rotation can be accomplished by adjusting the 12 DC control voltages (1 for each RF blade + 5 for each DC blade).

infinite hyperbolic electrodes (rather than cylinders), then the transverse potential would be analytically soluble, and given by [77]:

$$V = \frac{1}{2} V_0 \cos(\Omega t) \left(1 + \frac{x^2 - y^2}{R^2}\right) \tag{2.2}$$

where R is the distance from the trap center to an electrode, as shown in figure 2.4. When the hyperbolic electrodes are deformed into cylinders, the potential is no longer analytically soluble. However, equation 2.2 remains approximately true close to the trap axis.

The axial potential has the approximate form:

$$U = \frac{\kappa U_0}{Z^2} \left(z^2 - \frac{1}{2}\left(x^2 + y^2\right)\right) \tag{2.3}$$

where κ is a geometric factor (of order 1) and Z is the distance from the origin to

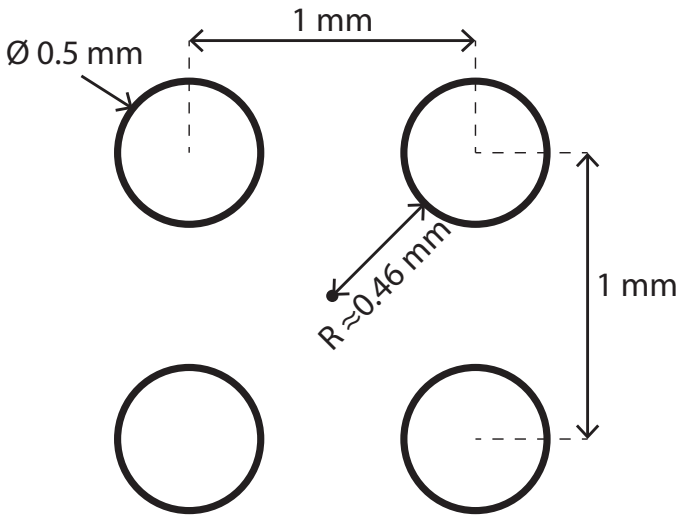

Figure 2.4: Four rod trap dimensions.

an endcap. The total potential at the trap center is therefore:

$$V_{\text{tot}} = V + U = \frac{1}{2}V_0 \cos(\Omega t)\left(1 + \frac{x^2 - y^2}{R^2}\right) + \frac{\kappa U_0}{Z^2}\left(z^2 - \frac{1}{2}\left(x^2 + y^2\right)\right) \tag{2.4}$$

From equation 2.4, the electric field is given by [78]:

$$\begin{aligned}\mathbf{E}(x, y, z, t) &= -\nabla V_{\text{tot}} \\ &= -V_0\left(\frac{x\hat{x} - y\hat{y}}{R^2}\right)\cos(\Omega t) - \frac{\kappa U_0}{Z^2}\left(-x\hat{x} - y\hat{y} + 2z\hat{z}\right)\end{aligned} \tag{2.5}$$

where $\hat{x}$, $\hat{y}$, and $\hat{z}$ are unit vectors in the respective directions. Using equation 2.5, The differential equations governing the motion of an ion with mass m and charge e follow directly from Newton's second law:

$$\ddot{\mathbf{r}} = \frac{\mathbf{F}}{m} = \frac{e}{m}\mathbf{E}(x, y, z, t) \tag{2.6}$$

where $\mathbf{r} = x\hat{x} + y\hat{y} + z\hat{z}$ and $\mathbf{F}$ is the total force on the ion. Let $r_x = x$, $r_y = y$, and $r_z = z$. Combining equations 2.5 and 2.6 show that the ion motion is each dimension is governed by the Mathieu equation:

$$\ddot{r}_i + \frac{\Omega^2}{4}\left(a_i + 2q_i \cos[\Omega t]\right) r_i = 0 \tag{2.7}$$

where $i = x, y, z$. The a_i and q_i parameters characterize the trap in each dimension. They are given by:

$$\begin{aligned} a_x &= -\frac{4e\kappa U_0}{mZ^2\Omega^2} & a_y &= -\frac{4e\kappa U_0}{mZ^2\Omega^2} & a_z &= \frac{8e\kappa U_0}{mZ^2\Omega^2} \\ q_x &= \frac{2eV_0}{mR^2\Omega^2} & q_y &= -\frac{2eV_0}{mR^2\Omega^2} & q_z &= 0 \end{aligned} \tag{2.8}$$

Note that $q_z = 0$ in equations 2.8. Substituting this into equation 2.7 shows that the equation of motion in the axial direction reduces to that of a simple harmonic oscillator. The frequency is given by:

$$\omega_z = \sqrt{\frac{\Omega^2}{4}\frac{8e\kappa U_0}{mZ^2\Omega^2}} = \left(\sqrt{\frac{2e\kappa}{m}}\right)\frac{\sqrt{U_0}}{Z} \tag{2.9}$$

The first term in parentheses is determined by the choice of ion and by the trap geometry. The axial frequency is then determined entirely by the endcap voltage and the distance to the endcaps. This is true in the idealized hyperbolic geometry solved here; any real trap will have a small but non-zero value for q_z. However, the above result remains approximately true. Describing the motion in the transverse directions requires solving equation 2.7, discussed below.

2.1.1 Solution

In general, there is no closed form solution to equation 2.7. There are series solutions; general derivations of those solutions can be found in [76]. For the purposes of this thesis, the trap is operated in a regime where $a_i \ll 1$ and $q_i \ll 1$. In that case, equation 2.7 can be solved to lowest order in a_i and q_i. The result is [77]:

$$r_i(t) = r_{0_i}\cos\left(\omega_i t + \phi_{S_i}\right)\left(1 + \frac{q_i}{2}\cos\left(\Omega t + \phi_M\right)\right) \tag{2.10}$$

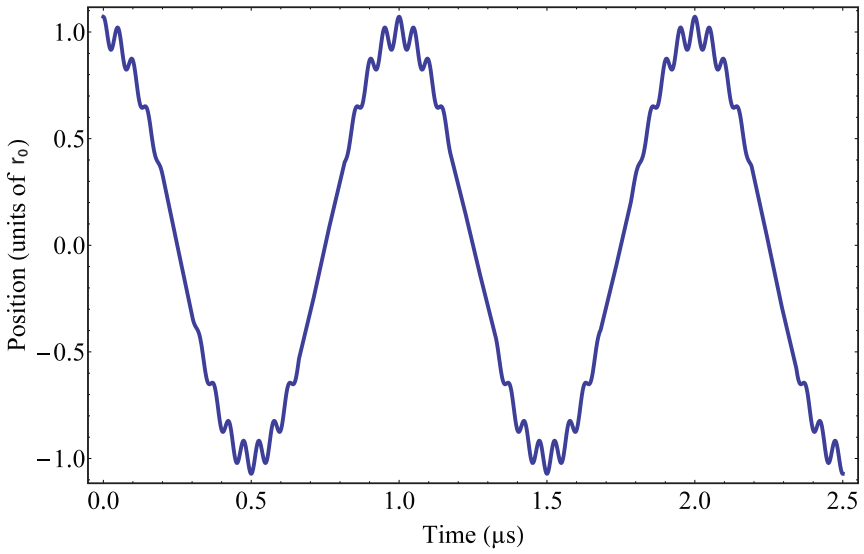

Figure 2.5: Trapped ion position as a function of time along one transverse dimension (x or y). The main behavior is the ordinary oscillations of a harmonic oscillator, known as the secular motion. It is superimposed with a faster oscillation at the RF drive frequency, known as micromotion. The evolution shown here is for typical parameters used in experiments described in this thesis (see sections 2.1.4 and 2.3): A $^{171}Yb^{+}$ ion with $\Omega/2\pi = 20$ MHz, $\omega/2\pi = 1$ MHz, $V_0 = 500$ V, and $R = 500$ μm. These parameters lead to $q = 0.14$.

where r_{0_i} is the amplitude (determined by initial conditions), ω_i and ϕ_{S_i} are the frequency and phase of the *secular motion*, and ϕ_M is the phase of the *micromotion*. ω_i is given by:

$$\omega_i = \frac{\Omega}{2}\sqrt{a_i + q_i^2/2} \tag{2.11}$$

Examining equation 2.10, it is clear that the condition $q_i \ll 1$ means that the behavior is very close to that of a simple harmonic oscillator. This harmonic motion at frequency ω_i (known as the secular motion of the ion) is slightly modulated by the RF drive at frequency Ω. This small modulation, known as the micromotion of the ion, is an unavoidable aspect of RF traps. Figure 2.5 shows equation 2.10 as a function of time for typical trap parameters.

2.1.2 Excess Micromotion

Equation 2.10 is correct if the electric field is determined entirely by the trap electrodes. However, in realistic experimental situations there may be uncontrolled stray electric fields present in the trap as well. These stray electric fields will cause the equilibrium position defined by the RF fields (the RF null) and that defined by the DC fields (the DC null) to be in different positions. In other words, the stray fields will effectively "push" the ion away from the RF null. This will result in additional micromotion beyond the intrinsic micromotion present in equation 2.10. When a background electric field is added, the equation of motion in equation 2.10 becomes [78]:

$$r_i(t) = [B_i + r_{0_i} \cos(\omega_i t + \phi_{S_i})] \left(1 + \frac{q_i}{2} \cos(\Omega t + \phi_M)\right) \tag{2.12}$$

where B_i is determined by the magnitude of the background field:

$$B_i = \frac{eE_i}{m\omega_i^2} \tag{2.13}$$

where E_i is the magnitude of the stray electric field in direction i. This equation stems from the fact that the new equilibrium point B_i is that where the trap restoring force $m\omega_i^2 r_i$ is equal to the background force eE_i.

Micromotion causes the ion to oscillate at the RF frequency. This motion causes Doppler shifts in the laser frequencies as the ion moves towards or away from the beams. This can reduce the efficiency of both cooling and state detection (which are discussed in chapter 3). More generally, micromotion causes the ion motion to be less harmonic. As trapped ion gates often rely on the harmonic character of the

ion motion, it is important to eliminate micromotion to the highest degree possible. This is done by applying small DC voltages to each of the four rods in such a way as to cancel out the background field at the trap center. There are several techniques for minimizing the micromotion, they are described in detail in [78].

There are two other potential sources of excess micromotion: a phase difference between the two RF rods, and RF pickup on one of the DC electrodes. It is important to try to minimize these sources as well; how this is done is described in section 2.3.

2.1.3 Equation of Motion from Position and Momentum

The above equations express the ion position at any time t as a function of the initial amplitude r_{0_i} and the secular motion phase ϕ_{S_i}. However, for the application in chapter 5, it is more convenient to express the position at a later time t as a function of initial position and momentum. Here I will rewrite equation 2.12 in terms of position and momentum.

No Micromotion Consider a perfectly harmonic trap[3] along one direction with frequency ω. Let $x(t)$ and $p(t)$ represent the ion's position and momentum along this direction, respectively. Define dimensionless coordinates $X(t)$ and $P(t)$ as:

$$X(t) = \frac{x(t)}{x_0} \tag{2.14}$$

$$P(t) = \frac{p(t)}{p_0} \tag{2.15}$$

[3]This corresponds to $q = 0$ in equation 2.10, as would be the case for the axial direction in an idealized trap.

where x_0 is a natural length scale[4], and $p_0 = m\omega x_0$. In terms of these coordinates, the ion motion is given by:

$$X(t) = A\cos(\omega t + \phi) \tag{2.16}$$

$$P(t) = \frac{1}{\omega}\dot{X}(t) = -A\sin(\omega t + \phi) \tag{2.17}$$

where A is the (dimensionless) amplitude, and ϕ is the phase. We can then form the complex phase space parameter:

$$\alpha(t) = X(t) + iP(t) = Ae^{-i\phi}e^{-i\omega t} \tag{2.18}$$

Now noting that $\alpha(0) = Ae^{-i\phi}$, we can write this as:

$$\alpha(t) = \alpha_0 e^{-i\omega t} \tag{2.19}$$

where $\alpha_0 = \alpha(0)$. This expresses the ion's state at any time t in terms of its initial position and momentum. It also shows the well-known result that a freely evolving harmonic oscillator executes circles in phase space. We would like an analogous expression for the case of an ion with micromotion.

With Micromotion Define the following function:

$$M(t) = 1 + \frac{q}{2}\cos(\Omega t + \phi_M) \tag{2.20}$$

$$\Rightarrow \dot{M}(t) = -\frac{q\Omega}{2}\sin(\Omega t + \phi_M) \tag{2.21}$$

From equation 2.12, the ion's (dimensionless) position and momentum are given by:

$$X(t) = A\cos(\omega t + \phi_S)\, M(t) + BM(t) \tag{2.22}$$

$$P(t) = \frac{1}{\omega}\dot{X}(t) = -A\sin(\omega t + \phi_s)\, M(t) + \frac{1}{\omega}\left[B + A\cos(\omega t + \phi_S)\right]\dot{M}(t) \tag{2.23}$$

[4]For a quantum harmonic oscillator, x_0 and p_0 are normally given by $x_0 = \sqrt{\hbar/2m\omega}$ and $p_0 = \sqrt{m\omega\hbar/2}$, although note that the entire discussion in this section is classical.

Proceeding as before, we can construct $\alpha(t)$ as:

$$\alpha(t) = X(t) + iP(t) \tag{2.24}$$

$$= Ae^{-i\phi_s}e^{-i\omega t}M(t) + BM(t) + \frac{i}{\omega}\left[B + A\cos\left(\omega t + \phi_S\right)\right]\dot{M}(t) \tag{2.25}$$

$$= \tilde{A}e^{-i\omega t}\left(M(t) + \frac{i}{2\omega}\dot{M}(t)\right) + \frac{i}{2\omega}\tilde{A}^* e^{i\omega t}\dot{M}(t) + B\left(M(t) + \frac{i}{\omega}\dot{M}(t)\right) \tag{2.26}$$

where $\tilde{A} = Ae^{-i\phi_s}$. Note that $\tilde{A} = \alpha_0$ if there is no micromotion.

Let $M_0 = M(0)$ and $\dot{M}_0 = \dot{M}(0)$. To determine the final state from the initial state, we must rewrite equation 2.26 in terms of α_0:

$$\alpha_0 = \tilde{A}M_0 + BM_0 + \frac{i}{\omega}\left[B + \mathrm{Re}(\tilde{A})\right]\dot{M}_0 \tag{2.27}$$

$$\Rightarrow \tilde{A} = \frac{1}{M_0}\left[\alpha_0 - BM_0 - \frac{i\dot{M}_0}{\omega M_0}\mathrm{Re}(\alpha_0)\right] \tag{2.28}$$

Substituting equation 2.28 into equation 2.26 yields:

$$\begin{aligned}\alpha(t) =& \frac{1}{M_0}\left(\alpha_0 - BM_0 - \frac{i\dot{M}_0}{\omega M_0}\mathrm{Re}(\alpha_0)\right)\left(M(t) + \frac{i}{2\omega}\dot{M}(t)\right)e^{-i\omega t} + \\ & \frac{i}{2\omega}\frac{1}{M_0}\left(\alpha_0^* - BM_0 + \frac{i\dot{M}_0}{\omega M_0}\mathrm{Re}(\alpha_0)\right)\dot{M}(t)e^{i\omega t} + \\ & B\left(M(t) + \frac{i}{\omega}\dot{M}(t)\right)\end{aligned} \tag{2.29}$$

Equation 2.29 is the desired equation. Note that unlike in equation 2.19, the evolved position does not depend only on the initial position and momentum. It also depends on the initial phase of the RF drive ϕ_M, through M_0 and $\dot{M}_0$.

2.1.4 Trap Parameter Estimation

Using equations 2.8 and 2.11, we can now get an idea for the physical parameters appropriate for an ion trap. As explained in chapter 3, the ion is cooled via

Doppler cooling along a single direction. In order to minimize the total ion energy, the Doppler cooling direction is chosen to have an equal projection along each of the three principal axes [79]. In this configuration, the lowest achievable total energy along a single principal axis is given by [79]:

$$E_{\min} = \frac{\hbar\Gamma}{4} \tag{2.30}$$

where Γ is the spontaneous emission rate of the cooling transition. This equation is valid so long as the cooling transition can be approximated as a two-level system, the Doppler cooling beam intensity is well below saturation, and its detuning from resonance is $\Gamma/2$ (Doppler cooling is discussed in chapter 3). Ideally the Doppler cooling process will reduce the ion's energy sufficiently such that the average number of harmonic oscillator phonons $\bar{n}$ is small along the direction which is used for quantum information purposes. The energy of a one-dimensional harmonic oscillator of frequency ω with $\bar{n}$ phonons is well-known to be $\hbar\omega\,(\bar{n} + 1/2)$ [80]. Setting this equal to equation 2.30 yields:

$$\omega = \frac{\Gamma}{4(\bar{n} + 1/2)} \tag{2.31}$$

For $^{171}\mathrm{Yb}^{+}$, $\Gamma = 1.23 \times 10^{8}$ s^{-1}. Therefore, a Doppler-limited phonon number of $\bar{n} < 10$ is achieved for frequencies $\omega/2\pi > 0.47$ MHz. From equations 2.8 and 2.11, the secular frequency in the transverse direction (x or y) is given by:

$$\omega \approx \left(\frac{e}{\sqrt{2}m}\right)\left(\frac{V_0}{R^2\Omega}\right) \tag{2.32}$$

The first term is fixed by the choice of ion, while the second term contains the design parameters: RF voltage, RF frequency, and trap size. From equation 2.32 it

is clear that the secular frequency will increase (and hence $\bar{n}$ will decrease) as the trap is made smaller, the RF drive frequency is made slower, or the RF voltage is made larger. In order for the first order approximation made in writing equation 2.10 to be valid, we must have $\Omega \gg \omega$. If the target ω is in the MHz range, this constrains Ω to be at least tens of MHz. The drive voltage V_0 is limited to be < 1 kV for practical reasons – for typical distances between the wires leading to the RF and DC electrodes, voltages around 1 kV can create an RF discharge, which can destroy the trap. Because of the dire consequences of applying too much voltage, the RF voltage is normally kept well below 1 kV. For an RF voltage of 500 V and frequency of 20 MHz, a 1 MHz transverse trap frequency is achieved for an ion-electrode distance of $R \approx 500$ μm. These estimates typify parameters for an ion trap. Similar estimates could be done for the axial direction; however the gates described in chapter 6 are all done using transverse modes for reasons described there. Other trapped ion gates also benefit from using transverse modes, see [81].

As a side point, equation 2.32 also explains one motivation for the entire line of research described in this thesis. In order to improve existing gates, there is strong motivation to make the ion secular frequency as large as possible. This is because, as discussed in chapter 1, gate speed is limited by the frequency of the ion's motion. Moreover, high trap frequencies result in a lower $\bar{n}$ after Doppler cooling. For the reasons described above, the only free parameter available to significantly increase the trap frequency for a given ion is the ion-electrode distance R. For this reason, many ion trapping groups have endeavored to make their traps as small as possible [11]. However, these small traps are plagued by high heating rates.

These high heating rates interfere with entangling operations and reduce fidelities. The source of these heating rates is poorly understood, but it seems to scale as $1/R^4$ [82]. Because of this unfavorable scaling and the high desirability of small traps, a number of research groups are working on studying and eliminating this heating. By contrast, the entangling operation described in chapter 6 is not limited by the trap frequency and does not require the ions to have a low $\bar{n}$. It is therefore not necessary to have large trap frequencies, and relatively large, macroscopic traps can be used.

2.2 Two Ion Normal Modes

Equation 2.11 gives $\omega_{x,y,z}$ for a single ion. For two ions, there will be six normal mode frequencies. In each direction, the ions can oscillate in phase (called the *center of mass* mode) and out of phase (called the *relative motion* mode, or "stretch" mode for z and "tilt" or "rocking" mode for x and y). I will label these frequencies ω_{x_C} and ω_{x_R}, respectively, and similarly for y and z.

2.2.1 Axial Modes

The axial mode case is shown in figure 2.6(a). Let $z = 0$ be the trap center, and z_1 and z_2 be the positions of ions 1 and 2. In the harmonic approximation, the confining force of the trap on ion i is given by $F_{\mathrm{trap}} = -m\omega_z^2 z_i$. The Coulombic repulsion between the ions is $F_{\mathrm{Coulomb}} = \frac{e^2/4\pi\epsilon_0}{|z_1 - z_2|^2}$. The equations of motion for z_1 and

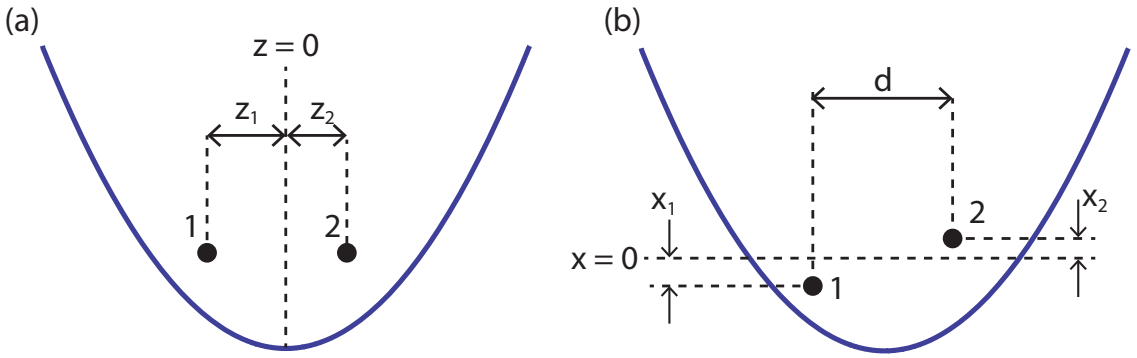

Figure 2.6: Coordinates for analysis of two ion normal modes. (a) axial modes, (b) transverse modes.

z_2 are therefore:

$$m\ddot{z_1} = -m\omega_z^2 z_1 - \frac{e^2/4\pi\epsilon_0}{|z_1 - z_2|^2} \tag{2.33}$$

$$m\ddot{z_2} = -m\omega_z^2 z_2 + \frac{e^2/4\pi\epsilon_0}{|z_1 - z_2|^2} \tag{2.34}$$

At equilibrium, the ions are a distance d apart, and sit at positions $z_1 = -d/2$ and $z_2 = d/2$. d is obtained by setting 2.33 or 2.34 equal to zero:

$$d = \left[\frac{e^2/4\pi\epsilon_0}{m\omega_z^2/2}\right]^{1/3} \tag{2.35}$$

Define the displacements from equilibrium $\tilde{z}_1 = z_1 + d/2$, $\tilde{z}_2 = z_2 - d/2$. Moreover, assume that the displacement from equilibrium is small: $\tilde{z}_{1,2} \ll d$. In that case, we have:

$$\frac{e^2/4\pi\epsilon_0}{|z_1 - z_2|^2} = \frac{m\omega_z^2 d^3/2}{|\tilde{z}_1 - \tilde{z}_2 - d|^2} \approx m\omega_z^2 \left(d/2 + \tilde{z}_1 - \tilde{z}_2\right) \tag{2.36}$$

Equations 2.33 and 2.34 then become:

$$\ddot{\tilde{z}}_1 = \omega_z^2 \left(-2\tilde{z}_1 + \tilde{z}_2\right) \tag{2.37}$$

$$\ddot{\tilde{z}}_2 = \omega_z^2 \left(\tilde{z}_1 - 2\tilde{z}_2\right) \tag{2.38}$$

Taking the sum and difference of these equations shows that the sum and difference oscillations are decoupled:

$$\frac{d^2}{dt^2}\left(\tilde{z}_1+\tilde{z}_2\right)=-\omega_z^2\left(\tilde{z}_1+\tilde{z}_2\right) \tag{2.39}$$

$$\frac{d^2}{dt^2}\left(\tilde{z}_1-\tilde{z}_2\right)=-3\omega_z^2\left(\tilde{z}_1-\tilde{z}_2\right) \tag{2.40}$$

This shows the well-known result that the axial center-of-mass frequency ω_{z_C} is equal to the single ion frequency ω_z, while the relative motion frequency ω_{z_R} is $\sqrt{3}$ times larger:

$$\omega_{z_C}=\omega_z \qquad \omega_{z_R}=\sqrt{3}\omega_z \tag{2.41}$$

2.2.2 Transverse Modes

The transverse mode case is shown in figure 2.6(b). In this case, the equilibrium position of both ions is at $x=0$. As for the axial modes, assume that the displacement from equilibrium is small compared to the ion separation: $x_{1,2} \ll d$. The Coulomb force in the x direction on ion 1 is given by:

$$F_{\text{Coulomb}}=\left(\frac{e^2/4\pi\epsilon_0}{d^2+(x_1-x_2)^2}\right)\left(\frac{x_1-x_2}{d}\right) \tag{2.42}$$

$$=\left(\frac{m\omega_z^2 d^3/2}{d^2+(x_1-x_2)^2}\right)\left(\frac{x_1-x_2}{d}\right) \tag{2.43}$$

$$\approx \frac{m\omega_z^2}{2}\left(x_1-x_2\right) \tag{2.44}$$

The differential equations for ion 1 and 2 are therefore:

$$\ddot{x}_1=-\omega_x^2 x_1+\frac{\omega_z^2}{2}\left(x_1-x_2\right) \tag{2.45}$$

$$\ddot{x}_2=-\omega_x^2 x_2+\frac{\omega_z^2}{2}\left(x_2-x_1\right) \tag{2.46}$$

As in the axial case, the sum and difference oscillations are decoupled:

$$\frac{d^2}{dt^2}(x_1 + x_2) = -\omega_x^2 (x_1 + x_2) \tag{2.47}$$

$$\frac{d^2}{dt^2}(x_1 - x_2) = -\left(\omega_x^2 - \omega_z^2\right)(x_1 - x_2) \tag{2.48}$$

The frequencies are therefore:

$$\omega_{x_C} = \omega_x \qquad \omega_{x_R} = \sqrt{\omega_x^2 - \omega_z^2} \tag{2.49}$$

Equation 2.49 shows that the ratio of normal mode frequencies for the transverse modes can be adjusted by changing the axial potential. By contrast, the frequency ratio for axial modes is fixed at $\sqrt{3}$ according to equation 2.41. This fact will become important in the discussion of ultrafast gates in chapter 6.

2.2.3 Two Ion Hamiltonian

Continuing with the previous discussion of normal mode frequencies, I will show here how the Hamiltonian for two ions can be recast in terms of normal modes. I will consider only the transverse modes in one dimension; extension to axial modes is straightforward.

In terms of each ion's displacement from equilibrium, the Hamiltonian is:

$$H = \frac{1}{2}m\omega_x^2 x_1^2 + \frac{1}{2}m\omega_x^2 x_2^2 + \frac{p_1^2}{2m} + \frac{p_2^2}{2m} + \frac{e^2}{4\pi\epsilon_0}\left(\frac{1}{\sqrt{d^2 + (x_1 - x_2)^2}} - \frac{1}{d}\right) \tag{2.50}$$

$$\approx \frac{1}{2}m\omega_x^2 x_1^2 + \frac{1}{2}m\omega_x^2 x_2^2 + \frac{p_1^2}{2m} + \frac{p_2^2}{2m} - \frac{m\omega_z^2}{4}(x_1 - x_2)^2 \tag{2.51}$$

The first four terms represent each ion's kinetic and potential energy, while the last term represents the Coulomb potential energy. In equation 2.51 I have used equation 2.35, and made the small displacement approximation.

Define the normal mode positions and momenta as:

$$x_C = \frac{1}{2}(x_1 + x_2) \qquad p_C = p_1 + p_2 \tag{2.52}$$

$$x_R = \frac{1}{2}(x_1 - x_2) \qquad p_R = p_1 - p_2 \tag{2.53}$$

In terms of these coordinates, we have:

$$x_1^2 + x_2^2 = 2(x_C^2 + x_R^2) \tag{2.54}$$

$$p_1^2 + p_2^2 = \frac{1}{2}(p_C^2 + p_R^2) \tag{2.55}$$

The Hamiltonian in equation 2.51 can therefore be recast in terms of normal mode coordinates as:

$$H = \frac{1}{2}m\omega_x^2 2x_C^2 + \frac{1}{2}m\omega_x^2 2x_R^2 + \frac{1}{2}\frac{p_C^2}{2m} + \frac{1}{2}\frac{p_R^2}{2m} - \frac{1}{2}2m\omega_z^2 x_R^2 \tag{2.56}$$

$$= \frac{1}{2}M\omega_{x_C}^2 x_C^2 + \frac{1}{2}M\omega_{x_R}^2 x_R^2 + \frac{p_C^2}{2M} + \frac{p_R^2}{2M} \tag{2.57}$$

where in equation 2.57 I have used equation 2.49. Here I have defined the *effective mass* of the normal modes: $M = 2m$. As discussed above, the two harmonic oscillators are now decoupled. The important point about equation 2.57 is that with the normal modes defined as in equations 2.52 and 2.53, the effective mass of the normal mode oscillations is equal to twice the mass of a single ion. I will use this result in chapter 6.

As a side point, note that the coordinate choice in equation 2.52 and 2.53 is not unique. Indeed, normal modes could be defined as $x_{C,R} = (x_1 \pm x_2)/a$, $p_{C,R} = a\,(p_1 \pm p_2)\,/2$, for any value of a. Normal modes defined as such will have an effective mass of $M = (a^2/2)m$. For example, $a = \sqrt{2}$ produces a more symmetric

definition than $a = 2$. I have chosen $a = 2$ because the result is that x_C and p_C correspond to the physical center of mass and total momentum of the system. Other choices do not necessarily have as clear a physical interpretation. Of course, all choices result in the same physics.

2.3 Experiment Construction

Almost all of the experiments described in this thesis were performed using a four rod trap, as shown in figure 2.2. The trap was made out of tungsten wire, with dimensions as shown in figure 2.4. Towards the end of my graduate school career, we built a new trap, as shown in figure 2.9. This blade trap featured several improvements over the four rod trap.

The four rod trap was nearly completed when I joined the lab. However, I was heavily involved in the construction of the blade trap. I will therefore describe the blade trap construction procedure below. The four rod trap procedures were very similar to those described in [83].

2.3.1 Vacuum Chamber

Trapped ion experiments require ultrahigh vacuum (UHV), so as to keep the collision rate with background gas to a minimum. Collisions can cause the ion to fall into the $^2\mathrm{F}_{7/2}$ state, which requires the experiment to be paused until the ion can be returned to the cooling cycle (this is discussed in chapter 3). Collisions can

also form the YbH^+ molecule, which often requires reloading the trap[5]. In general, collisions do not result in the ion being expelled from the trap, as the trap is much deeper than the energy of a room temperature molecule. At a pressure of $< 10^{-10}$ Torr, the ion falls ion the $^2F_{7/2}$ state at a rate of a few times per hour.

To create an ultrahigh vacuum, the chamber was built out of ConFlat (CF) stainless steel vacuum components. An AutoCAD image of the experiment chamber is shown in figure 2.7. Each metal piece was wrapped in foil and baked in air at 250° C for a week. This was to reduce outgassing once the chamber was assembled [85]. The chamber was then assembled as in figure 2.7. OFHC copper gaskets were used to seal each mating surface.

In order to maintain UHV, it is necessary to continuously pump the chamber during operation. This is because outgassing of materials from the chamber walls must be removed. For this reason, two pumps are integrated into the chamber – an ion pump and a non-evaporable getter (NEG) pump. The ion pump works by ionizing background atoms and then accelerating them into a surface using a high voltage. The NEG pump, by contrast, works via passive chemical adsorption of background gas. The NEG is is an alloy of zirconium and aluminum. Once activated via heating, it will continuously remove gas from the vacuum chamber. The NEG cartridge is designed to have a very high surface area, to increase pumping speed. In addition to the NEG cartridge, pieces of NEG ribbon material were placed directly in the spherical octagon containing the trap. This is because pumping

[5]It is possible that the YbH^+ molecule can be resonantly dissociated by the cooling laser, see [84].

speed is ultimately limited by the diameter of the tube leading to the pumps. By placing some NEG material near the ion, the local pressure can in principle be improved. Anecdotal evidence suggests that the nearby NEG material does improve the pressure near the ion. However, no careful measurements were performed.

Once the chamber was fully assembled, a turbomolecular pump was used to pump it down to $\sim 2 \times 10^{-6}$ Torr. The chamber was then placed in an oven and heated to 200° C for a week. At this temperature, the water that is adsorbed onto the walls of the chamber can evaporate and be pumped out of the system. During the first half of the bakeout, a large external ion pump pumped gas out of the chamber. Halfway through, the valve was closed and the internal ion pump turned on. The bakeout also activates all of the NEG material in the chamber.

A UHV ionization gauge was used to monitor the pressure in the chamber both during and after the bakeout. Once the chamber had cooled to room temperature, it reached a steady pressure of 7×10^{-11} Torr. This is higher than expected – the final pressure should have been closer to $< 1 \times 10^{-11}$ Torr. The reason for this anomalously high pressure reading is unknown. It could be a contaminant in the vacuum chamber, or the gauge could be improperly calibrated. However, the pressure is still in the UHV regime, and is sufficiently low to enable the experiments presented here.

2.3.2 Blade Trap

The ion trap itself is made out of four gold coated alumina blades. The design of the blade is shown in figure 2.8. Before gold coating, 50 μm channels are cut

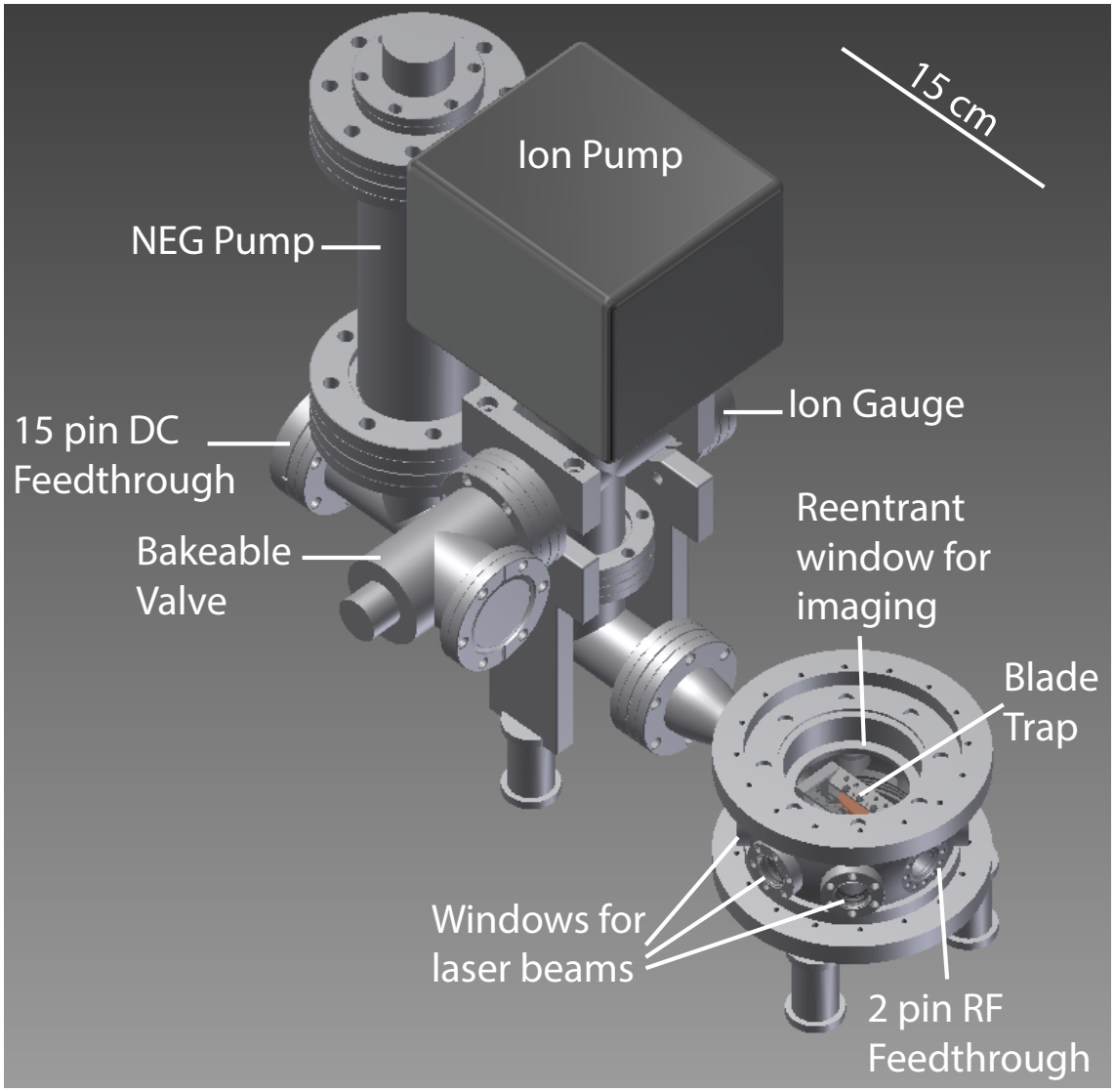

Figure 2.7: Vacuum chamber for ion trap. After bakeout, the system was continuously pumped by an ion pump and a non-evaporable getter pump. These were sufficient to maintain a pressure of 7×10^{-11} Torr. Two electrical feedthroughs on either side of the chamber pass through the signals for the blade voltages and the oven currents. The large top window is made reentrant so as to allow maximal light collection from the ion(s).

Part	Quantity	Vendor	Part Number
Spherical Octagon Chamber	1	Kimball Physics	MCF450-SphOct-E2A8
Groove grabbers	5	Kimball Physics	MCF450-GrvGrb-C01
4-Way Standard Cross	1	Kurt J. Lesker	C-0275
Standard Tee	2	Kurt J. Lesker	T-0275
Conical Reducer Nipple	1	Kurt J. Lesker	CRN275X133
Full Nipple	1	Kurt J. Lesker	FN-0337
All metal bakeable valve	1	Kurt J. Lesker	VZCR40R
Macor Blade Holder	1	Maryland Machine	N/A
Gold coated blade	4	Laser Micromachining Ltd.	N/A
In vacuum capacitors	10	ATC	116UL821M100TT
Isotopically enriched ^{171}Yb	a few mg	ORNL	N/A
Natural abundance Yb oven	1	Alvasource	AS-2-Yb-95-F
Natural abundance Ba oven	1	Alvasource	AS-2-Ba-55-F
15 Pin vacuum feedthrough	1	MDC	9162002
2 Pin vacuum feedthrough	1	MDC	9422011
1.33” window	6	MDC	9722013
4.5” reentrant top window	1	UKAEA	N/A
4.5” large bottom window	1	UKAEA	N/A
Ion gauge	1	Agilent Technologies	9715007
Ion pump	1	Agilent Technologies	9191145
NEG cartridge	1	SAES Getters	4H04193
NEG cartridge feedthrough	1	SAES Getters	4H04023
NEG ribbon	40 cm	SAES Getters	4F0280D

Table 2.1: List of important vacuum chamber parts. Standard gaskets, screws, wire, etc. are not listed.

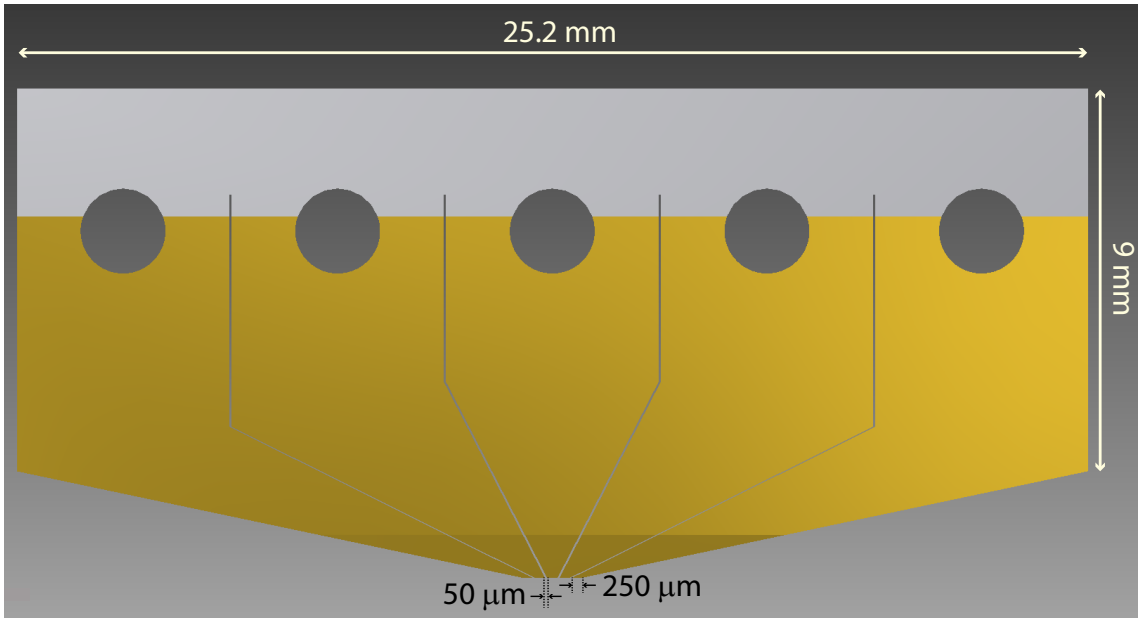

Figure 2.8: One of the DC blades used in the blade trap. The segmentation electrically isolates the segments from one another, allowing each of the five segments to be set to a different voltage. The RF blades look the same, except that the gold coating extends over the entire surface, such that the entire blade is at a single voltage.

through the alumina, creating five separate "prongs" or segments. The DC blades are then gold coated only on the segmented section, as seen in the figure. This creates five separate electrically isolated electrodes, which can each be set to a different voltage. By contrast, the RF blades are uniformly gold coated across their entire surface, such that the entire blade is at one voltage. The channels cut in the RF blades are irrelevant; they are present simply because all the blades are identical before they are gold coated. The segmentation of the DC electrodes creates the axial trap. The inner segment is set to a lower voltage than the outer segments, which provides axial confinement. This is in contrast to the four rod trap, in which axial confinement is provided by separate endcap electrodes. The segmentation also allows rotation of the trap's transverse principal axes. In the four rod trap, the two transverse principal axes are fixed to lie in the plane joining the RF rods and the

plane joining the DC rods. In the blade trap, the principal axes can be rotated by adjusting the voltages on the DC electrodes [86]. Lastly, the segmentation allows the creation of a more "flat-bottomed" trap, in which more ions can be held with equidistant spacing.

To connect the blades to the electrical feedthroughs, gold ribbon wire was wire-bonded to each electrode. That wire was then spot welded to pieces of constantan foil, which were in turn spot welded to Kapton coated copper wire. The constantan foil was used simply because it is extremely difficult to make a good spot weld between two wires. By using a folded piece of constantan foil, a good connection can be made between each wire and the foil, thereby connecting the wires.

The blades were attached via screws to a custom machined holder made out of Macor. Macor is a ceramic which is well-suited for this purpose. It is machinable, vacuum-compatible, and has a low coefficient of thermal expansion. The four blades were carefully aligned by eye under a microscope. When viewed from the side, the lines joining the short edge of each blade form a rectangle, as shown in figure 2.9(c). This rectangle has dimensions 1215 μm $\times$ 539 μm. This was larger than the design goal, but still sufficiently small to attain transverse secular frequencies > 1 MHz.

It is important to minimize RF pickup (and other noise) on the DC blades. For this reason, each signal going to the DC blades is filtered. However, as can be seen in figure 2.7, the DC feedthrough is relatively far from the trap itself (~50 cm). The effectiveness of a filter external to the vacuum chamber is therefore limited by the inductance of the internal wire leading from the trap to the feedthrough. For this reason, 820 pF ceramic capacitors were attached next to each blade segment, as

can be seen in figure 2.9(a). By reducing the blade to capacitor distance to ~1 cm, the RF pickup could in theory be significantly reduced. However, no measurements were attempted to determine how much (or if) the nearby capacitors helped.

2.3.3 Helical Resonator

As discussed in section 2.1, the voltage on the RF blades must be at a frequency in the tens of MHz, with an amplitude in the hundreds of volts. However, ideally no current is driven, so that the power required is nearly zero. The logical choice to provide such a signal is a quarter-wave resonator [75]. However, at a frequency of 20 MHz, a simple coaxial quarter wave resonator would be almost four meters long. This would be experimentally impractical. To solve this, the inner conductor of the resonator can be wound into a helix, creating a *helical resonator* [87, 88]. Such helical resonators are dramatically smaller, and can still attain high Q factors. Straightforward design guidelines for such a resonator are given in [87, 88]. The resonator consists of a copper shield with a helical coil of copper wire inside. The coil is grounded to the shield at the input side. RF power at the resonance frequency is inductively coupled in at the input, resulting in high RF voltage on the output end of the coil. Such a resonator is shown in figure 2.10.

The description above is slightly complicated by the need to compensate for stray electric fields at the trap center. Because of this requirement, it is important to be able to bias the RF electrodes with small DC voltages. Moreover, it is important to be able to have different biases on each RF electrode. For that reason, the helical resonator is constructed with two closely spaced inner helices rather than

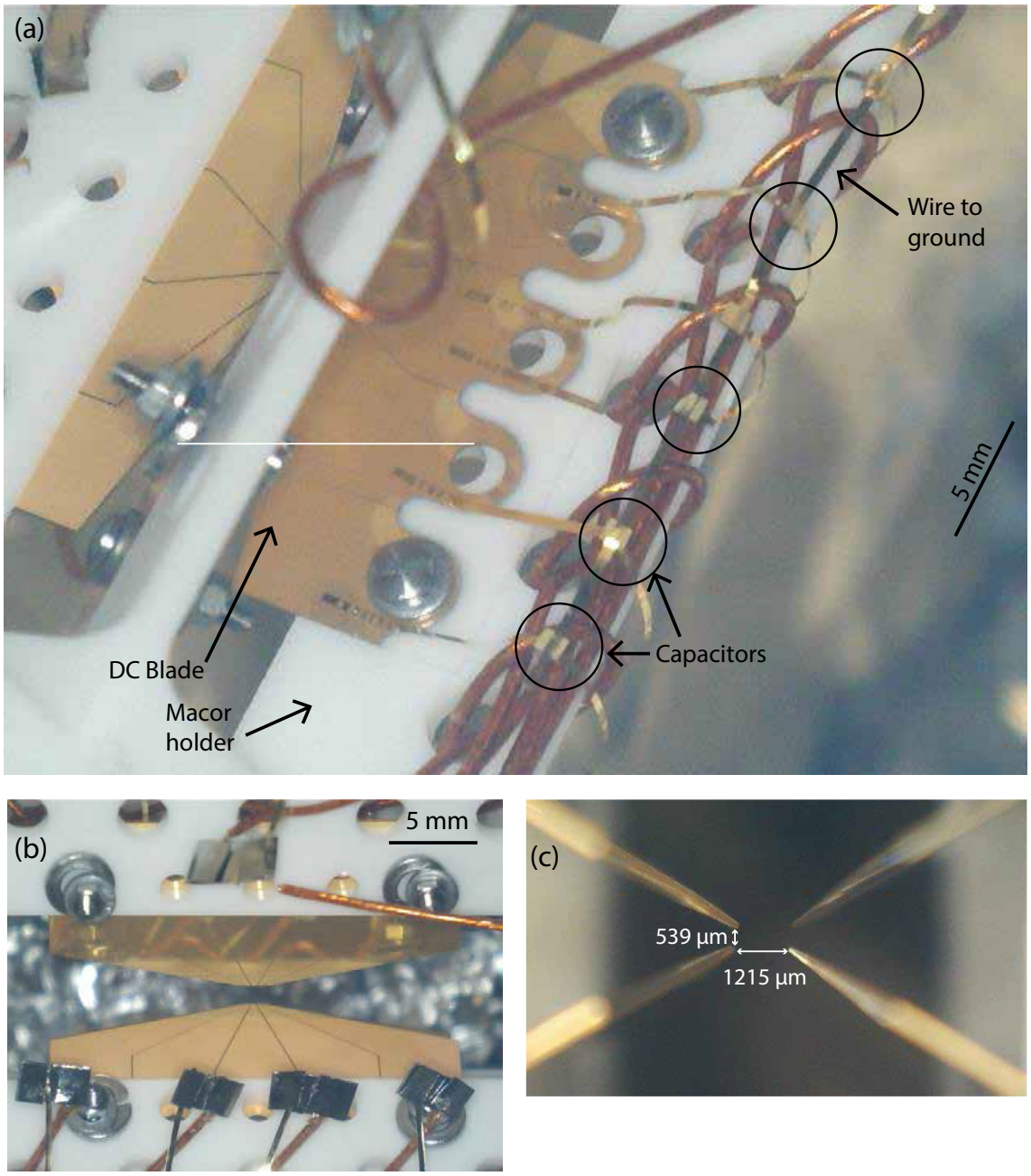

Figure 2.9: (a) view of the assembled trap, with one of the DC blades seen clearly. Note the segmented gold coating. The small chip capacitors are each circled; their bottom layer is connected to the blade, while their top layer is connected to a grounding wire. (b) Top down view of the trap. (c) Side-on view of the trap, showing dimensions.

one (a "bifilar"). The input side of each coil is connected to an SMA feedthrough to allow for the application of a DC bias voltage. It is also connected to a filter, which provides a capacitive ground for the RF voltage. The output side of each coil connects to one of the RF electrodes, via the feedthrough. It is also very important that there be no phase difference between the two RF electrodes. A phase difference between the RF electrodes leads to ion micromotion [78]. To match the phase on each electrode, a large capacitor is placed between the two coils right before the feedthrough. This capacitor acts as an RF short, guaranteeing that the RF voltage is the same while allowing for a different DC bias.

To couple power into the resonator, a small antenna coil is wound on the input side of the resonator, with its ends connected to an SMA bulkhead. The antenna coil is placed inside the larger helical coil. The antenna is shown in figure 2.10(a). RF is applied to the SMA connector, thereby inductively coupling to the resonator. The procedure to tune the coupling is as follows: First, the RF frequency applied to the resonator is scanned around the design frequency, while monitoring the reflected power. Away from resonance, all the power is reflected. However, a small dip in reflected power will be seen at some frequency, hopefully close to the design frequency. This is the resonance frequency. The antenna position inside the coil is then adjusted to minimize the reflected power on resonance. Sometimes the antenna will have to be modified in order to achieve good coupling. Without too much difficulty, the reflected power can be reduced to 0.1% of the incident power. The resonator Q is typically 100-200.

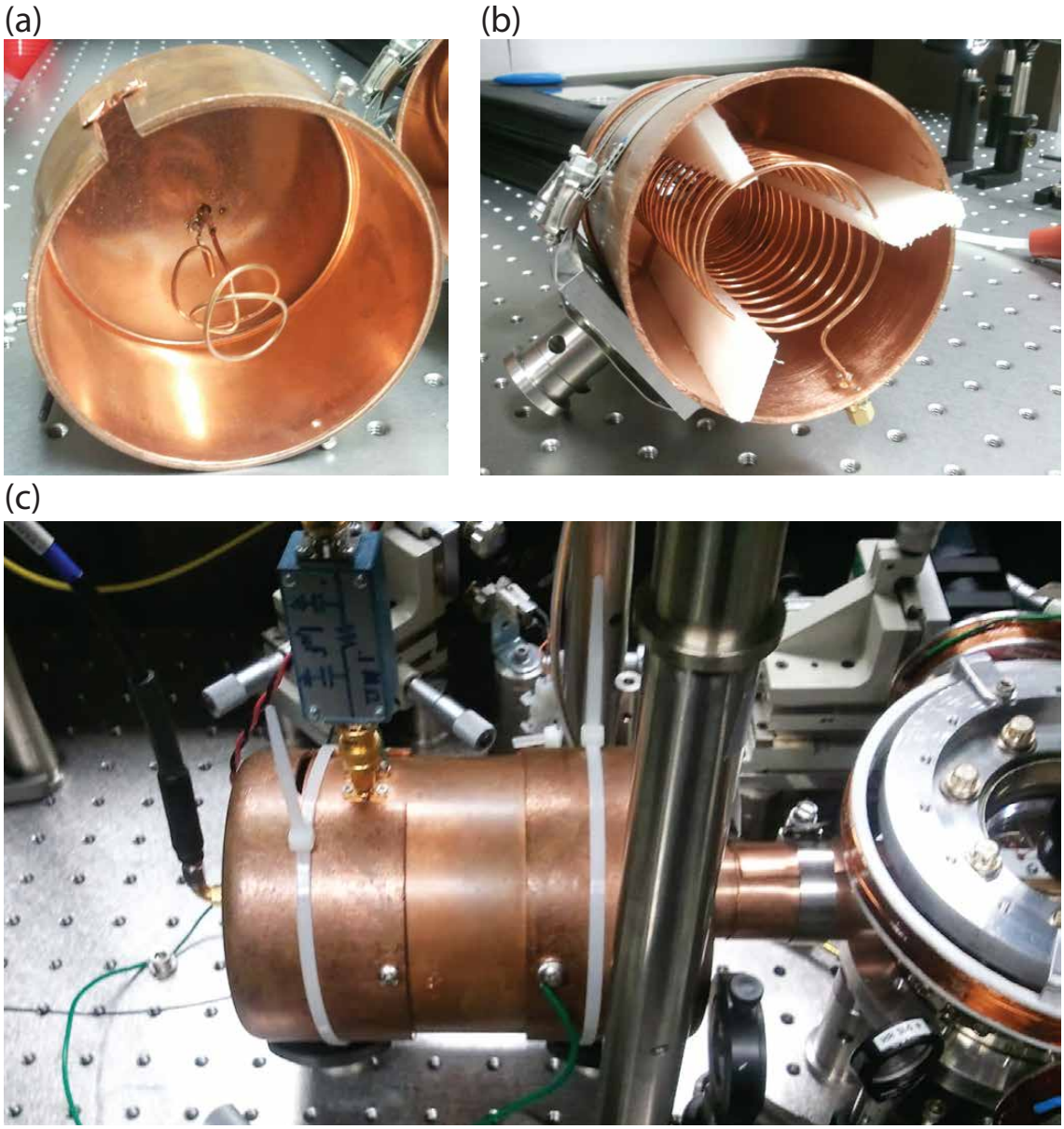

Figure 2.10: Pictures of a typical helical resonator. One inch spacing of table holes provides a scale. (a) Antenna for coupling in RF power. Antenna shape is adjusted by trial-and-error to minimize reflection. (b) Typical helical resonator. Coil is held in place with Teflon pieces, and connected to an SMA feedthrough to allow for DC bias. Shown here is a single coil resonator, as opposed to the two coil configuration discussed in the text. (c) Assembled resonator attached to vacuum chamber. At the output end (not shown), the coil is bent out into a straight line, which is then connected to the feedthrough using an in-line barrel connector.

Chapter 3

The Ytterbium Qubit

The previous chapter dealt with the theory and implementation of ion trapping. This chapter now turns to the specific ion used. The list of ions which are appropriate for trapped ion quantum information is rather limited. As a first limitation, the ion should be able to be easily Doppler cooled. That restricts the list to those ions which are alkali-like, meaning they have a single unpaired valence electron. In order for the ion to be useful as a qubit, it must have a long lived pair of energy levels which can be identified as the qubit levels. Moreover, there must be a mechanism by which to initialize, detect, and couple those levels. With these restrictions, there is a short list of appropriate atoms. Figure 3.1 shows the periodic table, with those atoms whose ions have been Doppler cooled highlighted. Each of these ions has various advantages and disadvantages for quantum information. The work in this thesis was all done using the 171 isotope of the Ytterbium ion, using the methods described in [89].

The $^{171}Yb^{+}$ ion is appealing for a number of reasons. Its $^{2}S_{1/2} \rightarrow {}^{2}P_{1/2}$ transition is at 369 nm, which is relatively long wavelength UV. At this wavelength, fibers

can be used, simplifying optical setups. The hyperfine splitting ω_{hf} in the $^2\mathrm{S}_{1/2}$ ground state manifold is 12.6 GHz, which is large enough to enable efficient state preparation and detection, described below. The fine structure splitting between the $^2\mathrm{P}_{1/2}$ and $^2\mathrm{P}_{3/2}$ levels is 100 THz, which is extremely large. This enables operating with a very large detuning in between the P states, which reduces spontaneous emission and differential light shifts of the qubit levels. Lastly, all the research discussed in this thesis requires a high power, picosecond mode-locked laser. The ideal center frequency for this laser is located between the P states, such that the differential light shifts from the two P states partially cancel while the Raman transition amplitudes coherently add (discussed later). Coincidentally, such a laser exists and is readily available. The third harmonic of solid state neodymium vanadate (Nd:YVO4) lasers is at 355 nm, which is extremely close to the ideal wavelength (see figure 4.3). This coincidence makes the $^{171}\mathrm{Yb}^+$ system uniquely well-suited for this work.

3.1 Ionization

To create a source of Ytterbium, a tube packed with Ytterbium metal is placed in the vacuum chamber. The tube has a single opening, which is directed towards the center of the ion trap. To load ions into the trap, two amps of current are then run through this tube, resistively heating it. This acts as an effusive oven, creating a stream of Yb atoms flowing through the trap.

Ionization then proceeds via a two photon process known as resonantly enhanced multi-photon ionization (REMPI) [90]. A 399 nm laser beam with 1.5 mW

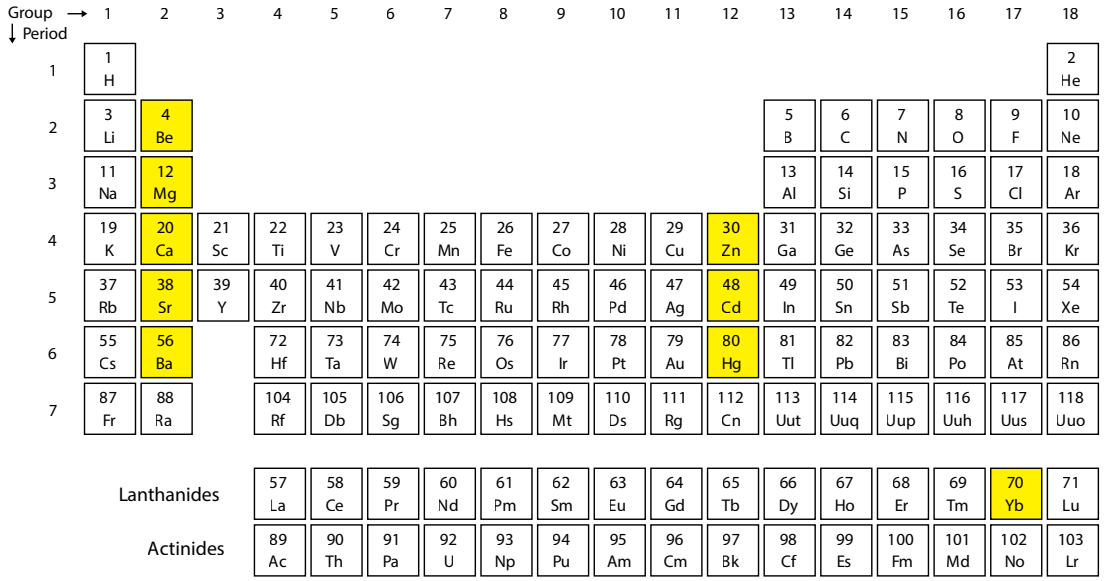

Figure 3.1: Periodic table of elements. Highlighted are those atoms which have been Doppler cooled when singly ionized.

of power is focused at the center of the trap to a waist of ~50 μm[1]. This excites the $^1S_0 \rightarrow {}^1P_1$ transition in the neutral Yb emanating from the oven. A second laser at 369 nm (also focused at the center of the trap) then ionizes the atom, producing Yb^+. The 369 nm beam has approximately 50 μW of power, and is focused to a waist of ~15-30 μm[2]. Because this process takes place at the trap center, the atom is trapped as soon as it is ionized. Moreover, the 369 nm beam which ionizes the neutral Yb is at the appropriate frequency for Doppler cooling Yb^+. Therefore, as soon as the atom is ionized it is trapped and cooled. Once a single ion is observed on the camera, the 399 beam and the oven are turned off. This process works well, producing a trapping rate of one ion every ~2 minutes for the optical powers and oven current mentioned.

[1]The 399 waist was not measured, and this is an extremely rough estimate based on the focusing lenses used.

[2]Also a rough estimate.

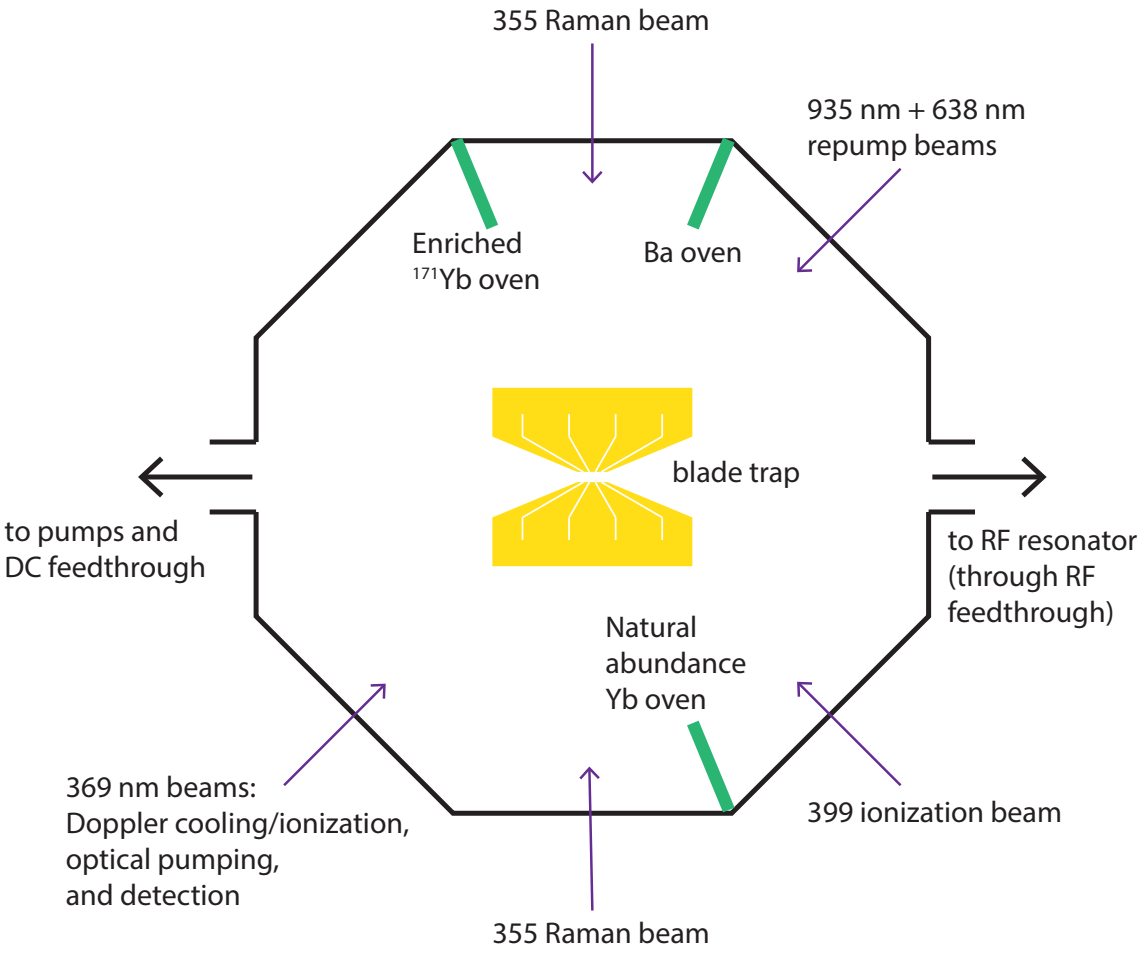

Figure 3.2: Top down view of experimental octagon, showing laser beam paths and oven locations. Light from the ion is collected from above. The barium oven is for possible future experiments, and was not used in any of the experiments in this thesis. In principle, isotopic selectivity during loading would be improved if the 399 beam were closer to orthogonal with the atomic beam emanating from the ovens, thereby minimizing Doppler shifts. However, this was not found to be a problem.

The $^{171}Yb^{+}$ isotope has a nuclear spin of 1/2, resulting in a hyperfine interaction with its valence electron. This level splitting creates the states which define the qubit levels, and is therefore critical. However, it also complicates the cooling process, as there are a number of dark states which must be continuously depopulated during the cooling process (discussed below). It is therefore often useful to trap $^{174}Yb^{+}$ for diagnostics. The 174 isotope has a nuclear spin of 0, resulting in a simpler level structure and fewer dark states. Because there is less that can go wrong, $^{174}Yb^{+}$ is typically trapped when the experiment is first getting set up, and for troubleshooting. Isotopic selectivity is achieved via the frequency of the 399 laser. The 399 beam is only resonant with the $S \rightarrow P$ transition of one isotope of Yb, meaning only that isotope is ionized.

The natural abundance of ^{174}Yb is 32%, while that of ^{171}Yb is 14%. In principle, a single oven loaded with natural abundance Yb could therefore be used as a source of both isotopes. However, the isotopic selectivity provided by the 399 frequency is imperfect due to Doppler broadening in the atomic beam. Because the abundance of ^{171}Yb is only 14%, using a natural abundance source to trap ^{171}Yb would often result in trapping the wrong isotope, especially when attempting to trap long chains of $^{171}Yb^{+}$ ions. For that reason, two Yb ovens are placed in the vacuum chamber. One of them contains naturally occurring Yb, and is used to load $^{174}Yb^{+}$. The second oven is isotopically enriched with ^{171}Yb, and enables efficient trapping of $^{171}Yb^{+}$. In addition to improving isotopic selectivity, the enriched oven also enables much faster loading of $^{171}Yb^{+}$ for the same total oven flux. The locations of the ovens, together with the laser beam paths, are shown in figure 3.2.

3.2 Qubit Initialization and Detection

The 369 nm light is split into three beams which are used to cool (and ionize), optically pump, and detect the ion. Electro-optic modulators (EOMs) add appropriate sidebands to the cooling and optical pumping beams, as shown in figure 3.4. The 369 nm light is generated by frequency doubling light from a 739 nm diode laser. The timings of the events are controlled by gating the RF applied to acousto-optic modulators (AOMs)[3] in each beam. The AOMs also allow separate control of the optical frequency of each beam, and their amplitudes.

3.2.1 Cooling

Cooling is accomplished via the standard technique of Doppler cooling [91]. The cooling laser beam is red-detuned from the $^2S_{1/2} \rightarrow {}^2P_{1/2}$ transition and focused onto the ion. The ion's temperature is reduced due to the preferential scattering of photons when moving towards the cooling beam. The cooling is maximally efficient when detuned by half the 20 MHz transition linewidth away from resonance. A single cooling direction is sufficient to cool all three dimensions, so long as the laser is not perpendicular to a principal axis of the trap [79]. There are however a number of dark states into which the ion can fall, and leave the cooling cycle. Here "dark state" refers to any long-lived state which does not fluoresce in response to the main, single frequency 369 nm cooling beam. It is necessary to continuously repump out of each dark state, described below.

[3] IntraAction ASM-2002B8

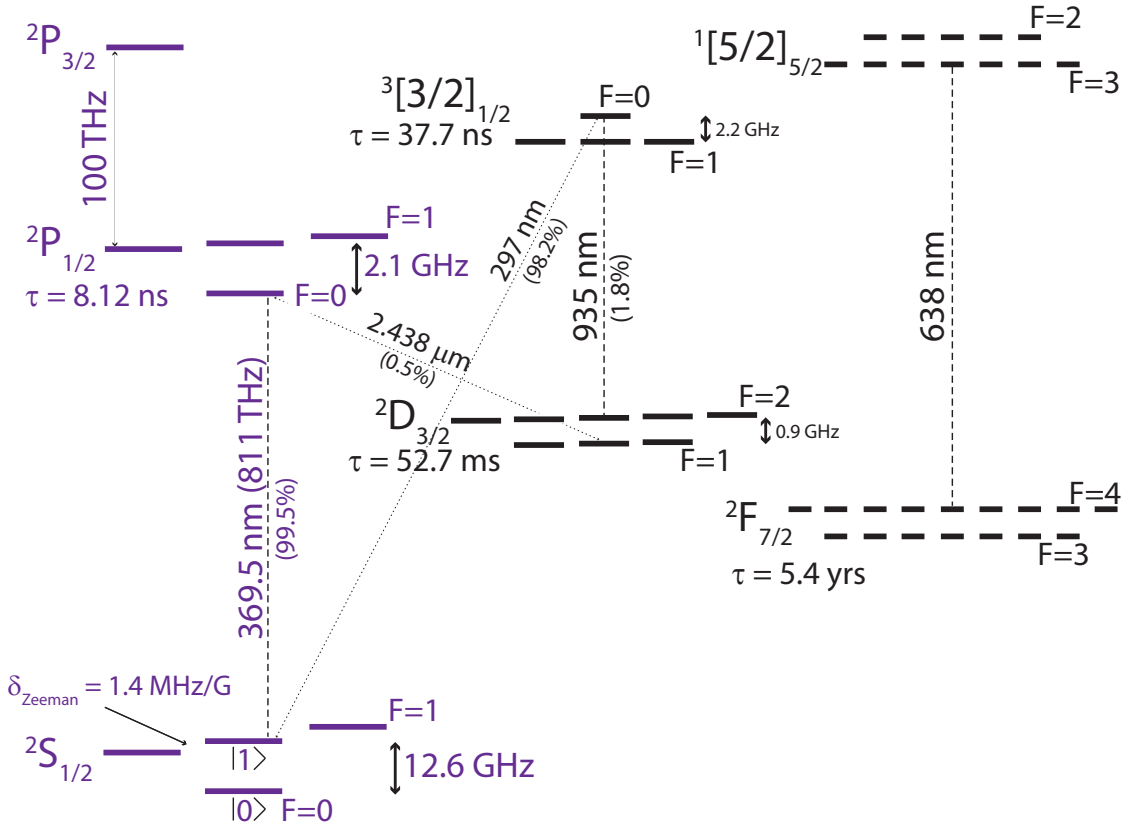

Figure 3.3: Relevant energy levels of $^{171}Yb^+$. The $^2S_{1/2}$ and $^2P_{1/2}$ levels at 369 nm (811 THz) nearly form a cycling transition, allowing for efficient Doppler cooling. 0.5% of scattering events place the ion in the $^2D_{3/2}$ state, from which it must be repumped by a 935 nm (321 THz) laser. To repump out of both hyperfine states of the D level, sidebands at 3.07 GHz are added to the repump laser. To prevent population trapping in the $F = 0$, $m_F = 0$ level of the $^2S_{1/2}$ manifold, sidebands at 14.7 GHz are added to the 369 nm cooling laser. A final repump laser at 638 nm (469 THz) is used to pump out of the $^2F_{7/2}$ state, which is populated via collisions with background gas atoms a few times per hour.

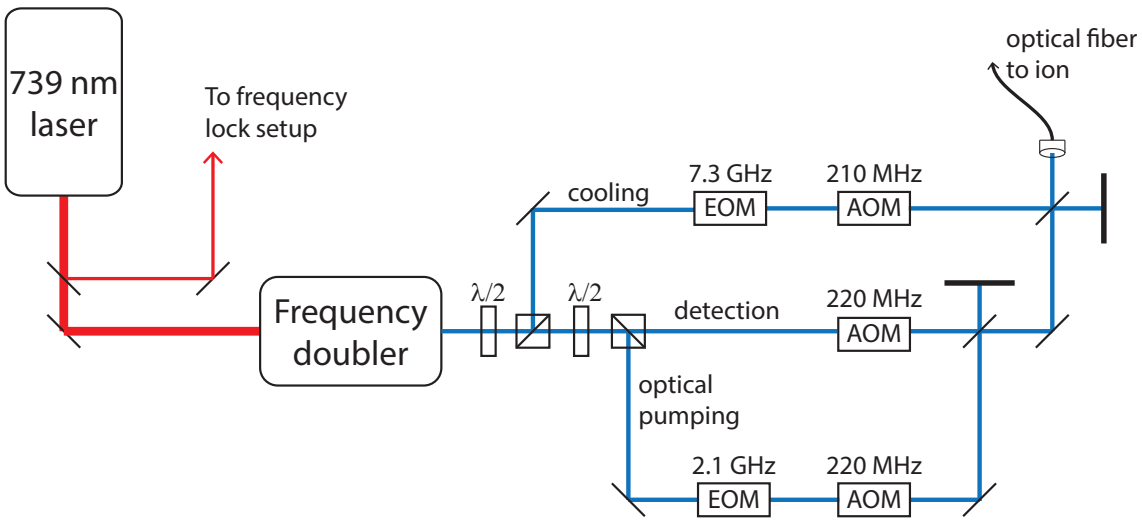

Figure 3.4: Beam paths for the 369 nm beams. Half-wave plates and polarizing beam splitters allow adjustment of how much power goes into each beam. EOMs add the appropriate sidebands to the cooling and optical pumping beams. AOMs in each beam line allow for fast switching, frequency control, and amplitude control. The detection and optical pumping beams are on resonance, and the cooling beam is 10 MHz red detuned. The beams are combined on beam splitters and sent to the ion through a single fiber.

The cooling laser normally cycles the ion between the $^2S_{1/2}$, $F = 1$ manifold and the $^2P_{1/2}$, $F = 0$ state. The $^2P_{1/2}$, $F = 0$ state cannot decay to $^2S_{1/2}$, $F = 0$ due to selection rules. Occasionally through off-resonant excitation the $^2P_{1/2}$, $F = 1$ state is populated, which can decay to the $^2S_{1/2}$, $F = 0$ state. Once there, the cooling laser is far off resonance and the ion goes dark. To avoid this, the cooling beam has 14.7 GHz sidebands added to repump out of that state. This is shown in figure 3.5(a). As a technical point, it is very difficult to obtain a resonant EOM at 14.7 GHz, so instead a 7.3 GHz EOM is used[4]. The second sideband then acts as the repump sideband.

Without a magnetic field, the cooling process will pump the ion into a coherent dark state, in which it no longer fluoresces [91]. To avoid this coherent population

[4]New Focus model 4851 EOM

trapping, a 2.9 gauss magnetic field is created at the ion position using three copper coils. Three coils are used to allow control over both the magnitude and direction of the magnetic field. This magnetic field creates a Zeeman splitting of 4 MHz (= 2.9 gauss × 1.4 MHz/gauss). This 4 MHz splitting is sufficient to eliminate the coherent dark state. Increasing the field further, however, results in a decreased cooling efficiency, as the cooling laser becomes further and further from resonance with the shifted $F = 1, m_F = \pm 1$ Zeeman states. 3 gauss is near an optimum field for cooling efficiency, balancing the coherent dark state and off-resonant effects. The magnetic field direction also defines the quantization axis, which is discussed later.

One out of every 200 scattering events, the ion decays into the $^2D_{3/2}$ state, which has a lifetime of 52.7 ms. Because of this long lifetime, it is important to continuously pump out of this state. This is done with a 935 nm laser[5], which excites the $^2D_{3/2} \rightarrow {}^3[3/2]_{1/2}$ transition. Similar to the cooling beam, this beam also requires sidebands at 3.1 GHz to pump out of the different hyperfine levels. From the $^3[3/2]_{1/2}$ state, the ion can quickly decay back to the cooling cycle.

This four level cooling scheme is nominally closed. However, occasionally a collision with a background gas atom can populate the low-lying $^2F_{7/2}$ state. This state is extremely long lived [92], and an ion which is not repumped from this state is effectively lost. A second repump laser[6] at 638 nm repumps from this state. Population of the $^2F_{7/2}$ state is relatively rare (every 30 minutes - an hour), so it is not necessary to use sidebands to depopulate both hyperfine levels. Instead, the

[5]Toptica Photonics DL100
[6]Toptica Photonics DL100

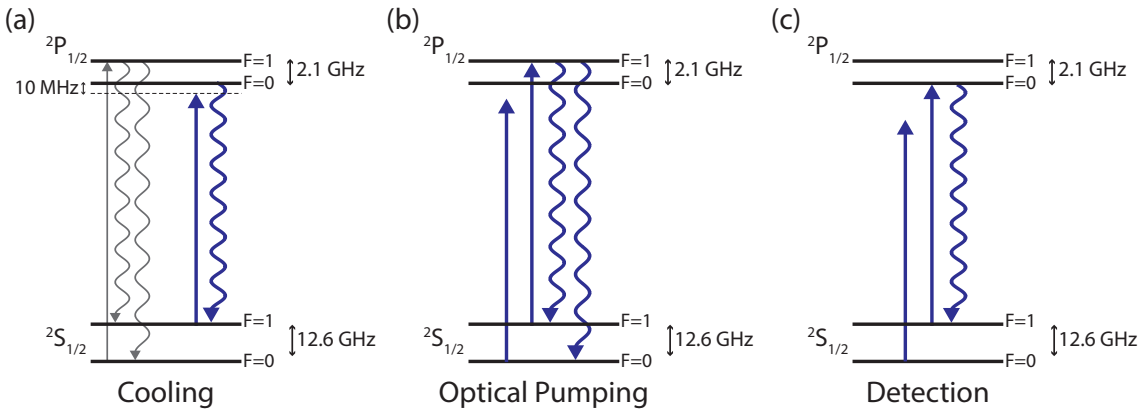

Figure 3.5: The processes performed by the 369 nm laser (not to scale). The magnetic sublevels of the F=1 hyperfine triplets are not shown for clarity. Also not shown is the 935 repump transition, which is present in all three processes. (a) Doppler cooling. The light is 10 MHz detuned from resonance, and cycles the ion between $^2S_{1/2}$, $F = 1$ and $^2P_{1/2}$, $F = 0$. Occasional off-resonant excitation to $^2P_{1/2}$, $F = 1$ allows decay to $^2S_{1/2}$, $F = 0$, which requires a repump sideband, shown in gray. (b) Optical pumping. A sideband at 2.1 GHz excites the ion from $^2S_{1/2}$, $F = 1$ to $^2P_{1/2}$, $F = 1$. From there it can decay to $^2S_{1/2}$, $F = 0$, where it is trapped. (c) Detection. The light is on resonance. This scatters many photons from $^2S_{1/2}$, $F = 1$, and almost no photons from $^2S_{1/2}$, $F = 0$.

638 nm laser frequency is slowly scanned back and forth between the resonance frequencies for the two hyperfine manifolds.

For a single ion experiment, population in the $^2F_{7/2}$ state is evidenced by a lack of fluorescence during Doppler cooling. When this happens, the experiment is paused until fluorescence returns. After a few minutes, the ion is assumed lost and the trap is reloaded.

3.2.2 Optical Pumping

Initialization of the qubit is done via the technique of optical pumping [93]. Instead of the 14.7 GHz EOM used in the cooling beam, a 2.1 GHz EOM[7] is used to add sidebands to the 369 nm light. After Doppler cooling, the ion is in a mixed

[7]New Focus model 4431

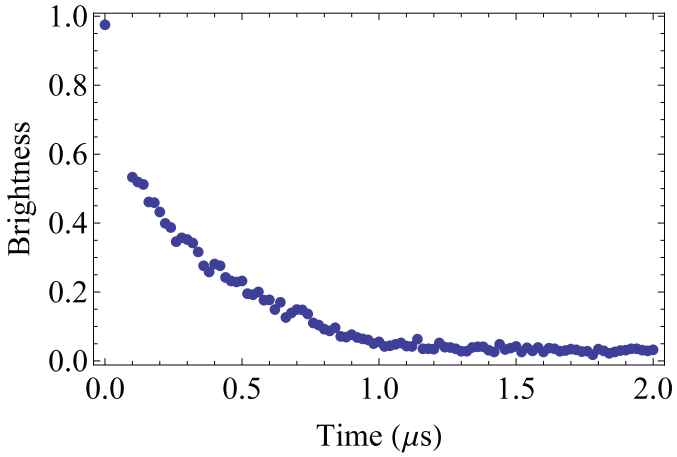

Figure 3.6: Optical pumping decay curve. After a few μs, the ion is primarily in $|0\rangle$.

state of all the levels in the $^2S_{1/2}$ hyperfine manifold. The 2.1 GHz sideband drives population from the $^2S_{1/2}$, $F = 1$ levels to the $^2P_{1/2}$, $F = 1$ level. From this excited state, the ion can decay back down to the $F = 1$ or $F = 0$ levels. However, any population which decays to the $F = 0$ level is trapped there, because the light is far off-resonant. Therefore, after a few cycles, the ion is entirely in the $^2S_{1/2}$, $F = 0$ state with high fidelity. This state is identified as the qubit level $|0\rangle$. In effect the 2.1 GHz optical pumping sideband plays the opposite role from the 14.7 GHz cooling sideband. This is shown in figure 3.5(b).

Figure 3.6 shows the state as a function of optical pumping time. The ion is initially Doppler cooled, and then the optical pumping beam is turned on for a variable length of time, followed by state detection. After just a few μs, the state is in $|0\rangle$ with high fidelity. The curve continues to decay beyond what is shown in figure 3.6, typically reaching a minimum value of 0.5% afer a few tens of μs. This is likely limited by state detection errors, as will be discussed in the next section.

3.2.3 State Detection

State detection is accomplished through state-dependent fluorescence [77, 94]. For the state detection beam, no EOM is necessary. The frequency is set to be resonant with the $^2S_{1/2},\ F = 1 \rightarrow {}^2P_{1/2},\ F = 0$ transition. If the ion is in the state $|1\rangle$, the light is resonant. It will therefore cycle between the S and P states, scattering photons. If the ion is in the state $|0\rangle$, the light is far off-resonant. It will therefore scatter no photons. The presence or absence of scattered photons thus indicates the state of the ion. This is shown in figure 3.5(c).

During detection, the detection beam is switched on for 500 μs. Light scattered by the ion is collected by a microscope objective[8] with a numerical aperture (NA) of 0.27. This results in a collection efficiency of about 2% of the total light emitted by the ion. This light is sent onto a photomultiplier tube (PMT) with a quantum efficiency of 15%. The combined result, together with losses in other optics, is that roughly one photon is detected out of every thousand emitted.

While the detection beam is on, the total number of photons detected by the PMT is counted. If the number of photons counted during detection is greater than one, the ion is considered "bright," and is therefore determined to be in the $|1\rangle$ state. If zero or one photon is detected, the ion is in the "dark" state $|0\rangle$. For an arbitrary quantum state $|\psi\rangle = c_0 |0\rangle + c_1 |1\rangle$, the measurement procedure causes the state to "collapse" into $|0\rangle$ or $|1\rangle$ with probability $|c_0|^2$ or $|c_1|^2$, respectively. Typically an experiment is repeated hundreds of times to build up sufficient statistics

[8] Special Optics 54-17-29-370nm

to reconstruct $|\psi\rangle$. So, for example, if 1000 experiments were performed in which 300 scattered ≤ 1 photon and 700 scattered > 1 photon, the ion would be considered 70% bright: $|c_1|^2 = 0.7$, $|c_0|^2 = 0.3$. Determining the complex phase relationship of c_0 and c_1 requires another set of experiments in which $|\psi\rangle$ is rotated by $\pi/2$ on the Bloch sphere.

This simple counting procedure is sufficient to determine the state of the ion with 97% fidelity. This is shown in figure 3.7. Each histogram shows the number of photons collected for 10,000 runs of the experiment. In figure 3.7(a), the ion was prepared in $|0\rangle$ via optical pumping. In 99.41% of those experiments, zero or one photon was detected. In figure 3.7(b), the ion was prepared in $|1\rangle$ via optical pumping followed by a microwave π-pulse (see below). In that case, in 97.7% of experiments two or more photons were detected. As in the case of the cooling beam, the 935 nm repump laser is critical during detection, so that the ion continues scattering light throughout the detection process.

The primary source of detection error is off-resonant pumping from the bright state to the dark state [95]. During the detection cycle, it is possible for the detection beam to turn a bright ion dark. When that happens, no more fluorescence will be detected from the now-dark ion. If this happens before > 1 photon is detected, the ion will be incorrectly determined to be dark. This effect can be seen clearly in figure 3.7(b). Ordinarily one would expect the distribution to be a perfect Poissonian, as shown in red. Indeed, the data is very close to a Poissonian, but the zero and one bins are higher than would be expected. This is due to the bright$\rightarrow$dark leakage. Analogously, a dark ion can be pumped bright. However, the detection light is 14.7

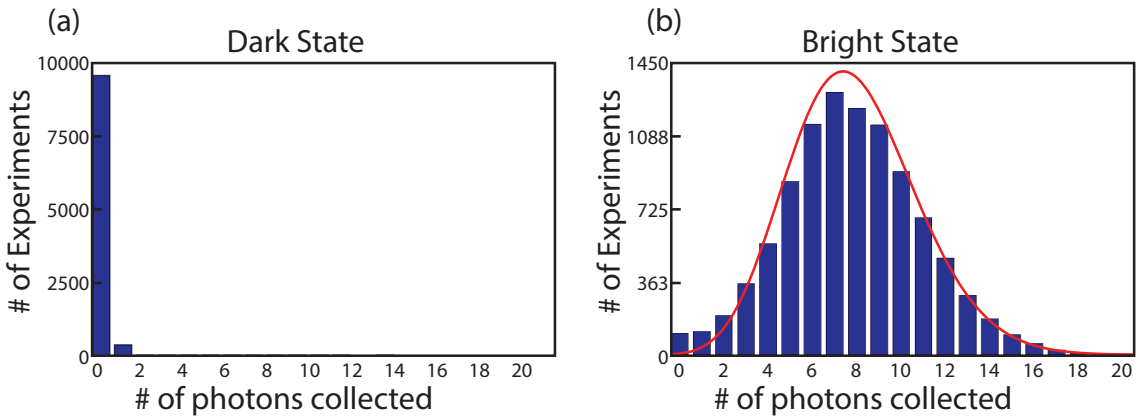

Figure 3.7: Histograms showing number of photons collected for 10,000 experiments, for ion in $|0\rangle$ vs $|1\rangle$. In (a), the ion was optically pumped to $|0\rangle$, followed by 500 μs of detection light. In the vast majority of experiments zero photons are collected. The small number of experiments in which one photon is collected is primarily due to dark counts. There are also a very small number of experiments in which more photons are collected due to off-resonant pumping to $|1\rangle$, but there are so few that they cannot be seen on this scale. In (b), a microwave π-pulse was used after optical pumping to move the ion to $|1\rangle$. The number of collected photons has a nearly Poissonian distribution. A perfect Poissonian is shown in red. The unexpectedly high "shelf" in the zero and one bins is caused by off-resonant pumping to $|0\rangle$.

GHz off-resonant for pumping a dark ion, as compared to 2.1 GHz off-resonant for pumping a bright ion. This effect is therefore so small that it can barely be seen in figure 3.7(a). A detailed analysis of the expected distributions can be found in [95]. Both types of off-resonant pumping can be dramatically reduced by increasing the photon collection efficiency, using a high NA lens or a better detector. With a high NA lens, detection fidelities as high as 99.92% have been measured in $^{171}Yb^{+}$ [96].

The functions discussed above – Doppler cooling, optical pumping, and detection – form the setup for any experiment performed. A standard experimental sequence is shown in figure 3.8. The ion is Doppler cooled for 1.4 ms, followed by 30 μs of optical pumping. This prepares the ion in the state $|0\rangle$ with a relatively cold motional state. The experiment is then performed (whatever it might be). At the

Wavelength	Precise Frequency	Purpose
369 nm	811288.860 GHz	$S \rightarrow P$ transition (and ionization)
399 nm	751527.140 GHz	Ionization
935 nm	320569.257 GHz	repump from D state
638 nm	469445 GHz/469442 GHz	repump from F state
355 nm	Broad bandwidth	qubit Raman transitions

Table 3.1: Laser frequencies used for $^{171}Yb^{+}$ experiments. 1 MHz is the precision of the wavemeter, hence that is the precision quoted here. However, only the 369 nm laser need be accurate to 1 MHz. The 399 nm laser can vary by up to $\pm$100 MHz without much affecting loading, due to the thermal distribution of the atomic beam. The 935 nm laser is sufficently intense to power broaden the repump transition, hence it can vary by several MHz without any effect.

Frequency	Purpose
12.642815 GHz	qubit microwave rotations
2.105 GHz	Sidebands for optical pumping
3.070 GHz	Sidebands for 935 nm repump
14.748 GHz	Sidebands for Doppler cooling
4.855 GHz	EOM frequency for iodine lock

Table 3.2: Microwave frequencies used for $^{171}Yb^{+}$ experiments.

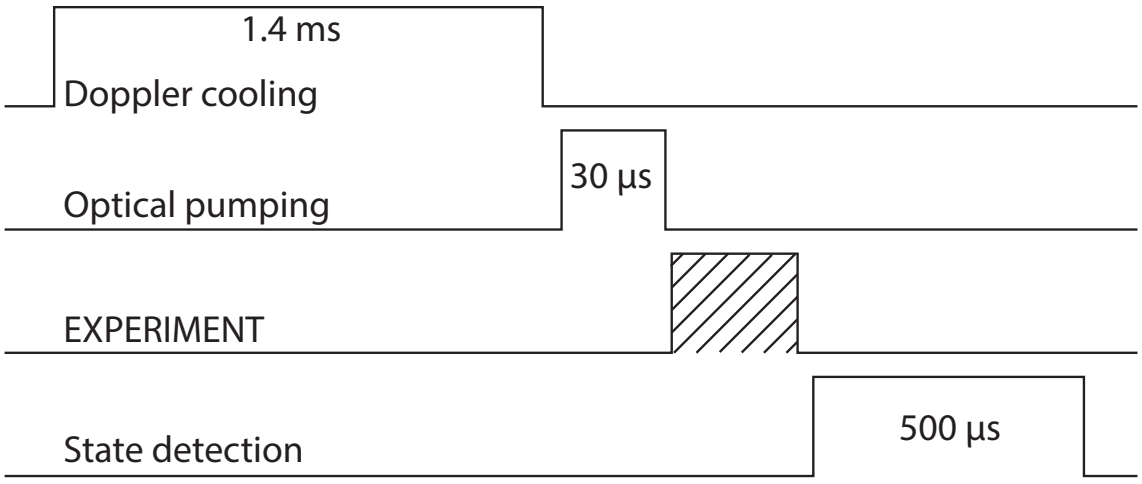

Figure 3.8: Standard experimental sequence. The ion is Doppler cooled for 1.4 ms, followed by optical pumping for 30 μs. This keeps the ion's motional state cold, and prepares the ion in $|0\rangle$. An experiment is then performed, followed by 500 μs of state detection. This sequence is typically repeated hundreds of times to build up statistics.

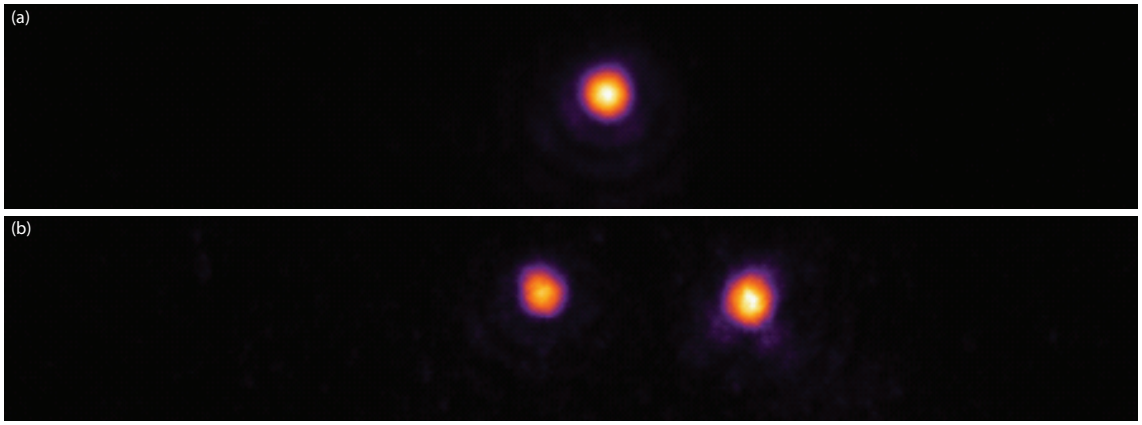

Figure 3.9: False color images of trapped ions. In these images, light scattered by the ions during Doppler cooling was sent onto an ICCD camera. (a) One ion. (b) Two ions. The two ions sit ~5 μm apart.

conclusion of the experiment, the state detection beam is turned on for 500 μs, and the state of the ion ($|0\rangle$ or $|1\rangle$) is determined by counting the number of photons detected by the PMT, as discussed above. This experimental sequence is repeated several hundred times for any given experiment.

Camera The light collected can also be directed onto a camera rather than a PMT. A camera typically has a lower quantum efficiency than a PMT, and is therefore worse for state detection. However, a camera provides spatial information, which is crucial for knowing how many ions there are, the ion spacing, whether there are any dark ions, whether the ions are in focus, etc. The camera used is an intensified CCD (ICCD)[9]. Images of one and two trapped ions obtained with the camera are shown in figure 3.9.

[9]Cooke corporation DiCam Pro

3.2.4 Laser Locking

As mentioned previously, the linewidth of the $^2S_{1/2} \rightarrow {}^2P_{1/2}$ transition is 20 MHz. It is therefore critically important that the frequency of the 369 laser be stable to < 1 MHz. To this end, a series of locks are used to stabilize the frequency on different time scales.

The 739 nm laser used to produce the 369 nm light is an external cavity diode laser (ECDL)[10]. The frequency can be controlled by adjusting the voltage on a piezoelectric transducer (PZT) on the diffraction grating, or by changing the current going to the laser diode. The grating control is slower but can scan further, while the current control is faster. Both the grating and the current are locked to a confocal cavity using the Pound-Drever-Hall (PDH) technique [97].

The cavity consists of two spherical mirrors glued to a hollow tube of Invar-36. The low coefficient of thermal expansion of Invar-36 makes it an excellent material for building an optical cavity whose length is stable. However, the optical path length between the mirrors does drift slowly over the course of seconds. The primary contribution to this drift is likely the changing temperature and pressure of air inside the cavity. This in turn can change the index of refraction and hence the effective optical path length of the cavity. One of the cavity end mirrors is therefore mounted to a PZT, which allows small adjustments of the cavity length. The length is then stabilized to a transition in molecular iodine. This absolute reference leads to a stable frequency.

[10]Toptica Photonics TA-100

Finally, the doubling cavity which produces the 369 nm light is stabilized to be resonant with the 739 nm frequency, through another PDH lock. The doubling cavity is a commercial doubling system[11].

Cavity Lock The 739 nm cavity lock layout is shown in figure 3.10. A 22 MHz oscillator[12] is used to modulate the current on the 739 laser, producing FM sidebands (the modulation index is small, meaning very little power is in these sidebands). The light from the laser is then directed into the confocal cavity described above. The light reflected is measured on a photodiode, and the signal is mixed with the original 22 MHz oscillator. The low frequency signal is then the lock signal [97]. On resonance with the cavity, the signal will be zero. Off resonance it will be either positive or negative. The mixed down signal is then divided and sent through two PIDs, one to the grating and one to the current. The current lock compensates for high frequency noise, while the grating lock compensates for slower drifts.

The sidebands on the 739 nm light do not appear on the 369 nm light. This is because the sidebands are not resonant with the doubling cavity, and are therefore not doubled.

Iodine Lock The iodine lock layout is shown in figure 3.11. The lock signal is obtained using Doppler-free saturated absorption spectroscopy of iodine [98]. Iodine has many absorption lines in the visible and infrared, making it a useful reference. Consulting an atlas of transitions in iodine shows that there are several transitions

[11]Spectra-Physics WaveTrain
[12]Protek DDS B8040FD

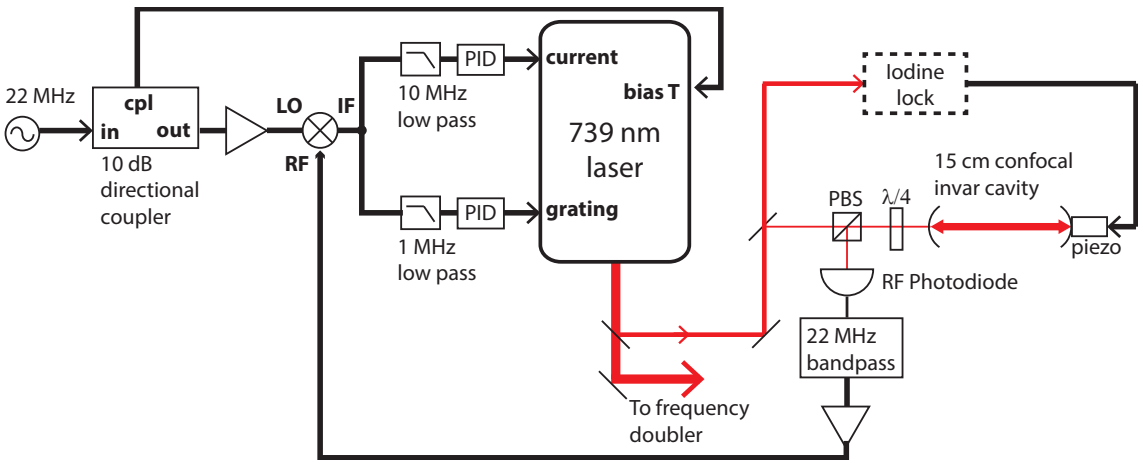

Figure 3.10: Cavity locking schematic. Optical paths are shown in red, electronic paths in black. A 22 MHz oscillator is used to modulate the current on the 739 nm laser via a bias-T. The light from the laser is sent into a 15 cm confocal optical cavity. The reflected light from that cavity is picked up on a fast photodiode, which is then mixed with the original 22 MHz signal. The resulting low frequency signal is used as the error signal. It is sent through a PID into the grating and current control ports of the laser, which stabilizes the laser's frequency to the cavity length. The cavity length itself is stabilized to molecular iodine.

within a few GHz of the desired frequency for $^{171}Yb^{+}$ [99, 100]. However, those absorption lines are very weak at room temperature. For this reason, the glass cell containing iodine[13] is heated to 530 °C. At this temperature, the relevant absorption lines are significantly stronger [101]. The cell also features a "cold finger," which is a small glass projection kept at room temperature. This cold finger reduces pressure broadening of the transition [101].

To lock to one of the iodine lines, the laser frequency must be shifted to the proper value. Examining the iodine atlas shows that there are three candidate features close to the $^{171}Yb^{+}$ transition. They are at -5 GHz, $+10$ GHz, and $+13$ GHz [99]. We used the feature at -5 GHz. The laser frequency was shifted using a free space resonant EOM[14] at 4.855 GHz.

[13] Triad Technologies TT-I2/19x300-V-Q
[14] New Focus EOM model 4431

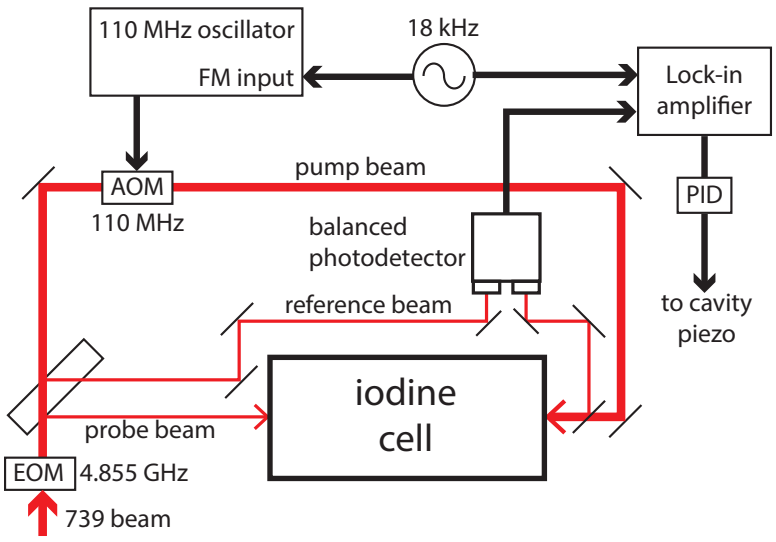

Figure 3.11: Iodine lock schematic. Optical paths are in red, electronic paths in black. The laser is sent through an EOM, and then split into the pump, probe, and reference beams. The pump and probe beams are sent counterpropagating through the iodine cell, with the pump beam passing through a frequency modulated AOM. The probe beam and reference beam are sent into the two ports of a balanced photodetector. The photodetector output is then sent into a lock-in amplifier, together with the modulation signal on the AOM. The resultant signal is used to stabilize the cavity length.

After the EOM, the 739 nm light is divided into a pump beam, a probe beam and a reference beam. The pump beam is sent through a 110 MHz AOM[15], which shifts its frequency up. It is then sent through the iodine cell, counterpropagating with the probe beam. For those iodine molecules whose velocity is such that the pump beam is Doppler shifted 55 MHz red and probe beam shifted 55 MHz blue, the pump and probe beam have the same frequency[16]. When that frequency matches resonance, the probe beam transmission is increased due to the saturated absorption effect. This increased transmission only occurs for that unique velocity class, and is therefore "Doppler-free."

[15]Crystal Technology 3310-110

[16]Traditionally this sort of spectroscopy is done with the zero velocity class. However, that would have required a second AOM on the probe beam, and would have resulted in a reduction in probe beam intensity. It also would not have increased the signal to noise by any appreciable amount.

The power in the reference beam is matched to that of the probe beam, so that it differs only in that the probe beam passed through the iodine cell. Both beams are then sent onto a balanced photodetector[17], which takes the difference of the signals. This allows elimination of amplitude fluctuations that are common to both beams, and leaves only the signal due to the iodine. Measuring the differential transmitted probe intensity as a function of laser frequency then results in very narrow peaks, on top of the large, Doppler-broadened background absorption.

The signal is then differentiated to produce a lock signal using FM spectroscopy and lock-in detection. The oscillator[18] driving the pump beam AOM is frequency modulated at 18 kHz. This modulation can only appear on the probe beam via the pump-probe interaction in iodine, which strongly suppresses DC noise. The output of the balanced photodetector is then sent to a lock-in amplifier[19], together with the 18 kHz modulation signal. The resultant DC output is sent through a PID and then to the cavity PZT. The integration time on the lock-in amplifier is 100 ms, meaning the bandwidth of the signal sent to the cavity PZT is < 10 Hz. An example of the output of the lock-in as a function of frequency is shown in figure 3.12. The lock point is the highest frequency zero crossing, which is the farthest right zero crossing in the plot.

[17]Thorlabs PDB150A
[18]HP 8640B
[19]Stanford Research Systems SR510

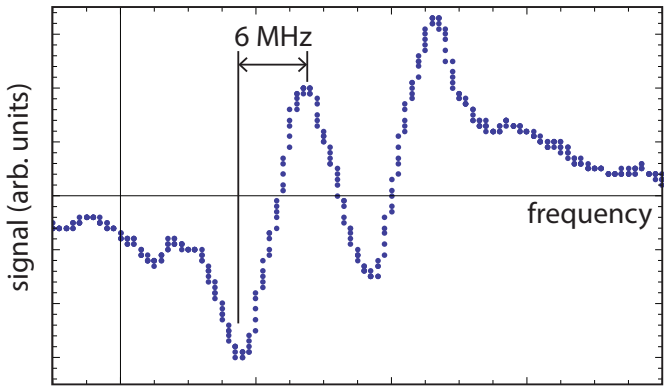

Figure 3.12: Signal out of lock-in amplifier as a function of frequency. The laser is locked to the farthest right zero-crossing. The sharp slope over a 6 MHz range allow for a stable, sub-MHz lock.

3.3 Microwave Transitions

The simplest way to drive transitions between the two qubit levels is by directly applying microwave radiation which is resonant with the qubit splitting. The oscillating magnetic field component of the microwaves creates a coupling between $|0\rangle$ and $|1\rangle$, which drives magnetic dipole transitions. The result is Rabi flopping between $|0\rangle$ and $|1\rangle$. More details on the coupling mechanism between the microwaves and qubit can be found in [83].

Experimentally, the microwaves are introduced via a microwave horn[20] pointing at the trap center. About one Watt of microwave power is sufficient to drive a π-pulse in 36 μs. Figure 3.13 shows typical Rabi flopping driven by microwaves.

Microwave transitions are useful as a tool for diagnostics, detection characterization, and Ramsey-type experiments. However, they cannot be used for two-ion gates based on the Coulomb interaction. This is because these gates rely on spin-

[20]Pasternack PE9854/SF-10

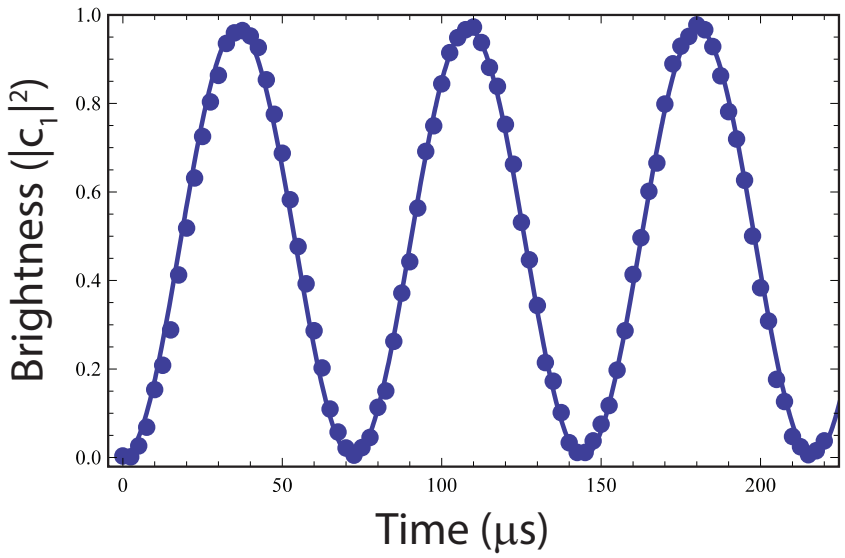

Figure 3.13: Data showing microwave Rabi flopping. The experiment consists of applying microwave radiation for a variable time t to an ion initially in $|0\rangle$. The measured brightness of the ion ($|c_1|^2$) is shown as a function of time t.

dependent momentum transfer, as explained in chapters 5 and 6. The momentum transferred by a single microwave photon is five orders of magnitude weaker than that transferred by optical photons, and is insufficient to drive the gate in a reasonable amount of time[21].

In addition, the transition strength is much weaker for the $|0\rangle \rightarrow |1\rangle$ magnetic dipole transition than it is for the $S \rightarrow P$ electric dipole transition. This means that laser based transitions can in general be far faster. The ultrafast Raman transitions discussed in chapter 4 are six orders of magnitude faster than the microwave transitions shown here.

[21]It should be noted, however, that it is possible to drive two-ion Coulomb gates via near field microwave gradients; see [45].

Chapter 4

Ultrafast Spin Control

The principal way in which the $|0\rangle$ and $|1\rangle$ states are coupled is via a *stimulated Raman transition*. A Raman transition is a three level "λ" process, whereby two electronic ground levels are coupled via virtual excitation of a third, excited level. The atom is able to undergo a transition between the qubit levels by absorbing light at a frequency ω and emitting at frequency $\omega \pm \omega_{\rm hf}$, where $\omega_{\rm hf}$ is the ion's hyperfine splitting. The laser frequency ω is detuned by Δ from resonance with the excited state. For sufficiently large Δ the Raman process results in negligible population in the excited state, and the system behaves as an effective two-level system.

Traditionally, Raman transitions have been driven with two CW laser beams, which have a frequency difference between them of $\omega_{\rm hf}$. The ion can then execute transitions by absorbing from one beam and emitting into the other. Alternatively, a single fast pulse can drive a Raman transition, if its bandwidth is significantly larger than $\omega_{\rm hf}$. This is the approach I will present. The light driving the transition will consists of one (or many) ~10 picosecond laser pulses. This chapter deals primarily with processes that do not couple to the ion's motion, but only drive transitions

between the qubit levels.

4.1 Schrödinger equation

The time-dependent Schrödinger equation is (setting $\hbar = 1$):

$$i\frac{\partial}{\partial t}\left|\Psi\right\rangle = \mathcal{H}\left|\Psi\right\rangle \tag{4.1}$$

The system consists of an atom interacting with an electromagnetic field. The Hamiltonian $\mathcal{H}$ can thus be divided into three parts, corresponding to the internal energy of the atom $\mathcal{H}_{\text{atom}}$, the internal energy of the applied field $\mathcal{H}_{\text{field}}$, and the interaction energy between them $\mathcal{H}_{\text{int}}$ [91]:

$$\mathcal{H} = \mathcal{H}_{\text{atom}} + \mathcal{H}_{\text{field}} + \mathcal{H}_{\text{int}} \tag{4.2}$$

I will proceed in the semi-classical limit, in which the field is treated classically. The energy of the field can therefore be neglected ($\mathcal{H}_{\text{field}} = 0$), so that $\mathcal{H}$ becomes:

$$\mathcal{H} = \mathcal{H}_{\text{atom}} + \mathcal{H}_{\text{int}} \tag{4.3}$$

Next assume that $\mathcal{H}_{\text{atom}}$ has some known set of atomic eigenstates $|\psi_n\rangle$. These atomic eigenstates are the levels shown in figure 3.3. Moreover, the lifetime of any atomic eigenstate will be assumed to be infinite, i.e. spontaneous emission is ignored throughout. This approximation is justified so long as population only accumulates in states whose lifetime is many orders of magnitude longer than the duration of an experiment, which will be seen to be true.

An arbitrary wave function $|\Psi\rangle$ can be decomposed in terms of the atomic

eigenstates:

$$|\Psi\rangle = \sum_n c_n |\psi_n\rangle \tag{4.4}$$

which is possible because the set $|\psi_n\rangle$ is a complete orthonormal basis. This can then be used to rewrite equation 4.1 as [102]:

$$i\dot{c}_n = \omega_n c_n + \sum_m V_{nm} c_m \tag{4.5}$$

where ω_n and V_{nm} are defined as:

$$\omega_n = \langle\psi_n | \mathcal{H}_{\text{atom}} | \psi_n\rangle \tag{4.6}$$

$$V_{nm} = \langle\psi_n | \mathcal{H}_{\text{int}} | \psi_m\rangle \tag{4.7}$$

Equation 4.5 is just the Schrödinger equation rewritten in the basis of atomic eigenstates, in terms of the matrix elements of the interaction Hamiltonian V_{nm}.

Without any interaction ($V_{nm} = 0$), the solutions to equation 4.5 are $c_n = Ae^{-i\omega_n t + B}$, where A and B are constants. This zero-field precession can be absorbed into the c_n by moving to the *rotating reference frame*. Define:

$$\tilde{c}_n = c_n e^{i\omega_n t} \tag{4.8}$$

$$\Rightarrow \dot{\tilde{c}}_n = e^{i\omega_n t}\left(\dot{c}_n + i\omega_n c_n\right) \tag{4.9}$$

In terms of these rotating variables, equation 4.5 becomes:

$$i\dot{\tilde{c}}_n = \sum_m V_{nm} e^{i\delta_{nm}} \tilde{c}_m \tag{4.10}$$

where I have defined δ_{nm} to be the frequency difference between states $|n\rangle$ and $|m\rangle$:

$$\delta_{nm} = \omega_n - \omega_m \tag{4.11}$$

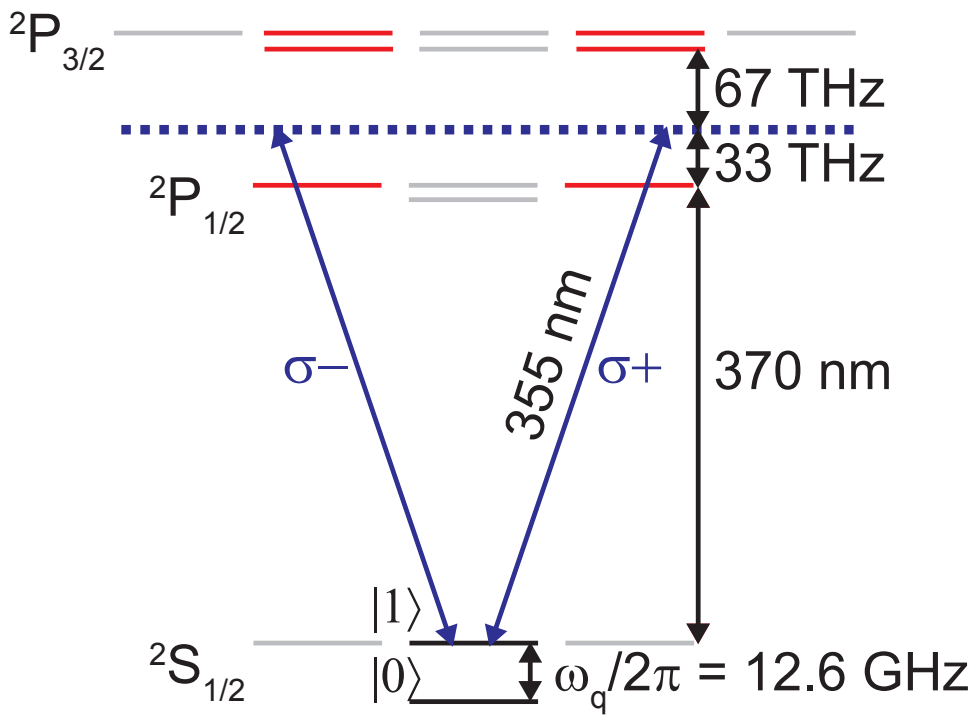

Figure 4.1: The 355 nm laser drives Raman transitions between $|0\rangle$ and $|1\rangle$ via virtual excitation to the $^2P_{1/2}$ levels. This can be done either using σ^+ or σ^- light.

Equation 4.10 now encapsulates the dynamics of the Schrödinger equation that are driven by the interaction. The levels that are relevant to the interaction considered here are shown in figure 4.1. The transition can proceed via σ^+ or σ^- polarized light. Note that π-polarized light cannot drive transitions. This is because neither of the $^2P_{1/2}$, $m_F = 0$ levels have dipole allowed transitions to both of the $^2S_{1/2}$, $m_F = 0$ levels, due to selection rules.

To begin, I will only consider these three atomic levels:

$$|0\rangle \equiv \left|^2S_{1/2}, F = 0, m_F = 0\right\rangle \tag{4.12}$$

$$|1\rangle \equiv \left|^2S_{1/2}, F = 1, m_F = 0\right\rangle \tag{4.13}$$

$$|2\rangle \equiv \left|^2P_{1/2}, F = 1, m_F = 1\right\rangle \tag{4.14}$$

This will be generalized to include the other excited states later. For these three levels, $\delta_{10} = \omega_{\rm hf} = 2\pi \times 12.6$ GHz (the hyperfine splitting), $\delta_{20} = \omega_2 = 2\pi \times 405657\,\text{GHz}$ (the energy of the excited state), and $\delta_{21} = \omega_2 - \omega_{\rm hf} = 2\pi \times 405645\,\text{GHz}$. In addition, the laser does not directly couple $|0\rangle$ and $|1\rangle$, so $V_{01} = V_{10} = 0$. Equation 4.10 then becomes:

$$i\dot{\tilde{c}}_0 = V_{02} e^{-i\omega_2 t} \tilde{c}_2 \tag{4.15}$$

$$i\dot{\tilde{c}}_1 = V_{12} e^{-i(\omega_2 - \omega_{\rm hf})t} \tilde{c}_2 \tag{4.16}$$

$$i\dot{\tilde{c}}_2 = V_{02}^* e^{i\omega_2 t} \tilde{c}_0 + V_{12}^* e^{i(\omega_2 - \omega_{\rm hf})t} \tilde{c}_1 \tag{4.17}$$

4.1.1 Matrix Elements

To proceed, we need to determine the matrix elements V_{nm} for the interaction at hand. We will initially consider a single laser beam incident from one direction. The laser beam will consist of picosecond pulses, meaning the electric field has a time-dependent envelope $\mathcal{E}(t)$. That envelope is slowly varying compared to the laser frequency ω. The electric field can be written as:

$$\mathbf{E} = \text{Re}\left[\hat{\boldsymbol{\epsilon}} \mathcal{E}(t) e^{-i(\omega t + \phi)}\right] \tag{4.18}$$

where $\hat{\boldsymbol{\epsilon}}$ is the complex polarization vector, $\mathcal{E}(t)$ is the envelope, ω is the laser frequency, and ϕ is a phase factor. Here the position dependence of the beam is encapsulated in ϕ; it will not be important until the motional coupling is discussed. $\mathcal{E}(t)$ is assumed to vary slowly compared to ω, and is real. The interaction is an electric dipole transition, meaning that the interaction Hamiltonian is given by [91]:

$$\mathcal{H}_{\rm int} = -\boldsymbol{\mu} \cdot \mathbf{E} = -\boldsymbol{\mu} \cdot \left(\frac{1}{2} \hat{\boldsymbol{\epsilon}} \mathcal{E}(t) e^{-i(\omega t + \phi)} + \frac{1}{2} \hat{\boldsymbol{\epsilon}}^* \mathcal{E}(t) e^{i(\omega t + \phi)}\right) \tag{4.19}$$

where $\boldsymbol{\mu}$ is the electric dipole moment. We now define the single photon Rabi frequencies:

$$g_{02}(t) = -\mathcal{E}(t)e^{-i\phi}\left\langle 0\left|\boldsymbol{\mu}\cdot\hat{\boldsymbol{\epsilon}}\right|2\right\rangle \tag{4.20}$$

$$g_{12}(t) = -\mathcal{E}(t)e^{-i\phi}\left\langle 1\left|\boldsymbol{\mu}\cdot\hat{\boldsymbol{\epsilon}}\right|2\right\rangle \tag{4.21}$$

Here I have made the electric dipole approximation, in that I have assumed that the wavelength of the light is far larger than the size of the atomic wave packet [103]. From the Hermiticity of $\mathcal{H}_{\rm int}$, it follows that $\left\langle 0\left|\boldsymbol{\mu}\cdot\hat{\boldsymbol{\epsilon}}\right|2\right\rangle = \left\langle 2\left|\boldsymbol{\mu}\cdot\hat{\boldsymbol{\epsilon}}^*\right|0\right\rangle$. The interaction matrix elements are therefore given by:

$$V_{02} = -\left\langle 0\left|\boldsymbol{\mu}\cdot\mathbf{E}\right|2\right\rangle = \frac{1}{2}g_{02}(t)e^{-i\omega t} + \frac{1}{2}g_{02}^*(t)e^{i\omega t} \tag{4.22}$$

$$V_{12} = -\left\langle 1\left|\boldsymbol{\mu}\cdot\mathbf{E}\right|2\right\rangle = \frac{1}{2}g_{12}(t)e^{-i\omega t} + \frac{1}{2}g_{12}^*(t)e^{i\omega t} \tag{4.23}$$

Equations 4.15-4.17 now become:

$$i\dot{\tilde{c}}_0 = \frac{1}{2}\left(g_{02}e^{-i(\omega+\omega_2)t} + g_{02}^*e^{-i\Delta t}\right)\tilde{c}_2 \tag{4.24}$$

$$i\dot{\tilde{c}}_1 = \frac{1}{2}\left(g_{12}e^{-i(\omega+\omega_2)t} + g_{12}^*e^{-i\Delta t}\right)e^{i\omega_{\rm hf}t}\tilde{c}_2 \tag{4.25}$$

$$i\dot{\tilde{c}}_2 = \frac{1}{2}\left(g_{02}^*e^{i(\omega+\omega_2)t} + g_{02}e^{i\Delta t}\right)\tilde{c}_0 + \frac{1}{2}\left(g_{12}^*e^{i(\omega+\omega_2)t} + g_{12}e^{i\Delta t}\right)e^{-i\omega_{\rm hf}t}\tilde{c}_1 \tag{4.26}$$

Here I have defined the laser's detuning from the excited state Δ:

$$\Delta = \omega_2 - \omega \tag{4.27}$$

For the physical system in question, $\omega \approx \omega_2 \approx 5\times10^{15}$ s^{-1}, $\Delta \approx 2\times10^{14}$ s^{-1}, $\dot{\mathcal{E}}(t)/\mathcal{E}(t) \lesssim 10^{11}$ s^{-1}, and $\omega_{\rm hf} \approx 8\times10^{10}$ s^{-1}. Therefore:

$$\omega_{\rm hf} \lesssim \dot{\mathcal{E}}/\mathcal{E} \ll \Delta \ll \omega + \omega_2 \tag{4.28}$$

Upon integration, terms that oscillate as $\omega + \omega_2$ will be scaled by a factor of $\frac{1}{\omega+\omega_2}$, while those oscillating at Δ will be scaled by $\frac{1}{\Delta}$. The evolution will therefore be dominated by the *co-rotating* terms ($e^{i\Delta t}$), while the *counter-rotating* terms ($e^{i(\omega+\omega_2)}$) will be negligibly small. We can therefore make the *Rotating Wave Approximation* (RWA) and set the counter-rotating terms to zero [91]:

$$i\dot{\tilde{c}}_0 = \frac{1}{2} g_{02}^* e^{-i\Delta t} \tilde{c}_2 \tag{4.29}$$

$$i\dot{\tilde{c}}_1 = \frac{1}{2} g_{12}^*(t) e^{-i(\Delta-\omega_{\mathrm{hf}})t} \tilde{c}_2 \tag{4.30}$$

$$i\dot{\tilde{c}}_2 = \frac{1}{2} g_{02}(t) e^{i\Delta t} \tilde{c}_0 + \frac{1}{2} g_{12}(t) e^{i(\Delta-\omega_{\mathrm{hf}})t} \tilde{c}_1 \tag{4.31}$$

4.1.2 Adiabatic Elimination

We now wish to eliminate reference to the excited state in equations 4.29 - 4.31. To do this, we make the ansatz that $\tilde{c}_0$, $\tilde{c}_1$, $g_{02}(t)$, and $g_{12}(t)$ vary far more slowly than $e^{i\Delta t}$ in equation 4.31. We therefore can directly integrate equation 4.31, assuming everything is constant except the exponential terms. This process is known as *adiabatic elimination*, and can be formalized [104]. Taking $\tilde{c}_2 = 0$ at time $t = 0$, integration yields:

$$\tilde{c}_2 = \frac{g_{02}(t)}{2\Delta}\left(1 - e^{i\Delta t}\right)\tilde{c}_0 + \frac{g_{12}(t)}{2(\Delta - \omega_{\mathrm{hf}})}\left(1 - e^{i(\Delta-\omega_{\mathrm{hf}})t}\right)\tilde{c}_1 \tag{4.32}$$

Substituting equation 4.32 into equations 4.29 and 4.30 yields a pair of differential equations for $\tilde{c}_0$ and $\tilde{c}_1$:

$$i\dot{\tilde{c}}_0 = \frac{|g_{02}|^2}{4\Delta}\left(e^{-i\Delta t} - 1\right)\tilde{c}_0 + \frac{g_{02}^* g_{12} e^{-i\omega_{\mathrm{hf}}t}}{4(\Delta - \omega_{\mathrm{hf}})}\left(e^{-i(\Delta-\omega_{\mathrm{hf}})t} - 1\right)\tilde{c}_1 \tag{4.33}$$

$$i\dot{\tilde{c}}_1 = \frac{g_{12}^* g_{02} e^{i\omega_{\mathrm{hf}}t}}{4\Delta}\left(e^{-i\Delta t} - 1\right)\tilde{c}_0 + \frac{|g_{12}|^2}{4\left(\Delta - \omega_{\mathrm{hf}}\right)}\left(e^{-i(\Delta-\omega_{\mathrm{hf}})t} - 1\right)\tilde{c}_1 \tag{4.34}$$

As in equation 4.28, note that $\Delta \gg \omega_{\mathrm{hf}}$. This means that $\Delta - \omega_{\mathrm{hf}} \approx \Delta$. We can again apply the RWA, this time eliminating the $e^{i\Delta t}$ terms:

$$i\dot{\tilde{c}}_0 = -\frac{|g_{02}|^2}{4\Delta}\tilde{c}_0 - \frac{g_{02}^* g_{12} e^{-i\omega_{\mathrm{hf}}t}}{4\Delta}\tilde{c}_1 \tag{4.35}$$

$$i\dot{\tilde{c}}_1 = -\frac{g_{12}^* g_{02} e^{i\omega_{\mathrm{hf}}t}}{4\Delta}\tilde{c}_0 - \frac{|g_{12}|^2}{4\Delta}\tilde{c}_1 \tag{4.36}$$

We now define the effective Rabi frequency Ω, together with the two-photon light shifts δ_{L_0} and δ_{L_1}:

$$\Omega = \frac{g_{02}^* g_{12}}{2\Delta} \tag{4.37}$$

$$\delta_{\mathrm{L}_0} = \frac{|g_{02}|^2}{4\Delta} \tag{4.38}$$

$$\delta_{\mathrm{L}_1} = \frac{|g_{12}|^2}{4(\Delta - \omega_{\mathrm{hf}})} \tag{4.39}$$

With these substitutions, equations 4.35 - 4.36 become:

$$i\dot{\tilde{c}}_0 = -\delta_{\mathrm{L}_0}\tilde{c}_0 - \frac{\Omega}{2}e^{-i\omega_{\mathrm{hf}}t}\tilde{c}_1 \tag{4.40}$$

$$i\dot{\tilde{c}}_1 = -\frac{\Omega}{2}e^{i\omega_{\mathrm{hf}}t}\tilde{c}_0 - \delta_{\mathrm{L}_1}\tilde{c}_1 \tag{4.41}$$

In the non-rotating frame, this becomes:

$$i\dot{c}_0 = -\left(\frac{\omega_{\mathrm{hf}}}{2} + \delta_{\mathrm{L}_0}\right)c_0 - \frac{1}{2}\Omega c_1 \tag{4.42}$$

$$i\dot{c}_1 = -\frac{1}{2}\Omega c_0 - \left(-\frac{\omega_{\mathrm{hf}}}{2} + \delta_{\mathrm{L}_1}\right)c_1 \tag{4.43}$$

which corresponds to an effective two-level Hamiltonian:

$$\mathcal{H}_{\mathrm{eff}} = -\frac{1}{2}\begin{pmatrix} \omega_{\mathrm{hf}} + 2\delta_{\mathrm{L}_0} & \Omega \\ \Omega & -\omega_{\mathrm{hf}} + 2\delta_{\mathrm{L}_1} \end{pmatrix} \tag{4.44}$$

$$= -\frac{1}{2}\left[\Omega\hat{\sigma}_x + \left(\omega_{\mathrm{hf}} + \delta_{\mathrm{L}_0} - \delta_{\mathrm{L}_1}\right)\hat{\sigma}_z + \left(\delta_{\mathrm{L}_0} + \delta_{\mathrm{L}_1}\right)\mathbb{1}\right] \tag{4.45}$$

where in the second equality of equation 4.45, the Hamiltonian has been expressed in terms of Pauli spin operators. Note that the hyperfine precession frequency is now modified by the differential light shift, $\delta_{\mathrm{L}_0} - \delta_{\mathrm{L}_1}$, and x rotations are driven by Ω.

4.1.3 Multiple Excited States, Multiple Beams

While the above analysis was done for the case of a single excited state, it is not difficult to generalize it to multiple excited states. For σ^+ light incident on $^{171}\mathrm{Yb}^+$, there are three nearby excited states:

$$\left|^2P_{1/2}, F = 1, m_F = 1\right\rangle \equiv |2\rangle \tag{4.46}$$

$$\left|^2P_{3/2}, F = 1, m_F = 1\right\rangle \equiv |3\rangle \tag{4.47}$$

$$\left|^2P_{3/2}, F = 2, m_F = 1\right\rangle \equiv |4\rangle \tag{4.48}$$

The states $|2\rangle$ and $|3\rangle$ couple to $|0\rangle$ and $|1\rangle$, while $|4\rangle$ couples only to $|1\rangle$. let g_{ij} denote the single photon Rabi frequency between states $|i\rangle$ and $|j\rangle$. Let $\Delta_j = \omega_0 - \omega_j$. The couplings to each excited state add, and the result is a modification of equation 4.37-4.39:

$$\Omega = \frac{g_{02}^* g_{12}}{2\Delta_2} + \frac{g_{03}^* g_{13}}{2\Delta_3} \tag{4.49}$$

$$\delta_{\mathrm{L}_0} = \frac{|g_{02}|^2}{4\Delta_2} + \frac{|g_{03}|^2}{4\Delta_3} \tag{4.50}$$

$$\delta_{\mathrm{L}_1} = \frac{|g_{12}|^2}{4(\Delta_2 - \omega_{\mathrm{hf}})} + \frac{|g_{13}|^2}{4(\Delta_3 - \omega_{\mathrm{hf}})} + \frac{|g_{14}|^2}{4(\Delta_4 - \omega_{\mathrm{hf}})} \tag{4.51}$$

Similarly, the result can also be generalized to multiple laser beams. The net single photon Rabi frequency between states i and j from multiple beams is given

by the sum over the single photon Rabi frequency from each individual beam. This can be seen by replacing equation 4.18 with a sum over each electric field from each beam, which then appears in equations 4.20 and 4.21. If g_{ij_k} is the single photon Rabi frequency between states i and j from beam k, equation 4.49 becomes:

$$\Omega = \frac{1}{2\Delta_2}\left(\sum_k g^*_{02_k}\right)\left(\sum_k g_{12_k}\right) + \frac{1}{2\Delta_3}\left(\sum_k g^*_{03_k}\right)\left(\sum_k g_{13_k}\right) \tag{4.52}$$

Here I am assuming that the multiple beams are all of the same frequency. Recall that g_{ij}, defined in equation 4.20, is complex. Its complex nature stems from the $e^{i\phi}$ coefficient in equation 4.20. The optical phase ϕ is determined by the ion position (i.e. $\phi = \mathbf{k}\cdot\mathbf{r} + \phi_0$, where $\mathbf{k}$ is the wave vector of the laser, $\mathbf{r}$ is the ion position, and ϕ_0 is a constant offset). When multiple beams are added, each with a different wave vector $\mathbf{k}$, the complex character of the Rabi frequency results in position-dependent cross terms in equation 4.52. These cross terms are what will create the spin-motion coupling, discussed in chapter 5.

4.1.4 Calculation of Single Photon Rabi Frequencies

To determine the single photon Rabi frequencies, we need to know the dipole matrix element $\langle i\,|\boldsymbol{\mu}\cdot\hat{\boldsymbol{\epsilon}}|\,j\rangle$ in equations 4.20-4.21. This matrix element will depend on the details of the electronic wave function. Ab initio calculations of matrix elements for large atoms such as $^{171}Yb^+$ are extraordinarily difficult, and are an active area of research [105, 106]. However, the matrix element can be written in terms of the spontaneous emission rate of the P state, which can then be determined experimentally.

As discussed in chapter 3, $^{171}\mathrm{Yb}^{+}$ has a single valence electron, and is therefore approximately hydrogenic. The $^{2}\mathrm{S}_{1/2}$ and $^{2}\mathrm{P}_{1/2}$ energy eigenstates of $^{171}\mathrm{Yb}^{+}$ are characterized by the valence electron's spin S and orbital angular momentum L, the nuclear spin I, total atomic angular momentum F and atomic angular momentum projection m_F. J represents the total electron angular momentum $L+S$. For $^{171}\mathrm{Yb}^{+}$, $S=1/2$ and $I=1/2$.

Using the Wigner-Eckart theorem [91, 107], the dipole matrix element can be expressed in terms of a reduced matrix element and angular momentum coupling coefficients as:

$$\begin{aligned}
&\langle \alpha' F' M_F' \left| \boldsymbol{\mu} \cdot \hat{\boldsymbol{\epsilon}} \right| \alpha F M_F \rangle = \\
&(-1)^{J'+I-M_F'} \sqrt{(2F+1)(2F'+1)} \begin{Bmatrix} J' & F' & I \\ F & J & 1 \end{Bmatrix} \begin{pmatrix} F & 1 & F' \\ M_F & q & -M_F' \end{pmatrix} \langle \alpha' J' || \mu || \alpha J \rangle \\
&= C(F, m_F, J, F', m_F', J', I, q) \langle \alpha' J' || \mu || \alpha J \rangle
\end{aligned} \tag{4.53}$$

Where q indicates the polarization $\hat{\boldsymbol{\epsilon}}$: $q=-1$ is σ^{-}-polarized, $q=0$ is π-polarized, and $q=+1$ is σ^{+}-polarized. The above formula applies for pure polarizations; generalizing to arbitrary polarization is straightforward. The coefficient of the reduced matrix element are Wigner 3j and 6j symbols [108], which are products of Clebsch-Gordan coefficients. The reduced matrix element can then be found in terms of the spontaneous emission rate γ between J and J' using Fermi's golden rule for an atom coupled to free space [109]:

$$\left| \langle \alpha' J' || \mu || \alpha J \rangle \right|^2 = \frac{3\pi\epsilon_0 \hbar c^3 (2J'+1)\gamma}{\omega_0^3} \tag{4.54}$$

Combining equations 4.20, 4.53 and 4.54 yields an expression for the single

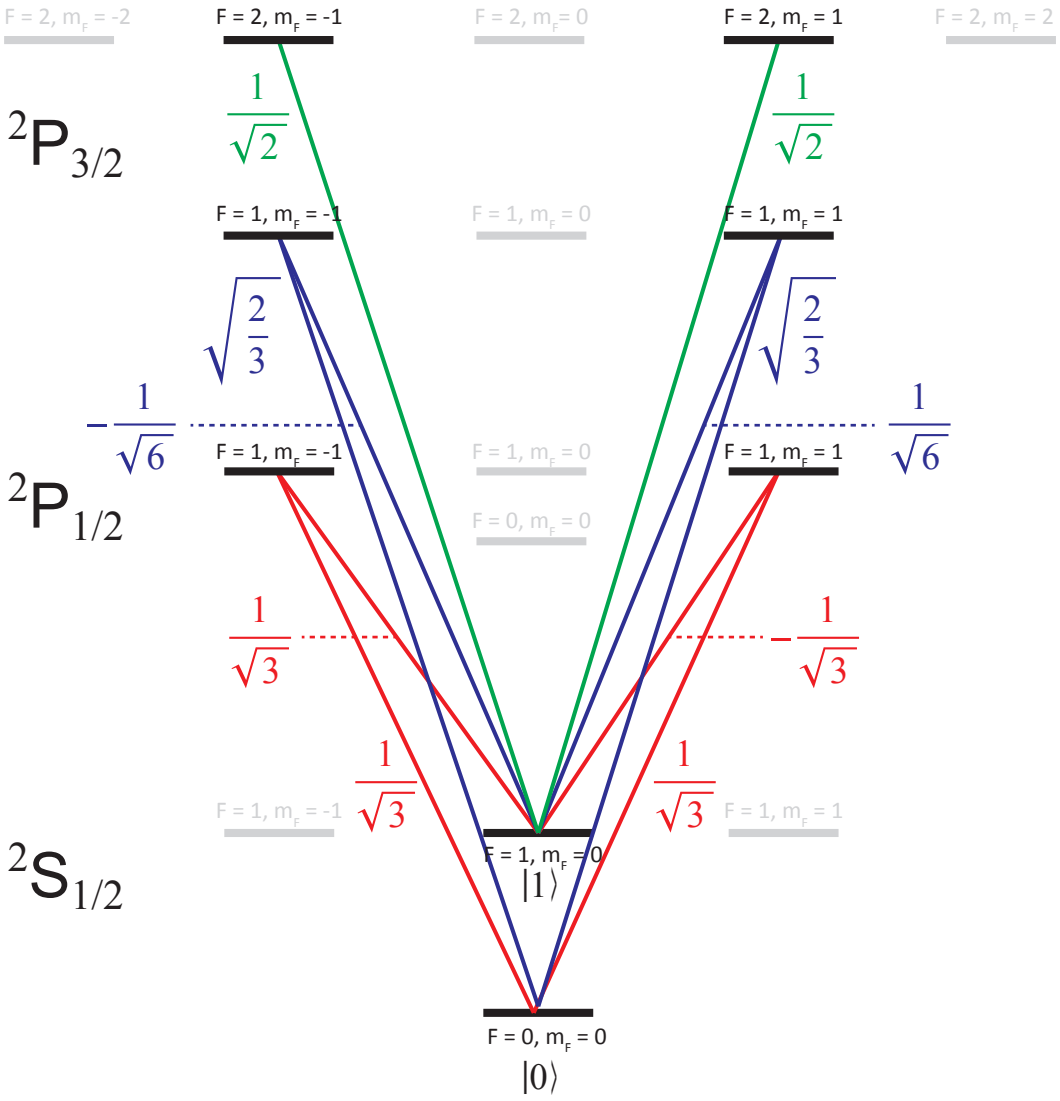

Figure 4.2: Angular momentum coupling coefficients for relevant $^{171}\mathrm{Yb}^+$ transitions. Single photon Rabi frequency is $C\gamma e^{i\phi}\sqrt{\frac{I}{2I_{\mathrm{sat}}}}$, where C is the number labeled on the transition.

	$^2\mathrm{S}_{1/2}$: $F=0, m_F=0$	$^2\mathrm{S}_{1/2}$: $F=1, m_F=0$
$^2\mathrm{P}_{1/2}$: $F=1, m_F=+1$	$1/\sqrt{3}$	$-1/\sqrt{3}$
$^2\mathrm{P}_{3/2}$: $F=1, m_F=+1$	$\sqrt{2/3}$	$1/\sqrt{6}$
$^2\mathrm{P}_{3/2}$: $F=2, m_F=+1$	0	$1/\sqrt{2}$
$^2\mathrm{P}_{1/2}$: $F=1, m_F=-1$	$1/\sqrt{3}$	$1/\sqrt{3}$
$^2\mathrm{P}_{3/2}$: $F=1, m_F=-1$	$\sqrt{2/3}$	$-1/\sqrt{6}$
$^2\mathrm{P}_{3/2}$: $F=2, m_F=-1$	0	$1/\sqrt{2}$

Table 4.1: Single-photon coupling coefficients relevant for Raman transitions in $^{171}\mathrm{Yb}^+$. Numbers follow from equation 4.53.

photon Rabi frequency:

$$\begin{aligned} g_{ij} &= -\mathcal{E}(t)e^{-i\phi}\left\langle i\left|\boldsymbol{\mu}\cdot\hat{\boldsymbol{\epsilon}}\right|j\right\rangle \\ &= -\mathcal{E}(t)e^{-i\phi}C(F,m_F,J,F',m'_F,J',I,q)\sqrt{\frac{3\pi\epsilon_0 c^3(2J'+1)\gamma}{\hbar\omega_0^3}} \end{aligned} \tag{4.55}$$

This can be simplified by defining the saturation intensity I_{sat} [91], and replacing the electric field envelope $\mathcal{E}(t)$ with the intensity envelope $I(t)$:

$$I_{\text{sat}} = \frac{\hbar\omega_0^3\gamma}{12\pi c^2} \tag{4.56}$$

$$I(t) = \frac{c\epsilon_0\mathcal{E}(t)^2}{2} \tag{4.57}$$

The single photon Rabi frequency then becomes:

$$g_{ij} = \tilde{C}(F,m_F,J,F',m'_F,J',I,q)e^{-i\phi}\gamma\sqrt{\frac{I(t)}{2I_{\text{sat}}}} \tag{4.58}$$

where $\tilde{C} = C\sqrt{(2J'+1)}$. The values of $\tilde{C}$ are shown in figure 4.2 and table 4.1 for relevant transitions. Equation 4.58 allows us to calculate the Rabi frequency and light shifts in equations 4.49 - 4.51:

$$\Omega(t) = \frac{I(t)}{12}\left[-\frac{\gamma_2^2}{\Delta_2 I_{\text{sat}_2}} + \frac{\gamma_3^2}{\Delta_3 I_{\text{sat}_3}}\right] \tag{4.59}$$

$$\delta_{\text{L}_0}(t) = \frac{I(t)}{24}\left[\frac{\gamma_2^2}{\Delta_2 I_{\text{sat}_2}} + \frac{2\gamma_3^2}{\Delta_3 I_{\text{sat}_3}}\right] \tag{4.60}$$

$$\delta_{\text{L}_1}(t) = \frac{I(t)}{24}\left[\frac{\gamma_2^2}{(\Delta_2-\omega_{\text{hf}})I_{\text{sat}_2}} + \frac{\gamma_3^2}{2(\Delta_3-\omega_{\text{hf}})I_{\text{sat}_3}} + \frac{3\gamma_4^2}{2(\Delta_4-\omega_{\text{hf}})I_{\text{sat}_4}}\right] \tag{4.61}$$

The relevant atomic parameters are shown in table 4.2. Substituting these values into equations 4.59-4.61 yields numerical values for Ω, δ_{L_0}, and δ_{L_1} in terms of the intensity profile:

	$^2P_{1/2}$	$^2P_{3/2}$
Spontaneous emission rate γ	1.238×10^8 s^{-1}	1.627×10^8 s^{-1}
Saturation intensity I_{sat}	510.3 W/m^2	950.6 W/m^2
Detuning $\Delta/2\pi$	+33 THz	−67 THz
Ratio γ^2/I_{sat}	3.003×10^{13} s/kg	2.785×10^{13} s/kg

Table 4.2: Spontaneous emission rate, saturation intensity and detuning for $^2P_{1/2}$ and $^2P_{3/2}$. Spontaneous emission rate values were taken from [110, 111]. Saturation intensity was calculated from equation 4.56.

$$\Omega(t) = \left[-1.76 \times 10^{-2} \frac{\text{s}^{-1}}{\text{W/m}^2}\right] I(t) \tag{4.62}$$

$$\delta_{\text{L}_0}(t) = \left[5.231 \times 10^{-4} \frac{\text{s}^{-1}}{\text{W/m}^2}\right] I(t) \tag{4.63}$$

$$\delta_{\text{L}_1}(t) = \left[5.264 \times 10^{-4} \frac{\text{s}^{-1}}{\text{W/m}^2}\right] I(t) \tag{4.64}$$

$$\Rightarrow \delta_{\text{L}_1}(t) - \delta_{\text{L}_0}(t) = \left[3.3 \times 10^{-6} \frac{\text{s}^{-1}}{\text{W/m}^2}\right] I(t) \tag{4.65}$$

The small values for the light shifts relative to the Rabi frequency are due to the fact that the laser frequency is blue detuned of the $^2S_{1/2} \rightarrow {}^2P_{1/2}$ line and red detuned of the $^2S_{1/2} \rightarrow {}^2P_{3/2}$ line. The detunings Δ_2 and $\Delta_{3,4}$ therefore have opposite signs, leading to partial cancellation between the light shifts from the two P states in equations 4.60 and 4.61. However, the coupling coefficients in table 4.1 also have opposite sign, resulting in constructive interference in equation 4.59. The net result is that the differential light shift is vanishingly small compared to the Rabi frequency:

$$\frac{\delta_{\text{L}_0} - \delta_{\text{L}_1}}{\Omega} = 1.88 \times 10^{-4} \tag{4.66}$$

This excellent suppression of the light shift is due to the laser wavelength (355 nm) being near optimal for $^{171}Yb^+$. Figure 4.3 shows the differential light shift to Rabi

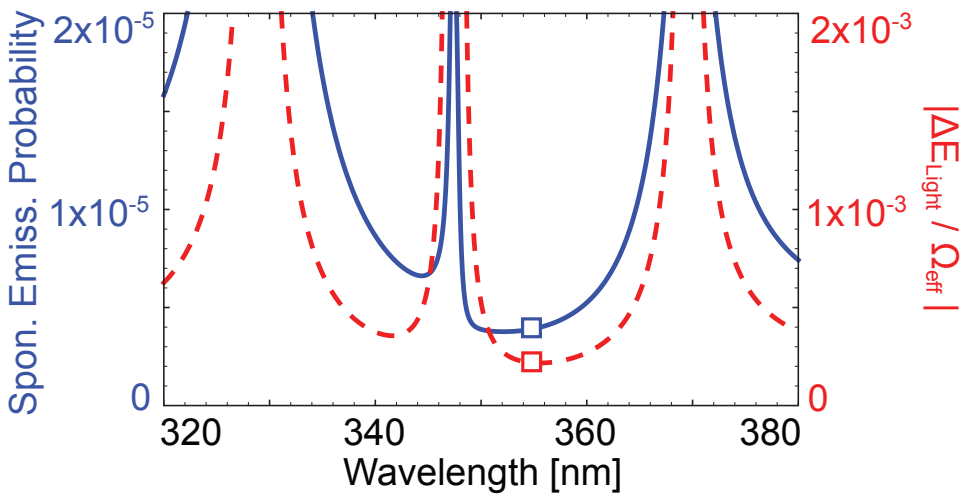

Figure 4.3: Differential light shift (as a fraction of the Rabi frequency) and spontaneous emission probability during a π- pulse as a function of laser wavelength. The white squares indicate 355 nm, which is nearly at the minimum for both processes. The plot has a broad divergence at the 369 nm (resonance for the $^2P_{1/2}$ state) and 329 nm (resonance for the $^2P_{3/2}$ state). There is also a narrow divergence at 348 nm due to the presence of a bracket state at that frequency, not discussed in the text.

frequency ratio as a function of wavelength. The minimum is extremely close to 355 nm. Note that the light shift does not pass through zero (i.e. there is no "magic wavelength") because what is relevant here is the *differential* light shift between $|0\rangle$ and $|1\rangle$, rather than the absolute light shift of either level. Each separately pass through zero at different points, but the difference does not.

Also shown in figure 4.3 is the spontaneous emission probability during a Raman π-pulse. This plot uses the approximation for spontaneous emission probability given in [57, 112, 113]. Because of the large detuning from each excited state, the spontaneous emission rate is also nearly minimal.

Because of the strong suppression seen in equation 4.66, the differential light shift can be neglected in equation 4.45, resulting in the following two-level Hamil-

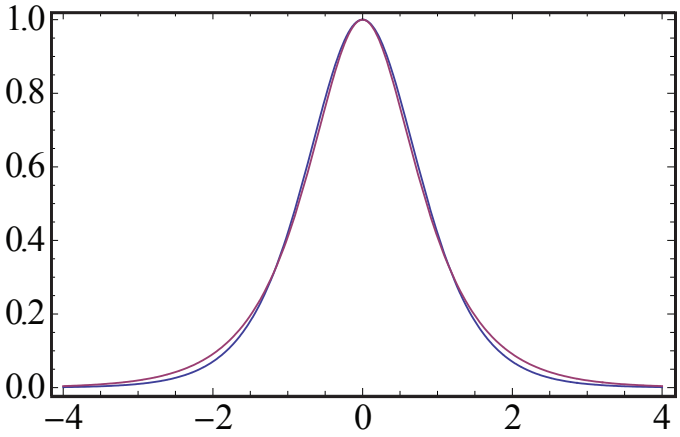

Figure 4.4: Comparison of sech and sech^2. The blue curve is $\mathrm{sech}^2(x)$. The red curve is $\mathrm{sech}(1.542x)$.

tonian:

$$\mathcal{H}_{\text{eff}} = -\frac{1}{2}\Omega(t)\hat{\sigma}_x - \frac{1}{2}\omega_{\text{hf}}\hat{\sigma}_z \tag{4.67}$$

Equation 4.67 must now be solved for a given pulse shape.

4.2 Pulse Shape

From equations 4.20, 4.21 and 4.49, the Raman Rabi frequency is proportional to the square of the electric field envelope of the laser pulse, which is its intensity envelope. For mode-locked lasers pulses, the electric field envelope is theoretically given by a hyperbolic secant [114, 115]. Because the fundamental pulse at 1064 nm is frequency tripled, one would expect the 355 nm pulse envelope to go as $\mathrm{sech}^3(t)$, and its intensity envelope to go as $\mathrm{sech}^6(t)$. However, the shape of powers of sech are very similar to the shape of sech itself, as is seen in figure 4.4. We can make the approximation:

$$\mathrm{sech}^2(x) \approx \mathrm{sech}(1.542x) \tag{4.68}$$

Using this approximation, we will assume that the intensity of the pulse, and hence the Rabi frequency, has a sech envelope. This assumption will allow an analytic solution. Numerical simulations show that using the more exact pulse shape does not lead to any significant modification of the results. I will therefore assume that the intensity profile of the pulse is given by:

$$I(t) = I_0 \operatorname{sech}\left(\frac{\pi t}{\tau}\right) \tag{4.69}$$

where τ is the *pulse duration*, and I_0 is the peak intensity. With this definition, the full width half max (FWHM) of the pulse is 0.838τ. From equation 4.59, the Raman Rabi frequency is proportional to the intensity:

$$\Omega(t) = \frac{\theta}{\tau} \operatorname{sech}\left(\frac{\pi t}{\tau}\right) \tag{4.70}$$

where θ is the *pulse area*, given by:

$$\theta = \frac{I_0 \tau}{12}\left[-\frac{\gamma_2^2}{\Delta_2 I_{\mathrm{sat}_2}} + \frac{\gamma_3^2}{\Delta_3 I_{\mathrm{sat}_3}}\right] \tag{4.71}$$

$$= \left[-1.76 \times 10^{-2} \, \frac{\mathrm{s}^{-1}}{\mathrm{W/m^2}}\right] I_0 \tau \tag{4.72}$$

θ can also be expressed in terms of the laser's average intensity $\bar{I}$ and repetition frequency ω_{rep} (equal to $2\pi/T$, where T is the time between pulses), using the relation $I_0\tau = 2\pi\bar{I}/\omega_{\mathrm{rep}}$:

$$\theta = \left[-1.76 \times 10^{-2} \, \frac{\mathrm{s}^{-1}}{\mathrm{W/m^2}}\right] \frac{2\pi\bar{I}}{\omega_{\mathrm{rep}}} \tag{4.73}$$

This is typically the more useful form, as $\bar{I}$ and ω_{rep} are far easier to measure than I_0 and τ. With θ defined as in equation 4.70, the integrated Rabi frequency is equal

to the pulse area:

$$\int \Omega(t)dt = \int_{-\infty}^{\infty} \frac{\theta}{\tau} \operatorname{sech}\left(\frac{\pi t}{\tau}\right) dt = \theta \tag{4.74}$$

Equation 4.73 allows us to estimate the intensity necessary to produce a pulse of area $\theta = \pi$. For a repetition rate of 80 MHz, a single pulse has area π if the average intensity is given by $\bar{I} = 1.4 \times 10^{10}$ W/m^2. This would be achieved, for example, with a 4 Watt beam focused down to a spot with a ~13 μm waist.

To measure the pulse shape, we used the setup shown in figure 4.5(a) to perform an electric field autocorrelation [116]. As shown in the figure, a pulse is split and then recombined with a variable delay. In a traditional autocorrelation measurement, there is no AOM. When the pulses in the two paths overlap in time, interference fringes appear. This measurement requires the setup to be stable to much less than one wavelength in order to get meaningful results. The function of the AOM is to relax this requirement. The AOM effectively averages out the optical frequency fringes, leaving a signal that oscillates at the AOM frequency. The contrast of that signal is then proportional to the amount of overlap between the pulses.

The results of this measurement are shown in figure 4.5(b). The autocorrelation signal is given by:

$$V(t) \propto \int \mathcal{E}(t')\mathcal{E}(t+t')dt' = 2t \operatorname{csch}\left(\frac{2.036t}{\tau}\right) \tag{4.75}$$

The best fit corresponds to a pulse duration of $\tau = 7.51$ ps.

The above analysis is only an accurate reflection of the pulse duration if the pulse is transform-limited, meaning that the pulse carrier wave is of a fixed frequency.

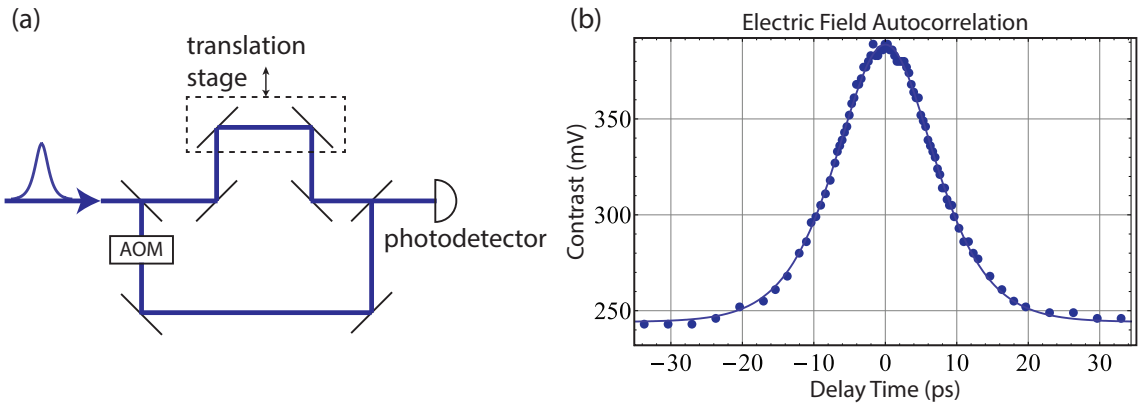

Figure 4.5: (a) Experimental setup to perform electric field autocorrelation. The AOM effectively averages out the fast fringes, such that the apparatus does not require interferometric stability. (b) Results of electric field autocorrelation. For each delay time, the signal contrast output by the photodetector is recorded. The curve is a best fit to equation 4.75.

If this is not true, the pulse is called *chirped*. For a chirped pulse, the electric field autocorrelation described above will yield a shorter pulse duration than is accurate. This is because the leading edge and trailing edge of the pulse have slightly different frequencies, and so the interference is reduced.

For a linear pulse chirp, the pulse carrier wave becomes $e^{i\omega t+bt^2}$. The measurement above then yields approximately $1/(b\tau)$, rather than τ. To separately determine b and τ, we would ideally perform an intensity autocorrelation. However, this is very difficult with UV pulses. While there do exist methods to do this [117–119], we instead inferred the values from measurements made with the ion, as will be described later.

4.3 Rosen-Zener Solution: Single Pulse

Equations 4.67 and 4.70 show that the effective Hamiltonian is:

$$\mathcal{H}_{\text{eff}}(t) = -\frac{1}{2}\frac{\theta}{\tau}\,\text{sech}\left(\frac{\pi t}{\tau}\right)\hat{\sigma}_x - \frac{1}{2}\omega_{\text{hf}}\hat{\sigma}_z \tag{4.76}$$

This Hamiltonian is rare in that it has an analytic solution in terms of well-known special functions. It was solved by Rosen and Zener in 1932 [120]. The solution is derived in appendix A. The Rosen-Zener solution provides a solution for all time t to the Hamiltonian in equation 4.76. However, for our purposes this is overly general – we are only interested in the resultant state after the pulse, not the dynamics during the pulse. We can therefore write down an evolution operator U which takes the state directly to the final state [121, 122]:

$$U = \begin{pmatrix} A & iB \\ iB & A^* \end{pmatrix} \tag{4.77}$$

where A and B are given by:

$$A = \frac{\Gamma^2(\xi)}{\Gamma\left(\xi - \frac{\theta}{2\pi}\right)\Gamma\left(\xi + \frac{\theta}{2\pi}\right)} \tag{4.78}$$

$$B = -\sin\left(\frac{\theta}{2}\right)\,\text{sech}\left(\frac{\omega_{\text{hf}}\tau}{2}\right) \tag{4.79}$$

$$\xi = \frac{1}{2} + i\frac{\omega_{\text{hf}}\tau}{2\pi} \tag{4.80}$$

where Γ is the Gamma function. For an ion initialized to $|0\rangle$, the final state will be:

$$|\psi_{\text{final}}\rangle = A\,|0\rangle + iB\,|1\rangle \tag{4.81}$$

At first glance the physics described by these equations is perhaps a little opaque. To understand them better, first consider the limiting case of an infinitesimally short

"δ-function" pulse: $\tau = 0$. In that case:

$$A \to \cos\left(\frac{\theta}{2}\right) \tag{4.82}$$

$$B \to -\sin\left(\frac{\theta}{2}\right) \tag{4.83}$$

$$U \to \begin{pmatrix} \cos(\theta/2) & -i\sin(\theta/2) \\ -i\sin(\theta/2) & \cos(\theta/2) \end{pmatrix} = \cos(\theta/2)\,\mathbb{1} - i\sin(\theta/2)\,\hat{\sigma}_x \tag{4.84}$$

This corresponds to a rotation about the x axis of the Bloch sphere by an angle θ. For a δ-function pulse, the action is a pure $\hat{\sigma}_x$ rotation. For non-zero pulse duration, equations 4.78-4.80 represent a correction to the simple delta function case. If the pulse is fast compared to the hyperfine frequency ($\omega_{\rm hf}\tau < 1$), the correction will be small.

From equation 4.81, the probability that an ion initialized to $|0\rangle$ will be subsequently measured in $|1\rangle$ after a pulse is given by:

$$P_{0\to 1} = |iB|^2 = \operatorname{sech}^2\left(\frac{\omega_{\rm hf}\tau}{2}\right)\sin^2\left(\frac{\theta}{2}\right) \tag{4.85}$$

As a function of θ, the maximum achievable population transfer occurs at $\theta = \pi$, and is given by $\operatorname{sech}^2(\omega_{\rm hf}\tau/2)$. For non-zero τ, this function is always less than one. This leads to the conclusion that a single sech pulse cannot fully transfer the ion from $|0\rangle$ to $|1\rangle$. Conceptually, this is not due to insufficient pulse area (indeed, the result is true for any pulse area), but rather due to how that area is spectrally distributed. By reshaping the spectrum, the pulse can fully transfer population to $|1\rangle$. This will be revisited later.

Figure 4.6 shows the state of the ion described by equations 4.78-4.80 as a function of pulse area θ for $\omega_{\rm hf} = 12.6$ GHz, $\tau = 15$ ps. Note that what is shown here

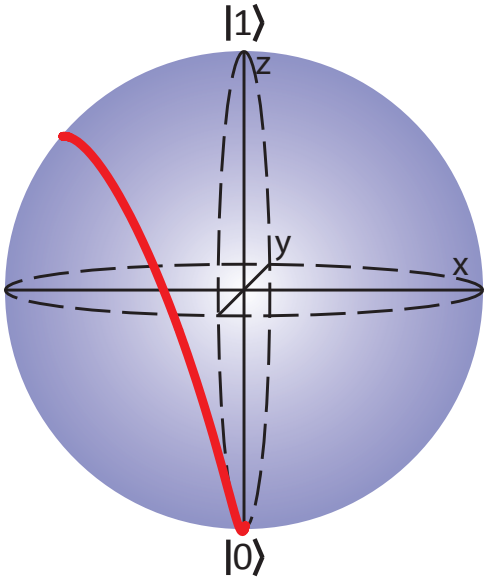

Figure 4.6: Final ion state as a function of θ for hyperbolic secant pulse, as θ goes from 0 to π.

is not the trajectory as a function of time governed by the Rosen-Zener dynamics derived in appendix A. Rather, it is the final state as a function of θ. Note that for small values of θ, the evolution is nearly exactly a rotation about the x-axis, as in the δ-function case. As θ increases, the "twist" becomes larger and larger.

4.4 Single Pulse Experimental Results

Two different lasers were used to study the effect of a single pulse: the Paladin[1] and the PicoTrain[2]. Their properties are tabulated in table 4.3. Both lasers are frequency tripled mode-locked Nd:YVO_4 lasers.

To control how many pulses are directed onto the ion, a fast Pockels cell followed by a PBS acts as a pulse picker[3]. When no signal is applied to the Pockels

[1]Coherent Paladin Compact 355-4000
[2]High Q PicoTrain Model: IC-1064-50000/532-20000/355-8000 ps, 80MHz
[3]Fast Pulse Technology model 5046SC

	Paladin	PicoTrain
Pulse Duration τ	14.8 ps	7.6 ps
Repetition rate $\omega_{\text{rep}}/2\pi$	118.30575 MHz	80.160000 MHz
Average power	4 Watts	8 Watts

Table 4.3: Laser properties for mode-locked lasers used in experiments.

cell, the pulses are rejected by the PBS. When a voltage pulse is applied, the cell rotates the polarization and the pulses are transmitted by the PBS. This system works well and can allow a single pulse to be picked from the train, with extinction ratio $> 100 : 1$. Moreover, controlling the amplitude of the applied voltage pulse allows control over the energy.

As a first experiment, the pulse picker was used to select a single pulse from the pulse train, which was then focused onto the ion. The final state of the ion was then measured as a function of pulse area, by adjusting the power in the 355 beam. Losses in the pulse picker and other optics resulted in a maximum power of approximately 3 Watts arriving at the ion. The results are shown in figure 4.7. Some of the pulse was sampled and sent onto a fast photodiode. The maximum voltage on the photodiode was then measured on an oscilloscope. That voltage is the x-axis in figures 4.7(b) and (c). The correspondence between the voltage and the actual pulse area is not known to a high degree. For the Paladin data in figure 4.7(c), the peak corresponds to 12 ± 2 nJ pulse energy. From equation 4.73, the maximum spin flip of slightly less than 2π corresponds to a waist of approximately 7 μm, which is consistent with the expected performance of the focusing lens.

The data agree with equation 4.85. The behavior is Rabi flopping as a function of θ, but with a maximum brightness limited by the non-zero pulse duration. Figure

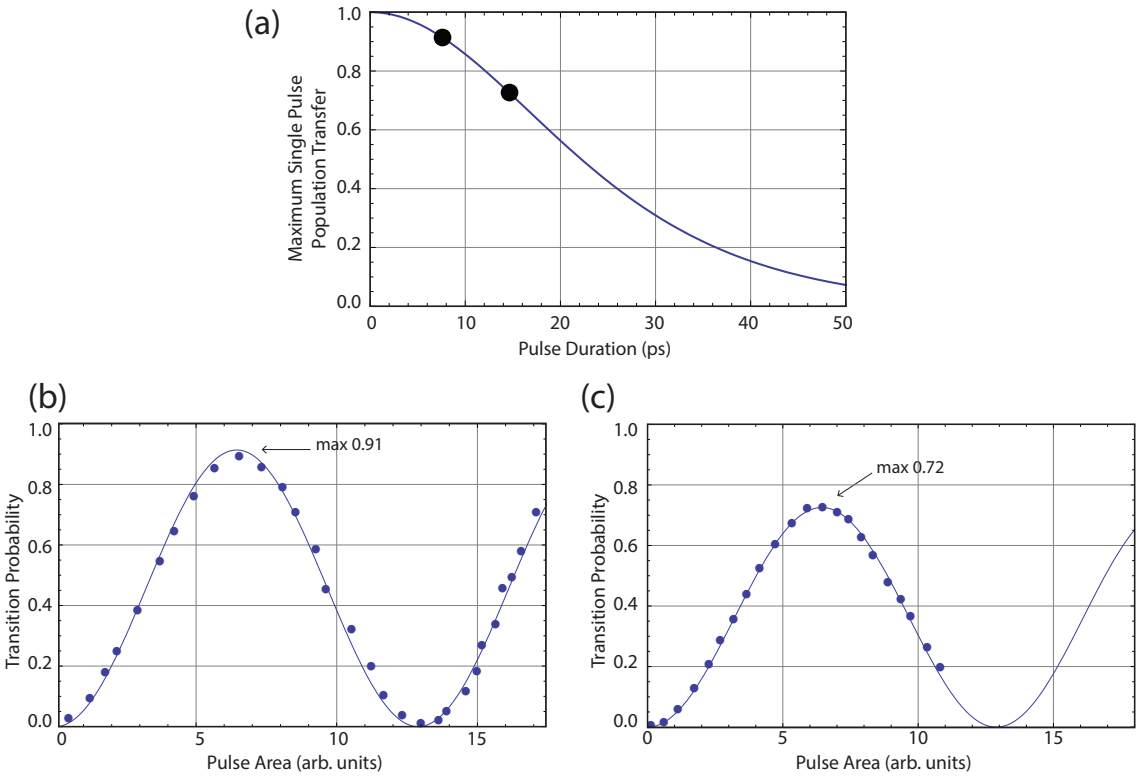

Figure 4.7: Response of an ion to a single laser pulse as a function of pulse area. (a) Theoretical maximum as a function of pulse duration, from equation 4.85. Black dots show points corresponding to (b) and (c). (b) Data showing Rabi flopping from a single pulse for the PicoTrain laser. The maximum at 0.91 indicates a pulse duration of 7.6 ps. (c) Single pulse Rabi flopping from the Paladin laser, showing a 14.8 ps pulse duration. The fit curve in (b) and (c) is a best fit to theory.

4.7(a) shows the theoretical maximum from equation 4.85, with black dots indicating the pulse durations that correspond to the maxima in (b) and (c).

The autocorrelation data shown in section 4.2 was done for the Paladin laser. The data there showed a pulse duration of 7.5 ps, significantly less than the 14.8 ps indicated by the ion data. We believe this discrepancy is due to a chirp in the pulse carrier. The two pulse data shown in figure 4.9 supports this assertion, as will be discussed there.

4.5 Multiple Pulses

We now wish to consider the effect of N such pulses, with a repetition period $T = 2\pi/\omega_{\text{rep}}$. The combined operator for a pulse followed by free evolution for a time T is given by taking the product of U with the free evolution operator. The result is:

$$\tilde{U} = \begin{pmatrix} Ae^{i\omega_{\text{hf}}T/2} & iBe^{i\omega_{\text{hf}}T/2} \\ iBe^{-i\omega_{\text{hf}}T/2} & A^*e^{-i\omega_{\text{hf}}T/2} \end{pmatrix} \tag{4.86}$$

The operator $\tilde{U}$ represents a rotational transformation of the Bloch sphere. According to Euler's fixed point theorem, any such operator can always be written as a pure rotation operator by some angle φ about a single axis $\hat{n}$:

$$\begin{aligned} \tilde{U} &= e^{i\varphi\hat{n}\cdot\vec{\sigma}/2} \\ &= \cos\left(\frac{\varphi}{2}\right)\mathbb{1} + i(\hat{n}\cdot\vec{\sigma})\sin\left(\frac{\varphi}{2}\right) && (4.87) \\ &= \begin{pmatrix} \cos(\varphi/2) + in_z\sin(\varphi/2) & i\sin(\varphi/2)(n_x - in_y) \\ i\sin(\varphi/2)(n_x + in_y) & \cos(\varphi/2) - in_z\sin(\varphi/2) \end{pmatrix} && (4.88) \end{aligned}$$

Setting equation 4.88 equal to equation 4.86 yields four equations for the rotation

axis $\hat{n}$ and rotation angle φ [116]:

$$\cos\left(\frac{\varphi}{2}\right) = \mathrm{Re}\left(Ae^{i\omega_{\mathrm{hf}}T/2}\right) \tag{4.89}$$

$$n_z \sin\left(\frac{\varphi}{2}\right) = \mathrm{Im}\left(Ae^{i\omega_{\mathrm{hf}}T/2}\right) \tag{4.90}$$

$$n_x \sin\left(\frac{\varphi}{2}\right) = B\cos\left(\omega_{\mathrm{hf}}T/2\right) \tag{4.91}$$

$$n_y \sin\left(\frac{\varphi}{2}\right) = -B\sin\left(\omega_{\mathrm{hf}}T/2\right) \tag{4.92}$$

Equation 4.88 allows the evolution operator to quickly be extended to N equally spaced pulses – N rotations by φ about $\hat{n}$ is equal to a single rotation by $N\varphi$:

$$\tilde{U}^N = e^{iN\varphi\hat{n}\cdot\vec{\sigma}/2} \tag{4.93}$$

The transition probability after N pulses can be read off from equation 4.88, replacing φ with $N\varphi$:

$$\begin{aligned} P_{0\to1} &= \left| i\sin\left(\frac{N\varphi}{2}\right)(n_x + in_y)\right|^2 \\ &= \left(\frac{|B|^2}{\sin^2\left(\frac{\varphi}{2}\right)}\right)\sin^2\left(\frac{N\varphi}{2}\right) \end{aligned} \tag{4.94}$$

Equation 4.94 represents discretized Rabi flopping with the number of pulses N, with contrast given by $|B|^2/\sin^2(\varphi/2)$. Setting this equal to one gives the condition under which population can be fully transferred:

$$\sin^2\left(\frac{\theta}{2}\right)\mathrm{sech}^2\left(\frac{\omega_{\mathrm{hf}}\tau}{2}\right) = \sin^2\left(\frac{\varphi}{2}\right) \tag{4.95}$$

If equation 4.95 is satisfied, then equation 4.94 goes to 1 for $\phi = \pi/N$. This result shows that for $N > 1$ the transition probability can be made exactly equal to 1 even for non-zero pulse duration. Note that for $N = 1$ there is no solution, because

$\phi = \pi$ sets the RHS equal to 1 in equation 4.95, while the LHS is strictly less than 1.

To understand the condition in equation 4.95, consider again the limiting case of the δ-function pulse, $\tau \to 0$. In that case, equation 4.95 becomes:

$$\sin^2\left(\frac{\theta}{2}\right) = \sin^2\left(\frac{\varphi}{2}\right) \tag{4.96}$$

From equation 4.89,

$$\cos\left(\frac{\varphi}{2}\right) = \cos\left(\frac{\theta}{2}\right)\cos\left(\frac{\omega_{\mathrm{hf}}T}{2}\right) \tag{4.97}$$

$$= \cos\left(\frac{\theta}{2}\right)\cos\left(\frac{\pi\omega_{\mathrm{hf}}}{\omega_{\mathrm{rep}}}\right) \tag{4.98}$$

Equation 4.96 and equation 4.98 can only both be true if $\cos(\pi\omega_{\mathrm{hf}}/\omega_{\mathrm{rep}}) = \pm 1$, which implies the resonance condition:

$$\omega_{\mathrm{hf}} = n\omega_{\mathrm{rep}},\ n \in \mathbb{Z} \tag{4.99}$$

This condition has a straightforward physical interpretation. In order for the pulses to coherently add, each pulse must arrive at the same phase of the hyperfine precession. This is equivalent to the statement that the hyperfine frequency must be an integer multiple of the repetition rate.

As before, introducing a non-zero pulse duration will result in a slight correction to equation 4.99. To extract this correction, first let the complex phase of A in equation 4.78 be given by $\pi\delta$:

$$A = e^{i\pi\delta}|A| \tag{4.100}$$

Substituting this expression for A into equation 4.89 yields:

$$\cos\left(\frac{\varphi}{2}\right) = \mathrm{Re}\left(|A|e^{i(\pi\delta+\omega_{\mathrm{hf}}T/2)}\right) \tag{4.101}$$

$$= |A|\cos\left[\pi\left(\delta + \frac{\omega_{\mathrm{hf}}}{\omega_{\mathrm{rep}}}\right)\right] \tag{4.102}$$

From the unitarity of the evolution operator U, we know that $|A|^2 + |B|^2 = 1$. Therefore, the resonance condition in equation 4.95 is equivalent to the condition:

$$|A|^2 = \cos^2\left(\frac{\varphi}{2}\right) \tag{4.103}$$

Equations 4.102 and 4.103 require that $\cos\left[\pi\left(\delta + \omega_{\mathrm{hf}}/\omega_{\mathrm{rep}}\right)\right] = \pm 1$, which implies the new resonance condition:

$$\omega_{\mathrm{hf}} + \delta\omega_{\mathrm{rep}} = n\omega_{\mathrm{rep}},\ n \in \mathbb{Z} \tag{4.104}$$

The non-zero pulse duration therefore results in an effective shift in the hyperfine frequency, by an amount $\delta\omega_{\mathrm{rep}}$. This shift can be thought of as a higher order light shift, and will be discussed more in section 4.7. From equation 4.100 and unitarity,

$$\delta = \frac{1}{i\pi}\log\left[\frac{A}{\sqrt{1-B^2}}\right] \tag{4.105}$$

δ can be expanded as a series in $\omega_{\mathrm{hf}}\tau$ and θ:

$$\delta = \frac{2}{\pi}\sum_{m=0}^{\infty}\sum_{n=0}^{\infty}\frac{(-1)^{m+1}\psi^{(2n+2m+2)}\left(\frac{1}{2}\right)}{(2m+1)!(2n+2)!}\left(\frac{\omega_{\mathrm{hf}}\tau}{2\pi}\right)^{2m+1}\left(\frac{\theta}{2\pi}\right)^{2n+2} \tag{4.106}$$

where $\psi^{(j)}$ is the polygamma function of order j. To lowest order, the resonance shift is given by:

$$\delta\omega_{\mathrm{rep}} \approx -\left(\frac{\psi^{(2)}(\frac{1}{2})}{8\pi^4}\right)\theta^2\omega_{\mathrm{hf}}\tau\omega_{\mathrm{rep}} \approx 0.0216\,\theta^2\omega_{\mathrm{hf}}\tau\omega_{\mathrm{rep}} \tag{4.107}$$

This shows that for small θ, the shift is quadratic in the pulse area, and hence in the laser intensity. This is very different from the ordinary light shift, which is linear in the laser intensity. This also shows that the shift is positive, resulting in a larger effective hyperfine frequency.

4.6 Two Pulse Experimental Results

An experimental schematic for the two pulse experiments[4] is shown in figure 4.8. A single pulse was split, with a variable delay T_d between the two halves. The pulse energy of each half was set to transfer 50% of the population to $|1\rangle$ when σ^+ polarized. The final state was then measured as a function of delay T_d between the two pulse halves. In the time domain, this can be thought of as a fast Ramsey experiment.

Using removable waveplates in the two counterpropagating arms, this experiment was performed for three different polarization configurations: both beams circularly polarized in the same direction (σ^+/σ^+), circularly polarized in opposite directions (σ^+/σ^-), and orthogonal linear (lin$\perp$lin). To derive expressions for the Rabi frequency in each case, I will use equation 4.52. Allow each beam to have arbitrary polarization. Since the beams are both propagating along the quantization axis, they cannot contain π light. Their polarizations $\hat{\boldsymbol{\epsilon}}_1$ and $\hat{\boldsymbol{\epsilon}}_2$ can therefore be

[4]These experiments were all done with the Paladin laser.

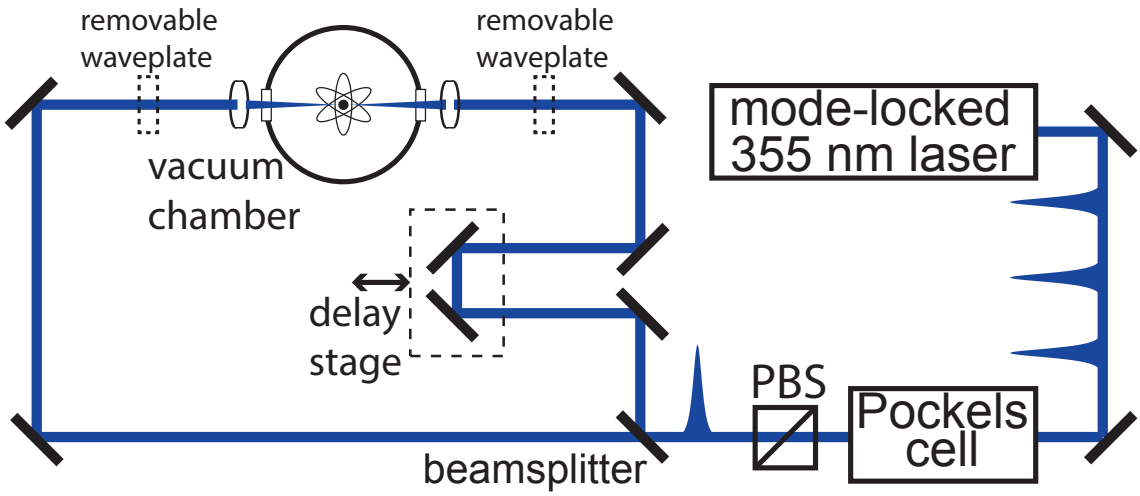

Figure 4.8: Experimental schematic for counterpropagating pulses. A fast pulse picker (Pockels cell + PBS) is used to select a single pulse from the pulse train. That pulse is split, and each half is sent onto the ion from opposite directions. A variable delay T_d allows control over the relative arrival time of each pulse, and removable waveplates in each arm allow control over the two polarizations. The pulse energy is set such that each half separately transfers 50% of the population to $|1\rangle$ when the polarization is pure σ^+.

described as a superposition of σ^+ and σ^-:

$$\hat{\boldsymbol{\epsilon}}_1 = \cos(\beta_1)\,\sigma^+ + \sin(\beta_1)\,\sigma^- \tag{4.108}$$

$$\hat{\boldsymbol{\epsilon}}_2 = \cos(\beta_2)\,\sigma^+ + \sin(\beta_2)\,\sigma^-, \tag{4.109}$$

where β_i then determines the polarization of beam i. Expanding equation 4.52 using equation 4.58 then gives a general expression for the Rabi frequency from two counter-propagating pulse trains:

$$\begin{aligned}\Omega =&\Omega_1(t)\cos(2\beta_1) + \Omega_2(t-T_d)\cos(2\beta_2) + \\ &2\cos(\beta_1+\beta_2)\sqrt{\Omega_1(t)\Omega_2(t-T_d)}\cos(\Delta k x + \Delta\phi)\end{aligned} \tag{4.110}$$

where $\Omega_i(t)$ is the Rabi frequency for beam i alone (arriving at $t=0$), T_d is the delay time between the two pulses, x is the ion position, Δk and $\Delta\phi$ are the differences between the pulses in wave vector and phase, respectively. Note that one immediate

consequence of equation 4.110 is that if the pulses overlap in time, the Rabi frequency may acquire a dependence on the ion position. This in turn will lead to a spin-motion coupling. The three polarization configurations now correspond to different values of β_1 and β_2:

$$\beta_1 = 0,\ \beta_2 = 0\text{:}\ \ \sigma^+/\sigma^+$$

$$\beta_1 = 0,\ \beta_2 = \frac{\pi}{2}\text{:}\ \ \sigma^+/\sigma^-$$

$$\beta_1 = \frac{\pi}{4},\ \beta_2 = -\frac{\pi}{4}\text{:}\ \ \text{lin} \perp \text{lin}$$

From equation 4.110, the Rabi frequencies in each case are:

$$\Omega_{\sigma^+/\sigma^+} = \Omega_1(t) + \Omega_2(t - T_d) + 2\sqrt{\Omega_1(t)\Omega_2(t - T_d)}\cos\left(\Delta k x + \Delta\phi\right) \tag{4.111}$$

$$\Omega_{\sigma^+/\sigma^-} = \Omega_1(t) - \Omega_2(t - T_d) \tag{4.112}$$

$$\Omega_{\text{lin}\perp\text{lin}} = 2\sqrt{\Omega_1(t)\Omega_2(t - T_d)}\cos\left(\Delta k x + \Delta\phi\right) \tag{4.113}$$

I will address each of these cases separately.

4.6.1 σ^+/σ^+ case

If the pulses do not overlap in time ($T_d \gtrsim 2\tau$), equation 4.111 becomes $\Omega_{\sigma^+/\sigma^+} = \Omega_1(t) + \Omega_2(t - T_d)$. As the two pulses are of equal area, the multiple pulse solution in section 4.5 applies. The results of scanning the delay T_d are shown in figure 4.9(a). Away from the overlap region, the population transfer oscillates between 0 and 1 with a period given by $2\pi/\omega_{\text{hf}}$. The first maximum is not at exactly $2\pi/\omega_{\text{hf}}$ because of the shift δ in equation 4.104 – the maxima occur at delays given by $T_d = 2\pi(n - \delta)/\omega_{\text{hf}}$, for n an integer.

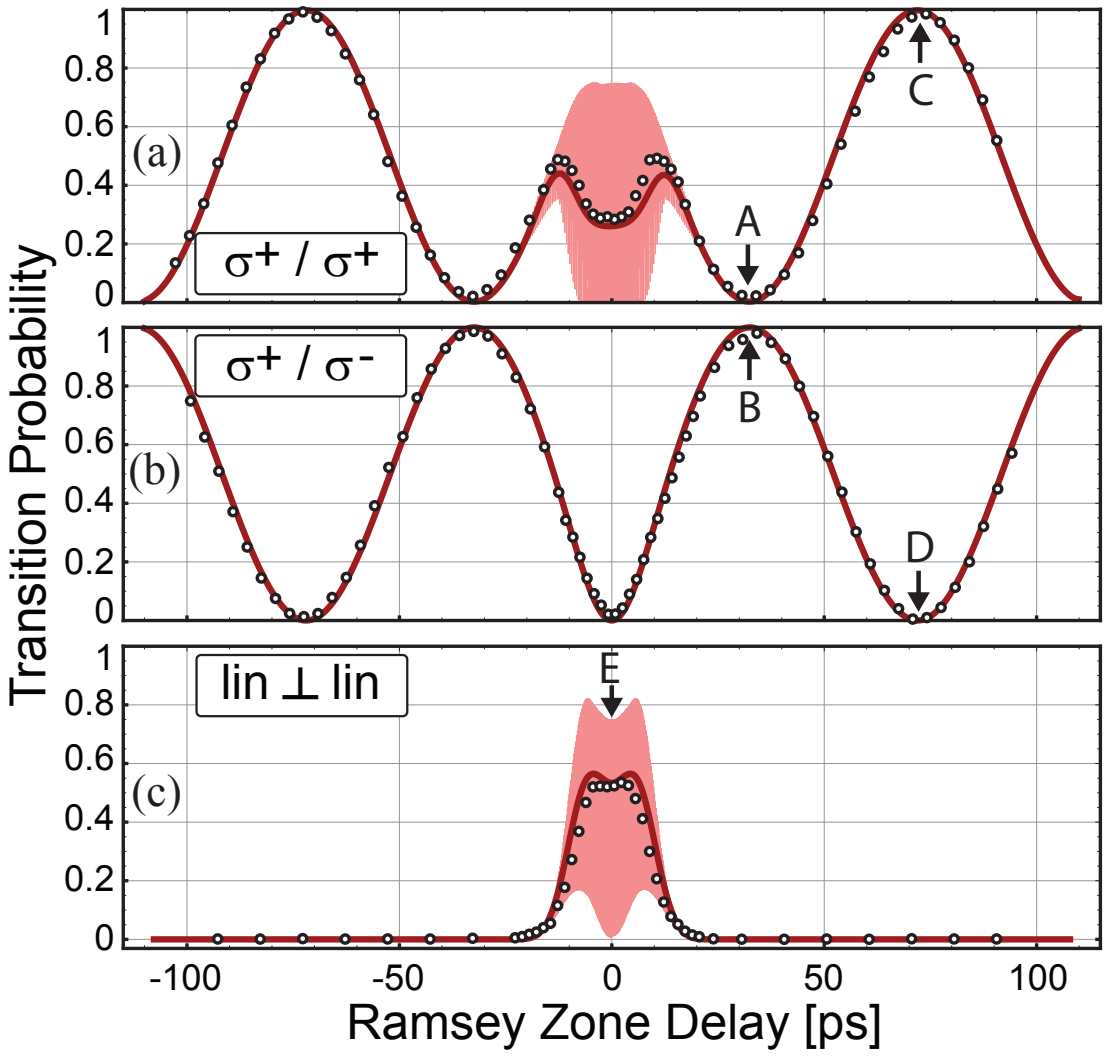

Figure 4.9: Transition probability as a function of delay for the three polarization configurations of the two arms in figure 4.8. The light pink lines in (a) and (c) correspond to equations 4.111-4.113, with no free fit parameters. The oscillations are so fast that the curves appears as continuous shaded pink regions in the figure. The dark red line in (a) and (c) correspond to taking a thermal average, which washes out the optical fringes. Points B and C correspond to fast π rotations ($\sim$40 and 80 ps, respectively). Points A and D correspond to pure $\hat{\sigma}_z$ rotations. In the interference region in (c), all transitions include momentum transfer. The zero delay point, marked E, is the operating point for the spin-motion entanglement experiments discussed in chapter 5.

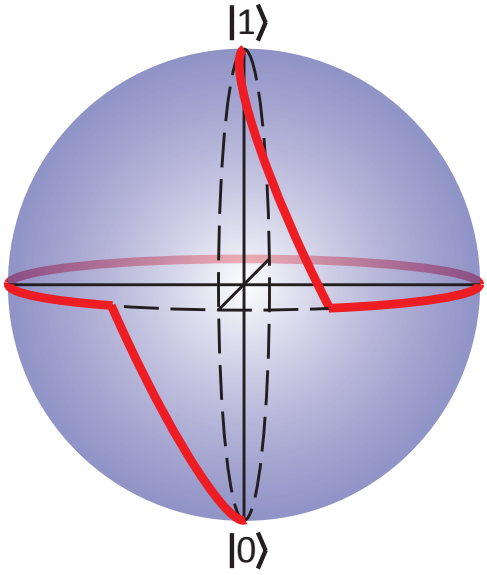

Figure 4.10: Effective Bloch sphere path for two pulse spin flip. A single pulse rotates to the equator, and a second pulse with an appropriate delay rotates to the north pole.

The point labeled C corresponds to a π pulse in just 72 ps. It is difficult to quantify the fidelity of this π pulse, as the π-pulse fidelity is higher than the detection fidelity. By comparing to histograms obtained from resonant microwaves, the π-pulse fidelity can be bounded at $> 99\%$. For delay times away from the maximum, any other value of $|c_1|^2$ can be obtained, in a time on the order of tens of picoseconds.

As previously mentioned, the first maximum should occur at $T_d = 2\pi(1 - \delta)/\omega_{\mathrm{hf}}$. Substituting $\tau = 14.8$ ps and $\theta = 1.968$ (obtained from the single pulse data in figure 4.7) into equation 4.106 yields $\delta = 0.099$, corresponding to a predicted maximum at $T_d = 71.24$ ps. This agrees with the measured value of $T_d = 73 \pm 2$ ps in figure 4.9(a).

The effective Bloch sphere path for two pulses with 73 ps delay is shown in figure 4.10. A single pulse drives effective rotations about a tilted circle. By rotating

up to the equator, a second pulse can transfer the population to $|1\rangle$. This picture also makes clear that two pulses can fully transfer the population only if one pulse can reach the equator. This corresponds to a constraint on the pulse duration of $\tau < 22$ ps. Above that, at least three pulses would be required.

When the pulses begin to overlap in time, equation 4.111 predicts interference fringes in the Rabi frequency. The thin pink line shows a numerical solution. However, because the ion is in a hot thermal state, what is actually observed is a thermal average over those fringes, shown in the thick red line. This agrees well with the observed data. Significantly, the red line is *not* a fit to the data. Rather, it uses the pulse duration obtained from the single pulse result in figure 4.7, and the pulse chirp obtained from the autocorrelation measurement in section 4.2. The good agreement with the data therefore lends credence to the validity of the model.

4.6.2 σ^+/σ^- Case

In the σ^+/σ^- case, there is no interference term. This is because the overlap produces linear polarized light, which cannot drive transitions. At zero delay, the transition probability therefore goes to zero. Away from zero, the behavior is very similar to the σ^+/σ^+ case. However, the Rabi angle for the second pulse has the opposite sign from that of the first pulse. The oscillations are therefore exactly out of phase with the σ^+/σ^+ case. This produces a slightly faster π-pulse, in approximately 40 ps.

The non-sinusoidal nature of this curve is evident in the figure, and is once again caused by the shift δ. The maxima occur at $T_d = 2\pi(n + 1/2 - \delta)/\omega_{\mathrm{hf}}$. The

distance between the two maxima closest to zero is therefore $4\pi(1/2-\delta)/\omega_{\rm hf} = 63.4$ ps, while the distance from either to the next maximum is $2\pi/\omega_{\rm hf} = 79.1$ ps.

4.6.3 lin $\perp$ lin Case

In the lin $\perp$ lin case, each beam separately cannot drive transitions, because their σ^+ and σ^- contributions destructively interfere. However, when the pulses overlap, they produce a polarization gradient, which oscillates between circularly polarized and linearly polarized [91]. This gradient can drive transitions. In this case, *all* transitions are accompanied with momentum transfer, as the ion can only execute transitions by absorbing from one beam and emitting into the other. This feature will be used in chapter 5.

4.6.4 $\hat{\sigma}_z$ Rotations

The results in figures 4.9(a) and (b) demonstrate arbitrary x rotations. However, the same experimental setup can be used to execute arbitrary z rotations, using the four photon light shift. For the strong pulses described here, the light shift is considerable. Consider the point labeled A in figure 4.9(a). At this point, the transition probability is zero, meaning that there is no rotation of the qubit around the x-axis. This is because the $\hat{\sigma}_x$ contribution from each pulse exactly cancel. The $\hat{\sigma}_z$ contributions, however, do not cancel. These two pulses therefore correspond to a pure $\hat{\sigma}_z$ operator on the ion.

This was demonstrated using a microwave Ramsey experiment. Two microwave $\pi/2$ pulses were applied to the ion. The frequency of the microwaves was

then scanned, resulting in the pattern of fringes shown in the blue curve in figure 4.11(a). When the two pulse $\hat{\sigma}_z$ operator is then inserted, those fringes shift, as shown in the red curve in figure 4.11(a). The net σ_z rotation caused by the two pulses can then be determined from the fringe shift. Controlling the strength of the two laser pulses allows control over the rotation angle. The achieved rotation angle as a function of pulse energy is shown in figure 4.11(c). The fit curve is derived from equation 4.106. The only free parameter is the scale factor between the measured pulse height using a photodiode and the actual pulse area. Note the approximately quadratic behavior for small θ.

Taken together, these results show that a single ultrafast pulse from a mode-locked laser allows complete control over both of the qubit's spin degrees of freedom in $\sim$50 ps. This is 5 orders of magnitude faster than what is normally done with trapped ions. By way of comparison, the best coherence time measured for the $^{171}Yb^{+}$ qubit was > 1000 s [67]. This operation is 13 orders of magnitude faster than that coherence time.

4.7 Weak Pulses and Frequency Combs

The time domain analysis in section 4.5 can be thought of as a "bottom up" approach, in which the response to a pulse train is understood by examining the response pulse by pulse. By contrast, a frequency domain analysis is a "top down approach," in which the behavior is understood by examining aggregate properties of the spectrum of the pulse train. Both pictures are valuable.

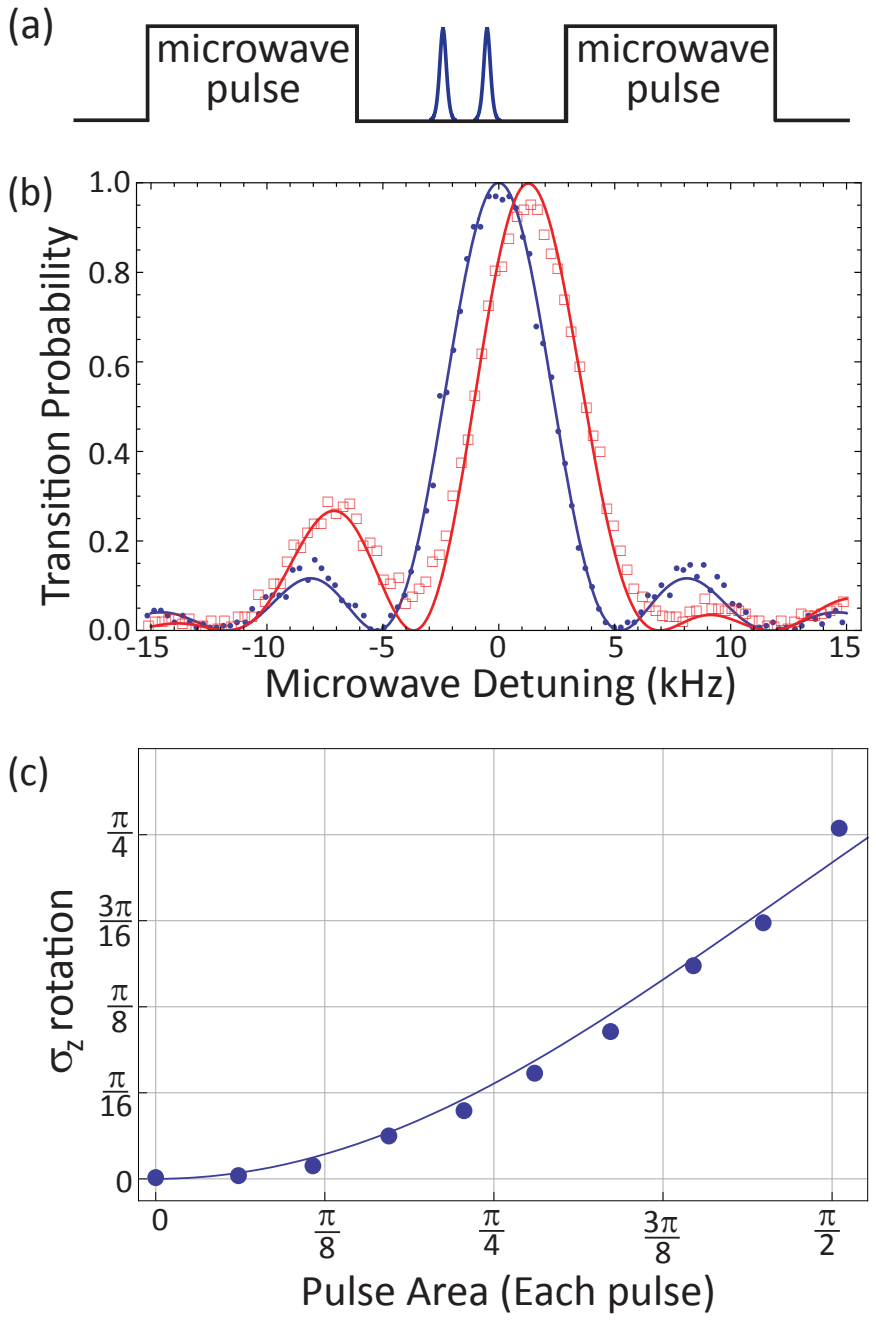

Figure 4.11: (a) Experiment to demonstrate ultrafast $\hat{\sigma}_z$ rotations. The ion brightness is measured as the frequency of two microwave pulses is scanned. In between, the two σ^+ pulses with a 32 ps delay are inserted, which causes z rotations without x rotations. (b) Two example curves from this experiment. The blue circle data is the microwave scan without the pulses. The red square data is the scan with pulses. The shift in the fringes yields the degree of rotation. (c) Plot of the z rotation angle as a function of pulse area per pulse. The fit curve is derived from equation 4.106.

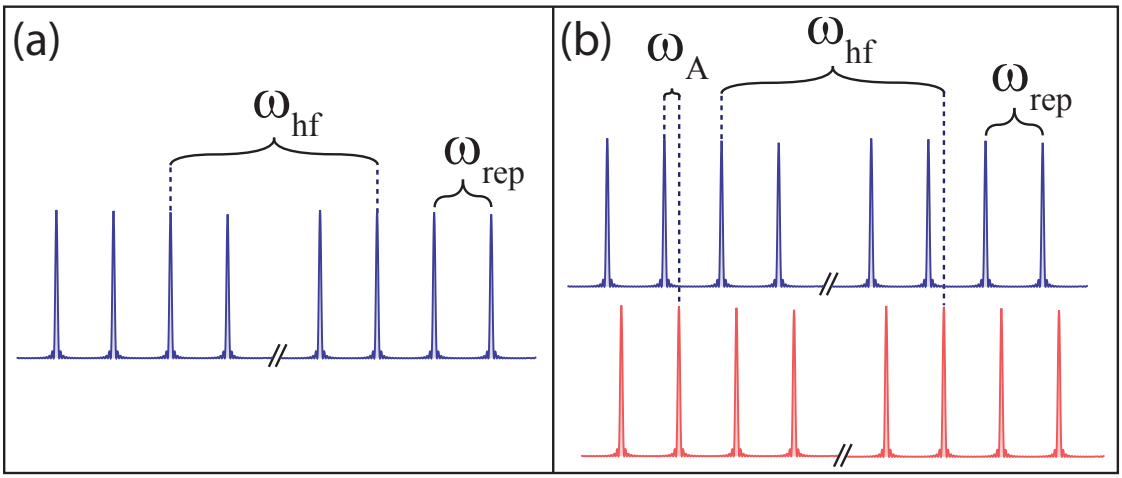

Figure 4.12: (a) One frequency comb can drive Raman transitions if pairs of comb lines are separated by the qubit frequency, leading to the condition in equation 4.114. (b) Two frequency combs can drive Raman transitions together if a frequency offset ω_A between the combs causes lines from the separate beams to be spaced by the qubit frequency, leading to the condition in equation 4.115.

If individual pulses are very weak ($\theta \ll 1$), then many pulses will be required to drive a π-pulse. In that case, examining the Fourier spectrum of the pulses will be instructive. The Fourier transform of a train of equally spaced pulses with a fixed phase relationship is a frequency comb, with teeth spaced by the repetition frequency ω_{rep}. The width of an individual tooth in an N pulse train scales like ω_{rep}/N. If the width of a tooth is small compared to the tooth spacing ($N \gg 1$), then the comb can be thought of as an ensemble of CW lasers. Transitions can then be driven if the frequency comb contains teeth which are separated by ω_{hf}. This is shown in figure 4.12(a). This immediately leads to the resonance condition:

$$\omega_{\text{hf}} = n\omega_{\text{rep}},\ n \in \mathbb{Z} \tag{4.114}$$

which is identical to the condition in equation 4.99, derived above.

The frequency space picture also provides an insight which is perhaps not clear

from the time domain analysis. A frequency comb with a non-resonant repetition rate can also drive transitions if it is split in two halves, and a frequency offset ω_{A} is introduced between the two halves. By tuning the offset frequency, transitions can be driven by the beat notes between the combs. The resonance condition is then given by:

$$\omega_{\mathrm{hf}} = n\omega_{\mathrm{rep}} \pm \omega_{\mathrm{A}},\ n \in \mathbb{Z} \tag{4.115}$$

Indeed, this is in general the more useful configuration, as it allows for the spin-motion interaction discussed in chapter 5. Note that because the transition is driven by both pulse trains, the individual pulses must arrive at the ion simultaneously. If the trains are counterpropagating, this will necessarily be accompanied by motional transitions. However, if the trains are co-propagating, no motion will be driven.

4.7.1 RF Comb

To calculate the Rabi frequency and resonance condition from the comb picture, it will be useful to introduce the concept of the *RF Comb*, which refers to the spectrum of beat notes rather than the optical spectrum. All pairs of comb teeth which are separated by $k\omega_{\mathrm{rep}}$ ($k \in \mathbb{Z}$) will act as an RF frequency at that splitting. The single photon Rabi frequency from the comb line at frequency $k\omega_{\mathrm{rep}}$ is given by $g_k = g_0 \operatorname{sech}(k\omega_{\mathrm{rep}}\tau)$. The net two photon Rabi frequency caused by the beat note at $\omega_{\mathrm{hf}} = n\omega_{\mathrm{rep}}$ is [56]:

$$\Omega = \sum_{k=-\infty}^{\infty} \frac{g_k g_{k+n}}{2\Delta} \tag{4.116}$$

$$\approx \Omega_0 \operatorname{sech}\left(\frac{\omega_{\mathrm{hf}}\tau}{2}\right) \tag{4.117}$$

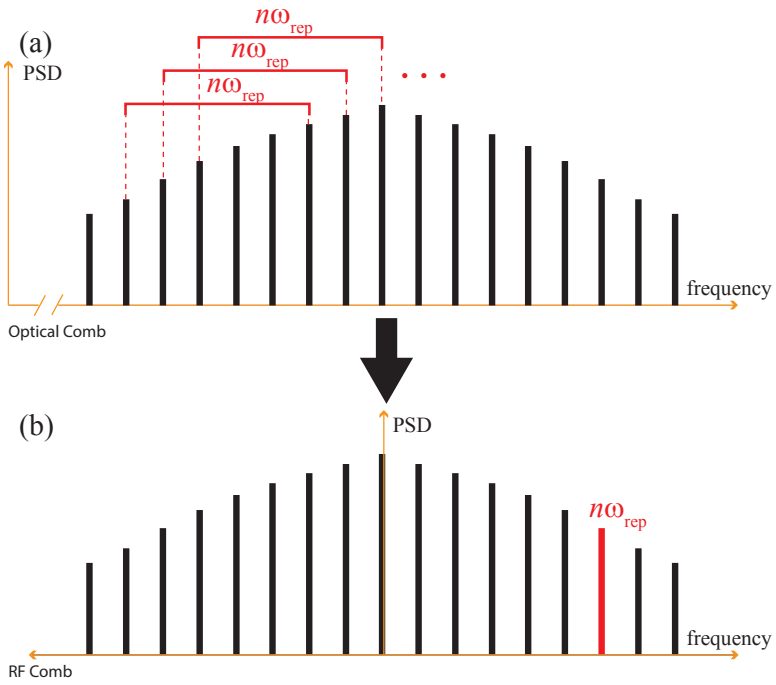

Figure 4.13: The RF comb corresponds to the spectrum of beat notes present in the optical comb. Each RF comb tooth is the sum over all pairs of optical comb teeth separated by that RF frequency.

Here I am making the approximation that all of the comb lines have the same optical detuning Δ from resonance: $\Delta - k\omega_{\text{rep}} \approx \Delta$.

Equation 4.117 can be connected to the time domain analysis in section 4.5 in a straightforward manner. In equation 4.94, the number of pulses N can be replaced by time t using the relation $N = \omega_{\text{rep}} t/2\pi$. If the effect of a single pulse is small, then t is effectively continuous rather than discretized. This shows that the Rabi frequency is related to the rotation angle φ by:

$$\Omega = \omega_{\text{rep}} \varphi / 2\pi \tag{4.118}$$

If $\theta \ll 1$, equation 4.95 becomes:

$$\sin^2\left(\frac{\varphi}{2}\right) = \sin^2\left(\frac{\theta}{2}\right)\,\mathrm{sech}^2\left(\frac{\omega_{\mathrm{hf}}\mathcal{T}}{2}\right) \tag{4.119}$$

$$\Rightarrow \varphi \approx \theta\,\mathrm{sech}\left(\frac{\omega_{\mathrm{hf}}\mathcal{T}}{2}\right) \tag{4.120}$$

$$\Rightarrow \Omega = \Omega_0\,\mathrm{sech}\left(\frac{\omega_{\mathrm{hf}}\mathcal{T}}{2}\right) \tag{4.121}$$

The second line follows from the small angle approximation, and the third line is the second multiplied by $\omega_{\mathrm{rep}}/2\pi$. This shows that the constant $\Omega_0 = \omega_{\mathrm{rep}}\theta/2\pi$. This also makes clear that the approximation made in treating the pulse train as an ensemble of CW lasers is exactly equivalent to the time-domain assumption that the effect of an individual pulse is small.

In addition to the resonant beat note at the qubit frequency, there will also be many beat notes at integer multiples of ω_{rep} away from the qubit frequency. These other beat notes will shift the resonance frequency, just as an off-resonant CW laser shifts an optical resonance. However, the ordinary light shift discussed in section 4.1.2 is a two photon process – it can be understood as absorbing a photon and re-emitting a photon at the same frequency, returning to the same state. The process discussed here is caused by a nearby beat note, rather than a nearby optical frequency. As such, it can be thought of as a higher order four photon light shift.

As in equation 4.117, the RF beat note at frequency $k\omega_{\mathrm{rep}}$ has strength given by $\Omega_k \approx \Omega_0\,\mathrm{sech}(k\omega_{\mathrm{rep}}\tau/2)$. The shift in frequency caused by an off-resonant frequency

Ω_k is well-known to be [91]:

$$\delta_{\mathrm{L}_k} = -\frac{\Omega_k^2}{2\Delta_k} \tag{4.122}$$

$$= -\frac{\Omega_k^2}{2\left(k\omega_{\mathrm{rep}} - \omega_{\mathrm{hf}}\right)} \tag{4.123}$$

$$= -\frac{\Omega_0^2 \operatorname{sech}^2(k\omega_{\mathrm{rep}}\tau/2)}{2\omega_{\mathrm{rep}}(k-n)} \tag{4.124}$$

where Δ_k is the detuning of the k^{th} comb line from resonance, and $\omega_{\mathrm{hf}} = n\omega_{\mathrm{rep}}$. The net four photon shift is then found by summing over all non-resonant beat notes:

$$\begin{aligned}\delta_{\mathrm{L}} &= -\frac{\Omega_0^2}{2\omega_{\mathrm{rep}}} \sum_{\substack{k=-\infty \\ k\neq n}}^{\infty} \frac{\operatorname{sech}^2[k\omega_{\mathrm{rep}}\tau/2]}{k-n} \\ &= -\frac{\Omega_0^2}{2\omega_{\mathrm{rep}}} \sum_{\substack{j=-\infty \\ j\neq 0}}^{\infty} \frac{\operatorname{sech}^2[(j+n)\omega_{\mathrm{rep}}\tau/2]}{j}\end{aligned} \tag{4.125}$$

Because the comb lines are very closely spaced relative to the bandwidth ($\omega_{\mathrm{rep}}\tau \ll 1$), this sum can be approximated as an integral:

$$\delta_{\mathrm{L}} \approx -\frac{\Omega_0^2}{2\omega_{\mathrm{rep}}} \int_{\omega_{\mathrm{rep}}\tau/2}^{\infty} \frac{\operatorname{sech}^2(x + \omega_{\mathrm{hf}}\tau/2) - \operatorname{sech}^2(x - \omega_{\mathrm{hf}}\tau/2)}{x} dx \tag{4.126}$$

$$\approx \frac{\Omega_0^2\omega_{\mathrm{hf}}\tau}{\omega_{\mathrm{rep}}} \int_0^{\infty} \frac{\tanh(x)\operatorname{sech}^2(x)}{x} dx \tag{4.127}$$

$$= \left(\frac{7\zeta(3)}{\pi^2}\right) \frac{\Omega_0^2\omega_{\mathrm{hf}}\tau}{\omega_{\mathrm{rep}}} \tag{4.128}$$

$$\approx 0.853 \frac{\Omega_0^2\omega_{\mathrm{hf}}\tau}{\omega_{\mathrm{rep}}} \tag{4.129}$$

$$= 0.0216\,\theta^2\omega_{\mathrm{hf}}\tau\omega_{\mathrm{rep}} \tag{4.130}$$

Equation 4.127 is an approximation to first order in $\omega_{\mathrm{hf}}\tau$. Remarkably, equation 4.130 matches exactly with the first order shift found in the time domain in equation 4.107. These two shifts were calculated using radically different mathematical tools,

and their exact agreement is impressive. Note that while the time domain analysis gave the result to all orders, the analysis above only produces an answer to lowest order in the pulse area θ. This is because we made the small angle approximation in treating the comb lines as having zero width. Higher orders in θ would need to take into account the non-zero width. The same techniques can be used to extract the light shift for the two comb case, this is done in appendix B.

4.7.2 Beat Note Lock

In order to coherently drive Rabi flopping, it is important that the beat note at the qubit splitting be stable. In general, the repetition rate drifts by tens of Hz over the course of several seconds, as in figure 4.14. The hyperfine frequency beat note is driven by the 157^{th} harmonic, and therefore drifts by kHz in several seconds. This drift can be eliminated by actively stabilizing the repetition rate, using a PZT mounted end mirror [56]. This was the method used for the PicoTrain. A schematic of the lock is shown in figure 4.15. The signal from a photodiode monitoring the pulse train was mixed with a local oscillator at 80.16 MHz. The DC component of the mixed signal was then sent into a PID, which was fed back onto the PZT.

As an added complication, the range of travel of the PZT was often not sufficient to compensate for the drift in the repetition rate. The PZT mounted mirror was therefore also mounted on a motorized stage, which allowed far greater movements. A Labview program monitored the voltage being applied to the PZT. If the voltage went outside of preset bounds (less than 20 V or more than 30 V), Labview would send a signal to an FPGA which would then shift the motorized stage until

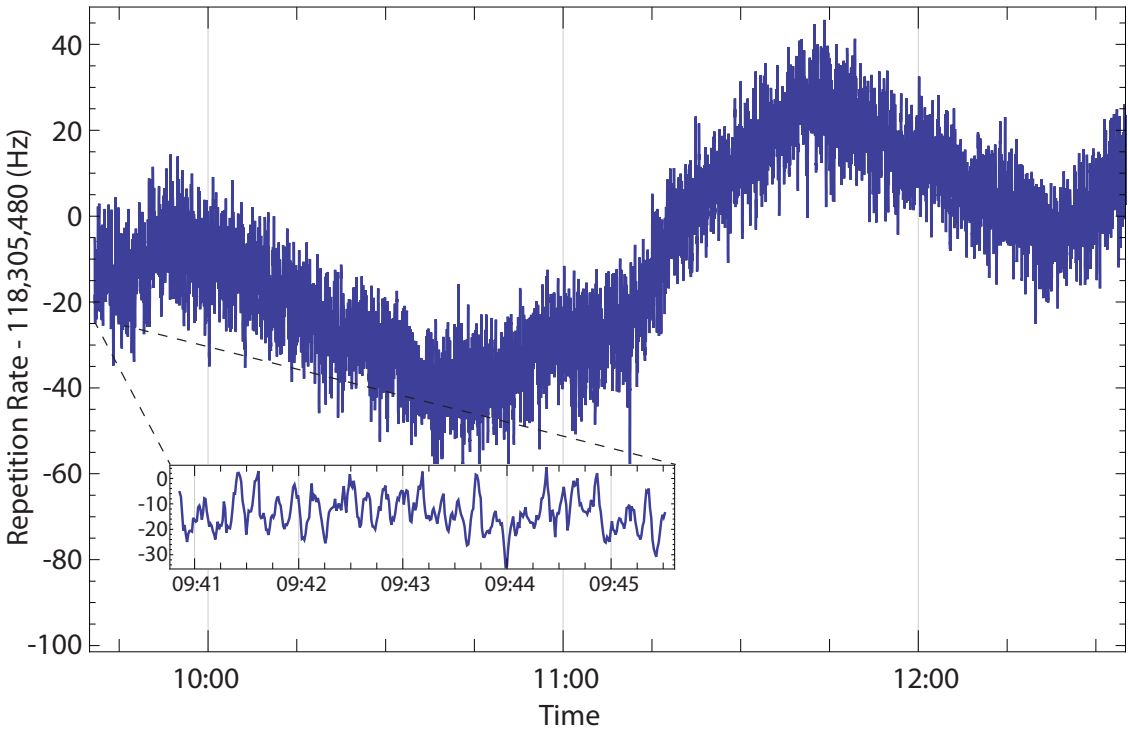

Figure 4.14: Drifts in the repetition rate over the course of three hours. The 20-30 Hz "fuzz" is caused by small thermal and mechanical fluctuations. The inset shows these effectively random fluctuations over five minutes. The long timescale drifts are due to fluctuations in the room temperature.

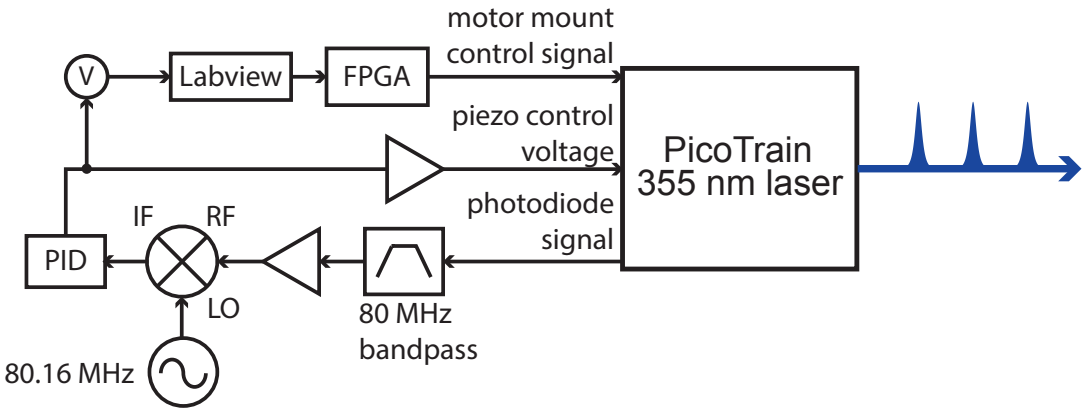

Figure 4.15: Schematic for repetition rate lock. A signal at the repetition rate of the pulse train is mixed with a local oscillator to produce an approximately DC signal. That signal is locked to zero via a PID feedback loop to a PZT-mounted end mirror. When the PZT control voltage goes out of bounds, a motorized mount is triggered which moves the end mirror until the PZT voltage is at the center of its range.

the PZT voltage was back in the center of its range. This would be necessary every few minutes. However, because the bandwidth of the PZT was so much higher than that of the motorized mount, the PZT was able to continuously lock the repetition rate even while the motorized mount was moving. Therefore, this did not interrupt the experiment.

4.7.2.1 AOM lock The Paladin laser did not feature a PZT-mounted mirror. It was therefore impossible to directly stabilize the repetition rate. As an alternative, the noise on the repetition rate can be inverted and written onto the AOM, thereby stabilizing the beat note at the qubit frequency in equation 4.115. Because the ion responds only to the beat note, it does not matter that the repetition rate and AOM frequency are independently noisy.

A schematic for the AOM beat note lock is shown in figure 4.16. The positive sign in equation 4.115 was chosen, and the two AOMs have frequency shifts in opposite directions. The resonance condition for driving transitions is therefore:

$$\omega_{\mathrm{hf}} = n\omega_{\mathrm{rep}} + \omega_{A_1} + \omega_{A_2} \tag{4.131}$$

The 103$^{\mathrm{rd}}$ harmonic of the pulse train at 12.185 GHz is picked out of the signal from a fast photodiode[5], using a bandpass filter. It is then mixed with a stable oscillator[6] at frequency $\omega_{\mathrm{osc}}/2\pi = 12.414$ GHz to produce a beat note at 229 MHz. A second oscillator[7] at 229 MHz is then mixed with that beat note, and the resultant DC signal is sent to a PID. The output of the PID goes to the FM input of the second oscillator,

[5]Alphalas UPD-30-VSG-P
[6]HP 8672A
[7]HP 8640B

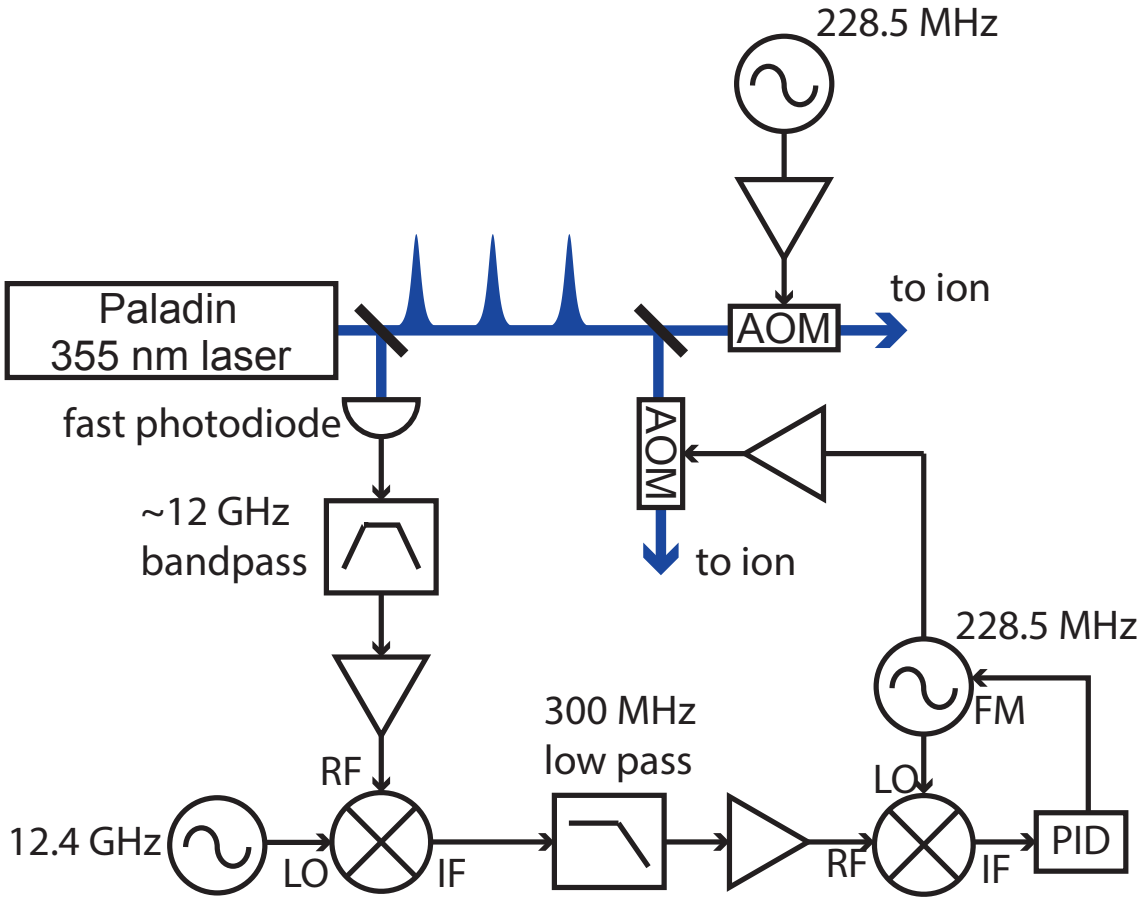

Figure 4.16: Experimental layout for stabilizing the beat note at the qubit frequency. A portion of the pulse train is sent onto a fast photodiode, and the relevant comb line is picked out using a microwave filter. That comb line is then mixed with a microwave oscillator to create a beat note at the appropriate AOM frequency. The oscillator driving the AOM is then locked to that frequency.

thereby locking that oscillator to the beat note. That oscillator is then used to drive one of the AOMs. The result is that the combination $103\omega_{\text{rep}} + \omega_{A_1} = \omega_{\text{osc}}$ is stable. The second AOM is driven by a different oscillator, at around the same frequency.

It is also important to note that these transitions are being driven by a frequency difference between comb lines, rather than by an absolute optical frequency. The carrier-envelope phase (CEP) is therefore irrelevant and does not need to be stabilized. Indeed, the carrier-envelope phase could be randomized pulse to pulse, and the process would be unchanged. This may be somewhat surprising, as with a random CEP the Fourier transform of the optical pulse train is no longer a frequency comb. However, the RF comb is unaffected. The RF comb is created by the beat note formed when each pulse is split, frequency shifted and recombined on the ion. The beat note phase is determined by the optical phase difference between the two arms when they reach the ion. Because the absolute optical phase is common to both arms, it does not affect the experiment.

4.7.3 Air Currents

One significant source of error is air currents passing through the Raman beams. In general it is necessary to completely enclose the beam path. We found that even a very small opening could significantly reduce the stability of the Raman transitions. There are three separate sources of error caused by air currents, all due to the change in index of refraction of air as a function of air temperature and

pressure. The change in the index of air Δn at 355 nm is given by [123, 124]:

$$\Delta n = -0.9 \times 10^{-7}/^{\circ}\mathrm{C} \tag{4.132}$$

$$\Delta n = +2.7 \times 10^{-6}/\mathrm{kPa} \tag{4.133}$$

As a first source of error, changes in the index of air can deflect the beam, which in turn leads to pointing instability at the ion. This causes the effective intensity seen by the ion to fluctuate. This is mainly a problem for fluctuations far from the ion, where small angular deflections can lead to large position displacements.

As a second source of error, in the counterpropagating geometry the phase difference between the two beams must remain stable over the course of one experiment. Small changes in the temperature over the beam line can change the effective optical path length for one or both sides, resulting in optical phase noise at the ion. If this happens during a Rabi flopping experiment, the phase noise will lead to decoherence. A change in index by Δn over a distance d will change the optical phase by $\Delta\phi = \Delta d/\lambda = d\Delta n/\lambda$, where λ is the wavelength.

Finally, air currents across the beam can result in different refractive indices in different parts of the beam. When the beam is small, this effect is negligible. However, in order to allow focusing to a tight spot at the ion, the beam waist right before the final focusing lens is typically quite large, with around a 5-7 mm waist. When different parts of the beam experience different optical path lengths to the focus, the intensity distribution at the focus changes. This in turn leads to intensity noise at the ion.

In order to mitigate all of these effects, the entire 355 beam path is enclosed.

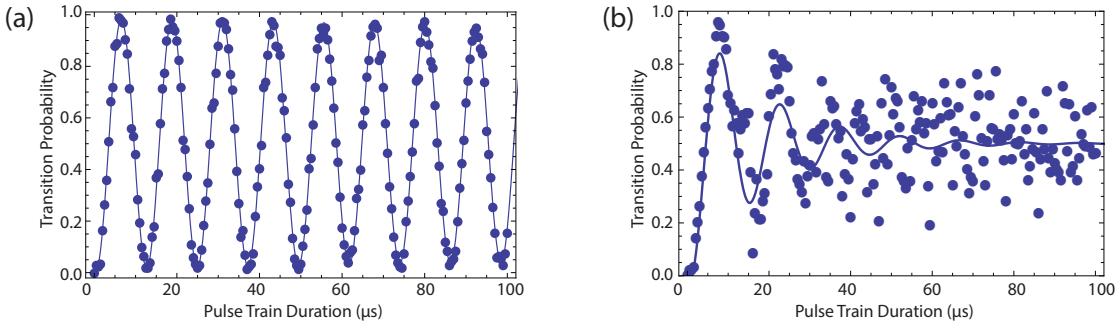

Figure 4.17: Rabi oscillations driven by a pair of copropagating combs with an AOM shift between them. In this data the repetition frequency is directly stabilized. (a) With the beam path completely covered. (b) With the final ~1% of the beam path (5 cm) uncovered. In both (a) and (b) the fit curve is a best fit to a sinusoid with decaying amplitude.

This isolates it from any air currents. Figure 4.17 shows how important this is. Shown is Rabi flopping from co-propagating combs with an AOM shift between them. Here the repetition rate is directly stabilized. In (a), stable Rabi flopping is seen, with little degradation of signal over the course of 8 oscillations. Here the entirety of the 4 m beam path is enclosed. In (b), the last 5 cm is uncovered. The oscillations now decay in just 1.5 cycles. The dominant source of error here is that caused by fluctuating indices in different parts of the transverse beam profile.

Chapter 5

Spin-Motion Entanglement

The previous chapter dealt with ultrafast spin control. We now turn to processes which couple to both spin and motion. This occurs when a Raman transition is driven by absorbing a photon from one beam and emitting a photon into a different beam, which causes a momentum change of $\hbar\Delta k$, where Δk is the difference in wave vector between the two beams. As mentioned in chapter 4, if the Raman beams are counterpropagating and their polarizations are in the lin $\perp$ lin configuration, then the spin flips are *always* accompanied by momentum transfer. This is therefore the most useful configuration for efficiently creating spin-motion entanglement. In addition, an AOM will be present in each beam, allowing for relative frequency shifts between the beams. I will show how a single pulse causes the wave function to diffract, while a sequence of pulses allows the creation of a spin-dependent kick (SDK).

5.1 Coherent States

The response of the ion to ultrafast momentum transfer is best understood in the basis of *coherent states*. Coherent states were first introduced by Schrödinger but fully developed and understood by Glauber [125]. They can be thought of as the "most classical" quantum mechanical state of an oscillator, as they correspond to the minimum uncertainty states of position and momentum. Here I will outline their main properties that are relevant for the analysis that follows. Derivations of these results, together with much more detail, can be found in [125, 126].

The eigenstates of the harmonic oscillator with frequency ω are the number states indexed by a non-negative integer n, denoted $|n\rangle$, with energy $E_n = \omega(n+1/2)$. As eigenstates, these states evolve as stationary states, acquiring a phase due to free evolution: $|n\rangle \to e^{-iE_n t}|n\rangle$. However, they are highly non-classical, as they are delocalized in both position and momentum. Indeed, this is clear from the fact that they are stationary under free evolution, while a classical harmonic oscillator not at rest is plainly not stationary.

By contrast, coherent states are denoted $|\alpha\rangle$, where α is a complex number. Coherent states are eigenstates of the annihilation operator:

$$a|\alpha\rangle = \alpha|\alpha\rangle \tag{5.1}$$

Because a is not Hermitian, α is not an observable. Let $\mathrm{Re}(\alpha) = \alpha_R$ and $\mathrm{Im}(\alpha) = \alpha_I$. Equation 5.1 shows that the real and imaginary parts of α are proportional to the

expectation values of position and momentum:

$$\frac{1}{2x_0}\langle\alpha\,|\hat{x}|\,\alpha\rangle = \alpha_R \tag{5.2}$$

$$\frac{1}{2p_0}\langle\alpha\,|\hat{p}|\,\alpha\rangle = \alpha_I \tag{5.3}$$

where $x_0 = \sqrt{\hbar/2m\omega}$ and $p_0 = \sqrt{m\omega\hbar/2}$ are the natural length and momentum units. Equation 5.1 also allows $|\alpha\rangle$ to be expressed in terms of number states as:

$$|\alpha\rangle = e^{-|\alpha|^2/2}\sum_{n=0}^{\infty}\frac{\alpha^n}{\sqrt{n!}}|n\rangle \tag{5.4}$$

The prefactor $e^{-|\alpha|^2/2}$ normalizes the coherent states. Note that the coherent state $|0\rangle$ is the same as the number state $|0\rangle$. The free evolution of $|\alpha\rangle$ can be quickly derived from equation 5.4:

$$|\alpha\rangle \to \left|\alpha e^{-i\omega t}\right\rangle \tag{5.5}$$

From this it is clear that $|\alpha\rangle$ is not stationary, but evolves to a different state with free evolution. Indeed, this evolution is the quantum mechanical analog of the classical harmonic oscillator with definite position x and momentum p, characterized by complex parameter $\alpha = x + ip$. It is also clear that $|\alpha\rangle$ does not acquire a phase (outside the ket) due to free evolution.

A coherent state $|\alpha\rangle$ can be moved to a new coherent state $|\alpha+\beta\rangle$ via the *displacement operator*, defined as:

$$D[\beta] = e^{\beta a^\dagger - \beta^* a} \tag{5.6}$$

The action of this operator on a coherent state is given by:

$$D[\beta]\,|\alpha\rangle = e^{\beta\alpha^* - \beta^*\alpha}\,|\alpha+\beta\rangle \tag{5.7}$$

This equation shows that in addition to the displacement action, the displacement operator imparts a phase to a coherent state.

The coherent states are an overcomplete basis, by a factor of π:

$$\frac{1}{\pi}\int d^2\alpha \,|\alpha\rangle\,\langle\alpha| = \mathbb{1} \tag{5.8}$$

Here the notation $d^2\alpha$ refers to integrating over both α_R and α_I (i.e. the whole complex plane). As an overcomplete basis, they are necessarily not orthogonal to one another:

$$\langle\alpha|\beta\rangle = e^{-\frac{1}{2}\left(|\alpha|^2+|\beta|^2-2\alpha^*\beta\right)} \neq \delta_{\alpha\beta} \tag{5.9}$$

Equation 5.9 shows that the coherent states are "approximately orthogonal," in the sense that if $|\alpha-\beta| \gg 1$, then $|\,\langle\alpha|\beta\rangle\,| \ll 1$.

Because the coherent states are complete, an arbitrary mixed state density matrix can be written as a superposition of coherent states:

$$\rho = \int d^2\alpha P(\alpha)\,|\alpha\rangle\,\langle\alpha| \tag{5.10}$$

where $P(\alpha)$ is known as the Glauber-Sudarshan P function [125,127]. For a thermal state with average phonon number $\bar{n}$, it is given by:

$$P(\alpha) = \frac{1}{\pi\bar{n}}e^{-|\alpha|^2/\bar{n}} \tag{5.11}$$

Finally, it will be important to determine the measured spin of an ion in a pure spin state and a mixed motional state. Let the initial spin state of the ion be given by $|\psi_i\rangle$, and the initial motional state be determined by $P(\alpha)$ as in equation 5.10. The combined spin-motion initial density matrix is therefore:

$$\rho_i = \int d^2\alpha P(\alpha)\,|\psi_i,\alpha\rangle\,\langle\psi_i,\alpha| \tag{5.12}$$

Now suppose an operator U is applied, potentially entangling spin and motion. The final density matrix is then given by:

$$\rho_f = U\rho_i U^\dagger \tag{5.13}$$

$$= \int d^2\alpha P(\alpha) U \left|\psi_i, \alpha\right\rangle \left\langle\psi_i, \alpha\right| U^\dagger \tag{5.14}$$

After the application of U, the spin is measured. Because the motion is not measured, the act of measuring will trace over the $\{1, 1\}$ spin quarter of the density matrix, $\langle 1, \beta \left|\rho_f\right| 1, \beta\rangle$. The final measured brightness is therefore [128]:

$$B = \frac{1}{\pi}\int d^2\beta \left\langle 1, \beta \left|\rho_f\right| 1, \beta\right\rangle \tag{5.15}$$

$$= \frac{1}{\pi}\int d^2\beta \left\langle 1, \beta \left| \int d^2\alpha P(\alpha) U \left|\psi_i, \alpha\right\rangle \left\langle\psi_i, \alpha\right| U^\dagger \right| 1, \beta \right\rangle \tag{5.16}$$

$$= \frac{1}{\pi}\int d^2\alpha P(\alpha) \int d^2\beta \left\langle 1, \beta \left|U\right| \psi_i, \alpha\right\rangle \left\langle\psi_i, \alpha\right| U^\dagger \left|1, \beta\right\rangle \tag{5.17}$$

$$= \int d^2\alpha P(\alpha) \left\langle \psi_i, \alpha \left| U^\dagger \left[\frac{1}{\pi}\int d^2\beta \left|1, \beta\right\rangle \left\langle 1, \beta\right|\right] U \right| \psi_i, \alpha \right\rangle \tag{5.18}$$

$$= \int d^2\alpha P(\alpha) \left\langle \psi_i, \alpha \left| U^\dagger \big[\left|1\right\rangle \left\langle 1\right| \otimes \mathbb{1}\big] U \right| \psi_i, \alpha \right\rangle \tag{5.19}$$

$$= \int d^2\alpha P(\alpha) B(\alpha) \tag{5.20}$$

Above, equation 5.18 follows from reversing the order of the pair of inner products in equation 5.17, and equation 5.19 follows from the normalization condition in equation 5.8. In equation 5.20 I have defined $B(\alpha)$ as the measured brightness for an ion initialized to a pure coherent state $|\alpha\rangle$, after application of U:

$$B(\alpha) = \left\langle \psi_i, \alpha \left| U^\dagger \left|1\right\rangle \left\langle 1\right| U \right| \psi_i, \alpha \right\rangle \tag{5.21}$$

Equation 5.20 shows an important result, which is that the brightness for a mixed state can be determined by taking a thermal average over the brightness for a pure

state. This result applies for any evolution operator U. Therefore, in the analysis below I will assume the ion is in a pure coherent state $|\alpha\rangle$, and results for thermal states will be obtained from equation 5.20.

5.2 Wave Packet Diffraction

Consider the Rabi frequency in equation 4.113 when the pulses arrive at the ion simultaneously ($T_d = 0$). This corresponds to point E in figure 4.9. Let t_0 be the arrival time of the pulses. From equation 4.67, the effective Hamiltonian is given by:

$$\mathcal{H}_{\text{eff}}(t) = -\frac{1}{2}\left(2\sqrt{\Omega_1(t-t_0)\Omega_2(t-t_0)}\cos\left[\Delta k\hat{x} + \Delta\phi(t-t_0)\right]\hat{\sigma}_x + \omega_{\text{hf}}\hat{\sigma}_z\right) \quad (5.22)$$

where $\hat{x}$ is the position operator for the ion. I have also allowed a time dependence in the phase difference between the two beams, caused by the presence of the AOMs:

$$\Delta\phi(t) = \omega_{\text{A}}t + \phi_0 \quad (5.23)$$

where ω_{A} is the AOM frequency difference and ϕ_0 is an optical phase offset, which is assumed to be constant over the course of one experiment.

Now suppose the two beams are of equal strength and the pulse is well approximated by a δ-function ($\tau = 0$):

$$\Omega_1(t) = \Omega_2(t) = \theta\delta(t) \quad (5.24)$$

(The δ-function approximation will prove sufficient for all of the results shown here; corrections for non-zero pulse duration are given in appendix C. Note that if the

two beams are of unequal strength, the results here apply by replacing the pulse area θ with an effective pulse area $\tilde{\theta}$, given by the geometric mean of the two pulse areas: $\tilde{\theta} = \sqrt{\theta_1 \theta_2}$.) Under this approximation, hyperfine evolution during the pulse can be ignored, and the effective Hamiltonian for the pulse pair becomes:

$$\mathcal{H}_{\text{eff}}(t) = -\theta\delta(t - t_0)\cos\left[\Delta k\hat{x} + \Delta\phi(t)\right]\hat{\sigma}_x \tag{5.25}$$

$$= -\theta\delta(t - t_0)\cos\left[\eta\left(a + a^\dagger\right) + \Delta\phi(t)\right]\hat{\sigma}_x \tag{5.26}$$

where in equation 5.26 I have replaced $\hat{x}$ with $x_0(a+a^\dagger)$, and defined the *Lamb-Dicke parameter*:

$$\eta = \Delta k x_0 = \Delta k\sqrt{\frac{\hbar}{2m\omega}} \tag{5.27}$$

Equation 5.26 commutes with itself at different times t (in contrast to the non-zero pulse duration Hamiltonian in equation 5.22). It can therefore be directly integrated to obtain the evolution operator for a single pulse pair arriving at time t_0:

$$U_{t_0} = \exp\left(-i\int \mathcal{H}_{\text{eff}}(t)dt\right) \tag{5.28}$$

$$= \exp\left(i\theta\int dt\,\delta(t - t_0)\cos\left[\eta\left(a + a^\dagger\right) + \Delta\phi(t)\right]\hat{\sigma}_x\right) \tag{5.29}$$

$$= \exp\left(i\theta\cos\left[\eta\left(a + a^\dagger\right) + \Delta\phi(t_0)\right]\hat{\sigma}_x\right) \tag{5.30}$$

$$= \sum_{n=-\infty}^{\infty} i^n J_n\left(\theta\hat{\sigma}_x\right) e^{in\left[\eta\left(a+a^\dagger\right)+\Delta\phi(t_0)\right]} \tag{5.31}$$

where J_n is the Bessel function of order n. Equation 5.31 follows from the Jacobi-Anger expansion of equation 5.30 [129]. From the series expansion of J_n, it can be seen that $J_n(\theta\hat{\sigma}_x) = J_n(\theta)\hat{\sigma}_x^n$. From the definition of the displacement operator in equation 5.6, we have a final expression for the spin-motion evolution operator for

a counterpropagating lin $\perp$ lin pulse pair:

$$U_{t_0} = \sum_{n=-\infty}^{\infty} i^n J_n(\theta) e^{in\Delta\phi(t_0)} D[in\eta]\hat{\sigma}_x^n \tag{5.32}$$

Equation 5.32 consists of operators of the form $D[in\eta]\hat{\sigma}_x^n$, which impart n momentum kicks of normalized size η together with n spin flips. Physically, this corresponds to the process of absorbing a photon from one beam, emitting a photon into the other beam, repeated n times. Each process of absorption followed by emission changes the momentum by η. The amplitude for the n^{th} such process is given by the Bessel function $J_n(\theta)$, together with a phase factor. The net action of this operator on a spin state $|0\rangle$ and coherent motional state $|\alpha\rangle$ is therefore to create a superposition of states of different size kicks, with alternating spin states. This is shown graphically in figure 5.1. Note that the requirement that a spin flip be accompanied by momentum transfer is enforced by the lin $\perp$ lin polarization configuration. If one of the arms contains circular polarization, then spin flips can be driven without momentum transfer.

This behavior can be understood as the scattering of the atomic wave packet off of the standing wave of light, known as Kapitza-Dirac scattering [130–133]. The two counter-propagating pulses form an instantaneous standing wave at the ion. The ion wave packet then diffracts off of that standing wave into different momentum orders, just as a beam of light diffracts off a thin grating. This has been directly observed in atomic beams [131,132,134] and in Bose-Einstein condensates [135]. It is also similar to the behavior observed in δ-kicked rotor experiments [136]. However, all of the work cited above dealt only with atomic motion, the interaction described

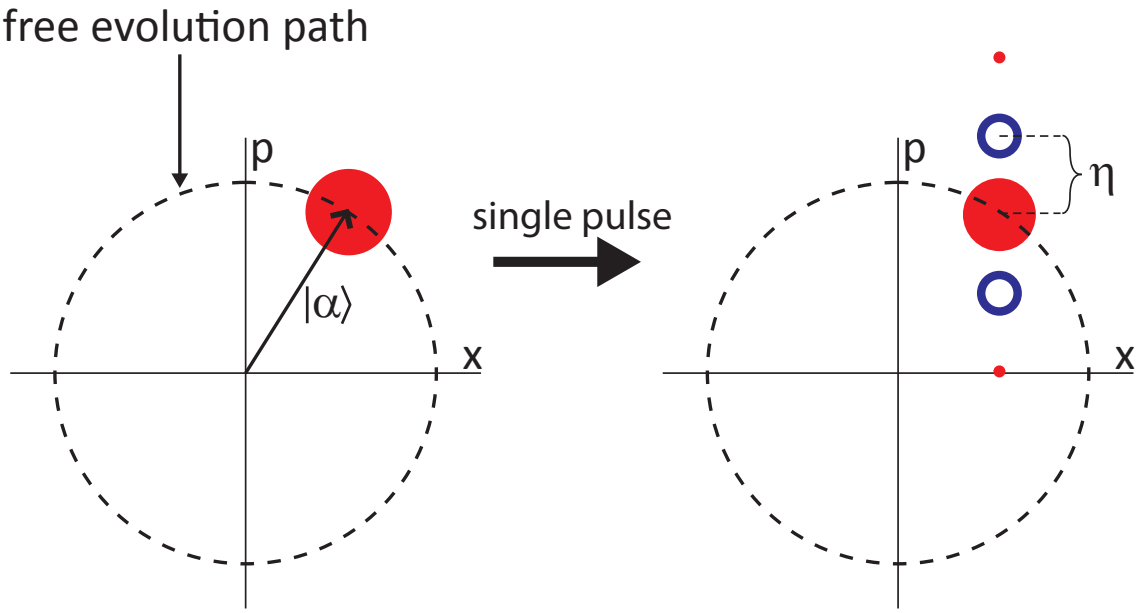

Figure 5.1: Phase space diagram of pulse action. Red closed circles indicate $|0\rangle$; blue open circles indicate $|1\rangle$. The size of the circle indicates the population in that state. Upon the arrival of a pulse pair, the ion is diffracted into a superposition of states as in equation 5.32.

here is complicated by the presence of the spin operator.

It is clear that the state created by the operator in equation 5.32 is an entangled state of spin and motion. However, the motional state created is not spin-dependent, in the sense that the pulse drives $|0, \alpha\rangle$ and $|1, \alpha\rangle$ to the same motional state (the final states are equivalent up to a spin flip). To execute a phase gate, we will need an operator which produces a different motional state for each spin state. This will be done by a sequence of such diffraction events. By setting the delays between the pulses appropriately, population can coherently accumulate in only the momentum orders of interest, and destructively interfere everywhere else. This is reminiscent of the temporal Talbot effect seen in matter waves [137], but with the various momentum states entangled with the spin.

5.3 Sequence of Diffracting Pulses

5.3.1 Frequency Domain

As in chapter 4, the frequency spectrum is a pair of frequency combs with an offset between them due to the AOMs, shown in figure 5.2(a). If the duration of the entire pulse train is much faster than the trap period, then the trap can be ignored during the pulse train. Because absorption and emission happen from opposite beams for $|0\rangle$ and $|1\rangle$, the two spin states get momentum kicks in opposite directions. This is shown graphically in figure 5.2(c). Kicks in the "wrong" directions are off-resonant by $2\omega_{\mathrm{A}}$. In order for the kick to be high fidelity, the comb lines must be sufficiently narrow that these "wrong way" kicks are strongly suppressed, i.e. $2\omega_{\mathrm{A}} \gg \omega_{\mathrm{rep}}/N$, where N is the number of pulses in the train.

Note that this behavior is qualitatively different from that seen when the pulse train is much longer than the trap period. In that case, the same experimental setup will drive spin flips without driving motion, so long as the ion is confined to the Lamb-Dicke regime. This will be discussed further later.

5.3.2 Time Domain

The evolution operator O_N for a train of N pulses will consist of a sequence of operators of the form 5.32, separated by free evolution:

$$O_N = U_{t_N} \ldots U_{\mathrm{FE}}(t_3 - t_2) U_{t_2} U_{\mathrm{FE}}(t_2) U_{t_1} \tag{5.33}$$

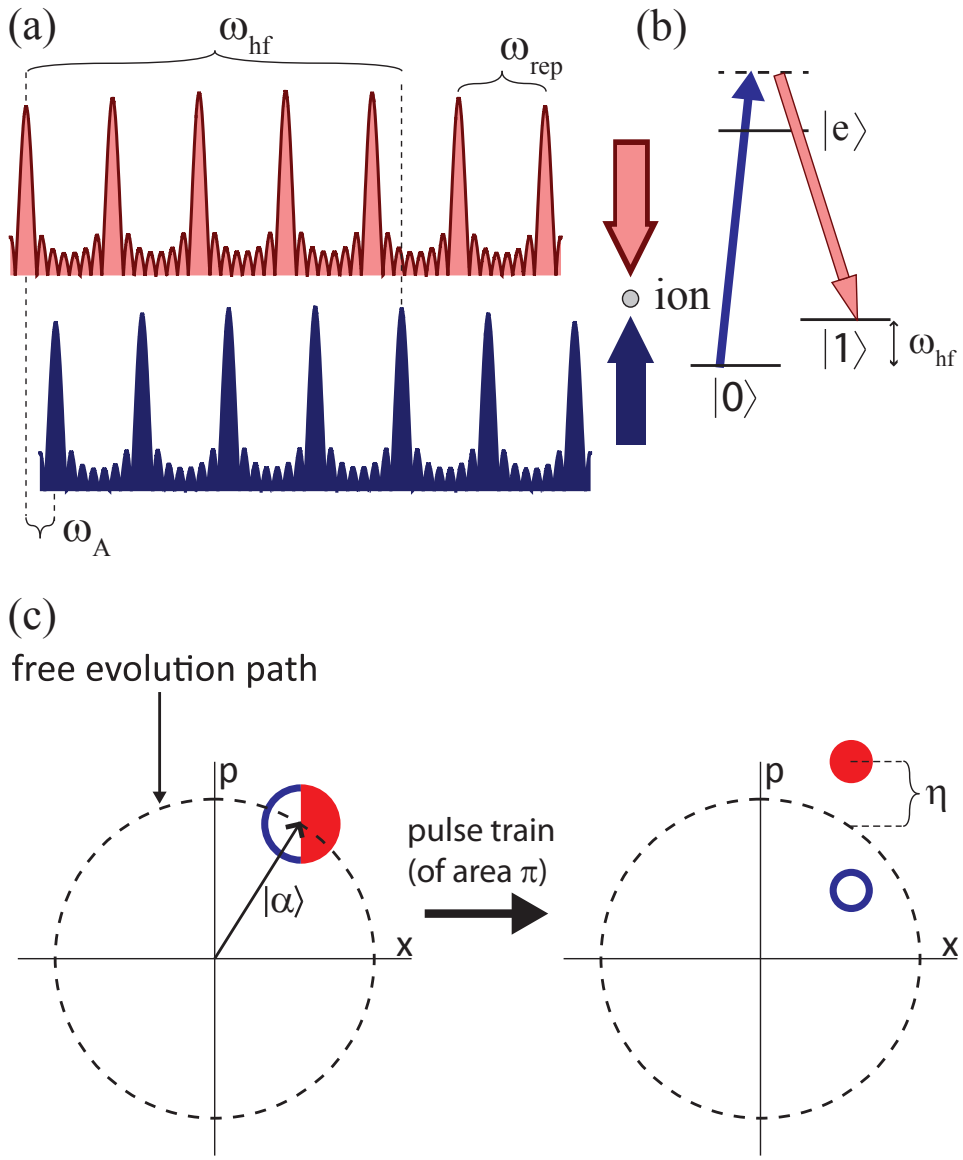

Figure 5.2: (a): Sketch of the optical spectrum seen by the ion for generating a spin-dependent momentum kick when equation 4.115 is satisfied. (b): Depiction of the wave vectors associated with the spectra in (a). An atom starting in $|0\rangle$ may be driven to $|1\rangle$ only by absorbing a photon from the blue beam and emitting a photon into the red beam, resulting in a momentum transfer of Δk in the upward direction. Similarly, an atom starting in the $|1\rangle$ state may only make a transition such that it receives Δk momentum in the downward direction. The "wrong-direction" kick is off-resonant; it is maximally suppressed when it corresponds to a zero in the sinc pattern in between the comb teeth. (c) Phase space diagram of this behavior. Red closed circles indicate $|0\rangle$; blue open circles indicate $|1\rangle$. An ion initially in a superposition of $|0\rangle$ and $|1\rangle$ is split into two motional wave packets with different momenta.

where t_n is the arrival time of the n^{th} pulse, and $U_{\text{FE}}(T)$ is the free evolution operator for time T for both spin and motion, given by:

$$U_{\text{FE}}(T) = e^{-i\omega_{\text{trap}}Ta^\dagger a}e^{-i\omega_{\text{hf}}T\hat{\sigma}_z/2} \tag{5.34}$$

Let the total pulse train area be given by Θ, so that a single pulse area is $\theta = \Theta/N$. Assume that N is sufficiently large such that the single pulse evolution operator in equation 5.32 can be approximated to first order in $1/N$:

$$U_{t_k} \approx 1 + \frac{i\Theta}{2N}\left(e^{i(\phi_0+\omega_{\text{A}}t_k)}D\left[i\eta\right] + e^{-i(\phi_0+\omega_{\text{A}}t_k)}D\left[-i\eta\right]\right)\hat{\sigma}_x \tag{5.35}$$

where I have used equation 5.23 for $\phi(t_k)$.

The free evolution can be absorbed into the pulse operator by transforming to the interaction picture. Define:

$$q_\pm = \omega_{\text{hf}} \pm \omega_{\text{A}} \tag{5.36}$$

In the interaction picture, U_{t_k} becomes:

$$V_{t_k} = U_{\text{FE}}^\dagger(t_k)U_{t_k}U_{\text{FE}}(t_k) \tag{5.37}$$

$$= 1 + \frac{i\Theta}{2N}\Big\{e^{i\phi_0}D\left[i\eta e^{i\omega_{\text{trap}}t_k}\right]\left(e^{iq_+t_k}\hat{\sigma}_+ + e^{iq_-t_k}\hat{\sigma}_-\right) + e^{-i\phi_0}D\left[-i\eta e^{i\omega_{\text{trap}}t_k}\right]\left(e^{-iq_+t_k}\hat{\sigma}_- + e^{-iq_-t_k}\hat{\sigma}_+\right)\Big\} \tag{5.38}$$

The pulse train operator in the interaction picture becomes:

$$\tilde{O}_N = \prod_{k=N}^{1} V_{t_k} \tag{5.39}$$

If the entire pulse train duration is much shorter than the trap period, the trap evolution can be approximated as frozen during the pulses, so that $\omega_{\text{trap}}t_k \approx 0$.

In that case, V_{t_k} becomes:

$$V_{t_k} = 1 + \frac{i\Theta}{2N}\Big\{ e^{i\phi_0} D\left[i\eta\right] \left(e^{iq_+ t_k}\hat{\sigma}_+ + e^{iq_- t_k}\hat{\sigma}_-\right) + e^{-i\phi_0} D\left[-i\eta\right] \left(e^{-iq_+ t_k}\hat{\sigma}_- + e^{-iq_- t_k}\hat{\sigma}_+\right) \Big\} \tag{5.40}$$

In general, the product in equation 5.39 will be extremely complicated. When expanded, the coefficients of each spin/motion operator will consist of terms of the form $\sum e^{iq_\pm t_k}$. In general, the norm of such sums is $\lesssim 1$. For large N, the $1/N$ suppression will result in $\tilde{O}_N \approx \mathbb{1}$, i.e. the pulses do nothing. However, suppose $q_+ t_k/2\pi \in \mathbb{Z}$ for all pulses, while $q_- t_k/2\pi \notin \mathbb{Z}$ (in frequency space, this is equivalent to satisfying the bottom sign resonance conditions in equation 4.115, but not the top sign). The q_+ terms in the product in equation 5.39 will then coherently add, while the q_- terms will not. As the number of pulses grows, the non-resonant terms are strongly suppressed and can be discarded. In frequency space, this is equivalent to the statement that the comb lines narrow with increasing N, resulting in decreased amplitude for non-resonant processes. Equation 5.40 therefore becomes:

$$V_{t_k} = 1 + \frac{i\Theta}{2N}\left(e^{i\phi_0} D\left[i\eta\right]\hat{\sigma}_+ + e^{-i\phi_0} D\left[-i\eta\right]\hat{\sigma}_-\right) \tag{5.41}$$

The pulse train operator is now a product of identical operators:

$$\tilde{O}_N = \left[1 + \frac{i\Theta}{2N}\left(e^{i\phi_0} D\left[i\eta\right]\hat{\sigma}_+ + e^{-i\phi_0} D\left[-i\eta\right]\hat{\sigma}_-\right)\right]^N$$

$$\xrightarrow{N\to\infty} \exp\left[\frac{i\Theta}{2}\left(e^{i\phi_0} D\left[i\eta\right]\hat{\sigma}_+ + e^{-i\phi_0} D\left[-i\eta\right]\hat{\sigma}_-\right)\right] \tag{5.42}$$

$$= \cos\frac{\Theta}{2} + i\sin\frac{\Theta}{2}\left(e^{i\phi_0} D\left[i\eta\right]\hat{\sigma}_+ + e^{-i\phi_0} D\left[-i\eta\right]\hat{\sigma}_-\right) \tag{5.43}$$

For a total pulse area of $\Theta = \pi$, Equation 5.43 becomes:

$$\tilde{O} = ie^{i\phi_0} D\left[i\eta\right]\hat{\sigma}_+ + ie^{-i\phi_0} D\left[-i\eta\right]\hat{\sigma}_- \tag{5.44}$$

This is the desired spin-dependent kick operator. In summary, if the following conditions are satisfied:

$$\frac{q_+ t_k}{2\pi} \in \mathbb{Z} \tag{5.45}$$

$$\frac{q_- t_k}{2\pi} \notin \mathbb{Z} \tag{5.46}$$

then in the limit $N \to \infty$, a pulse train will create a spin-dependent kick in which $|0\rangle$ is kicked up and $|1\rangle$ is kicked down. Alternatively, we could have chosen $q_- t_k/2\pi \in \mathbb{Z}$ and $q_+ t_k/2\pi \notin \mathbb{Z}$, in which case the final kick directions would be reversed. In essence, equation 5.45 says that for every pulse, the phase accumulated due to hyperfine precession ($\omega_{\rm hf} t_k$) plus that accumulated due to the RF modulation on the AOM ($\omega_{\rm A} t_k$) should be a multiple of 2π. If the pulses are equally spaced, then $t_k = 2\pi k/\omega_{\rm rep}$, and equation 5.45 is equivalent to equation 4.115. It is also important to note that this spin-dependent kick does not depend on being in the Lamb-Dicke regime.

The condition that only one of q_+ or q_- is resonant is equivalent to the condition that the hyperfine frequency not be an integer or half-integer multiple of the repetition rate:

$$\omega_{\rm hf} \neq \frac{n\omega_{\rm rep}}{2},\ n \in \mathbb{Z} \tag{5.47}$$

If $\omega_{\rm hf}/\omega_{\rm rep}$ is a half-integer or integer, then it is impossible to be resonant with a kick in one direction without also being resonant with a kick in the opposite direction. The net result will be that the kicks will cancel, and the pulse train will not drive any transitions at all.

It is clear from the time domain analysis that these pulse do not have to be

equally spaced. Indeed, numerical optimization shows that the best SDK fidelity is achieved for unequally spaced pulses. To understand this result, consider the product in equation 5.39 to lowest order in Θ/N:

$$\begin{aligned}\tilde{O}_N =& 1+ \\ & \frac{i\Theta}{2N}\Bigg\{\left[e^{i\phi_0}D[i\eta]\left(\sum_{k=1}^{N}e^{iq_+t_k}\right)\hat{\sigma}_+ + e^{-i\phi_0}D[-i\eta]\left(\sum_{k=1}^{N}e^{-iq_+t_k}\right)\hat{\sigma}_-\right]+ \\ & \left[e^{i\phi_0}D[i\eta]\left(\sum_{k=1}^{N}e^{iq_-t_k}\right)\hat{\sigma}_- + e^{-i\phi_0}D[-i\eta]\left(\sum_{k=1}^{N}e^{-iq_-t_k}\right)\hat{\sigma}_+\right]\Bigg\}+ \\ & O\left((\Theta/N)^2\right)\end{aligned} \tag{5.48}$$

When the resonance condition in equation 5.45 is satisfied, then the coefficents $\sum_{k=1}^{N} e^{\pm iq_+t_k} = N$, and the top term in brackets generates the spin-dependent kick. The bottom term, corresponding to the "wrong way" kick, will lead to infidelity in the SDK. Above I said that the coefficient $\sum_{k=1}^{N} e^{\pm iq_-t_k}$ is $O(1)$ away from resonance, leading to strong suppression for large N. However, maximal suppression occurs when this term is zero. This leads to the condition:

$$\sum_{k=1}^{N} e^{iq_-t_k} = 0 \tag{5.49}$$

Note that this is a second condition on the arrival times t_k (the first condition being the ordinary resonance condition in equation 5.45). Finding t_k which satisfy both of these conditions will result in a significantly improved SDK fidelity, as compared to satisfying resonance only. However, in general an equally spaced pulse train will not satisfy equation 5.49. This is why using an unequally spaced pulse train can allow higher SDK fidelity – it allows satisfying both equation 5.45 *and* equation 5.49.

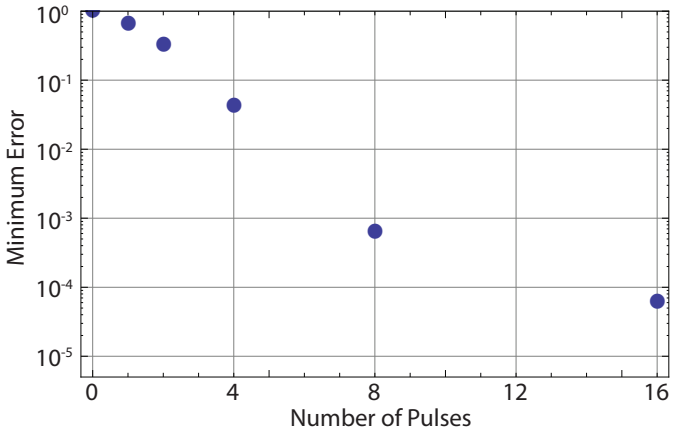

Figure 5.3: Numerically optimized fidelity of the spin-dependent kick as a function of number of pulses, for the experimental system described here.

Note that even with satisfying equation both the conditions mentioned, the SDK fidelity will still not be 1, as equation 5.48 is only to first order in Θ/N. Higher order terms will lead to infidelity. These terms will also have conditions under which they are zero. By numerically optimizing the arrival times t_k, the SDK infidelity can be suppressed to a very high order with only a small number of pulses. Ultimately, the degree to which the unwanted terms can be suppressed is limited by the number of degrees of freedom available in choosing the pulse arrival times.

Figure 5.3 shows the numerically optimized fidelity for different numbers of pulses, allowing unequal spacings. Because the pulse train is generated with delay lines (see section 5.4.1), the 8 pulse train has only 3 free parameters. Nevertheless, the simulations show that a fidelity better than 99.9% is achievable after only 8 pulses. With 16 pulses, the fidelity can be better than 99.99%. Here the AOM difference frequency is fixed at ~500 MHz (see details of the experimental system below). Higher AOM frequencies could potentially allow even higher fidelities.

5.3.3 Weak Pulses: Resolved Sidebands

As a tangentially related result, I will show here that if the pulse train is much longer than the trap cycle time ($t_N \gg 1/\omega_{\text{trap}}$), the same operator produces markedly different effects. In this "slow regime," I will assume that the ion is in the Lamb-Dicke regime[1]: $\eta\sqrt{\bar{n}+1} \ll 1$. In this regime, the displacement operators in equation 5.38 can be approximated to first order in η:

$$D\left[i\eta e^{i\omega_{\text{trap}}t_k}\right] \approx 1 + i\eta\left(e^{i\omega_{\text{trap}}t_k}a^\dagger + e^{-i\omega_{\text{trap}}t_k}a\right) \tag{5.50}$$

Substituting this approximation into equation 5.38 yields:

$$V_{t_k} = 1 + \frac{i\Theta}{2N}\left\{e^{i\phi_0}\left[1 + i\eta\left(e^{i\omega_{\text{trap}}t_k}a^\dagger + e^{-i\omega_{\text{trap}}t_k}a\right)\right]\left[e^{iq_+t_k}\hat{\sigma}_+ + e^{iq_-t_k}\hat{\sigma}_-\right] + \text{H.c.}\right\} \tag{5.51}$$

There are now six phases to consider, associated with six different operators: $e^{iq_\pm t_k}$, $e^{i(q_\pm+\omega_{\text{trap}})t_k}$, and $e^{i(q_\pm-\omega_{\text{trap}})t_k}$. The situation is then similar to the strong pulse regime: If one of these phases satisfies resonance (i.e. equal to 1 for all t_k) while the others do not, then the other terms will be negligible in the limit of large numbers of pulses. For example, suppose that $(q_+ + \omega_{\text{trap}})/2\pi \in \mathbb{Z}$, while none of the other phase terms satisfy this condition. In that case, equation 5.51 becomes:

$$V_{t_k} = 1 + \frac{i\Theta\eta}{2N}\left(ie^{i\phi_0}a^\dagger\hat{\sigma}_+ - ie^{-i\phi_0}a\hat{\sigma}_-\right) \tag{5.52}$$

As in the fast regime, the pulse train operator in equation 5.39 is now the product of identical operators, and converges to:

$$\tilde{O} = \cos\frac{\Theta\eta}{2} + i\sin\frac{\Theta\eta}{2}\left(ie^{i\phi_0}a^\dagger\hat{\sigma}_+ - ie^{-i\phi_0}a\hat{\sigma}_-\right) \tag{5.53}$$

[1]If this is not satisfied, then higher orders in η must be considered, and the pulse train will drive second (or higher) order sidebands.

This is Rabi flopping on the blue sideband, in which a spin flip comes together with the addition of a single phonon. Similarly, the other resonance conditions correspond to red sideband and carrier operations.

Figure 5.4 is experimental data showing the crossover between the slow and fast regimes. In this data, the transition probability was measured as a function of AOM detuning. In (a), sideband features are clearly resolved. The peaks correspond to the carrier and sidebands at each of the three trap frequencies (1.0, 0.9, 0.1) MHz. These transitions follow from equation 5.51. As the power is increased and the pulse train duration decreased, the sidebands become less resolved, as the behavior crosses over from the slow regime to the fast regime. In (e), all of this structure has been washed out, and only a single broad peak remains when the resonance condition is satisfied. The motional transition is now described better by impulsive kicks. From a sideband perspective, all sidebands are being driven simultaneously.

5.4 Spin-Dependent Kicks

5.4.1 Creating a Spin-Dependent Kick

As discussed above, creating a spin-dependent kick requires several pulses. However, because the repetition rate of the Paladin laser is 118.306 MHz while the trap frequency is 0.743 MHz, significant trap evolution would occur over the duration of even a few pulses from the laser. Ideally the entire pulse train will be at least 2-3 orders of magnitude faster than the trap period. To accomplish this, it is necessary to create a pulse train of shorter duration, by reshaping a single pulse into

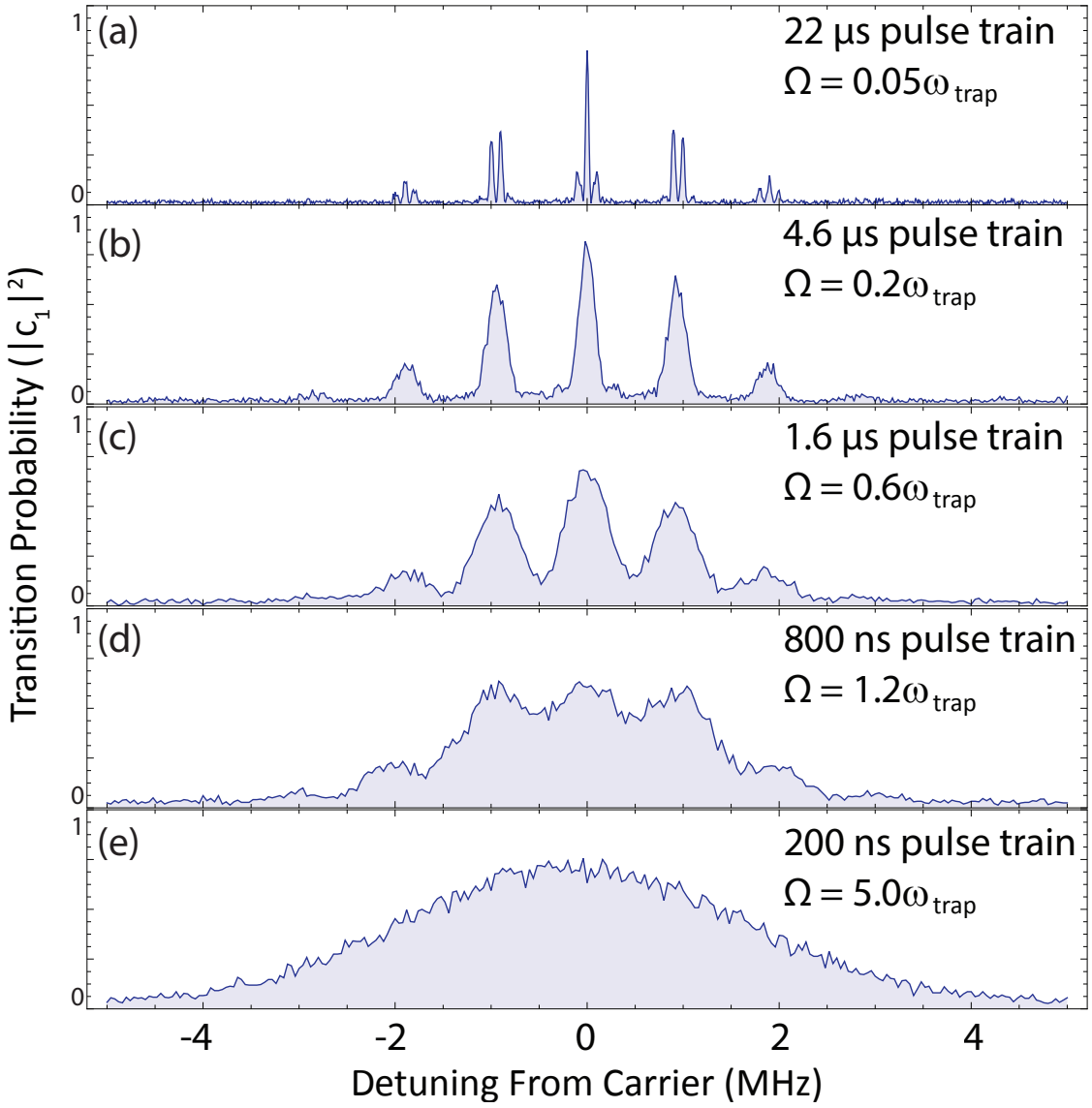

Figure 5.4: Data showing the crossover between the slow, resolved sideband regime and the fast, impulsive regime. Each plot corresponds to scanning the frequency of an AOM in one of the arms of counterpropagating pulse trains. In (a), $\Omega \ll \omega_{\text{trap}}$, and sidebands transitions are clearly resolved. As the pulse train power is turned up (and the length is shortened, keeping the total area constant), the Rabi frequency increases and the lines begin to blur together. In (e), no features are resolved at all, meaning all sidebands are being driven.

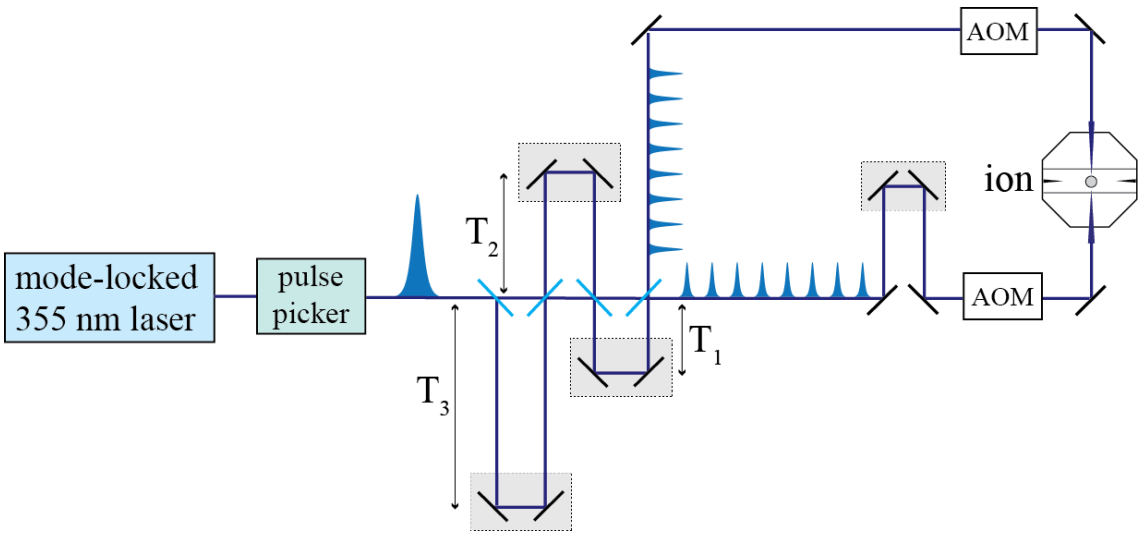

Figure 5.5: Experimental schematic for creating a spin-dependent kick. A single pulse is picked by the pulse picker, and is then divided into two sets of eight pulses by a sequence of delay lines. The two trains are sent counterpropagating onto the ion, with a frequency shift between them imparted by AOMs.

a train of pulses. This is done using concatenated delay lines. The delay lines split each pulse from the laser into a train of eight pulses with tunable relative delays, as shown in Fig. 5.5.

Because the optical phase at the ion only causes a global phase shift, it need only be stable for the duration of a single experiment. Therefore, no active stabilization of the interferometers is necessary. The AOMs[2] are each driven at 251.712 MHz in opposite directions, generating a frequency offset between the two beams of $\omega_{\mathrm{A}}/2\pi = 503.424$ MHz. Using Eq. 5.45, this sets the allowable delays between each of the eight pulses to:

$$T = \frac{2\pi n}{\omega_{\mathrm{hf}} + \omega_a} \tag{5.54}$$

This equation would seem to imply that the shortest delay could be as short as 76 ps (n=1 in equation 5.54). However, making the delays that short leads to a

[2]IntraAction ASM-240 series

significant reduction in fidelity for 8 pulses. This is due to poor suppression of off-resonant processes, as the comb teeth width scale as $1/T$. The shortest delay which produces high fidelity is $n = 5$. If the AOMs were higher frequency, this would be reduced. A higher AOM frequency shift could be achieved by double passing the AOMs or by using higher frequency AOMs, however both these options reduce the AOM diffraction efficiency. Unfortunately the pulse energy produced by the Paladin was already just barely sufficient to produce a full π pulse spin-dependent kick in a single pulse. We therefore could not tolerate any further losses in beam power. The IntraAction 240 MHz AOMs were able to achieve $75 - 80\%$ diffraction efficiency. Even with that relatively high efficiency, considerable effort was necessary to focus the beam down to a small enough spot on the ion, such that the intensity would be sufficient to drive a π-pulse.

As a slight complication, we must also account for the reflective phase shift introduced by the beam splitters: pulse pairs that travel through the final delay line will have a π phase shift relative to those that do not. To compensate for this, the final delay is set such that n is a half-integer, specifically $n = 5.5$ (corresponding to a delay of $T_1 = 419$ ps). Delays T_2 and T_3 are unaffected by this phase shift and are set to $n = 10$ and $n = 20$, respectively. In this way, an eight-pulse train with a nearly uniform 2.5 GHz repetition rate is created; it is 2.7 ns in duration. Numerical simulations show that these delays generate a spin-dependent kick with 98.9% fidelity (Mathematica code appears in appendix E). The simulations also show that this fidelity could be improved slightly to 99.85% by changing the n values of the delays to 6.5, 9, 16 (as was explained in the theoretical analysis in

section 5.3.2). This will likely be done on future iterations of this experiment. Of course, creating 16 pulses with 4 delay lines could increase the fidelity even further, as in figure 5.3. This process is ultimately limited by trap evolution between the pulses interfering with the spin-dependent kick process.

In order to accurately set these delays, the delay lengths were set in three stages. Each delay line was mounted on a manual translation stage[3]. First, the delay line lengths were carefully measured using a piece of string and a ruler. This was sufficient to set the delay lengths to within a few mm. Next, a high resolution time-to-digital converter (TDC)[4] was used to measure the delay lengths to within 8 ps (= 1.2 mm on the translation stage). To do this, a photodiode before the delay line and a photodiode after were used as the start and stop pulses of the TDC. The TDC measured the delay between the two photodiode signals with the delay path blocked, and then again with the straight through path blocked. The difference between those two signal was then the duration of the delay. Finally, the achievable spin flip of the ion was measured as a function of delay. The correct delay was then at the peak. This procedure enabled setting the delays to within 1 ps. This process was repeated for each delay line.

The pulse from each side was focused to approximate a 6 μm waist at the ion. At this focus, a single pulse produced a π-pulse. The fidelity of that pulse, determined by measuring the final spin state, was 94%. (This is reduced from the theoretical maximum for reasons discussed below.) It now remains to demonstrate

[3]New Focus 423 series stage
[4]PicoQuant PicoHarp 300

that the pairs of 8 pulses is indeed also changing the ion's momentum in a known, reversible way.

5.4.2 Detecting a Spin-Dependent Kick

Direct observation of the motional state of a trapped ion is extremely difficult, and motional information is typically determined by mapping to the spin [138]. Therefore, to detect that we created the operator in equation 5.44, it is necessary to infer the motional entanglement from its impact on the coherence of the measured spin state. To do this, we performed a Ramsey experiment using near-resonant microwaves. The experimental sequence was:

1. Initialize the spin state to $|0\rangle$
2. Perform a $\pi/2$ rotation using near resonant microwaves
3. Perform a spin-dependent kick using a single pulse through the interferometers
4. Wait a time T_{delay}
5. Perform a second spin-dependent kick (with a potentially different optical phase)
6. Perform a second $\pi/2$ microwave rotation
7. Measure the state of the ion

For a fixed T_{delay}, the microwave detuning δ was scanned. If the motion is disentangled from the spin, the result should be full contrast of the Ramsey fringe. On the

other hand, if the spin and motion are entangled, then the trace over the motion will destroy the phase coherence. The result will be no Ramsey fringes. If the pulses are truly creating a spin-dependent kick, then the contrast as a function of T_{delay} should exhibit revivals at integer multiples of the trap period. At those delays, the ion wave packet is acting as an interferometer. The SDK plays the role of a beam splitter, dividing the wave packet into two pieces which take different paths. The second SDK acts as a second beam splitter, rejoining the wave packet. A similar effect was discussed theoretically in [139]. It is also similar to the experiments done in [140], although those were done in the "slow" regime.

It should be noted that the degree to which contrast will vanish is a function of the size of the SDK, together with the initial motional state. For a thermal state, the Ramsey fringes will vanish if the kick size is larger than the thermal coherence length of the motional state. This is true even if the kick is much smaller than the phase space size of the state, meaning the $|0\rangle$ and $|1\rangle$ wave packets still have significant phase space overlap after the kicks. In short, what is relevant is the coherence length, not the phase space size.

For an ion initialized to $|0\rangle|\alpha\rangle$, the final state after the sequence described above is given by:

$$|\psi_{\text{final}}\rangle = \frac{1}{2}\Big[e^{i(\gamma+c)}\left(|0\rangle + ie^{-i\phi}|1\rangle\right)\left|(\alpha+i\eta)\,e^{-i\vartheta} - i\eta\right\rangle + \tag{5.55}$$

$$ie^{-i(\gamma+c)}\left(|0\rangle + ie^{i\phi}|1\rangle\right)\left|(\alpha-i\eta)\,e^{-i\vartheta} + i\eta\right\rangle\Big] \tag{5.56}$$

where ϕ is the phase lag between the hyperfine frequency and the microwave frequency, ϑ is the phase space evolution angle $\omega_{\text{trap}}T_{\text{delay}}$, and γ and c are given by:

$$c = \phi_1 - \phi_2 - \frac{\omega_{\text{hf}}T_{\text{delay}}}{2} \tag{5.57}$$

$$\gamma = \eta\left[\alpha_R(1-\cos\vartheta) - \alpha_I \sin\vartheta\right] \tag{5.58}$$

We can determine the final measured brightness as a function of α from equation 5.21, using equation 5.9 for the cross terms:

$$B(\alpha) = \frac{1}{2}\left(1 + e^{4\eta^2(\cos(\vartheta)-1)}\cos\left[4\gamma + 2c - \phi\right]\right) \tag{5.59}$$

We can now use equation 5.20 to determine the brightness for an initial thermal state:

$$B = \frac{1}{2}\left(1 + e^{4\eta^2(2\bar{n}+1)(\cos(\vartheta)-1)}\cos\left[2c - \phi\right]\right) \tag{5.60}$$

Scanning the microwave detuning is equivalent to scanning the phase lag ϕ, holding everything else constant. The contrast of the Ramsey experiment is therefore given by:

$$C(T_{\text{delay}}) = \exp\left[4\eta^2(2\bar{n}+1)(\cos(\omega_{\text{trap}}T_{\text{delay}}) - 1)\right] \tag{5.61}$$

This equation shows the behavior predicted above. When T_{delay} matches an integral multiple of $2\pi/\omega_{\text{trap}}$, the contrast is one. Close to the peak, the curve is approximately Gaussian, with width given by $\eta\omega_{\text{trap}}\sqrt{2\bar{n}+1}$.

5.4.3 Coupling to a Single Mode of Motion

All of the analysis above assumes that the SDK is occurring along a single mode of motion. Ideally this would be done by aligning the Δk vector of the Raman

beams to be parallel to one of the principal axes of the trap. This is unfortunately impossible in the four rod trap, as the principle transverse axes are along the lines joining the rods, and the four rod trap does not have enough degrees of freedom to allow rotating the axes. Δk *could* be along the axial direction, by sending the Raman beams in at 90° to one another, rather than counterpropagating. However, this would complicate the ultimate goal of using these kicks to execute a gate, as explained in chapter 6.

As an alternative, we made the two transverse trap frequencies degenerate. This was done by adjusting the bias voltages on the four rods until spectroscopy showed only a single transverse sideband peak. By making the frequencies degenerate, there are no longer unique "principal" axes in the transverse directions. All transverse directions are equivalent. It is then only necessary to make the Δk vector orthogonal to the axial direction. However, making the transverse trap degenerate means that one cooling beam is no longer sufficient to cool all degrees of freedom [79]. For this reason, we added a second Doppler cooling beam, sent vertically at a 45° angle through the trap. This was then sufficient to cool all three degrees of freedom.

5.4.4 Experimental Results

Experimental results of the experiment described above are shown in figure 5.6. The time between the two microwave $\pi/2$ pulses was kept fixed at 200 μs, so that the fringe frequency would not change. The time between the two pulses picked by the pulse picker[5] was varied. The detuning was scanned from -3.5 to 3.5

[5]ConOptics 350-105

kHz. For this experiment, $\omega_{\text{trap}}/2\pi = 743$ kHz. At integer multiples of that period, a clear revival of contrast appears. However, the shape of that contrast revival is different from that predicted in equation 5.61. Superimposed is a modulation at the RF drive frequency of 17.9 MHz. This is due to uncompensated micromotion. The source of this micromotion was never fully established – every attempt was made to eliminate it using offset electric fields. To model the effect of this micromotion on the contrast revival, it is necessary to modify the free evolution operator in step 4 of the analysis above. Instead of $|\alpha\rangle \rightarrow |\alpha e^{-i\omega_{\text{trap}}t}\rangle$, equation 2.29 derived in chapter 2 describes the evolution with micromotion. Here I am making the approximation that the coherent state evolution can be well described by the classical micromotion solution. In principle, a full quantum mechanical treatment such as that in [141] is necessary, as the micromotion will also lead to a "warping" of the coherent state. However, this is a very small effect. The theory curve shown in figures 5.6(b)-(c) is derived from this classical treatment of micromotion, and is a best fit to $\bar{n}$ and the amount of excess micromotion B. The best fit mean phonon number is $\bar{n} = 10.1$, which is consistent with the Doppler cooling limit discussed in chapter 2. The micromotion also causes the revival peak to be narrower than what would be predicted by the theory described above. This is because the micromotion increases the effective temperature of the ion.

It should be noted that the kick size is significantly smaller than the size of the wave packet. From equation 5.11, the wave packet size in natural units is given by $\sqrt{2\bar{n}} = 4.5$. By comparison, the separation created by a single spin-dependent kick is $2\eta = 0.44$. There is therefore significant overlap between $|0\rangle$ and $|1\rangle$ even after

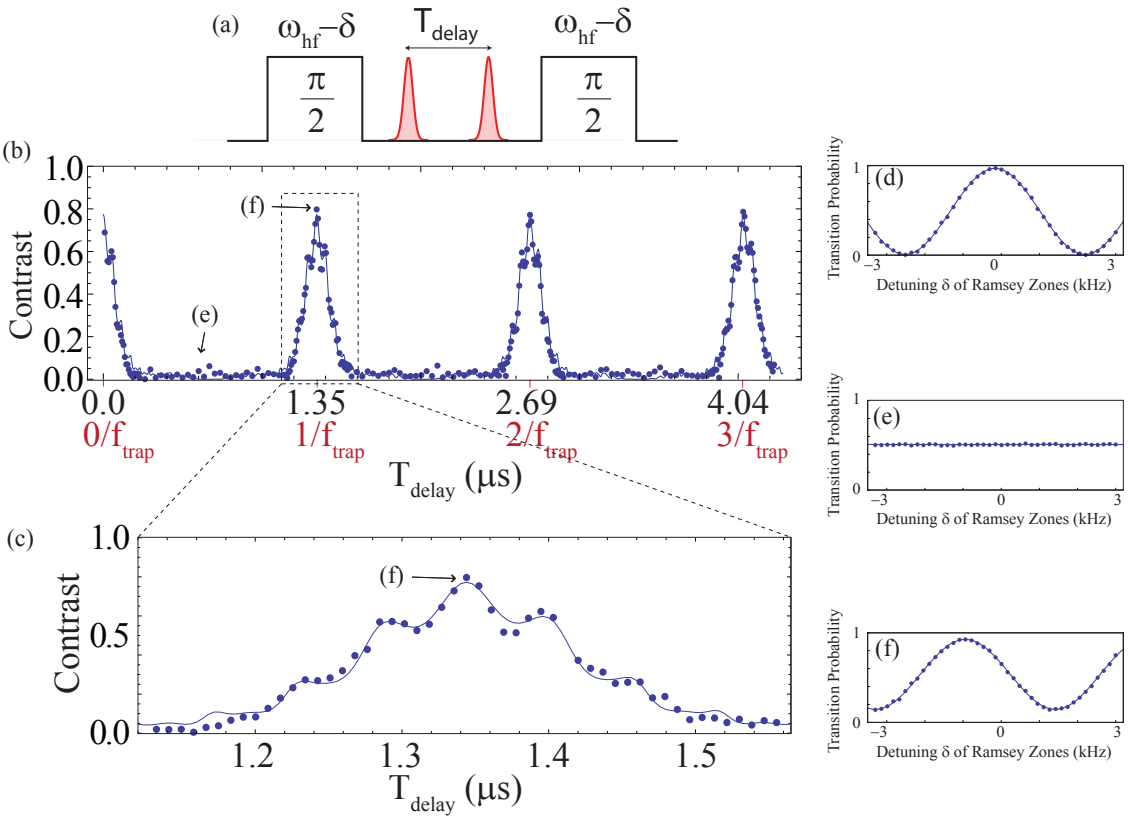

Figure 5.6: (a): Experimental sequence to measure effect of spin-dependent kicks. The ion is driven by two near resonant microwave $\pi/2$ pulses, with two spin-dependent kicks in between. For each delay T_{delay} between the kicks, the microwave detuning δ is scanned and a Ramsey fringe contrast obtained. (b) Plot of the results of the experiment in (a). At integer multiples of the trap period, contrast revives. (c) Close-up of the first revival peak in (b). The peak shape is a function of temperature and micromotion amplitude. The modulation of the peak is due to the better overlap of the $|0\rangle$ and $|1\rangle$ wave packets at integer multiples of the micromotion period. The best fit curve shown is a fit to theory. Free parameters are the micromotion amplitude, average phonon number $\bar{n}$, and maximum contrast revival ($\sim$80%). The fit shown corresponds to $\bar{n} = 10.1$. (d)-(f): Some example frequency scan data (with fits). (e) and (f) each correspond to single points in (b), as indicated. (d) No momentum kicks; microwave pulses only. Contrast is 97%. (e) Two kicks separated by half a trap period. Contrast is 0%. (f) Two kicks separated by full trap period. Contrast is 80%.

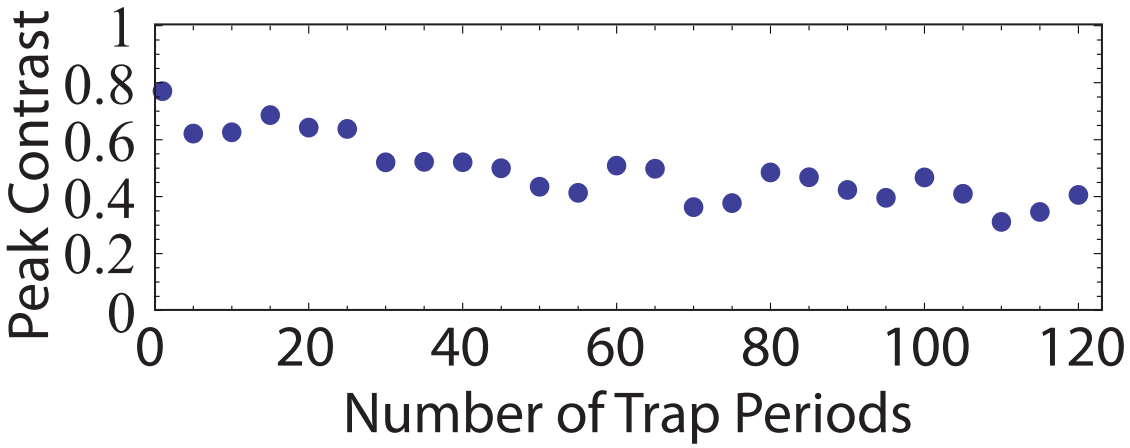

Figure 5.7: Contrast revival for many trap periods. Each point corresponds to an exact integer multiple of the trap period.

a spin-dependent kick, meaning the spin and motion are not maximally entangled. There is nevertheless some entanglement, as is evidenced by the disappearance and reappearance of fringes.

Fig. 5.7 is similar to Fig. 5.6(b), with data points only at multiples of the trap period, showing revivals even after the ion has gone through 120 oscillations in the trap. The slow decay here is due mainly to laser repetition rate instability, leading to timing jitter in the arrival time of the second kick relative to the first kick. This experiment was done with the Paladin laser, the repetition rate of which cannot be stabilized. If the time between the two SDKs changes, the optical phase difference imparted by each SDK changes. This corresponds to noise in c in equation 5.61, which causes the Ramsey fringe to have a noisy phase. This noisy phase causes a reduction in contrast. If this experiment were redone with the PicoTrain laser, it is likely that contrast could be seen for many hundreds of trap periods.

The maximum contrast revival seen is approximately 80%, as compared to

97% contrast seen in the control case without laser pulses (figure 5.6(d)). An SDK with fidelity F will produce a peak contrast of approximately F^2. Therefore, the 80% contrast corresponds to a single pulse SDK fidelity of approximately 91%, which falls far short of the theoretical maximum of 99%. While it is not certain of the reason for this drop, the most likely cause is micromotion during the SDK. The pulse train that creates the SDK is 2.7 ns long, while the RF drive period is 56 ns. The micromotion therefore executes 5% of an oscillation during a kick (as compared to 0.2% of an oscillation for the secular motion). This evolution may be sufficient to interfere with the SDK creation on the level seen. Fully simulating the eight pulse sequence while including the effects of micromotion is extremely computationally slow, and has not been attempted.

The ultrafast gate described in chapter 6 will require a significant number of SDKs (at least 24, see table 6.1). If errors simply compound, achieving a 90% fidelity gate would require 99.5% fidelity for a single SDK. It is therefore critical that the fidelity be improved. While the micromotion issue in the four rod trap was never satisfactorily resolved, the experiment has switched over to the blade trap. We have been able to compensate fully for micromotion in the blade trap. We have also switched over to the PicoTrain laser, whose energy per pulse is at least three times that of the Paladin. This allows enough power for active stabilization of the laser power, which should also improve the fidelity.

Chapter 6

Ultrafast Two-Ion Entanglement

In this chapter I will discuss using the spin-motion entangling interaction in chapter 5 to execute a two ion entangling gate. Unfortunately, as of this writing, the experiment has yet to successfully demonstrate ultrafast two ion entanglement. There will therefore be no experimental results in this section. However, I will go over the theoretical analysis of how such a gate would operate.

As mentioned previously, ultrafast gates are fundamentally different from previously implemented two ion Coulombic gates, as they do not address specific trap normal modes. Rather these gates excite all normal modes, and then carefully de-excite them. Such a gate was theoretically proposed by Garcia-Ripoll in [46], and later extended by Duan in [47]. Both schemes rely on using a sequence of fast spin-dependent momentum kicks of the sort described above. By carefully controlling the timing of the kicks, the motion returns to its original state at the end of the process, while a spin-dependent phase remains. Such an interaction generates two ion entanglement, as shown in appendix D.

6.1 Two-Ion Spin-Dependent Kick

Consider the action of the spin-dependent kick operator in equation 5.44 applied to two ions. If the ions are both in $|0\rangle$ or $|1\rangle$, then the ions are kicked in the same direction. In that case, the center of mass mode receives a kick. On the other hand, if the ions are in different states, the relative motion mode receives a kick. The four different spin states will therefore have four different motional excitations in response to an SDK, as shown in figure 6.2(a). The single ion SDK evolution operator is:

$$U = \hat{\sigma}_+ e^{i\phi(t_0)} e^{i\Delta k x} + \hat{\sigma}_- e^{-i\phi(t_0)} e^{-i\Delta k x} \tag{6.1}$$

This is just equation 5.44 again, but with displacement operators rewritten according to their definition in equation 5.6. For two ions, the evolution operator becomes a tensor product of 6.1 over each ion:

$$\begin{aligned} U_{\text{SDK}}(t_0) = &\left(\hat{\sigma}_{+_1} e^{i\phi(t_0)} e^{i\Delta k x_1} + \hat{\sigma}_{-_1} e^{-i\phi(t_0)} e^{-i\Delta k x_1}\right) \otimes \\ &\left(\hat{\sigma}_{+_2} e^{i\phi(t_0)} e^{i\Delta k x_2} + \hat{\sigma}_{-_2} e^{-i\phi(t_0)} e^{-i\Delta k x_2}\right) \qquad (6.2) \\ = &\ \hat{\sigma}_{+_1}\hat{\sigma}_{+_2} e^{2i\phi(t_0)} e^{i\Delta k(x_1+x_2)} + \hat{\sigma}_{+_1}\hat{\sigma}_{-_2} e^{i\Delta k(x_1-x_2)} + \\ &\hat{\sigma}_{-_1}\hat{\sigma}_{+_2} e^{i\Delta k(-x_1+x_2)} + \hat{\sigma}_{-_1}\hat{\sigma}_{-_2} e^{-2i\phi(t_0)} e^{i\Delta k(-x_1-x_2)} \qquad (6.3) \end{aligned}$$

where subscripts on the operators refer to the different ions. We can now recast this in terms of the normal modes defined in section 2.2, equations 2.52 and 2.53:

$$\begin{aligned} U_{\mathrm{SDK}}(t_0) =& e^{2i\phi(t_0)}\hat{\sigma}_{+_1}\hat{\sigma}_{+_2}e^{2i\Delta k x_C} + \hat{\sigma}_{+_1}\hat{\sigma}_{-_2}e^{2i\Delta k x_R} + \\ & e^{-2i\phi(t_0)}\hat{\sigma}_{-_1}\hat{\sigma}_{-_2}e^{-2i\Delta k x_C} + \hat{\sigma}_{-_1}\hat{\sigma}_{+_2}e^{-2i\Delta k x_R} \qquad (6.4) \\ =& e^{2i\phi(t_0)}\hat{\sigma}_{+_1}\hat{\sigma}_{+_2}D_C[i\eta_C] + \hat{\sigma}_{+_1}\hat{\sigma}_{-_2}D_R[i\eta_R] + \\ & e^{-2i\phi(t_0)}\hat{\sigma}_{-_1}\hat{\sigma}_{-_2}D_C[-i\eta_C] + \hat{\sigma}_{-_1}\hat{\sigma}_{+_2}D_R[-i\eta_R] \qquad (6.5) \end{aligned}$$

where D_C and D_R are the coherent state displacement operators for the two normal modes. Here I have defined the center of mass and relative motion kick sizes η_C and η_R, which are given by:

$$\eta_C = 2\Delta k\sqrt{\frac{1}{2M\omega_C}} = \sqrt{2}\Delta k\sqrt{\frac{1}{2m\omega}} = \sqrt{2}\eta \qquad (6.6)$$

$$\eta_R = 2\Delta k\sqrt{\frac{1}{2M\omega_R}} = \sqrt{2}\sqrt{\frac{\omega}{\omega_R}}\Delta k\sqrt{\frac{1}{2m\omega}} = \sqrt{2}\sqrt{\frac{\omega}{\omega_R}}\eta \qquad (6.7)$$

where ω is the single ion trap frequency, $\omega_C = \omega$ is the center of mass mode frequency of two ions, and ω_R is the relative motion mode frequency of two ions. The relationship between ω_R and ω is discussed in section 2.2.

Equations 6.6-6.7 follow from the discussion in section 2.2, where it is shown that the effective mass M of the normal modes is twice that of a single ion.

6.2 Reversing Kick Direction

Because the SDK also flips the ions' spins, two pulses from the laser will cancel each other (up to a small correction owing to trap evolution between the kicks). In order to execute a gate, it will be necessary to control the direction of a kick, such

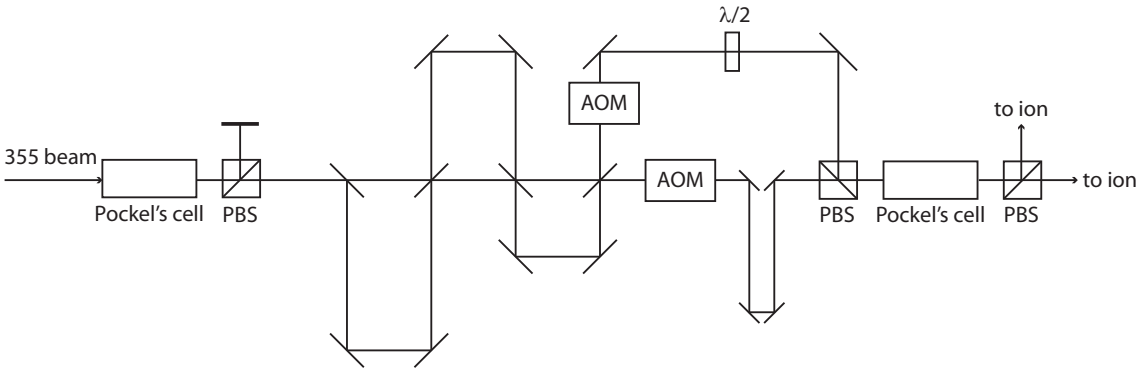

Figure 6.1: Method for controlling kick directions. The first Pockels cell and PBS act as a pulse picker, and controls which pulses are let through. The beam then goes through the delay lines and AOMs, after which the beams are combined on a PBS and sent through a second Pockels cell. This Pockels cell controls which beam is S-polarized and which is P-polarized. This then controls which gets reflected off the final beam cube and which gets transmitted, which controls the direction from which the ion sees each comb.

that a second pulse from the laser can continue kicking in the same direction as the first. Ideally, for each pulse from the laser, we will be able to choose whether it kicks in one direction, the other direction, or is rejected by the pulse picker.

The method we have chosen to control the direction is shown in figure 6.1. Up to the AOMs, the layout is the same as in figure 5.5. However, the beams are then recombined on a PBS, and sent through a second Pockels cell. If the Pockels cell rotates the polarization, then it changes which beam is transmitted and which is reflected at the second PBS, which controls the direction from which the ion sees each comb.

6.3 Focusing onto Two Ions

In order to kick both ions, the laser intensity must be sufficient on both ions. However, as mentioned in chapter 5, this experiment is already fairly close to the edge on available power. If the beam center is simply moved to halfway in between

the two ions, the ions would then be on the edge of the beam rather than in the center, resulting in greater sensitivity to pointing instability. Moreover, the intensity at each ion would likely be less than half what is achievable with a single ion, as increasing the beam waist to encompass two ions will cause the intensity to fall as the square of the waist. One way to mitigate the situation is to use a cylindrical lens to focus the beam to an oblong shape. This would increase the intensity at each ion to closer to 1/2 what could be achieved with a single ion, although the ions would still sit on the beam slope.

One novel idea for focusing onto two ions is to use the AOMs to create two spots, one for each ion. By driving the AOMs at two frequencies a few MHz apart, two beams will be created. The focusing system can be made such that those two beams will focus down onto the two separate ions. For small frequency separations, the diffraction efficiency for the two frequencies should be equal, meaning the power will be evenly split between the beams. Each ion would then sit at a local maximum in beam intensity, rather than on a slope. The optical phase at each ion would then be slightly different, but this would not affect the performance of the gate.

6.4 Example: Duan Scheme

To gain a better understanding of how such a gate works, I will begin by going through a straightforward version of the scheme proposed by Duan in [47]. Consider a sequence of three spin-dependent kicks applied to two ions:

1. $t = 0$: momentum kick of size $+N\hbar\Delta k$

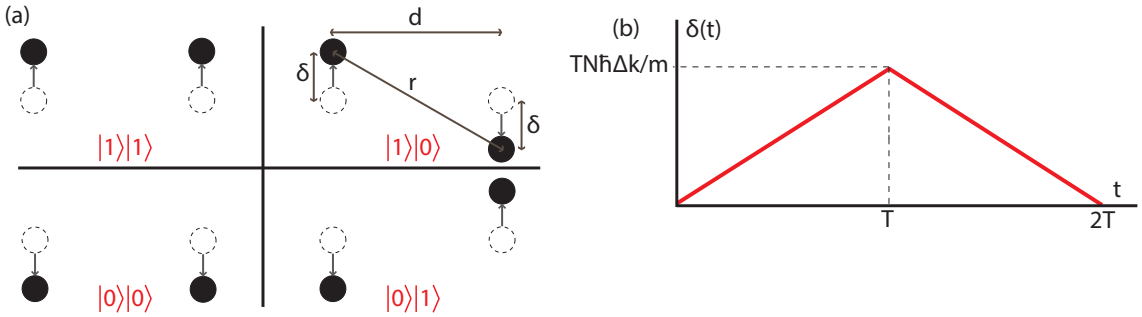

Figure 6.2: (a) A spin-dependent kick applied to two ions excites the motion into four different possible configurations depending on the two ion spin state. The dashed circles shows the original, equilibrium position of the ions. The arrow and solid circles show the path followed after a kick. (b) Displacement δ versus time for the simple kick sequence described in the text. The kicks are much faster than the trap period, so the trap evolution during the kicking sequence is negligible. The ions therefore behave nearly as free particles.

2. $t = T$: momentum kick of size $-2N\hbar\Delta k$

3. $t = 2T$: momentum kick of size $+N\hbar\Delta k$

The kick of size $N\hbar\Delta k$ is formed from a fast sequence of N laser pulses. I will show how this creates a phase gate, and derive the phase accumulated from two different perspectives.

6.4.1 Coulomb Picture

Suppose that the total length of the kicking sequence is much faster than the trap period: $\omega_{\text{trap}}T \ll 1$. In that case, trap evolution during the kicks can be ignored, and the ions behave as free particles. Also suppose that the ions are initially at rest[1]. The first kick imparts a momentum to each ion of $N\hbar\Delta k$. The ions then move at a constant velocity away from equilibrium, until the second kick reverses the direction. The third kick then stops the motion of the ions at (nearly) the original position. If the ion spin state is $|0\rangle|0\rangle$ or $|1\rangle|1\rangle$, the two ion energy

[1]This assumption is not necessary for the analysis, but it makes the discussion easier.

from the Coulomb interaction does not change during the sequence. However, for $|0\rangle|1\rangle$ and $|1\rangle|0\rangle$, the energy changes as the ions get further apart and then closer together. The time-dependent energy difference between these two configuration is:

$$\begin{aligned}\Delta E(t) &= \frac{e^2}{4\pi\epsilon_0}\left(\frac{1}{d} - \frac{1}{\sqrt{d^2+4\delta(t)^2}}\right) \\ &\approx \frac{e^2}{4\pi\epsilon_0}\left(\frac{2\delta(t)^2}{d^3}\right) \end{aligned} \tag{6.8}$$

where d is the distance between the ions in equilibrium and $\delta(t)$ is the time-dependent displacement of each ion from equilibrium (see figure 6.2). The acquired phase difference from this process is given by:

$$\Delta\phi = \int_0^{2T} \Delta E(t)dt \tag{6.9}$$

$$= \left(\frac{e^2}{4\pi\epsilon_0}\right)\frac{2}{d^3}\int_0^{2T}\delta(t)^2 dt \tag{6.10}$$

$$= \frac{4(e^2/4\pi\epsilon_0)N^2\Delta k^2 T^3}{3d^3m^2} \tag{6.11}$$

$$= \frac{2\omega_z^2 N^2\Delta k^2 T^3}{3m} \tag{6.12}$$

In equation 6.12, I have used equation 2.35 to replace the ion-ion distance with the axial trapping frequency. We see then that the motional state (nearly) returns to its original state at the end of the process, while $|0\rangle|1\rangle$ and $|1\rangle|0\rangle$ acquire a phase relative to $|0\rangle|0\rangle$ and $|1\rangle|1\rangle$. This is thus a phase gate. Note that the motion is entirely driven – equation 6.9 is valid only because the ions are effectively free particles. The natural harmonic motion in the trap does not lead to phase accumulation. The fidelity of the phase gate described above is limited by free evolution in the trap. Because the gate is not truly instantaneous, there will be a small amount of

residual entanglement with the motion at the end of the process. This infidelity can be eliminated by more complex kicking sequences, described below.

6.4.2 Normal Mode Picture

Alternatively, this process can be viewed as exciting the center of mass versus the relative mode of motion. Phase space diagrams of the kick sequence are shown in figure 6.3 for the two different modes, both in the non-rotating frame and in the rotating frame.

We can determine the evolution of a coherent state $|\alpha\rangle$ in a harmonic oscillator of frequency ω subjected to the kicks described above using equations 5.7 and 5.5. For simplicity in this example, I will treat the ground state $\alpha = 0$. This will later be generalized. The ground state evolution is as follows:

Initial state: $$|\psi_0\rangle = |0\rangle \tag{6.13}$$

Kick up, $N\eta$: $$|\psi_1\rangle = |iN\eta\rangle \tag{6.14}$$

Free evolution: $$|\psi_2\rangle = \left|iN\eta e^{-i\omega T}\right\rangle \tag{6.15}$$

Kick down, $-2N\eta$: $$|\psi_3\rangle = e^{-2iN^2\eta^2\sin(\omega T)}\left|-2iN\eta + iN\eta e^{-i\omega T}\right\rangle \tag{6.16}$$

Free evolution: $$|\psi_4\rangle = e^{-2iN^2\eta^2\sin(\omega T)}\left|iN\eta(-2+e^{-i\omega T})e^{-i\omega T}\right\rangle \tag{6.17}$$

Kick up, $N\eta$: $$|\psi_5\rangle = e^{iN^2\eta^2(-4\sin(\omega T)+\sin(2\omega T))}\times \left|iN\eta\left(1+(-2+e^{-i\omega T})e^{-i\omega T}\right)\right\rangle \tag{6.18}$$

Approximate result: $$|\psi_5\rangle \approx e^{-2iN^2\eta^2\omega T(1+\omega^2T^2/3)}\left|-iN\eta\omega^2T^2\right\rangle \tag{6.19}$$

The phases ϕ_C and ϕ_R acquired by the center of mass and relative motion modes can then be determined from equation 6.19, using equations 6.6 and 6.7 for

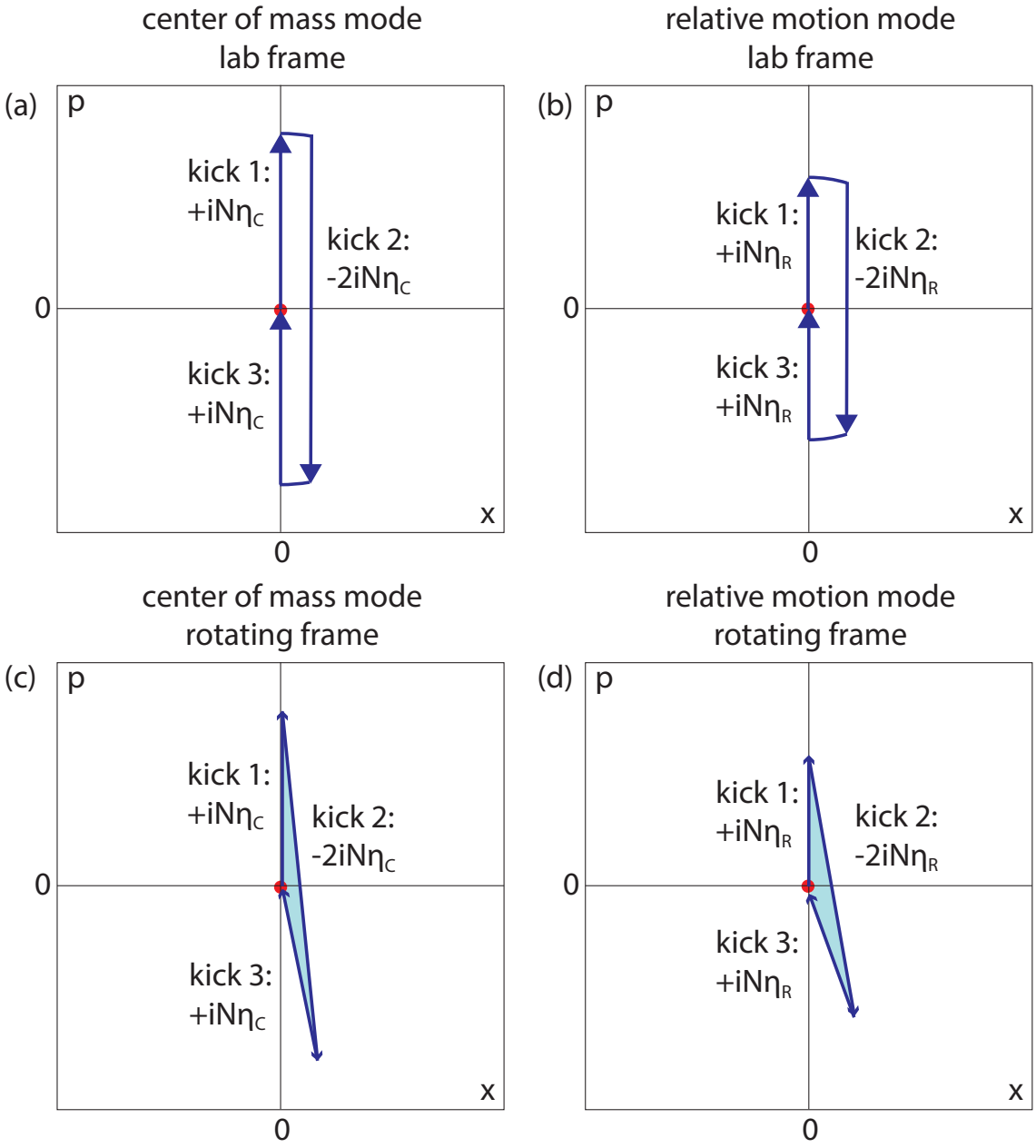

Figure 6.3: Phase space pictures of the kick sequence described above. (a) and (b) are in the non-rotating lab frame, in which the kicks are vertical displacements in phase space, and free evolution is along circles. (c) and (d) are in the rotating frame, in which the kick direction rotates while the ion does not. Twice the difference in area between the shaded regions in (c) and (d) is the phase difference accumulated.

the kick sizes:

$$\phi_C = -\frac{2N^2\Delta k^2 T}{m}\left(1+\frac{\omega_C^2 T^2}{3}\right) \tag{6.20}$$

$$\phi_R = -\frac{2N^2\Delta k^2 T}{m}\left(1+\frac{\omega_R^2 T^2}{3}\right) \tag{6.21}$$

$$\Delta\phi = \phi_R - \phi_C = \frac{2N^2\Delta k^2 T^3}{3m}\left(\omega_R^2 - \omega_C^2\right) \tag{6.22}$$

$$= \frac{2N^2\Delta k^2 T^3 \omega_z^2}{3m} \tag{6.23}$$

In equation 6.23 I used equation 2.49 to express the phase in terms of the axial trap frequency. Equation 6.23 is identical to the expression found in equation 6.12 using the Coulomb energy picture. It is therefore legitimate to think of this process using either picture.

Equation 6.22 applies equally for axial modes or transverse modes. For transverse modes, the term in parentheses is ω_z^2, while for axial modes it is $2\omega_z^2$. The gate therefore produces a factor of two more phase difference when applied to axial modes as compared to transverse modes. However, there is an added flexibility in using transverse modes, as will be discussed in section 6.5.

Phase Space Area As yet another way to extract the phase difference in equation 6.22, consider the phase space trajectories in figure 6.3. (a) and (b) show the paths in the non-rotating frame, in which the free evolution trajectories are circles. (c) and (d) show the trajectories in the frame which is rotating at the mode frequency. In that frame, the state does not evolve due to free evolution. Instead, the direction of the momentum kick rotates as the frame rotates. Crucially, in the rotating frame all paths are driven, which leads to phase accumulation.

If a coherent state is driven through a trajectory which encloses an area A in the rotating frame phase space, that coherent state acquires a phase $2A$ [142, 143]. This fact allows us to determine the phase acquired simply by calculating the area enclosed in figures 6.3(c) and (d). Because the phase space does not close perfectly, the shape enclosed is a quadrilateral. Calculating the area of the quadrilateral yields:

$$A = \frac{1}{2}N^2\eta^2\left(4\sin(\omega T) - \sin(2\omega T)\right) \tag{6.24}$$

The phase accumulated should equal $2A$, and indeed this expression matches that in equation 6.18.

6.4.3 Fidelity of Phase Gate

Setting equation 6.11 equal to $\pi/2$ allows us to relate the number of kicks N necessary for a maximally entangling controlled phase gate to the gate timing and ion spacing:

$$\Delta\phi = \frac{4(e^2/4\pi\epsilon_0)N^2\Delta k^2 T^3}{3d^3m^2} = \frac{\pi}{2} \tag{6.25}$$

$$\Rightarrow N = 0.056\left(\frac{d}{T}\right)^{3/2} \tag{6.26}$$

where d is in μm and T is in μs. This shows that the number of pulses necessary is reduced for ions which are closer (larger Coulomb force) or longer time (more time for Coulomb interaction).

The fidelity of the phase gate can be estimated by calculating the overlap of the final state in equation 6.19 with the initial state. I will do this for the higher

frequency mode, which evolves more:

$$\left|\langle 0| - iN\eta_R\omega_R^2 T^2\rangle\right|^2 = \exp\left[-N^2\eta_R^2\omega_R^4 T^4\right] \tag{6.27}$$

$$= \exp\left[-N^2\Delta k^2\omega_R^3 T^4/m\right] \tag{6.28}$$

$$= \exp\left[-\left(\frac{3\pi\omega_R^3}{8\omega_z^2}\right)T\right] \tag{6.29}$$

Here I have used equations 6.23 and 6.25. Equation 6.29 shows that the fidelity of the maximally entangling phase gate decays exponentially with gate time T (This is the same result arrived at by Duan [47], albeit through different arguments). Therefore, a sufficiently fast gate can be made arbitrarily high fidelity. However, the number of kicks necessary will also increase as T is reduced.

Note that for a sufficiently fast time T, this gate can also work to entangle two ions in an arbitrarily long chain, without affecting the rest of the ions. All the other ions are effectively frozen during the gate, and so do not participate. That makes this interaction scalable. This sort of local gate is shown graphically in figure 6.4.

The purpose of this exercise was to show how and why such a gate works. However, the gate as described is unfortunately experimentally unrealistic. The reason is because of the limited repetition rate of the laser used to create the kicks. We are using an 80 MHz laser, with a trap frequency of about 1 MHz. Therefore, even between 2 kicks there is already non-negligible trap evolution. We can see what would be required from equation 6.29. For 99% fidelity and typical trap frequencies, equation 6.29 says that T should be 2.8 ns. At that speed, equation 6.26 shows that $N = 4200$ kicks are required. This would require a laser with a repetition rate in the THz range, with power per pulse equal to our current laser. Unfortunately that

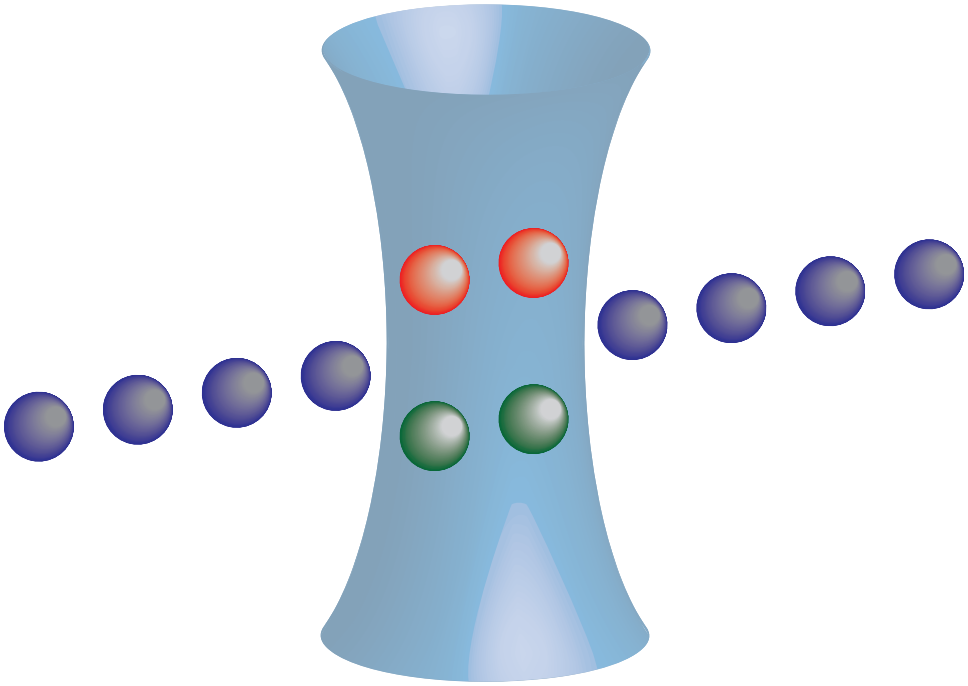

Figure 6.4: Two ions in a chain can be rapidly entangled and then disentangled with this sort of gate, without affecting the other ions.

is currently technologically infeasible, and would in any event create other problems with our choice of qubit.

Fortunately, more complex kicking sequences can solve this problem. The kick sequence {one kick up, two kicks down, one kick up} described above is part of a class of functions called *Walsh functions* [144]. Such sequences have been used to suppress errors in traditional two ion Mølmer-Sørensen gates [145]. Duan shows that using higher order Walsh functions can suppress the errors further [47]. Unfortunately, even with these higher order corrections, a higher repetition rate would be necessary to execute the Duan scheme. However, Garcia-Ripoll et. al. showed in [46] that there exist kick sequence which eliminate the error completely. This is shown in the next section.

6.5 García-Ripoll/Cirac/Zoller Gate

I will now describe the more general kick sequence, following the procedure laid out in [46]. Consider a coherent state $|\alpha_0\rangle$ subject to a sequence of n momentum kicks. The k^{th} kick arrives at time t_k and is of size z_k. Between each of these kicks, there is free evolution. Let the state immediately after the k^{th} kick be given by $e^{i\xi_k}|\alpha_k\rangle$. We can work out a recursive relationship for ξ_k and α_k:

$$\text{initial:} \quad \xi_0 = 0 \qquad \alpha_0 = \alpha_0 \tag{6.30}$$

$$t = t_1: \quad \xi_1 = z_1 \mathrm{Re}(\alpha_0) \qquad \alpha_1 = \alpha_0 + i z_1 \tag{6.31}$$

$$t = t_2: \quad \xi_2 = \xi_1 + z_2 \mathrm{Re}(\alpha_1 e^{-i\omega(t_2 - t_1)}) \qquad \alpha_2 = \alpha_1 e^{-i\omega(t_2-t_1)} + i z_2 \tag{6.32}$$

$$\ldots$$

$$t = t_k: \quad \xi_k = \xi_{k-1} + z_k \mathrm{Re}(\alpha_{k-1} e^{-i\omega(t_k - t_{k-1})}) \quad \alpha_k = \alpha_{k-1} e^{-i\omega(t_k - t_{k-1})} + i z_k \tag{6.33}$$

Without loss of generality, let $t_1 = 0$. After a bit of algebra, the recursive relations in equation 6.33 can be solved to yield expressions for the final state and phase:

$$\alpha_n = e^{-i\omega t_n} \left(\alpha_0 + i \sum_{k=1}^{n} z_k e^{i\omega t_k} \right) \tag{6.34}$$

$$\xi_n = \mathrm{Re}\left[\alpha_0 \sum_{k=1}^{n} z_k e^{-i\omega t_k} \right] - \sum_{k=2}^{n} \sum_{j=1}^{k-1} z_k z_j \sin\left[\omega(t_j - t_k)\right] \tag{6.35}$$

These equations are a dramatic generalization of the specific example discussed in the previous section. Indeed, those results can immediately be recovered from equations 6.34 and 6.35 by setting $z_1 = N\eta$, $z_2 = -2N\eta$, $z_3 = N\eta$, $t_1 = 0$, $t_2 = T$, and $t_3 = 2T$.

Examining equations 6.34 and 6.35, we see that if the following condition is

satisfied:

$$\sum_{k=1}^{n} z_k e^{i\omega t_k} = 0 \tag{6.36}$$

then the coherent state ends where it would have been without any kicks, and the phase becomes independent of α_0:

$$\alpha_n = e^{-i\omega t_n}\alpha_0 \tag{6.37}$$

$$\xi_n = \sum_{k=2}^{n}\sum_{j=1}^{k-1} z_k z_j \sin\left[\omega(t_k - t_j)\right] \tag{6.38}$$

This result is fairly remarkable: it means that if equation 6.36 is satisfied, then a phase is accrued which is completely independent of the motional state. Any motional state, no matter the temperature, will have the same phase at the end of the process. Moreover, the state itself will be unchanged.

This result can be understood intuitively, by turning to a geometric picture in phase space. In the rotating reference frame, a kick of size z_k at time t_k corresponds to displacement along a vector of length z_k at an angle ωt_k. Such a vector can be represented in the complex plane as $z_k e^{i\omega t_k}$. In order for the path traversed in phase space to return to the original position, the sum of those vectors must be zero. This is exactly the condition specified in equation 6.36. Moreover, the phase acquired by traversing such a path is given simply by twice the area enclosed. That phase is then clearly independent of initial position, just as the area of a polygon is independent of its location on the plane. The area of a polygon with side lengths z_k and angles ωt_k is given by equation 6.38 times one-half, as expected. This is depicted graphically in figure 6.5.

With this result in hand, we can now understand the response of a state to

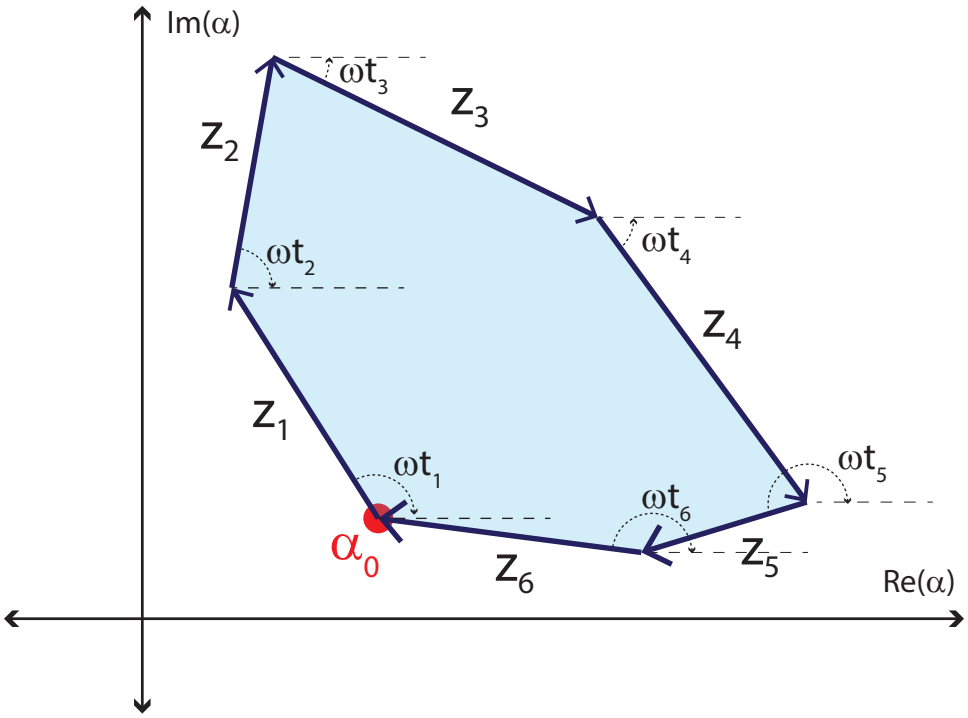

Figure 6.5: General path in (rotating) phase space of the sort described in the text. If the vectors $z_k e^{i\omega t_k}$ add to zero as in equation 6.36, then the motion disentangles from the spin and the phase is determined by the shaded area.

repeated applications of the operator in equation 6.5. In the theoretical analysis above I assumed an arbitrary z_k; the kicks here are of course of a fixed size $\eta_{C,R}$ for each mode. I will assume that the kicking direction is reversible: $z_k = b_k \eta_{C,R}$, where $b_k = \pm 1$. There will now be two conditions, namely that both the center of mass and relative motion separately close. From equation 6.38, the phase difference acquired between the two modes is:

$$\Phi = \sum_{k=2}^{n} \sum_{j=1}^{k-1} b_k b_j \left(\eta_R^2 \sin\left[\omega_R (t_j - t_k)\right] - \eta_C^2 \sin\left[\omega_C (t_j - t_k)\right] \right) \tag{6.39}$$

$$= 2\eta^2 \sum_{k=2}^{n} \sum_{j=1}^{k-1} b_k b_j \left(\frac{\omega}{\omega_R} \sin\left[\omega_R (t_j - t_k)\right] - \sin\left[\omega_C (t_j - t_k)\right] \right) \tag{6.40}$$

As a final condition, we require the net phase difference to be equal to $\pi/2$. Putting

these pieces together, we are left with the following three equations:

$$\sum_{k=1}^{n} b_k e^{i\omega_C t_k} = 0 \tag{6.41}$$

$$\sum_{k=1}^{n} b_k e^{i\omega_R t_k} = 0 \tag{6.42}$$

$$\Phi = \pi/2 \tag{6.43}$$

Choosing b_k and t_k to satisfy these conditions will produce a maximally entangling gate.

As an added complication, equation 6.5 shows that there will be another phase imparted to the center of mass mode from the phase of the light at the time of each kick. The sign alternates, because the spins flip at each kick:

$$\gamma = \phi(t_0) - \phi(t_1) + \phi(t_2) - \cdots \tag{6.44}$$

$$= \omega_A \left(t_0 - t_1 + t_2 - \cdots\right) + \begin{cases} 0 & n \text{ even} \\ -\phi_0 & n \text{ odd} \end{cases} \tag{6.45}$$

One immediate consequence of this phase is that it is important that the number of kicks used be even. Otherwise, the absolute optical phase ϕ_0 does not vanish, and the experiment becomes sensitive to the absolute optical phase (which may not be stable). By making the number of kicks even, the optical phase sensitivity disappears (also, the spins return to their original value). There does remain a relative phase determined by the RF on the AOMs, which may not be zero. However, it should be stable, and does not affect the entanglement operation (see appendix D). From equation 6.5, the states $|00\rangle$ and $|11\rangle$ acquire this phase with opposite sign.

From all of the above, we conclude that the effect of applying a sequence of

spin-dependent kicks, timed to satisfy equations 6.41 and 6.42, is the following:

$$|00\rangle \Rightarrow e^{i\gamma} i\,|00\rangle \tag{6.46}$$

$$|01\rangle \Rightarrow |01\rangle \tag{6.47}$$

$$|10\rangle \Rightarrow |10\rangle \tag{6.48}$$

$$|11\rangle \Rightarrow e^{-i\gamma} i\,|11\rangle \tag{6.49}$$

6.6 Realistic Gate

It now remains to find solutions to equations 6.41, 6.42, and 6.43. As a first constraint, the arrival time of each pulse t_k is restricted to be a multiple of the laser repetition rate. Within that constraint, the number of possible kick sequences is enormous. If we only search for sequences that are shorter than 2 μs there are 160 pulses that can be used. Each of those pulses could be a kick in one of two possible directions, or omitted entirely. There are therefore $3^{160} \approx 10^{77}$ kick sequences that could be created in that 2 μs span. We therefore restrict our search, at least initially, to relatively simple sequences with a high degree of symmetry.

The first sequence which one might investigate is the simplest: N consecutive kicks, all in the same direction. This sequence could, in principle, close both phase spaces. However, the lack of free parameters allows no control over the phase accrued or the duration of the gate, and highly constrains the possible trap frequencies and their ratio. To allow sufficient control, more free parameters are necessary.

6.6.1 First Pattern

The simplest symmetric kick pattern with three free parameters is:

1. N_1 kicks
2. wait for N_2 pulses
3. N_1 kicks (possibly in a different direction)
4. wait for N_3 pulses
5. repeat steps 1-3, possibly inverted

An example of this sequence is shown graphically in figure 6.6. This is similar to the first scheme introduced in [46], although there evolution during the pulses was neglected. I will denote a set of kicks as $\{z, N\}$, where N indicates the number of kicks in the set, and $z = \pm 1$ or 0 indicates whether the set of kicks is in one direction, the other direction, or omitted. So, for example, the sequence described above could be written in the shorthand: $\{\{1, N_1\}, \{0, N_2\}, \{1, N_1\}, \{0, N_3\}, \{-1, N_1\}, \{0, N_2\}, \{-1, N_1\}\}$. (Here I assumed the second set of N_1 kicks was in the same direction as the first, while the repetition of 1-3 was in the reverse direction.)

Intuitively, the logic of this sequence is as follows: The initial number of kicks N_1 is chosen to set the phase accumulated. The first wait time N_2 is chosen such that the second set of kicks N_1 will undo the action of the first set of kicks for one of the two phase spaces. At this point, one of the phase spaces is closed, while the other is not. The second wait time N_3 is then chosen so that the second two sets

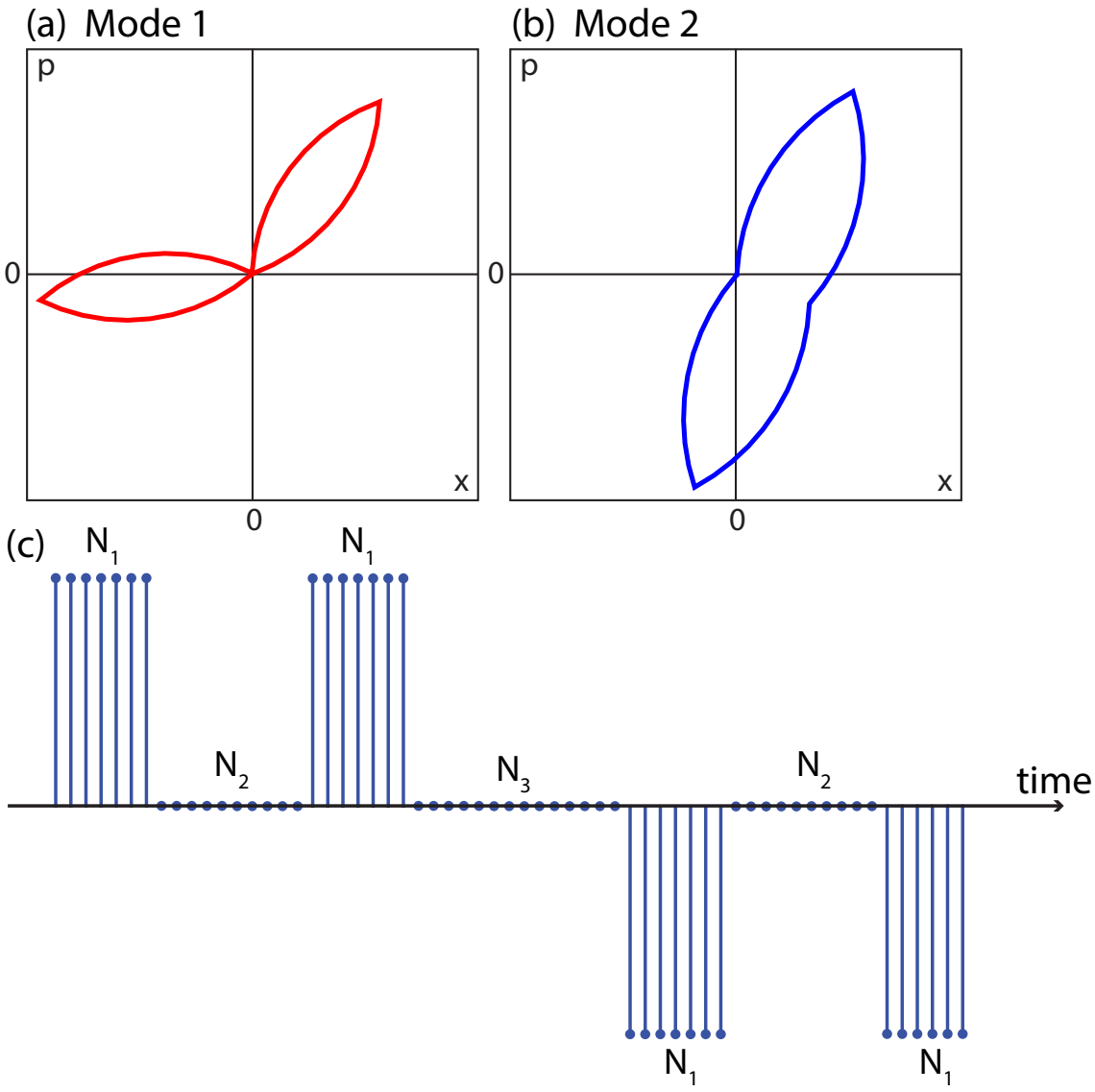

Figure 6.6: General kicking sequence that allows closing both phase spaces. (a) and (b) show the trajectories in each phase space (center of mass and relative motion). Here what is shown is the rotating frame phase space, rather than the lab frame phase space. In the rotating frame, it is the kick direction which rotates, rather than the ion state. The curve segments are composed of N_1 straight lines, with the curve arising due to the free trap evolution between the kicks. (c) General sequence. The number of pulses determines the phase. N_2 is chosen to close the first phase space, while N_3 is chosen to close the second.

of pulses will undo the effect of the first two sets of pulses for the second phase space. As the first phase space has already been closed, it is not affected by this wait. Finally, the second sets of pulses close the second phase space. Because this set of pulses is a mirror image of the first set, the first phase space is again opened and closed.

Because the number of pulses is discretized, the phase difference cannot be made exactly $\pi/2$ by adjusting N_1 only. The ratio of the two mode frequencies must also be adjusted. This is why it is important to execute this gate on transverse motional modes. With axial modes, the mode frequency ratio at $\sqrt{3}$ is fixed and cannot be changed. It is therefore not necessarily possible to achieve a maximally entangling gate using axial modes. For a discussion of performing this gate using axial modes, see [146].

6.6.1.1 Solution For the scheme described above, we can use equation 6.41, 6.42, and 6.43 to solve for N_1, N_2, and N_3. Let $\theta = 2\pi\omega/\omega_{\text{rep}}$, where ω can refer to either ω_C or ω_R. Equation 6.36 reduces to a sum of four geometric series, which can be summed to yield:

$$\left(\frac{1}{1-e^{i\theta}}\right)\left(1-e^{iN_1\theta}\right)\left(1\pm e^{i(N_1+N_2)\theta}\right)\left(1\pm e^{i(2N_1+N_2+N_3)\theta}\right)=0 \tag{6.50}$$

This equation can be satisfied under three possible scenarios:

$$1-e^{iN_1\theta}=0 \quad \text{or} \tag{6.51}$$

$$1\pm e^{i(N_1+N_2)\theta}=0 \quad \text{or} \tag{6.52}$$

$$1\pm e^{i(2N_1+N_2+N_3)\theta}=0 \tag{6.53}$$

These conditions admit a straightforward physical explanation. Equation 6.51, 6.52 and 6.53 correspond to closing the phase space after the first set, second set, and fourth set of pulses, respectively. As mentioned before, equation 6.51 is overly restrictive. Equations 6.52 and 6.53 allow us to use each one to close one of the phase spaces, while still allowing one free parameter to set the phase. For the phase space that closes first, we have:

$$(N_1 + N_2)\,\theta_1 = n\pi \quad n \in \mathbb{Z} \tag{6.54}$$

$$\Rightarrow N_2 = \frac{n\omega_{\text{rep}}}{2\omega_1} - N_1 \tag{6.55}$$

The fastest solution will be the smallest n for which N_2 is positive. Odd n corresponds to the first and second sets of kicks being in the same direction, while even n corresponds to a direction reversal between the first two sets. For the phase space that closes second,

$$(2N_1 + N_2 + N_3)\,\theta_2 = m\pi \quad m \in \mathbb{Z} \tag{6.56}$$

$$\Rightarrow N_3 = \frac{m\omega_{\text{rep}}}{2\omega_2} - 2N_1 - N_2 \tag{6.57}$$

These results show that for this kick pattern, the ratio $\omega_{\text{rep}}/\omega$ must be an integer for both phase spaces. The triple of integers $\{N_1, \omega_{\text{rep}}/\omega_C, \omega_{\text{rep}}/\omega_R\}$ will then determine the accumulated phase, following equation 6.40. All that remains is to search for solutions in which $\Phi = \pi/2$. The results of such a search are shown in table 6.1, for $\omega_{\text{rep}}/2\pi = 80.16$ MHz. The table shows all solutions with this algorithm for which $0.5\,\text{MHz} < \omega_{C,R}/2\pi < 2.5\,\text{MHz}$, $\omega_z < 0.8\,\text{MHz}$, $N_1 \leq 7$ and the phase difference is within 1% of $\pi/2$. All of these solutions include no reversal between the first two sets, and a reversal between the second and third sets, as shown in figure 6.6.

N_1	N_2	N_3	$\omega_z/2\pi$	$\omega_R/2\pi$	$\omega_C/2\pi$	Gate Duration (μs)	Error
6	30	22	0.574	1.113	1.253	1.32	0.009
6	21	29	0.729	1.294	1.484	1.19	0.007
6	26	18	0.693	1.253	1.431	1.17	-0.006
6	29	21	0.600	1.145	1.293	1.29	0.006
6	20	28	0.769	1.336	1.542	1.15	0.003
6	28	20	0.629	1.179	1.336	1.25	0.002
6	27	19	0.660	1.215	1.382	1.21	-0.002
7	22	16	0.683	1.382	1.542	1.10	0.007
7	20	14	0.765	1.484	1.670	1.02	-0.006
7	21	15	0.723	1.431	1.603	1.06	0.001

Table 6.1: Valid solutions to fast gate scheme $\{\{1, N_1\}, \{0, N_2\}, \{1, N_1\}, \{0, N_3\}, \{-1, N_1\}, \{0, N_2\}, \{-1, N_1\}\}$. Here $\omega_{\text{rep}}/2\pi = 80.16$ MHz. This table shows all solutions for which $0.5\,\text{MHz} < \omega_{C,R}/2\pi < 2.5\,\text{MHz}$, $\omega_z < 0.8\,\text{MHz}$, $N_1 \leq 7$, and the phase difference is within 1% of $\pi/2$. Frequencies are in MHz. The time shown is the total time for the entire gate. The error shown is $\Phi/(\pi/2) - 1$. The solutions all include a reversal between the second and third sets of kicks, as in figure 6.6.

Examining table 6.1, the gate durations for all of the solutions is approximately 1 μs. This is because the scheme presented here cannot be much faster than $2\pi/\omega_{C,R}$, as it relies on significant amounts of trap evolution to evolve the kicking direction. Indeed, most of the time is spent waiting. In the first solution in table 6.1, 24 pulses from the laser are used, but the gate duration is equivalent to 106 pulses. Increasing the speed of the gate requires either higher trap frequencies, or a different kick pattern.

6.6.2 Second Solution

The above algorithm can be made faster by introducing another degree of freedom. In between the first and second sets of pulses, another set is introduced in the opposite direction. The net sequence is then: $\{\{1, N_1\}, \{0, N_2\}, \{-1, N_3\}, \{0, N_2\}, \{1, N_1\}, \{0, N_4\}, \{\pm 1, N_1\}, \{0, N_2\}, \{\mp 1, N_3\}, \{0, N_2\}, \{\pm 1, N_1\}\}$. This sequence

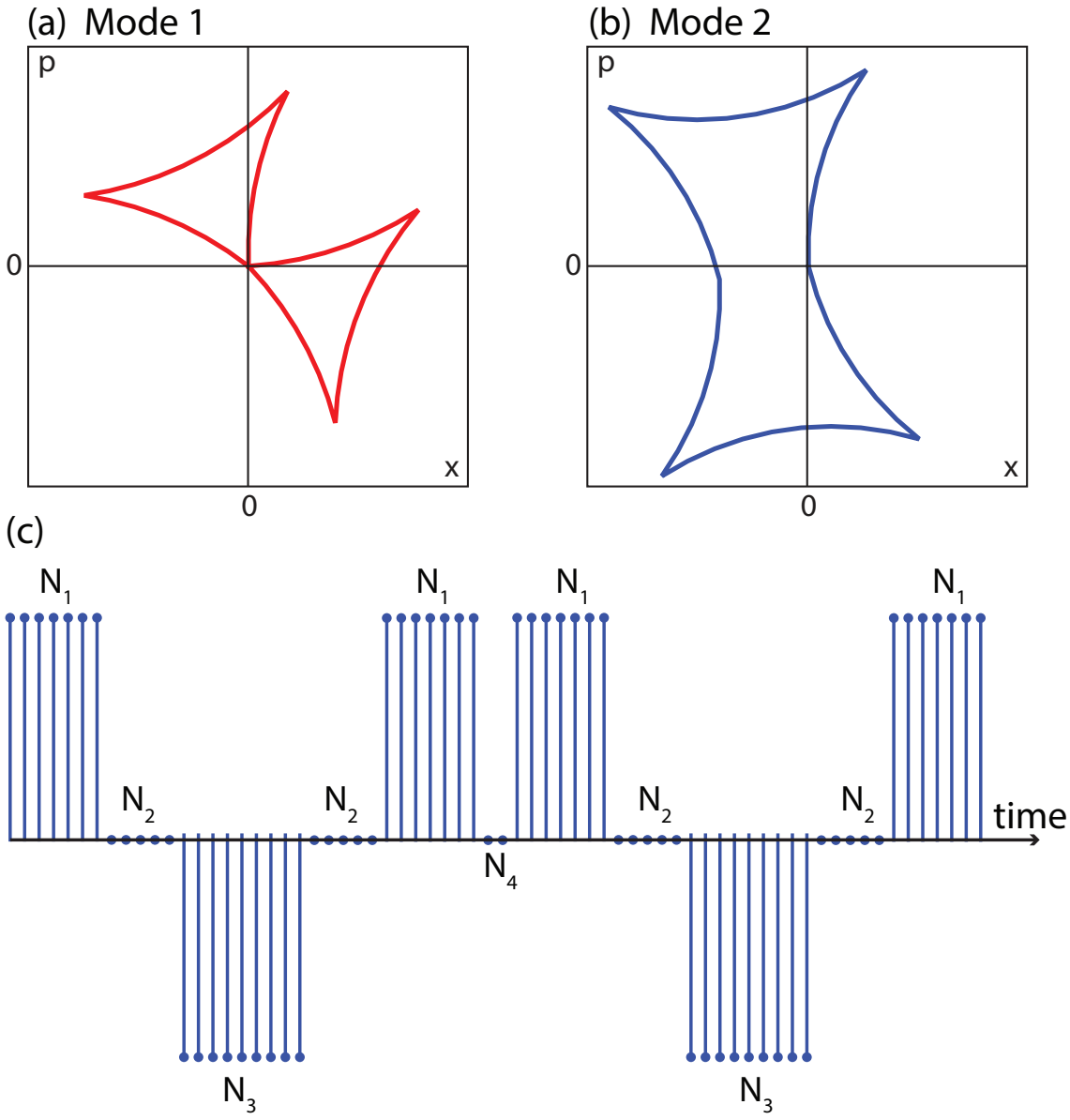

Figure 6.7: Kick sequence for the second fast gate pattern. This introduces a new degree of freedom, which allows for slightly faster gates. (a) and (b) show the trajectories in each phase space (in the rotating frame), which are now each composed of six segments. (c) General sequence.

N_1	N_2	N_3	N_4	$\omega_z/2\pi$	$\omega_R/2\pi$	$\omega_C/2\pi$	Gate Duration (μs)	Error
8	5	5	2	0.661	1.215	1.383	0.80	0.004
8	4	6	4	0.697	1.179	1.370	0.80	0.004
9	2	7	2	0.729	1.293	1.484	0.75	0.011
10	0	9	2	0.711	1.293	1.475	0.75	-0.018
7	4	9	2	0.776	0.934	1.215	0.80	-0.034
7	7	3	1	0.701	1.253	1.435	0.79	-0.035
7	5	5	6	0.793	1.145	1.393	0.80	0.036
9	0	12	1	0.767	1.041	1.293	0.76	-0.043
8	3	7	6	0.723	1.145	1.354	0.80	-0.047

Table 6.2: Valid solutions to fast gate pattern $\{\{1, N_1\}, \{0, N_2\}, \{-1, N_3\}, \{0, N_2\}, \{1, N_1\}, \{0, N_4\}, \{\pm 1, N_1\}, \{0, N_2\}, \{\mp 1, N_3\}, \{0, N_2\}, \{\pm 1, N_1\}\}$. All of the solutions shown here use the upper sign in the sequence described above, i.e. no reversal between the two sets as in figure 6.7. This table shows all solutions for which $0.5\,\text{MHz} < \omega_{C,R}/2\pi < 2.5\,\text{MHz}$, $\omega_z < 0.8\,\text{MHz}$, $\omega_{\text{rep}}/2\pi = 80.16$ MHz, the total gate duration is < 800 ns, and the phase difference is within 5% of $\pi/2$. Frequencies are in MHz. The time shown is the total time for the entire gate. The error shown is $\Phi/(\pi/2) - 1$.

and the corresponding phase space diagrams is shown in figure 6.7. Following a similar analysis to that done above, the conditions on N_1, N_2, N_3 and N_4 for the two phase spaces are:

$$2\cos\left[\frac{(N_1 + 2N_2 + N_3)\theta_1}{2}\right]\sin\left[\frac{N_1\theta_1}{2}\right] = \sin\left[\frac{N_3\theta_1}{2}\right] \tag{6.58}$$

$$(2N_1 + 2N_2 + N_3 + N_4)\,\theta_2 = n\pi \quad n \in \mathbb{Z} \tag{6.59}$$

As before, the first condition closes the first phase space, while the second condition uses N_4 to wait a sufficient amount of time to close the second phase space. Solutions to these equations can be found numerically, and are shown in table 6.2. The extra degree of freedom results in a slightly faster gate time of $750 - 800$ ns. Also note that more pulses are required now. The minimum required in table 6.2 is 34 pulses as opposed to 24 in table 6.1.

6.7 Conclusions and Outlook

The solutions presented here are not necessarily optimized. There may exist faster solutions involving more reversals; these are only the simplest solutions. A larger search may reveal unknown, faster solutions. However, it is unlikely that there exist solutions much faster than a few hundred nanoseconds, as the algorithms are ultimately limited by the repetition rate of the laser. The solutions above show that such a gate is possible, and achievable with the existing experimental apparatus.

Presently, the main obstacle to implementing this gate is the fidelity of a single spin-dependent kick. In order for the gate to work well, a single kick must be high fidelity, as the gate consists of many kicks. At present, it has not yet been determined how gate fidelity scales with individual SDK fidelity. The naive assumption would be that if a single kick has fidelity F, then a gate composed of N kicks would have fidelity F^N. However, this may not be true. The gate fidelity may depend on the exact nature of the errors in the SDK. If we assume that the gate fidelity is no worse than F^N, then in order to pass the 50% fidelity threshold for demonstrating two-ion entanglement, a single SDK will need to have a fidelity of at least $0.5^{1/24} = 97\%$.

There is no doubt that the entangling gate described in this section is experimentally challenging. However, a successful implementation of this gate would be a significant step forward towards the ultimate goal of a large scale trapped ion quantum computer. The gate described above is sensitive to 1) the arrival time of each pulse, and 2) the intensity of each pulse. Both of these can be stabilized to a high degree using conventional feedback loops. Significantly, the gate is highly *in-*

sensitive to the ions' temperature. It is also highly insensitive to small fluctuations in the trap frequency. In a sense, this gate represents a shift in complexity. Slower gates imposed many requirements on the ion, and relatively modest requirements on the laser. This gate imposes many requirements on the laser, but few or none on the ion. Laser stabilization is well understood and in many ways easier than ion stabilization.

It is always advantageous to go fast. It reduces noise, and enables more operations within the coherence time of the qubits. Indeed, the push for speed has driven the revolution in classical computing from its inception. Quantum computers of the future will need to be able to rapidly execute many gates, and techniques such as those presented here may ultimately enable ultrafast operation.

Appendix A

Derivation of Rosen-Zener Solution

Here I will go over the Rosen-Zener analytic solution [120] to the evolution due to equation 4.76. This derivation is largely based on that in [116]. From equations 4.40, 4.41 and 4.70, the coupled differential equations for $\tilde{c}_0$ and $\tilde{c}_1$ are:

$$\dot{\tilde{c}}_0 = \frac{i\theta}{2\tau} \operatorname{sech}\left(\frac{\pi t}{\tau}\right) e^{-i\omega_{\mathrm{hf}} t} \tilde{c}_1 \tag{A.1}$$

$$\dot{\tilde{c}}_1 = \frac{i\theta}{2\tau} \operatorname{sech}\left(\frac{\pi t}{\tau}\right) e^{i\omega_{\mathrm{hf}} t} \tilde{c}_0 \tag{A.2}$$

To solve this, Rosen and Zener made the substitution:

$$z(t) = \frac{1}{2}\left(1 + \tanh\left(\frac{\pi t}{\tau}\right)\right) \tag{A.3}$$

In terms of z, we have:

$$\operatorname{sech}\left(\frac{\pi t}{\tau}\right) = 2\sqrt{z(1-z)} \tag{A.4}$$

$$e^{-i\omega_{\mathrm{hf}} t} = \left(\frac{z}{1-z}\right)^{-i\omega_{\mathrm{hf}}\tau/2\pi} \tag{A.5}$$

$$\dot{\tilde{c}}_i = \frac{d\tilde{c}_i}{dz}\dot{z} \tag{A.6}$$

$$= \frac{\pi}{2\tau} \operatorname{sech}^2\left(\frac{\pi t}{\tau}\right) \frac{d\tilde{c}_i}{dz} \tag{A.7}$$

$$= \frac{2\pi}{\tau} z(1-z) \frac{d\tilde{c}_i}{dz} \tag{A.8}$$

Define:

$$\xi = \frac{1}{2} + i\frac{\omega_{\rm hf}\tau}{2\pi} \tag{A.9}$$

$$\vartheta = \frac{\theta}{2\pi} \tag{A.10}$$

With these substitutions, equations A.1 and A.2 become:

$$\frac{d\tilde{c}_0}{dz} = i\vartheta z^{-\xi}(1-z)^{-\xi^*}\tilde{c}_1 \tag{A.11}$$

$$\frac{d\tilde{c}_1}{dz} = i\vartheta z^{-\xi^*}(1-z)^{-\xi}\tilde{c}_0 \tag{A.12}$$

Decoupling equations A.11 and A.12 yields two second-order differential equations for $\tilde{c}_0$ and $\tilde{c}_1$:

$$z(1-z)\frac{d^2\tilde{c}_0}{dz^2} + (\xi - z)\frac{d\tilde{c}_0}{dz} + \vartheta^2\tilde{c}_0 = 0 \tag{A.13}$$

$$z(1-z)\frac{d^2\tilde{c}_1}{dz^2} + (\xi^* - z)\frac{d\tilde{c}_1}{dz} + \vartheta^2\tilde{c}_1 = 0 \tag{A.14}$$

The solutions to these equations are well-known special functions called *Gaussian hypergeometric functions*, denoted ${}_2F_1(a,b;c;z)$. For a pulse centered at $t=0$, the boundary conditions are that the ion is in $|0\rangle$ at $t=-\infty$: $\tilde{c}_0(-\infty)=1$, $\tilde{c}_1(-\infty)=0$. At $-\infty$, z is given by: $z(-\infty)=0$. Using these conditions, the solutions for $\tilde{c}_0$ and $\tilde{c}_1$ are:

$$\tilde{c}_0 = {}_2F_1\left(\vartheta, -\vartheta; \xi; z\right) \tag{A.15}$$

$$\tilde{c}_1 = -\left(\frac{i\vartheta z^{\xi}}{\xi}\right){}_2F_1\left(\xi+\vartheta, \xi-\vartheta; 1+\xi; z\right) \tag{A.16}$$

We are only interested in the final state at $t=\infty$, and not in the intermediate behavior. At ∞, z is given by $z(\infty)=1$. At $z=1$, ${}_2F_1$ can be written in terms of

the Γ function as [129]:

$$ {}_2F_1(a,b;c;1) = \frac{\Gamma(c)\Gamma(c-a-b)}{\Gamma(c-a)\Gamma(c-b)} \tag{A.17} $$

The final state is therefore given by:

$$ \tilde{c}_0 = \frac{\Gamma(\xi)^2}{\Gamma(\xi-\vartheta)\Gamma(\xi+\vartheta)} \tag{A.18} $$

$$ \tilde{c}_1 = -\left(\frac{i\vartheta}{\xi}\right)\left(\frac{\Gamma(1+\xi)\Gamma(1-\xi)}{\Gamma(1-\vartheta)\Gamma(1+\vartheta)}\right) \tag{A.19} $$

The expression for $\tilde{c}_1$ can be simplified using Euler's reflection formula, which states [129]:

$$ \Gamma(z)\Gamma(1-z) = \frac{\pi}{\sin(\pi z)} \tag{A.20} $$

This relationship allows reduction of both the numerator and denominator of equation A.19 into trigonometric functions:

$$ \tilde{c}_1 = -i\left(\frac{\sin(\pi\vartheta)}{\sin(\pi\xi)}\right) \tag{A.21} $$

$$ = -i\,\mathrm{sech}\left(\frac{\omega_{\mathrm{hf}}\tau}{2}\right)\sin\left(\frac{\theta}{2}\right) \tag{A.22} $$

Equations A.18 and A.22 prove the results stated in equations 4.78 and 4.79.

Appendix B

Derivation of Four Photon Light Shift from Two Combs

The light shift derived in section 4.7.1 was for a single, resonant comb. For two combs with an AOM offset between them, the total four photon shift from the RF comb picture must include all beat notes between both combs. However, because in the lin $\perp$ lin geometry a single comb cannot drive transitions, the beat notes of a single comb with itself do not contribute. Let the resonance condition be $n\omega_{\mathrm{rep}} + \omega_{\mathrm{A}} = \omega_{\mathrm{hf}}$. The net shift is given by:

$$\begin{aligned}
\delta_{\mathrm{L}} &= -\frac{\Omega_0^2}{2}\left(\sum_{\substack{m=-\infty \\ m\neq n}}^{\infty} \frac{\mathrm{sech}^2[(m\omega_{\mathrm{rep}}+\omega_{\mathrm{A}})\tau/2]}{m\omega_{\mathrm{rep}}+\omega_{\mathrm{A}}-\omega_{\mathrm{hf}}} + \sum_{m=-\infty}^{\infty} \frac{\mathrm{sech}^2[(m\omega_{\mathrm{rep}}-\omega_{\mathrm{A}})\tau/2]}{m\omega_{\mathrm{rep}}-\omega_{\mathrm{A}}-\omega_{\mathrm{hf}}}\right) \\
&= -\frac{\Omega_0^2}{2}\left(\sum_{\substack{m=-\infty \\ m\neq n}}^{\infty} \frac{\mathrm{sech}^2[(m\omega_{\mathrm{rep}}+\omega_{\mathrm{A}})\tau/2]}{(m-n)\omega_{\mathrm{rep}}} + \sum_{m=-\infty}^{\infty} \frac{\mathrm{sech}^2[(m\omega_{\mathrm{rep}}-\omega_{\mathrm{A}})\tau/2]}{(m-n)\omega_{\mathrm{rep}}-2\omega_{\mathrm{A}}}\right) \\
&= -\frac{\Omega_0^2}{2\omega_{\mathrm{rep}}}\left(\sum_{\substack{j=-\infty \\ j\neq 0}}^{\infty} \frac{\mathrm{sech}^2[((j+n)\omega_{\mathrm{rep}}+\omega_{\mathrm{A}})\tau/2]}{j} + \right. \\
&\qquad \left. \sum_{j=-\infty}^{\infty} \frac{\mathrm{sech}^2[((j+n)\omega_{\mathrm{rep}}-\omega_{\mathrm{A}})\tau/2]}{j-2\omega_{\mathrm{A}}/\omega_{\mathrm{rep}}}\right)
\end{aligned} \tag{B.1}$$

Experimentally, the AOM shift is typically larger than the repetition rate. For example, for the values given in chapter 5, $\omega_{\mathrm{A}}/2\pi = 503$ MHz, while $\omega_{\mathrm{rep}}/2\pi = 80$ MHz. Define the integer and fractional part of $\omega_{\mathrm{A}}/\omega_{\mathrm{rep}}$ as:

$$\frac{\omega_{\mathrm{A}}}{\omega_{\mathrm{rep}}} = k + \sigma \tag{B.2}$$

where $k \in \mathbb{Z}$ and $0 \leq \sigma < 1$, $\sigma \neq 0.5$. σ represents the fractional distance between the two offset combs. Let $\epsilon = \omega_{\mathrm{rep}}\tau/2$, $\beta = \omega_{\mathrm{hf}}\tau/2$. In terms of these variables, equation B.1 becomes:

$$\delta_L = -\frac{\Omega_0^2}{2\omega_{\mathrm{rep}}}\left(\sum_{\substack{j=-\infty \\ j\neq 0}}^{\infty} \frac{\operatorname{sech}^2[j\epsilon+\beta]}{j} + \sum_{j=-\infty}^{\infty} \frac{\operatorname{sech}^2[(j-2k-2\sigma)\epsilon+\beta]}{j-2\sigma}\right) \tag{B.3}$$

The first term is the same as in equation 4.125. The second term is similar. However, it contains three terms which could be arbitrarily large: $j = -1, 0,$ and 1. These correspond to the three closest RF comb teeth. It is not valid to approximate the sum as an integral for these three points. We therefore extract these points and approximate the remainder as an integral:

$$\begin{aligned}\delta_L = -\frac{\Omega_0^2}{2\omega_{\mathrm{rep}}}\Bigg[&\sum_{\substack{j=-\infty \\ j\neq 0}}^{\infty} \frac{\operatorname{sech}^2[j\epsilon+\beta]}{j} + \sum_{\substack{j=-\infty \\ j\neq -1,0,1}}^{\infty} \frac{\operatorname{sech}^2[(j-2k-2\sigma)\epsilon+\beta]}{j-2\sigma} + \\ &\operatorname{sech}^2(\beta)\left(\frac{1}{-2\sigma}+\frac{1}{-1-2\sigma}+\frac{1}{1-2\sigma}\right)\Bigg]\end{aligned} \tag{B.4}$$

$$\begin{aligned}\approx -\frac{\Omega_0^2}{2\omega_{\mathrm{rep}}}\Bigg[&2\int_{\epsilon}^{\infty} \frac{\operatorname{sech}^2(x+\beta) - \operatorname{sech}^2(x-\beta)}{x}dx + \\ &\operatorname{sech}^2(\beta)\left(\frac{1}{-2\sigma}+\frac{1}{-1-2\sigma}+\frac{1}{1-2\sigma}\right)\Bigg]\end{aligned} \tag{B.5}$$

$$\begin{aligned}\approx -\frac{\Omega_0^2}{2\omega_{\mathrm{rep}}}\Bigg[&-4\omega_{\mathrm{hf}}\tau\int_{0}^{\infty} \frac{\tanh(x)\operatorname{sech}^2(x)}{x}dx + \\ &\operatorname{sech}^2\left(\frac{\omega_{\mathrm{hf}}\tau}{2}\right)\left(\frac{1}{-2\sigma}+\frac{1}{-1-2\sigma}+\frac{1}{1-2\sigma}\right)\Bigg]\end{aligned} \tag{B.6}$$

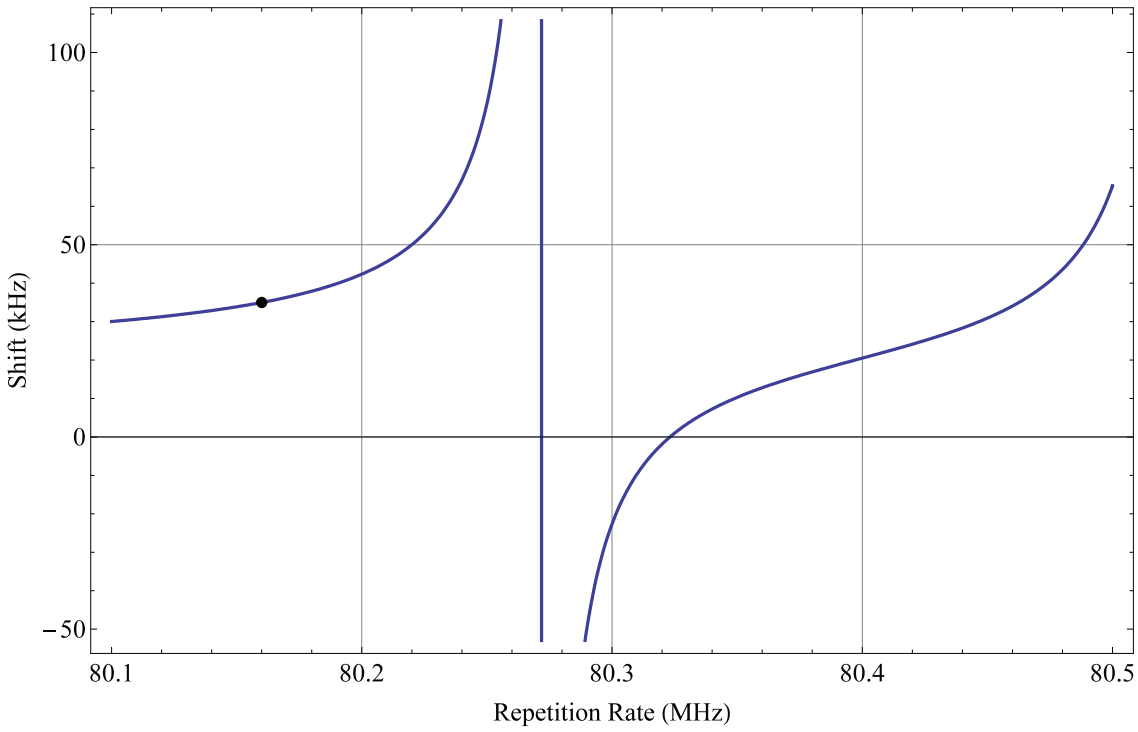

Figure B.1: Four photon light shift for two combs as a function of repetition rate for $\Omega_0/2\pi = 1$ MHz, $\tau = 10$ ps, and $\omega_{\rm hf}/2\pi = 12.6$ GHz.

$$\approx -\frac{\Omega_0^2}{2\omega_{\rm rep}}\left[-4\omega_{\rm hf}\tau\left(\frac{7\zeta(3)}{\pi^2}\right) + \operatorname{sech}^2\left(\frac{\omega_{\rm hf}\tau}{2}\right)\left(\frac{1}{-2\sigma}+\frac{1}{-1-2\sigma}+\frac{1}{1-2\sigma}\right)\right]$$

$$\approx \frac{\Omega_0^2\omega_{\rm hf}\tau}{\omega_{\rm rep}}\left[1.705 + \frac{\operatorname{sech}^2\left(\omega_{\rm hf}\tau/2\right)}{2\omega_{\rm hf}\tau}\left(\frac{1}{2\sigma}+\frac{1}{1+2\sigma}+\frac{1}{-1+2\sigma}\right)\right] \tag{B.7}$$

Equation B.7 is then the two comb four photon light shift, to first order in $\omega_{\rm hf}\tau$. This expression passes through zero for certain values of σ. For $\tau = 0$, the zero shift point is given by:

$$\frac{1}{2\sigma}+\frac{1}{1+2\sigma}+\frac{1}{-1+2\sigma} = 0 \tag{B.8}$$

$$\Rightarrow \sigma = \frac{1}{\sqrt{12}} \approx 0.289 \tag{B.9}$$

For a 10 ps pulse, zero shift occurs for $\sigma = 0.399$.

Figure B.1 shows the shift in kHz predicted by equation B.7 for $\Omega_0/2\pi = 1$ MHz and $\tau = 10$ ps, around 80 MHz repetition rates. The curve passes through

zero at 80.323 MHz, which corresponds to $\sigma = 0.399$.

Appendix C

Diffraction with Hyperbolic Secant Pulse

In chapter 5, equation 5.32 was derived by approximating the pulse as a δ-function. This section examines the validity of that approximation. The pulse duration is of order 10 ps, meaning it is several orders of magnitude faster than the trap frequency or the AOM frequency. Therefore, the trap and AOMs can be taken as frozen during the pulse, and the Rosen-Zener solution in chapter 4 can be used, with $\theta \to \theta \cos\left(\Delta k\hat{x} + \Delta\phi\right)$ in equations 4.78 and 4.79:

$$A = \frac{\Gamma^2\left(\xi\right)}{\Gamma\left(\xi - \frac{\theta}{2\pi}\cos\left(\Delta k\hat{x} + \Delta\phi\right)\right)\Gamma\left(\xi + \frac{\theta}{2\pi}\cos\left(\Delta k\hat{x} + \Delta\phi\right)\right)} \tag{C.1}$$

$$B = -\sin\left(\frac{\theta}{2}\cos\left(\Delta k\hat{x} + \Delta\phi\right)\right)\,\mathrm{sech}\left(\frac{\omega_{\mathrm{hf}}\tau}{2}\right) \tag{C.2}$$

The $\hat{\sigma}_x$ term in part of equation 4.77 is given by iB, which can be expanded using the Jacobi-Anger expansion as:

$$iB = \mathrm{sech}\left(\frac{\omega_{\mathrm{hf}}\tau}{2}\right)\sum_{\substack{n=-\infty \\ n\,\mathrm{odd}}}^{\infty} i^n e^{in\Delta\phi} J_n(\theta) D\left[in\eta\right] \tag{C.3}$$

This is nearly identical to the $\hat{\sigma}_x$ term in equation 5.32, but with an overall $\mathrm{sech}(\omega_{\mathrm{hf}}\tau/2)$ term modifying the populations. This is the same result found in [132]. The even order diffraction terms are considerably more complicated. However, they are of order

θ^2 or higher, which were assumed to be negligible for the results derived in chapter 5. Non-zero pulse duration can thus be accounted for by replacing $\theta \to \theta \text{ sech}\,(\omega_{\text{hf}}\tau/2)$. This will correspond to a slight reduction in the effective pulse area as compared to a δ-function pulse.

Appendix D

Equivalence of Phase Gate to Entangling Gate

Here I show that the state produced by the gate discussed above is maximally entangled. Assume the ions are initialized by a global $\pi/2$ rotation to the state:

$$|\psi_i\rangle = \frac{1}{2}\left(|00\rangle + |01\rangle + |10\rangle + |11\rangle\right) \tag{D.1}$$

After the $\pi/4$ phase gate discussed in chapter 6, the two ions state becomes:

$$|\psi_f\rangle = \frac{1}{2}\left(e^{i\gamma} i\,|00\rangle + |01\rangle + |10\rangle + i e^{-i\gamma}\,|11\rangle\right) \tag{D.2}$$

Define the following basis [147, 148]:

$$|e_1\rangle = \frac{1}{\sqrt{2}}\left(|11\rangle + |00\rangle\right) \tag{D.3}$$

$$|e_2\rangle = \frac{1}{\sqrt{2}} i\left(|11\rangle - |00\rangle\right) \tag{D.4}$$

$$|e_3\rangle = \frac{1}{\sqrt{2}} i\left(|10\rangle + |01\rangle\right) \tag{D.5}$$

$$|e_4\rangle = \frac{1}{\sqrt{2}}\left(|10\rangle - |01\rangle\right) \tag{D.6}$$

Note that this is the Bell basis $\{\Psi^{\pm}, \Phi^{\pm}\}$ with a phase of i on Φ^{-} and Ψ^{+} [148]. In terms of this basis, equations D.1 and D.2 can be written as:

$$|\psi_i\rangle = \frac{1}{\sqrt{2}}\big(\,|e_1\rangle - i\,|e_3\rangle\,\big) \tag{D.7}$$

$$|\psi_f\rangle = \frac{1}{\sqrt{2}}\big(i\cos(\gamma)\,|e_1\rangle - i\sin(\gamma)\,|e_2\rangle - i\,|e_3\rangle\,\big) \tag{D.8}$$

In [147, 148] it is shown how to quantify the amount of entanglement in terms of the coefficients in the basis $|e_i\rangle$. Here I'll follow their procedure. For a state $|\psi\rangle = \sum_i \alpha_i\,|e_i\rangle$, define the following function:

$$C(\psi) = \left|\sum_i \alpha_i^2\right| \tag{D.9}$$

where it is the complex value of α_i which is squared, not its norm. This function is known as the *concurrence* of $|\psi\rangle$. Using this function, we have:

$$C(\psi_i) = 0 \tag{D.10}$$

$$C(\psi_f) = -1 \tag{D.11}$$

Now define the following functions:

$$f(x) = \frac{1}{2}\left(1 + \sqrt{1 - x^2}\right) \tag{D.12}$$

$$H(x) = -\left[x\log_2(x) + (1-x)\log_2(1-x)\right] \tag{D.13}$$

The entanglement of a state $|\psi\rangle$ is then given by:

$$E(\psi) = H(f(C(\psi))) \tag{D.14}$$

$E = 0$ means that $|\psi\rangle$ has no entanglement (can be written as a product state), while $E = 1$ means that $|\psi\rangle$ is maximally entangled. Applying equation D.14 to

$|\psi_i\rangle$ and $|\psi_f\rangle$, we find:

$$E(\psi_i) = 0 \tag{D.15}$$

$$E(\psi_f) = 1 \tag{D.16}$$

This shows that the gate operation takes a product state and produces a maximally entangled state.

Appendix E

Mathematica Simulation

Here included, for reference, is the code I wrote to simulate the creation of a spin-dependent kick from a sequence of eight fast pulses.

This program uses the following terminology: A ket is an ordered triple of the form $\{c, s, \alpha\}$. It corresponds to the ket with spin state $s = |0\rangle$ or $|1\rangle$, coherent state $|\alpha\rangle$, and coefficient c. A state is an unordered list of kets in the form $\{\{c_1, s_1, \alpha_1\}$, $\{\{c_2, s_2, \alpha_2\}, \ldots\}$. It corresponds to a superposition of kets.

When a pulse arrives, each ket is diffracted into several diffraction orders. The function `UPulseState` computes the new state. It does the following: 1) Make a table of amplitudes, spin states, and motional states. Each term has a Bessel function coefficient, together with a phase, which consists of a geometric component and an arrival time component. The spin is conditionally flipped, with every odd diffraction order getting a spin flip. There is also a free evolution component. 2) Turn this table into a sequence, so that the new set of kets resulting from each ket will be merged into a single state. 3) Apply this sequence to each ket in the target state. 4) Combine kets which have coefficient sufficiently close to zero. The final

```
(*Defaults to use*)
ZeroThreshold = 10^-10; (*What to consider zero*)
fAOM = 503.424; (*AOM difference frequency, in MHz*)
η = 20;
(*Lamb-Dicke parameter -- making this much larger than the wavepacket size allows
  better measure of operator fidelity*)
nmax = 4; (*How many diffraction orders to keep track of. Sum goes from -nmax to nmax*)
fhf = 12 642.815; (*Hyperfine frequency, in MHz*)
ftrap = 0; (*Trap frequency, in MHz*)
```

Figure E.1: Constant declarations

result is the resultant state after a pulse arrives. The arguments are the initial state, the pulse arrival time, and the pulse area. The zero threshold, AOM frequency, AOM phase, Lamb-Dicke parameter and number of diffraction orders to use can also be optionally set.

The function `UNPulses` executes `UPulseState` for a list of pulses. For each pulse, the arrival time, area, and phase are specified.

The function `OverlapState` computes the overlap between two arbitrary states.

Finally, shown is the code that uses these functions to compute the kick fidelity for kicking the ground state for the two specific sets of delay lengths mentioned in chapter 5.

```
In[8]:= UPulseAndFreeState[ArrivalTime_, PulseArea_, PulsePhase_, FreeEvolutionTime_][
          state : {{_, _, _} ..}] :=
         DeleteCases[{Total[Transpose[#][[1]]](*sum coefficients*), #[[1, 2]], #[[1, 3]]} & /@
             GatherBy[#, {#1[[2]], #1[[3]]} &](*Rewrite {{c1,s,α},{c2,s,α}} as {{c1+c2,s,α}}*),
           ket : {_, _, _} /; Abs[ket[[1]]] ≤ ZeroThreshold] &(*Delete Cases which have coefficient zero,
          or sufficiently close to it*)[
          Sequence @@
            Table[{Exp[i (If[OddQ[n], -1 + 2 #1[[2]], 1 - 2 #1[[2]]] 2 π fhf - 2 π ftrap) FreeEvolutionTime / 2]
                BesselJ[n, PulseArea] Exp[i (2 π fAOM ArrivalTime + PulsePhase + π/2 + η Re[#1[[3]]]) n] #1[[1]],
               If[OddQ[n], 1 - #1[[2]], #1[[2]]], (#1[[3]] + i n η) e^(-i 2 π ftrap FreeEvolutionTime)},
              {n, -nmax, nmax}] & /@ state(*Apply pulse function to each ket in the state*)
         ];

       (*Pulse list is of the form {{first pulse arrive time, first pulse area, first pulse phase},...*)
       UNPulses[initstate : {{_, _, _} ..}, pulselist : {{_, _, _} ..}] :=
        Composition[
          Sequence @@
           Table[If[i ≠ Length[pulselist], UPulseAndFreeState[pulselist[[i, 1]], pulselist[[i, 2]],
              pulselist[[i, 3]], pulselist[[i + 1, 1]] - pulselist[[i, 1]]],
             UPulseAndFreeState[pulselist[[i, 1]], pulselist[[i, 2]], pulselist[[i, 3]], 0]],
            {i, Length[pulselist], 1, -1}]][initstate]
```

```
In[10]:= (*OverlapState calculates the braket of two states.  The first argument is the bra.*)
         OverlapState[state1 : {{_, _, _} ..}, state2 : {{_, _, _} ..}] :=
          OverlapState[state1, state2] =
           Sum[KroneckerDelta[state1[[i, 2]], state2[[j, 2]]] * Conjugate[state1[[i, 1]]] *
             state2[[j, 1]] *
             Exp[-1/2 Abs[state1[[i, 3]]]^2 - 1/2 Abs[state2[[j, 3]]]^2 + Conjugate[state1[[i, 3]]] * state2[[j, 3]]],
            {i, 1, Length[state1]}, {j, 1, Length[state2]}]
         OverlapState[{}, state2_] := 0;
         OverlapState[state1_, {}] := 0;
```

```
In[13]:= pulselist[t1_, t2_, t3_, θ_] :=
```

0	θ 0
t1	θ π
t2	θ 0
t1 + t2	θ π
t3	θ 0
t3 + t1	θ π
t3 + t2	θ 0
t1 + t2 + t3	θ π

```
In[14]:= initstate = {{1, 0, 0}};
         targetstate = {{1, 1, i η}};
         t[n_] := n/(fhf + fAOM);
         res[n1_, n2_, n3_, θ_] :=
           Abs[OverlapState[UNPulses[initstate, pulselist[t[n1], t[n2], t[n3], θ]], targetstate]]^2;

In[18]:= (*Result for delays used*)
         res[5.5, 10, 20, π / 8]
Out[18]= 0.989481

In[19]:= (*Highest fidelity found*)
         res[6.5, 9, 16, π / 8]
Out[19]= 0.998459
```

Figure E.2: Code for Mathematica simulations. Resulting overlap with the target state is shown for the delay sets $\{5.5, 10, 20\}$ and $\{6.5, 9, 16\}$.

Bibliography

[1] M. A. Nielsen and I. L. Chuang. *Quantum Computation and Quantum Information*. Cambridge University Press, 2000.

[2] A. Einstein, B. Podolsky, and N. Rosen. Can quantum-mechanical description of physical reality be considered complete? *Phys. Rev.*, 47:777–780, May 1935.

[3] J. S. Bell. On the Einstein Podolsky Rosen paradox. *Physics*, 1 (3):195–200, 1964.

[4] Stuart J. Freedman and John F. Clauser. Experimental test of local hidden-variable theories. *Phys. Rev. Lett.*, 28:938–941, Apr 1972.

[5] Y. Hasegawa, R. Loidl, G. Badurek, M. Baron, and H. Rauch. Violation of a Bell-like inequality in single-neutron interferometry. *Nature*, 425:45, Sept. 2003.

[6] D. L. Moehring, M. J. Madsen, B. B. Blinov, and C. Monroe. Experimental Bell inequality violation with an atom and a photon. *Phys. Rev. Lett.*, 93:090410, Aug 2004.

[7] D. N. Matsukevich, T. Chanelière, S. D. Jenkins, S.-Y. Lan, T. A. B. Kennedy, and A. Kuzmich. Entanglement of remote atomic qubits. *Phys. Rev. Lett.*, 96:030405, Jan 2006.

[8] D. N. Matsukevich, P. Maunz, D. L. Moehring, S. Olmschenk, and C. Monroe. Bell inequality violation with two remote atomic qubits. *Phys. Rev. Lett.*, 100:150404, Apr 2008.

[9] D. P. Divincenzo. The physical implementation of quantum computation. *ArXiv*, 0002077, 2008.

[10] T. D. Ladd, F. Jelezko, R. Laflamme, Y. Nakamura, C. Monroe, and J. L. O'Brien. Quantum computers. *Nature*, 464:45–53, 2010.

[11] Rainer Blatt and David Wineland. Entangled states of trapped atomic ions. *Nature*, 453:1008, 2008.

[12] H. Häffner, C. F. Roos, and R. Blatt. Quantum computing with trapped ions. *Phys. Rep.*, 469:155–203, 2008.

[13] C. Monroe and J. Kim. Scaling the ion trap quantum processor. *Science*, 339:1164, 2013.

[14] P. S. Jessen, I. H. Deutsch, and R. Stock. Quantum information processing with trapped neutral atoms. *Quant. Inf. Proc.*, 3:91, Oct. 2004.

[15] M. Anderlini, P. J. Lee, B. L. Brown, J. Sebby-Strabley, W. D. Phillips, and J. V. Porto. Controlled exchange interaction between pairs of neutral atoms in an optical lattice. *Nature*, 446:453, July 2007.

[16] J. C. F. Matthew, A. Politi, A. Stefanov, and J. L. O'Brien. Manipulation of multiphoton entanglement in waveguide quantum circuits. *Nat. Phot.*, 3:346–350, 2009.

[17] D. Press, T. D. Ladd, B. Y. Zhang, and Y. Yamamoto. Complete quantum control of a single quantum dot spin using ultrafast optical pulses. *Nature*, 456:218–221, Nov. 2008.

[18] Daniel Loss and David P. DiVincenzo. Quantum computation with quantum dots. *Phys. Rev. A*, 57:120–126, Jan 1998.

[19] J. Clarke and F. K. Wilhelm. Superconducting quantum bits. *Nature*, 453:1031–1042, June 2008.

[20] M. H. Devoret and R. J. Schoelkopf. Superconducting circuits for quantum information: An outlook. *Science*, 339:1169, 2013.

[21] M. V. Gurudev Dutt, L. Childress, L. Jiang, E. Togan, J. Maze, F. Jelezko, A. S. Zibrov, P. R. Hemmer, and M. D. Lukin. Quantum register based on individual electronic and nuclear spin qubits in diamond. *Science*, 316:1312, 2007.

[22] C. Monroe, D. M. Meekhof, B. E. King, W. M. Itano, and D. J. Wineland. Demonstration of a fundamental quantum logic gate. *Phys. Rev. Lett.*, 75:4714–4717, Dec 1995.

[23] J. Benhelm, G. Kirchmair, C. F. Roos, and R. Blatt. Towards fault-tolerant quantum computing with trapped ions. *Nature Physics*, 4:463–466, 2008.

[24] C. A. Sackett, D. Kielpinski, B. E. King, C. Langer, V. Meyer, C. J. Myatt, M. Rowe, Q. A. Turchette, W. M. Itano, D. J. Wineland, and C. Monroe. Experimental entanglement of four particles. *Nature*, 404:256, 2000.

[25] H. Häffner, W. Hansel, C. F. Roos, J. Benhelm, D. Chek al kar, M. Chwalla, T. Korber, U. D. Rapol, M. Riebe, P. O. Schmidt, C. Becher, O. Guhne, W. Dur, and R. Blatt. Scalable multiparticle entanglement of trapped ions. *Nature*, 438:643–646, 2005.

[26] P. C. Haljan, P. J. Lee, K-A. Brickman, M. Acton, L. Deslauriers, and C. Monroe. Entanglement of trapped ion clock states. *Phys. Rev. A*, 72:062316, 2005.

[27] Thomas Monz, Philipp Schindler, Julio T. Barreiro, Michael Chwalla, Daniel Nigg, William A. Coish, Maximilian Harlander, Wolfgang Hänsel, Markus Hennrich, and Rainer Blatt. 14-qubit entanglement: Creation and coherence. *Phys. Rev. Lett.*, 106:130506, Mar 2011.

[28] R. Islam, E. E. Edwards, K. Kim, S. Korenblit, C. Noh, H. Carmichael, G.-D. Lin, L.-M. Duan, C.-C. Joseph Wang, J. K. Freericks, and C. Monroe. Onset of a quantum phase transition with a trapped ion quantum simulator. *Nature Communications*, 2:377, 2011.

[29] J. T. Barreiro, M. Muller, P. Schindler, D. Nigg, T. Monz, M. Chwalla, M. Hennrich, C. F. Roos, P. Zoller, and R. Blatt. An open-system quantum simulator with trapped ions. *Nature*, 470:486, 2011.

[30] A. Friedenauer, H. Schmitz, J. T. Glueckert, D. Porras, and T. Schaetz. Simulating a quantum magnet with trapped ions. *Nature Physics*, 4:747–761, 2008.

[31] S. Gulde, M. Riebe, G. P. T. Lancaster, C. Becher, J. Eschner, H. Haffner, F. Schmidt-Kaler, I. L. Chuang, and R. Blatt. Implementation of the Deutsch-Josza algorithm on an ion-trap quantum computer. *Nature*, 421:48, 2003.

[32] K.-A. Brickman, P. C. Haljan, P. J. Lee, M. Acton, L. Deslauriers, and C. Monroe. Implementation of Grover's search algorithm in a scalable system. *Phys. Rev. A*, 72:050306, 2005.

[33] P. Schindler, J. T. Barreiro, T. Monz, V. Nebendahl, D. Nigg, M. Chwalla, M. Hennrich, and R. Blatt. Experimental repetitive quantum error correction. *Science*, 332:1059–1061, 2011.

[34] H. Weimer. http://www.quantenblog.net/physics/moores-law-quantum-computer, Sept. 2011.

[35] Q. A. Turchette, C. S. Wood, B. E. King, C. J. Myatt, D. Leibfried, W. M. Itano, C. Monroe, and D. J. Wineland. Deterministic entanglement of two trapped ions. *Phys. Rev. Lett.*, 81:3631–3634, Oct 1998.

[36] K. D. Raedt, K. Michielsen, H.D. Raedt, B. Trieu, G. Arnold, M. Richter, T. Lippert, H. Watanabe, and N. Ito. Massive parallel quantum computer simulator. *Comp. Phys. Comm.*, 176:121–136, 2007.

[37] Anders Sørensen and Klaus Mølmer. Quantum computation with ions in thermal motion. *Phys. Rev. Lett.*, 82:1971–1974, Mar 1999.

[38] A. Sørensen and K. Mølmer. Entanglement and quantum computation with ions in thermal motion. *Phys. Rev. A*, 62:022311, 2000.

[39] K. Mølmer and A. Sørensen. Multiparticle entanglement of hot trapped ions. *Phys. Rev. Lett.*, 82:1835, 1999.

[40] J. I. Cirac and P. Zoller. Quantum computations with cold trapped ions. *Phys. Rev. Lett.*, 74:4091–4094, May 1995.

[41] D. A. Hite, Y. Colombe, A. C. Wilson, K. R. Brown, U. Warring, R. Jördens, J. D. Jost, K. S. McKay, D. P. Pappas, D. Leibfried, and D. J. Wineland. 100-fold reduction of electric-field noise in an ion trap cleaned with *In Situ* argon-ion-beam bombardment. *Phys. Rev. Lett.*, 109:103001, Sep 2012.

[42] Jaroslaw Labaziewicz, Yufei Ge, Paul Antohi, David Leibrandt, Kenneth R. Brown, and Isaac L. Chuang. Suppression of heating rates in cryogenic surface-electrode ion traps. *Phys. Rev. Lett.*, 100:013001, Jan 2008.

[43] R. B Blakestad, C. Ospelkaus, A. P VanDevender, J. H Wesenberg, M. J Biercuk, D. Leibfried, and D. J Wineland. Near-ground-state transport of trapped-ion qubits through a multidimensional array. *Phys. Rev. A*, 84:032314, Sep 2011.

[44] J. Chiaverini, R. B. Blakestad, J. Britton, J. D. Jost, C. Langer, D. Leibfried, R. Ozeri, and D. J. Wineland. Surface-electrode architecture for ion-trap quantum information processing. *Quant. Inf. and Comp.*, 5:419–439, 2005.

[45] C. Ospelkaus, U. Warring, Y. Colombe, K. R. Brown, J. M. Amini, D. Leibfried, and D. J. Wineland. Microwave quantum logic gates for trapped ions. *Nature*, 476:181–184, 2011.

[46] J. J. Garcia-Ripoll, P. Zoller, and J. I Cirac. Speed optimized two-qubit gates with laser coherent control techniques for ion trap quantum computing. *Phys. Rev. Lett.*, 91(15):157901, 2003.

[47] Lu-Ming Duan. Scaling ion trap quantum computation through fast quantum gates. *Phys. Rev. Lett.*, 93(10):100502, 2004.

[48] Th. Udem, R. Holzwarth, and T. W. Hansch. Optical frequency metrology. *Nature*, 416:233, 2002.

[49] S.T. Cundiff and J. Ye. Colloquium: Femtosecond optical frequency combs. *Rev. Mod. Phys.*, 75:325, 2003.

[50] J. L. Hall. Nobel lecture: Defining and measuring optical frequencies. *Rev. Mod. Phys.*, 78:1279, 2006.

[51] T.W. Hansch. Nobel lecture: Passion for precision. *Rev. Mod. Phys.*, 78:1297, 2006.

[52] M. C. Stowe, A. Pe'er, and J. Ye. Control of four-level quantum coherence via discrete spectral shaping of an optical frequency comb. *Phys. Rev. Lett.*, 100:203001, 2008.

[53] M. Viteau, A. Chotia, M. Allegrini, N. Bouloufa, O. Dulieu, D. Comparat, and P. Pillet. Optical pumping and vibrational cooling of molecules. *Science*, 321:232–234, 2008.

[54] D. Press, K. De Greve, P. L. McMahon, T. D. Ladd, B. Friess, C. Schneider, M. Kamp, S. Höfling, A. Forchel, and Y. Yamamoto. Ultrafast optical spin echo in a single quantum dot. *Nature Photonics*, 4:367–370, 2010.

[55] A. Greilich, D. R. Yakovlev, A. Shabaev, Al. L. Efros, I. A. Yugova, R. Oulton, V. Stavarache, D. Reuter, A. Wieck, and M. Bayer. Mode locking of electron spin coherences in singly charged quantum dots. *Science*, 313:341–345, 2006.

[56] D. Hayes, D. N. Matsukevich, P. Maunz, D. Hucul, Q. Quraishi, S. Olmschenk, W. C. Campbell, J. Mizrahi, C. Senko, and C. Monroe. Entanglement of atomic qubits using an optical frequency comb. *Phys. Rev. Lett.*, 104:140501, 2010.

[57] W. C. Campbell, J. Mizrahi, Q. Quraishi, C. Senko, D. Hayes, D. Hucul, D. N. Matsukevich, P. Maunz, and C. Monroe. Ultrafast gates for single atomic qubits. *Phys. Rev. Lett.*, 105:090502, 2010.

[58] J. Mizrahi, C. Senko, B. Neyenhuis, K. G. Johnson, W. C. Campbell, C. W. S. Conover, and C. Monroe. Ultrafast spin-motion entanglement and interferometry with a single atom. *Phys. Rev. Lett.*, 110:203001, May 2013.

[59] J. Mizrahi, B. Neyenhuis, K. Johnson, W. C. Campbell, C. Senko, D. Hayes, and C. Monroe. Quantum control of qubits and atomic motion using ultrafast laser pulses. *arXiv*, 1307.0557, 2013.

[60] C. W. Chou, D. B. Hume, J. C. J. Koelemeij, D. J. Wineland, and T. Rosenband. Frequency comparison of two high-accuracy Al^+ optical clocks. *Phys. Rev. Lett.*, 104:070802, Feb 2010.

[61] S. A. Diddams, Th. Udem, J. C. Bergquist, E. A. Curtis, R. E. Drullinger, L. Hollberg, W. M. Itano, W. D. Lee, C. W. Oates, K. R. Vogel, and D. J. Wineland. An optical clock based on a single trapped $^{199}Hg^+$ ion. *Science*, 293:825, 2001.

[62] Y.-Y. Jau, H. Partner, P. D. D. Schwindt, J. D. Prestage, J. R. Kellogg, and N. Yu. Low-power, miniature ^{171}Yb ion clock using an ultra-small vacuum package. *Appl. Phys. Lett.*, 101:253518, 2012.

[63] K. Hosaka, S. A. Webster, A. Stannard, B. R. Walton, H. S. Margolis, and P. Gill. Frequency measurement of the $^2S_{1/2}$-$^2F_{7/2}$ electric octupole transition in a single $^{171}Yb^+$ ion. *Phys. Rev. A*, 79:033403, Mar 2009.

[64] V. Batteiger, S. Knünz, M. Herrmann, G. Saathoff, H. A. Schüssler, B. Bernhardt, T. Wilken, R. Holzwarth, T. W. Hänsch, and Th. Udem. Precision spectroscopy of the $3s$-$3p$ fine-structure doublet in Mg^+. *Phys. Rev. A*, 80:022503, Aug 2009.

[65] M. Herrmann, V. Batteiger, S. Knünz, G. Saathoff, Th. Udem, and T. W. Hänsch. Frequency metrology on single trapped ions in the weak binding limit: The $3s_{1/2} - 3p_{3/2}$ transition in $^{24}Mg^+$. *Phys. Rev. Lett.*, 102:013006, Jan 2009.

[66] O. A. Herrera-Sancho, N. Nemitz, M. V. Okhapkin, and E. Peik. Energy levels of Th^+ between 7.3 and 8.3 eV. *Phys. Rev. A*, 88:012512, Jul 2013.

[67] P.T.H. Fisk, M. J. Sellars, M. A. Lawn, and C. Coles. Accurate measurement of the 12.6 GHz "clock" transition in trapped $^{171}Yb^+$ ions. *IEEE Trans. Ultrason. Ferroelectr. Freq. Control*, 44:344–354, 1997.

[68] T. M. Fortier, N. Ashby, J. C. Bergquist, M. J. Delaney, S. A. Diddams, T. P. Heavner, L. Hollberg, W. M. Itano, S. R. Jefferts, K. Kim, F. Levi, L. Lorini, W. H. Oskay, T. E. Parker, J. Shirley, and J. E. Stalnaker. Precision atomic spectroscopy for improved limits on variation of the fine structure constant and local position invariance. *Phys. Rev. Lett.*, 98:070801, Feb 2007.

[69] C. W. Chou, D. B. Hume, T. Rosenband, and D. J. Wineland. Optical clocks and relativity. *Science*, 329:1630–1633, Sept. 2010.

[70] E. Peik, B. Lipphardt, H. Schnatz, T. Schneider, Chr. Tamm, and S. G. Karshenboim. Limit on the present temporal variation of the fine structure constant. *Phys. Rev. Lett.*, 93:170801, Oct 2004.

[71] D. J. Wineland, R. E. Drullinger, and F. L. Walls. Radiation-pressure cooling of bound resonant absorbers. *Phys. Rev. Lett.*, 40:1639–1642, Jun 1978.

[72] W. Neuhauser, M. Hohenstatt, P. Toschek, and H. Dehmelt. Optical-sideband cooling of visible atom cloud confined in parabolic well. *Phys. Rev. Lett.*, 41:233–236, Jul 1978.

[73] H. G. Dehmelt. Radiofrequency spectroscopy of stored ions I: Storage. *Adv. At. Mol. Phys*, 3:53, 1967.

[74] Wolfgang Paul. Electromagnetic traps for charged and neutral particles. *Rev. Mod. Phys.*, 62:531–540, Jul 1990.

[75] J. D. Jackson. *Classical Electrodynamics: Third Edition*. Wiley, 1998.

[76] F. G. Major and H. G. Dehmelt. Exchange-collision technique for the rf spectroscopy of stored ions. *Phys. Rev.*, 170:91–107, Jun 1968.

[77] D. J. Wineland, C. Monroe, W. M. Itano, D. Leibfried, B. E. King, and D. M. Meekhof. Experimental issues in coherent quantum-state manipulation of trapped atomic ions. *Journal of Research of the National Institute of Standards and Technology*, 103(3):259–328, May-June 1998.

[78] D. J. Berkeland, J. D. Miller, J. C. Bergquist, W. M. Itano, and D. J. Wineland. Minimization of ion micromotion in a paul trap. *J. Appl. Phys.*, 83 (10), May 1998.

[79] Wayne M. Itano and D. J. Wineland. Laser cooling of ions stored in harmonic and penning traps. *Phys. Rev. A*, 25:35–54, Jan 1982.

[80] D. J. Griffiths. *Introduction to Quantum Mechanics (2nd Edition)*. Pearson Prentice Hall, 2004.

[81] Shi-Liang Zhu, C. Monroe, and L.-M. Duan. Trapped ion quantum computation with transverse phonon modes. *Phys. Rev. Lett.*, 97:050505, Aug 2006.

[82] Q. A. Turchette, Kielpinski, B. E. King, D. Leibfried, D. M. Meekhof, C. J. Myatt, M. A. Rowe, C. A. Sackett, C. S. Wood, W. M. Itano, C. Monroe, and D. J. Wineland. Heating of trapped ions from the quantum ground state. *Phys. Rev. A*, 61:063418, May 2000.

[83] S. Olmschenk. Quantum teleportation between distant matter qubits. *Ph.D. Thesis, University of Michigan, Ann Arbor*, 2009.

[84] Kazuhiko Sugiyama and Jun Yoda. Production of YbH^+ by chemical reaction of Yb^+ in excited states with H_2 gas. *Phys. Rev. A*, 55:R10–R13, Jan 1997.

[85] K. Odaka and S. Ueda. Dependence of outgassing rate on surface oxide layer thickness in type 304 stainless steel before and after surface oxidation in air. *Vacuum*, 47:689–692, 1996.

[86] M. J. Madsen, W.K. Hensinger, D. Stick, J.A. Rabchuk, and C. Monroe. Planar ion trap geometry for microfabrication. *Appl. Phys. B*, 78:639, 2004.

[87] W. W. Macalpine and R. O. Schildknecht. Coaxial resonators with helical innner conductor. *Proc. IRE*, page 2099, 1959.

[88] A. I. Zverev and H. J. Blinchikoff. Realization of a filter with helical components. *IRE Transactions on Component Parts*, page 99, 1961.

[89] S. Olmschenk, K. C. Younge, D. L. Moehring, D. N. Matsukevich, P. Maunz, and C. Monroe. Manipulation and detection of a trapped Yb^+ hyperfine qubit. *Phys. Rev. A*, 76:052314, Nov 2007.

[90] Chr. Balzer, A. Braun, T. Hannemann, Chr. Paape, M. Ettler, W. Neuhauser, and Chr. Wunderlich. Electrodynamically trapped Yb^+ ions for quantum information processing. *Phys. Rev. A*, 73:041407, Apr 2006.

[91] H. Metcalf and P. van der Straten. *Laser Cooling and Trapping*. Springer, 1999.

[92] M. Roberts, P. Taylor, G. P. Barwood, W. R. C. Rowley, and P. Gill. Observation of the $^2S_{1/2}-^2F_{7/2}$ electric octupole transition in a single $^{171}Yb^+$ ion. *Phys. Rev. A*, 62:020501, Jul 2000.

[93] W. Demtröder. *Laser Spectroscopy: Basic Concepts and Instrumentation (Third Edition)*. Springer-Verlag, 2003.

[94] B. B. Blinov, D. Leibfried, C. Monroe, and D. J. Wineland. Quantum computing with trapped ion hyperfine qubits. *Quant. Inf. Proc.*, 3:45, 2004.

[95] M. Acton, K.-A. Brickman, P.C. Haljan, P. J. Lee, L. Deslauriers, and C. Monroe. Near-perfect simultaneous measurement of a qubit register. *Quant. Inf. and Comp.*, 6:465–482, 2006.

[96] R. Noek, G. Vrijsen, D. Gaultney, E. Mount, T. Kim, P. Maunz, and J. Kim. High speed, high fidelity detection of an atomic hyperfine qubit. *arXiv*, 1304.3511, 2013.

[97] E. D. Black. An introduction to Pound-Drever-Hall laser frequency stabilization. *Am. J. Phys.*, 69(1):79–87, April 2000.

[98] D. W. Preston. Doppler-free saturated absorption: Laser spectroscopy. *Am. J. Phys.*, 64:1432, 1996.

[99] S. Gerstenkorn, J. Verges, and J. Chevillard. *Atlas du spectre d'asorption de la molecule d'iode, 11000-14000 cm^{-1}*. Laboratoire Aime-Cotton, CNRS II, 91405 Orsay, France, 1982.

[100] S. Gerstenkorn and P. Luc. *Atlas du spectre d'asorption de la molecule d'iode, 14800-20000 cm^{-1}*. Centre National de la Recherche Scientifique, Paris, France, 1978.

[101] Pierre Dubé and Michael Trinczek. Hyperfine-structure splittings and absorption strengths of molecular-iodine transitions near the trapping frequencies of francium. *J. Opt. Soc. Am. B*, 21(6):1113–1126, Jun 2004.

[102] J.J. Sakurai. *Modern Quantum Mechanics*. Addison Wesley Publishing Company, 1994.

[103] R. Shankar. *Principles of Quantum Mechanics (second edition)*. Springer, 1994.

[104] E. Brion, L. H. Pedersen, and K. Mølmer. Adiabatic elimination in a lambda system. *J. Phys. A: Math. Theor.*, 40:1033–1043, 2007.

[105] U. I. Safronova, W. R. Johnson, M. S. Safronova, and J. R. Albritton. Relativistic many-body calculations of excitation energies and transition rates in ytterbiumlike ions. *Phys. Rev. A*, 66:022507, Aug 2002.

[106] U. I. Safronova and M. S. Safronova. Third-order relativistic many-body calculations of energies, transition rates, hyperfine constants, and blackbody radiation shift in $^{171}Yb^{+}$. *Phys. Rev. A*, 79:022512, Feb 2009.

[107] R. Zare. *Angular Momentum: Understanding Spatial Aspects in Chemistry and Physics*. Wiley-Interscience, 1988.

[108] A. R. Edmonds. *Angular Momentum in Quantum Mechanics*. Princeton University Press, 1985.

[109] D. Budker, D. Kimball, and D. Demille. *Atomic physics: An exploration through problems and solutions*. Oxford University Press, USA, 2008.

[110] E. H. Pinnington, G. Rieger, and J. A. Kernahan. Beam-laser measurements of the lifetimes of the $6p$ levels in Yb II. *Phys. Rev. A*, 56:2421–2423, Sep 1997.

[111] S. Olmschenk, D. Hayes, D. N. Matsukevich, P. Maunz, D. L. Moehring, K. C. Younge, and C. Monroe. Measurement of the lifetime of the $6p\,^2P^o_{1/2}$ level of Yb^{+}. *Phys. Rev. A*, 80:022502, Aug 2009.

[112] D. J. Wineland, M. Barrett, J. Britton, J. Chiaverini, B. DeMarco, W. M. Itano, B. Jelenković, C. Langer, D. Leibfried, V. Meyer, T. Rosenband, and T. Schätz. Quantum information processing with trapped ions. *Phil. Trans. R. Soc. A*, 361:1349–1361, 2003.

[113] R. Ozeri, W. M. Itano, R. B. Blakestad, J. Britton, J. Chiaverini, J. D. Jost, C. Langer, D. Leibfried, R. Reichle, S. Seidelin, J. H. Wesenberg, and D. J. Wineland. Errors in trapped-ion quantum gates due to spontaneous photon scattering. *Phys. Rev. A*, 75:042329, Apr 2007.

[114] A.E. Siegman. *Lasers*. University Science Books, Sausalito, CA, 1986.

[115] A. Yariv. *Optical Electronics in Modern Communications, 5th edition*. Oxford University Press, 1997.

[116] W. C. Campbell. Sech-pulse soup for the soul. *Unpublished manuscript*, June 2010.

[117] J. I. Dadap, G. B. Focht, D. H. Reitze, and M. C. Downer. Two-photon absorption in diamond and its application to ultraviolet femtosecond pulsewidth measurement. *Opt. Lett.*, 16(7):499, Apr. 1991.

[118] K. Ihara, S. Zaitsu, and T. Imasaka. Autocorrelator consisting of a solar-blind photomultiplier for use in the near-ultraviolet region. *Review of Scientific Instruments*, 76:026109, 2005.

[119] Yoshihiro Takagi. Simple autocorrelator for ultraviolet pulse-width measurements based on the nonlinear photoelectric effect. *Applied Optics*, 33:6328, 1994.

[120] N. Rosen and C. Zener. Double Stern-Gerlach experiment and related collision phenomena. *Phys. Rev.*, 40:502, 1932.

[121] N. V. Vitanov and P. L. Knight. Coherent excitation of a two-state system by a train of short pulses. *Phys. Rev. A*, 52:2245, 1995.

[122] R. T. Robiscoe. Extension of the Rosen-Zener solution to the two-level problem. *Phys. Rev. A*, 17:247, 1978.

[123] K. P. Birch. http://www.kayelaby.npl.co.uk/general_physics/2_5/2_5_7.html, July 2013.

[124] K. P. Birch and M. J. Downs. Correction to the updated Edlén equation for the refractive index of air. *Metrologia*, 31:315, 1994.

[125] R.J. Glauber. Coherent and incoherent states of the radiation field. *Phys. Rev.*, 131:2766–2788, 1963.

[126] R. J. Glauber. *Quantum Theory of Optical Coherence*. Wiley-VCH, 2007.

[127] E. C. G. Sudarshan. Equivalence of semiclassical and quantum mechanical descriptions of statistical light beams. *Phys. Rev. Lett.*, 10:277–279, Apr 1963.

[128] W. C. Campbell. Wes's notes on spin-dependent kicks. *Unpublished manuscript*, June 2011.

[129] M. Abramowitz and I. A. Stegun. *Handbook of Mathematical Functions*. National Bureau of Standards, June 1964.

[130] P.L. Kapitza and P.A.M. Dirac. The reflection of electrons from standing light waves. *Math. Proc. Cambridge Phil. Soc.*, 29:297–300, 1933.

[131] R. E. Sapiro, R. Zhang, and G. Raithel. Atom interferometry using Kapitza-Dirac scattering in a magnetic trap. *Phys. Rev. A*, 79:043630, 2009.

[132] Phillip L. Gould, George A. Ruff, and David E. Pritchard. Diffraction of atoms by light: The near-resonant Kapitza-Dirac effect. *Phys. Rev. Lett.*, 56:827, 1986.

[133] R. J. Cook and A. F. Bernhardt. Deflection of atoms by a resonant standing electromagnetic wave. *Phys. Rev. A*, 18:2533–2537, Dec 1978.

[134] Philip E. Moskowitz, Phillip L. Gould, Susan R. Atlas, and David E. Pritchard. Diffraction of an atomic beam by standing-wave radiation. *Phys. Rev. Lett.*, 51:370–373, Aug 1983.

[135] Yu. B. Ovchinnikov, J. H. Müller, M. R. Doery, E. J. D. Vredenbregt, K. Helmerson, S. L. Rolston, and W. D. Phillips. Diffraction of a released Bose-Einstein condensate by a pulsed standing light wave. *Phys. Rev. Lett.*, 83:284–287, Jul 1999.

[136] J.-A. Currivan, A. Ullah, and M.D. Hoogerland. The initial velocity dependence of the quantum resonance in the delta-kicked rotor. *EPL*, 85:30005, 2009.

[137] L. Deng, E. W. Hagley, J. Denschlag, J. E. Simsarian, Mark Edwards, Charles W. Clark, K. Helmerson, S. L. Rolston, and W. D. Phillips. Temporal, matter-wave-dispersion Talbot effect. *Phys. Rev. Lett.*, 83:5407–5411, Dec 1999.

[138] D. Leibfried, D. M. Meekhof, B. E. King, C. Monroe, W. M. Itano, and D. J. Wineland. Experimental determination of the motional quantum state of a trapped atom. *Phys. Rev. Lett.*, 77:4281–4285, Nov 1996.

[139] J. F. Poyatos, J. I. Cirac, R. Blatt, and P. Zoller. Trapped ions in the strong-excitation regime: Ion interferometry and nonclassical states. *Phys. Rev. A*, 54:1532–1540, Aug 1996.

[140] C. Monroe, D. M. Meekhof, B. E. King, and D. J. Wineland. A "Schrödinger Cat" superposition state of an atom. *Science*, 272:1131–1136, May 1996.

[141] I. A. Pedrosa, A. Rosas, and I. Guedes. Exact quantum motion of a particle trapped by oscillating fields. *J. Phys. A: Math. Gen.*, 38:7757–7763, 2005.

[142] A. Luis. Quantum mechanics as a geometric phase: phase-space interferometers. *J. Phys. A: Math. Gen.*, 34:7677–7684, 2001.

[143] Xiaoguang Wang and Paolo Zanardi. Simulation of many-body interactions by conditional geometric phases. *Phys. Rev. A*, 65:032327, Mar 2002.

[144] R. E. A. C. Paley. A remarkable series of orthogonal functions. *Proc. London Math. Soc.*, 34:241–279, 1931.

[145] D. Hayes, S. M. Clark, S. Debnath, D. Hucul, I. V. Inlek, K. W. Lee, Q. Quraishi, and C. Monroe. Coherent error suppression in multiqubit entangling gates. *Phys. Rev. Lett.*, 109:020503, Jul 2012.

[146] C. D. B. Bentley, A. R. R. Carvalho, D. Kielpinski, and J. J. Hope. Fast gates for ion traps by splitting laser pulses. *New Journal of Physics*, 15:043006, Apr. 2013.

[147] Charles H. Bennett, David P. DiVincenzo, John A. Smolin, and William K. Wootters. Mixed-state entanglement and quantum error correction. *Phys. Rev. A*, 54:3824–3851, Nov 1996.

[148] Scott Hill and William K. Wootters. Entanglement of a pair of quantum bits. *Phys. Rev. Lett.*, 78:5022–5025, Jun 1997.